

**TRACKING THE EVOLUTION OF MAGMATIC VOLATILES
FROM THE MANTLE TO THE ATMOSPHERE USING
INTEGRATIVE GEOCHEMICAL AND GEOPHYSICAL
METHODS**

by

Nathalie Vigouroux-Caillibot
M.Sc., University of Oregon, 2006
B.Sc., McGill University, 2003

THESIS SUBMITTED IN PARTIAL FULFILLMENT OF
THE REQUIREMENTS FOR THE DEGREE OF

DOCTOR OF PHILOSOPHY

In the
Department of Earth Sciences

© Nathalie Vigouroux-Caillibot 2011

SIMON FRASER UNIVERSITY

Spring 2011

All rights reserved. However, in accordance with the *Copyright Act of Canada*, this work may be reproduced, without authorization, under the conditions for *Fair Dealing*. Therefore, limited reproduction of this work for the purposes of private study, research, criticism, review and news reporting is likely to be in accordance with the law, particularly if cited appropriately.

APPROVAL

Name: Nathalie Vigouroux-Caillibot
Degree: Doctor of Philosophy
Title of Thesis: Tracking The Evolution Of Magmatic Volatiles From The Mantle To The Atmosphere Using Integrative Geochemical And Geophysical Methods

Examining Committee:

Chair: **Shahin Dashtgard**
[Correct title – Consult your Grad Secretary/Assistant

Dr. Glyn Williams-Jones
Senior Supervisor
Correct title – Consult your Grad Secretary/Assistant

Dr. Kirstie Simpson
Supervisor
Correct title – Consult your Grad Secretary/Assistant

Dr. Kelly Russell
Supervisor
Correct title – Consult your Grad Secretary/Assistant

Dr. Dan Marshall
Internal Examiner
Correct title – Consult your Grad Secretary/Assistant

Dr. Laurence Coogan
External Examiner
Correct title – Consult your Grad Secretary/Assistant
University of Victoria

Date Defended/Approved: January 7th 2011



SIMON FRASER UNIVERSITY
LIBRARY

Declaration of Partial Copyright Licence

The author, whose copyright is declared on the title page of this work, has granted to Simon Fraser University the right to lend this thesis, project or extended essay to users of the Simon Fraser University Library, and to make partial or single copies only for such users or in response to a request from the library of any other university, or other educational institution, on its own behalf or for one of its users.

The author has further granted permission to Simon Fraser University to keep or make a digital copy for use in its circulating collection (currently available to the public at the "Institutional Repository" link of the SFU Library website <www.lib.sfu.ca> at: <<http://ir.lib.sfu.ca/handle/1892/112>>) and, without changing the content, to translate the thesis/project or extended essays, if technically possible, to any medium or format for the purpose of preservation of the digital work.

The author has further agreed that permission for multiple copying of this work for scholarly purposes may be granted by either the author or the Dean of Graduate Studies.

It is understood that copying or publication of this work for financial gain shall not be allowed without the author's written permission.

Permission for public performance, or limited permission for private scholarly use, of any multimedia materials forming part of this work, may have been granted by the author. This information may be found on the separately catalogued multimedia material and in the signed Partial Copyright Licence.

While licensing SFU to permit the above uses, the author retains copyright in the thesis, project or extended essays, including the right to change the work for subsequent purposes, including editing and publishing the work in whole or in part, and licensing other parties, as the author may desire.

The original Partial Copyright Licence attesting to these terms, and signed by this author, may be found in the original bound copy of this work, retained in the Simon Fraser University Archive.

Simon Fraser University Library
Burnaby, BC, Canada

ABSTRACT

This thesis characterizes the transfer of magmatic volatiles through the mantle and the crust to the atmosphere through the integration of melt inclusion data for pre-eruptive volatile contents with surface measurements of volcanic degassing (recorded in micro-gravity changes and volcanic fumarole and plume gas compositions) at two contrasting volcanoes: Sierra Negra, Galápagos Islands and Kawah Ijen, Indonesia. In particular, it explores the process of fluid transfer in the mantle, the partitioning of volatile elements during mantle melting and degassing of the magma through the crust, and the effect of near-surface (e.g., interactions with groundwater and hydrothermal fluids), and surface processes (e.g., cooling and mixing with air) on the gas species. The effects of differences in initial volatile content and internal volcano structure on the types of eruptions and emissions recorded at each volcano are also discussed.

The comparison of Sierra Negra and Kawah Ijen volcanoes reveals that differences in style of volcanic activity are primarily a function of magmatic plumbing system as opposed to differences in initial volatile content. In both cases, permeability of the crust and degassing style have exerted a dominant control over the recent style of activity (last century). Recent eruptions at Sierra Negra are not necessarily associated with magma recharge into shallow reservoirs but can be caused by subtle changes in the pressure regime of a magma chamber, a process which is closely associated with degassing and system permeability. Large explosive eruptions at Kawah Ijen are currently impeded by the open system (permeable) flow of magma and gas through the plumbing system. Hydrothermal systems play an important role in controlling the permeability of a system and the composition of the gases measured at the surface. The comparison of theoretically modeled gas compositions with actual measured compositions is an effective approach to studying the influence of hydrothermal systems at open vent volcanoes.

Keywords: Magmatic degassing; volcanic plume; melt inclusion; hydrothermal system; fumarole; micro-gravity; Sierra Negra; Kawah Ijen.

ACKNOWLEDGEMENTS

First and foremost I'd like to acknowledge my senior supervisor Glyn Williams-Jones for offering me the opportunity to research and travel to active volcanoes around the world. His guidance and support were invaluable. A big thank you to my supervisory committee: Kelly Russell and Kirstie Simpson for their support during my Ph.D and their review of this thesis. I'd also like to acknowledge Dan Marshall and Laurence Coogan for acting on the examining committee and reviewing this thesis.

Numerous other people have proved invaluable in enabling and assisting with the field work: Dennis Geist, Andres Gorki Ruiz, Bill Chadwick, Kim Berlo and members of the Galápagos National Park and the Charles Darwin Research Station for work in the Galápagos; Willy Williams-Jones, Vincent van Hinsberg, Guillaume Mauri, Samantha Scher, Stephanie Palmer, Kim Berlo as well as numerous volunteer field assistants and local miners Pa Im and Jumanto for work in Indonesia. Thank you to Paul Wallace for his continued support and assistance with some of the geochemical modeling. To my friends and colleagues at Simon Fraser University, you have made these last few years very memorable, in particular, Jolane Sorge, Shannon Frey, Nicholas Roberts and Dan Shugar. Finally, a special thank you to Matt for encouraging me to pursue my career goals and to my parents for their continued support over the years.

TABLE OF CONTENTS

Approval	ii
Abstract	iii
Acknowledgements	iv
Table of Contents	v
List of Figures	viii
List of Tables	xi
1: Introduction	1
1.1 Motivation	1
1.2 Methods	4
1.2.1 Melt inclusions.....	4
1.2.2 UV correlation spectrometry.....	7
1.2.3 MultiGAS plume sensors.....	8
1.2.4 “Giggenbach” fumarole sampling.....	9
1.2.5 Dynamic micro-gravity surveys	9
1.3 Approach	10
1.4 References	15
2: 4D Gravity Changes Associated with the 2005 Eruption of Sierra Negra Volcano, Galápagos	23
2.1 Abstract.....	23
2.2 Introduction	24
2.3 Geologic Setting and the 2005 Eruption	25
2.4 Methods	27
2.5 Gravity and Deformation Results	29
2.6 Discussion	32
2.7 Conclusions	40
2.8 Acknowledgments.....	42
2.9 Figures.....	43
2.10 Tables	49
2.11 References	50
3: The Source Components of Volatile and Fluid-Mobile Elements in Subduction Zones: a Melt Inclusion Study from Kawah Ijen Volcano, Indonesia	54
3.1 Abstract.....	54
3.2 Introduction	55
3.3 Geologic Setting	57

3.4	Methodology	60
3.4.1	Post-entrapment modification correction.....	62
3.5	Results.....	63
3.6	Discussion	67
3.6.1	Mantle source composition	68
3.6.2	Sediment, crust and serpentinite contributions to arc magmas	72
3.7	Conclusions	95
3.8	Acknowledgement	97
3.9	Figures.....	98
3.10	Tables	107
3.11	References	112

4: Integrated Geochemical Modeling of Magmatic Degassing and Hydrothermal Interaction: a Case Study from Kawah Ijen Volcano, Indonesia **124**

4.1	Abstract.....	124
4.2	Introduction	126
4.3	Geologic Setting	128
4.3.1	Kawah Ijen volcano	128
4.3.2	Crater lake and Banyu Pahit river	130
4.4	Methodology	131
4.4.1	Petrological sampling and analysis.....	131
4.4.2	Fumarole gas sampling and analysis.....	134
4.5	Results.....	135
4.5.1	Melt inclusion and matrix glass major and volatile element composition.....	135
4.5.2	Sulphur speciation and oxygen fugacity.....	140
4.5.3	Fumarole gas chemistry.....	140
4.6	Discussion	141
4.6.1	Magma evolution.....	141
4.6.2	Volatile evolution.....	142
4.6.3	Degassing modeling.....	148
4.6.4	Model magmatic fluid composition and comparison with measured fumarole compositions	154
4.7	Summary and Conclusions	161
4.8	Acknowledgments.....	164
4.9	Figures.....	165
4.10	Tables	180
4.11	References	186

5: Underestimating Volcanic Degassing: the case of Kawah Ijen Volcano, Indonesia **193**

5.1	Abstract.....	193
5.2	Introduction	194
5.3	Geologic Setting and Magmatic History.....	195
5.4	Sample Description and Methods.....	197

5.5	Effects of Dilution, Reaction with Air and Precipitation of Native S on Plume Compositions	199
5.6	Discussion	201
5.7	Acknowledgments.....	205
5.8	Figures.....	206
5.9	Tables	210
5.10	References	213
6:	Conclusions	216
6.1	Volatile Transfer During Slab Subduction.....	216
6.2	Volatile Transfer During Magma Ascent Through the Crust and Degassing	218
6.3	Volatile Ratios in Volcanic Plumes and Effects of Cooling and Mixing with Air	223
6.4	Concluding Remarks.....	224
	Appendices.....	226
	Appendix A.....	227
	Appendix B.....	228
	Sample preparation.....	228
	Infrared spectroscopy	229
	Electron microprobe.....	231
	References	232
	Appendix C.....	244
	Modeling procedure for $D^{\text{vap-melt}}$ values	244
	References	250
	Appendix D.....	252

LIST OF FIGURES

Figure 2-1 Digital Elevation Map of the Galápagos archipelago showing the location of Sierra Negra and Fernandina calderas.....	43
Figure 2-2 Digital Elevation Map of the summit area of Sierra Negra showing the location of the gravity and continuous GPS stations referred to in this study.....	44
Figure 2-3 Residual gravity change (BCFAG corrected) recorded at all stations referenced to June 2001.....	44
Figure 2-4 Maximum $\Delta g/\Delta h$ gradient for the time period 2002-2005 and 2006-2007 and theoretical FAG and calculated BCFAG	45
Figure 2-5 Simplified cross-section through the caldera showing the location and geometry of the magma body in 2D (A), and in 3D (B).....	46
Figure 2-6 Modeled gravity change between June 2002 and 2005 caused by a 800-m thick homogeneous sill with 10% vesiculation.....	47
Figure 2-7 Modeled gravity change between June 2002 and 2005 caused by a 700-m thick sill with 10% vesiculation and a 50 m thick foam layer with 50% vesicularity at the top.....	48
Figure 3-1 Map showing the locations of the volcanic arcs discussed in this study.....	98
Figure 3-2 Major element composition, K_2O versus SiO_2 , of the Sunda arc magmas compared to other arcs discussed in this study.....	99
Figure 3-3 Multi-element spider diagram normalized to depleted MORB mantle.	100
Figure 3-4 CO_2 versus H_2O contents of melt inclusions from Kawah Ijen.....	101
Figure 3-5 Dy/Yb versus Nb/Y of average melt inclusion compositions from each arc volcano.	102
Figure 3-6 Th-La-Sm ternary showing the composition of arc magmas	103
Figure 3-7 a) Th/La, b) Sr/Nd and c) Cl/Nd versus H_2O/Ce of arc magmas.	104
Figure 3-8 Ternary diagram Sr-Nd-Ba illustrating the role of the three subduction component reservoirs	105
Figure 3-9 Variations in volatile content (a) H_2O ; b) Cl; c) S and d) F) of parental subduction zone magmas with respect to Sr.....	106
Figure 4-1 a) The location of the Ijen Caldera Complex on the island of Java, Indonesia, b) The location of Kawah Ijen volcano within the Ijen Caldera Complex.....	165

Figure 4-2 Compositional profiles (length and width) through an olivine phenocryst.	166
Figure 4-3 K ₂ O variation diagrams versus: a) SiO ₂ and b) MgO	167
Figure 4-4 MgO variation diagrams versus: a) CaO/Al ₂ O ₃ ratio, b) FeO _{total} (all iron is reported as FeO) and c) TiO ₂	168
Figure 4-5 Variation in P ₂ O ₅ content versus a) SiO ₂ and b) MgO.	169
Figure 4-6 H ₂ O versus CO ₂ content of: a) the mafic melt inclusions (basaltic and basaltic-andesite) and b) the dacitic melt inclusions and matrix glasses.	170
Figure 4-7 Variation of H ₂ O content with a) S, b) Cl, and c) F contents in the melt inclusions and matrix glasses.....	171
Figure 4-8 a) Sulphur contents in the basaltic and dacitic melt inclusions versus oxygen fugacity, b) calculated oxygen fugacity versus melt inclusion H ₂ O content and volatile saturation pressure	172
Figure 4-9 H ₂ O-CO ₂ -S _{total} ternary diagram comparing the Kawah Ijen fumarole gases with high temperature (> 350 °C) fumarole gases from other arc volcanoes	173
Figure 4-10 He-N ₂ -Ar ternary diagram for the Kawah Ijen fumarole gases.....	174
Figure 4-11 HF-HCl-S _{total} ternary diagram comparing the Kawah Ijen fumarole gases with high temperature (> 350 °C) fumarole gases from other arc volcanoes	175
Figure 4-12 Variation in the ratio of a) H ₂ O, b) S, c) Cl and d) F over K ₂ O contents as a function of melt inclusion trapping pressure and depth.....	176
Figure 4-13 Variation of the K ₂ O/P ₂ O ₅ ratio with a) K ₂ O content (wt%), b) K ₂ O/Cl ratio and c) K ₂ O/F ratio.....	177
Figure 4-14 Pressure (and depth) versus modeled D ^{vap-melt} values for S within the Kawah Ijen basaltic magma and for the evolution of basaltic to dacitic compositions.....	178
Figure 4-15 Pressure (and depth) versus modeled D ^{vap-melt} values for Cl within the dacitic magma and for a system where basaltic magma is evolving to dacitic compositions.	179
Figure 5-1 a) The location of the Ijen Caldera Complex on the island of Java, Indonesia, b) the location of Kawah Ijen volcano within the Ijen Caldera Complex	206
Figure 5-2 H ₂ O-CO ₂ -SO ₂ ternary diagram comparing the fumarole and plume compositions.....	207
Figure 5-3 Volatile ratios a) H ₂ O/CO ₂ , b) H ₂ O/SO ₂ and c) CO ₂ /SO ₂ versus the % dilution by air calculated for each plume sample.....	208
Figure 5-4 Saturation of Kawah Ijen fumarole gases with respect to native S.....	209
Figure 6-1 Microphotographs of a) tephra, b-c) olivine crystals and d-f) melt inclusions from sample layers OT and TO at Kawah Ijen.....	242
Figure 6-2 Ba contents versus volatile elements (both ratioed to La).....	243

Figure 6-3 Concentration pathlength of SO₂ through the plume versus time
(minutes) taken to traverse..... 254

LIST OF TABLES

Table 2-1 Summary of gravity and deformation data at Sierra Negra.....	49
Table 3-1 Kawah Ijen melt inclusions (corrected for post-entrapment modifications).	107
Table 4-1 Kawah Ijen melt inclusion and matrix glass compositions	180
Table 4-2 Fumarole gas compositions and sampling temperatures (2007 & 2008)	184
Table 4-3 Model magmatic fluid compositions	185
Table 5-1 MultiGAS plume measurements	210
Table 5-2 Flyspec SO ₂ flux measurements.....	211
Table 5-3 Partial fumarole compositions.....	212
Table 6-1 Major and volatile element concentrations in basaltic glasses and melt inclusions from Sierra Negra	227
Table 6-2 Analyzed olivine-hosted melt inclusion compositions from Kawah Ijen (uncorrected for post-entrapment modification).....	234
Table 6-3 Description of melt inclusions analysed	240
Table 6-4 Additional analysed olivine-hosted melt inclusion compositions from Kawah Ijen (uncorrected for post-entrapment modification).....	251

1: INTRODUCTION

1.1 Motivation

The study of magmatic volatiles (e.g., H₂O, CO₂, S, Cl and F) is fundamental to our understanding of a variety of volcanic and geologic processes such as magma generation, ascent, eruptability and eruption style (explosivity). Most research on magmatic volatiles focuses on one of following aspects: 1) the geochemistry and flux of these species into the atmosphere or the hydrosphere, with the aim of understanding changes in volcanic activity or modeling the effects on climate and water resources; 2) the abundance and geochemistry of magmatic volatiles in various reservoirs (e.g., mantle, oceanic and continental crust) and their transfer (flux) between these reservoirs (e.g., via mantle melting, devolatilization of the oceanic lithosphere during subduction); 3) the behaviour of these volatile species in near-surface magmas when they become saturated and exsolve into a supercritical fluid or vapour phase, with the aim of better understanding the effects of degassing on eruption dynamics and measured volatile contents at the surface; and 4) the nature of exsolved volatile phases in the upper crust in relation to the formation of hydrothermal fluids and mineral deposits.

Our understanding of magmatic volatiles through these different research themes has expanded greatly in the last 40 years due to improved analytical techniques for measuring volatile concentrations in both silicate glasses and

minerals as well as in volcanic gases emitted at the surface. Different methodologies target different problems. For example, the analysis of mineral-hosted melt inclusions reveals the pre-eruptive volatile content of a magma as it ascends, crystallizes and degasses, whereas the collection of surface fumarole/plume samples reveals the composition of the exsolved fraction. With our current “tool box” of field- and laboratory-based analytical techniques for measuring volatile concentrations, a logical step is to integrate these methodologies and merge our understanding of the different stages of volatile evolution. Numerous recent studies have adopted this philosophy and approach; some have combined melt inclusion data with plume gas compositions at active volcanoes to gain insight into magma degassing depths and magma recharge processes (e.g., Roberge et al., 2009; Edmonds et al., 2009), others have combined fumarole gas compositions with SO₂ flux determinations to constrain the total volatile budget of an actively degassing volcano (e.g., Goff et al., 1998; Aiuppa et al., 2005a,b). These studies have demonstrated the potential of integrative geochemical studies but have also raised numerous new questions/issues that need to be addressed with more complete, thorough integrative studies (e.g. total S flux underestimates due to the lack of H₂S determinations in the plume; Aiuppa et al., 2005b).

This thesis integrates geochemical and geophysical methods with modeling in order to characterize the transfer of volatiles through the mantle and the crust to the atmosphere. The two questions/themes guiding this research are:

- 1) How do volatile ratios change as magma ascends from the mantle, through

the crust and out to the atmosphere? What does this reveal about the process of fluid transfer in the mantle, the partitioning of volatile elements during mantle melting and degassing of the magma through the crust, and finally the effect of near-surface (e.g., interactions with groundwater and hydrothermal fluids), and surface processes (e.g., cooling and mixing with air) on the gas species? 2) How do differences in initial volatile contents and internal volcano structure influence the types of eruptions and the emissions recorded at a volcano?

More specifically, this thesis offers insight into the following problems previously recognized by other workers:

- In subduction zones, how are volatile elements transferred from the subducting slab to the overlying mantle wedge? What is the reservoir for these elements in the oceanic slab? Do the volatile elements fractionate from each other during transfer from the slab to the mantle wedge? (Chapter 3).
- How do volatile elements exsolve from a silicate melt upon ascent through the crust? Is this process occurring in a closed or open fashion (with respect to the transfer of mass into and out of the magma)? How are the volatile elements fractionated from each other during this process? (Chapters 2 and 4).
- How do the volatile species fractionate from each other in the vapour phase upon shallow ascent and degassing at the surface? (Chapter 4).

- How are the volatile species fractionated from each other at the surface, when the magmatic vapours cool and interact with ambient air? What affect does this have on the measured SO₂ flux and the calculated total volatile flux? How does this affect estimates of magma mass and volume flux rates in the subsurface? (Chapter 5).

1.2 Methods

The following sections introduce the different methodologies employed in this research. A more detailed account of the methods used can be found in each chapter (2-5).

1.2.1 Melt inclusions

Almost 40 years ago, E. Roedder and V.S. Sobolev simultaneously pioneered the use of melt inclusions from different ends of the globe. Roedder explored silicate melt inclusions in the lunar basalts brought back from the Apollo 11 and 12 missions (e.g., Roedder and Weiblen, 1970), while Sobolev was working with other former USSR scientists to develop the heating stage for the determination of crystallization temperatures of minerals with trapped melt inclusions and attempted to make the first determinations of volatile contents in these melt inclusions (e.g., Sobolev et al., 1971). Results of these early works are summarized in Sobolev and Kostyuk (1975) and Roedder (1979; 1984).

These early efforts where not widely adopted for lack of reliable analytical techniques and uncertainty over the nature of melt inclusions. 1) They were suspected of representing boundary layer (diffusion limited) melts at the edge of

crystals (e.g., Watson et al., 1982) or melts that had been trapped but later experienced post-entrapment diffusion and crystallization (e.g., Gaetani and Watson, 2000), 2) melt inclusion compositions were suggesting highly heterogeneous melts (e.g., Nielsen et al., 1995), and 3) homogenization temperatures were exceeding those determined by other methods (see review by Lowenstern, 2003). In the last 15-20 years, with the development of more advanced micro-analytical techniques (electron microprobe, ion microprobe, IR microspectroscopy) along with more in-depth studies, melt inclusions have become one of the most widely used petrographic tools for geochemists and igneous petrologists. It is important to note that melt inclusions are still not without their limitations. Workers have long recognized the effects of post-entrapment cooling, crystallization and diffusion in high temperature melt inclusions (e.g., olivine-hosted melt inclusions; Nielsen et al., 1998; Gaetani and Watson, 2000) and numerous studies have been aimed at quantifying this effect and correcting for it (e.g., Danyushevsky et al., 2000; 2002). Boundary layer diffusion-limited effects may be important in some systems (e.g., Baker, 2008) although many melt inclusion studies have concluded that in most cases, boundary layer effects are limited or can be avoided by analyzing the largest melt inclusions present (e.g., Anderson, 1974; Wallace, 2005; Métrich and Wallace, 2008). Other processes such as dissolution-reaction-mixing effects are still a factor of concern for some melt inclusion datasets (e.g., Danyushevsky et al., 2004), but if care is taken when interpreting the melt inclusion record, these effects can be identified.

Early workers studied the degassing pattern of S and Cl in magmas using electron microprobe analyses (e.g., Métrich and Clocchiatti, 1989). Workers now analyse for S and Cl using both the electron and the ion microprobe (e.g., Hauri, 2002). The analysis of F with the microprobe is complicated by the position of its primary X-ray energy on the shoulder of a more dominant energy peak of Fe in Fe-bearing glasses and matrix effects affect F determination using the ion probe. However, recent advances in data manipulation have improved our ability to analyse F with both of these analytical techniques (e.g., Hauri, 2002; Witter and Kuehner, 2004).

For H and C contents, different analytical techniques are required for these atomically light elements (although ion microprobe analysis is now calibrated to analyse for these). Vibrational microspectroscopy in the infrared and near-infrared range has provided researchers with the means to obtain H₂O and CO₂ contents in silicate melts as well as information on the speciation of these volatiles (e.g., OH⁻ versus molecular H₂O; Stolper, 1982). The advent of microspectroscopic techniques (micro Fourier Transform Infrared – FTIR spectroscopy, micro Raman spectroscopy and the ion microprobe) has allowed for H₂O and CO₂ contents to be determined in melt inclusions (see Devine et al., 1995 for review).

Melt inclusions are now routinely analysed in a variety of different igneous minerals across all types of igneous rocks in an effort to characterize a range of processes including: 1) mantle melting mechanisms (e.g., Gurenko and Chaussidon, 1995; Vigouroux et al., 2008a), 2) mantle enrichment processes

(e.g., Schiano et al., 1994; Vigouroux et al., 2008a), 3) fluid and volatile transport in the mantle from a variety of tectonic settings (e.g., Sobolev and Chaussidon, 1996; Saal et al., 2002; Portnyagin et al., 2007), 4) magma ascent, storage and mixing processes in the middle to upper crust (e.g., Hervig and Dunbar, 1992; Blundy and Cashman, 2005; Reubi and Blundy, 2008; Vigouroux et al., 2009) and 5) exsolution of magmatic volatiles, degassing mechanisms and link to eruption dynamics (e.g., Barclay et al., 1996; Roggensack et al., 1997; Spilliaert et al., 2006; Johnson et al., 2008).

1.2.2 UV correlation spectrometry

When the UV correlation spectrometer (COSPEC) emerged as a tool for estimating the SO₂ flux from a polluting source (e.g., Sperling, 1975), the volcanological community could now measure degassing in a passive, remote manner, which limited risky exposure to active volcanoes (e.g., Crafford, 1975). Differential optical absorption spectroscopy (DOAS) was also being used for tracking atmospheric trace pollutants (Global Ozone Monitoring Experiment) aboard the satellite ERS-2 (e.g., Eisinger and Burrows, 1998) as well as for estimating SO₂ fluxes at active volcanoes via land-based remote measurement (e.g., Edner et al., 1994). The COSPEC was the preferred monitoring tool over the next 25-30 years until smaller, portable versions of the DOAS and the COSPEC emerged (mini-DOAS; Galle et al., 2003, FLYSPEC; Horton et al., 2006). Although the COSPEC is still used by some researchers, the portable nature of the mini-DOAS and the FLYSPEC, as well as their more cost-effective nature, allow them to be deployed more frequently and at more volcanoes,

including those where access by road or plane is not feasible (see review by Nadeau and Williams-Jones, 2008). Recent studies have advanced our understanding of the sources of uncertainty, namely wind speed determination at plume height (e.g., Williams-Jones et al., 2006; Nadeau and Williams-Jones, 2009), and have reduced the errors associated with each measurement.

1.2.3 MultiGAS plume sensors

With the advent of portable gas sensors for environmental monitoring in the industrial work place, volcanologists have been able to custom build a portable Multi-component Gas Analyser System (MultiGAS) for the determination of gas species in an accessible volcanic plume (Shinohara, 2005; Aiuppa et al., 2005a). This instrument has three main advantages over other multi-component gas detectors (e.g., Open-Path FTIR; Francis et al., 1996; McGee and Gerlach, 1998) in that it is portable, does not require an external source of radiation (UV or IR) and is more cost-effective. Due to advances in miniature electrochemical cells and IR sensors (e.g., Alphasense Ltd.), the MultiGAS is able to analyse for the major volcanic gas species: H₂O (using pressure, temperature and relative humidity sensors), CO₂, CO, SO₂, H₂S, HCl with the potential to add more species in the near future. There is also the potential to incorporate portable stable isotope sensors (e.g., the Picarro ¹³C isotope analyser) with the MultiGAS, making it a more complete geochemical tool and more comparable to the traditional evacuated-flask sampling technique for fumarole gases (e.g., Giggenbach, 1975).

1.2.4 “Giggenbach” fumarole sampling

Volcanologists commonly use the evacuated-flask method to sample fumarole gases. The method was initially developed by researchers at the Hawaiian Volcano Observatory in the 1940s (e.g., Jaggar, 1940). This technique was improved over the years to minimize contamination of the gas samples by the sampling material (e.g., Giggenbach, 1975) and improve the capture and subsequent analysis of the gas species (e.g., Giggenbach and Matsuo, 1991; Giggenbach et al., 2001; Montegrossi et al., 2001; Sortino et al., 2006). The main advantage of this sampling technique, commonly termed “Giggenbach” sampling (after the Pyrex bottle that Werner Giggenbach developed), is the full range of gas species that can be analysed (uncontaminated or diluted with air), the potential to analyse minor species including trace metals (e.g., Fischer et al., 1998) and the possibility of analyzing the isotopic composition of the gas species. The main disadvantages are the nature of the sampling (the need to access the high temperature gases in-situ) and the laboratory processing times required.

1.2.5 Dynamic micro-gravity surveys

A long-standing geophysical tool, used for a range of applications from mineral exploration to volcanic monitoring, is the spring gravimeter (e.g., Lacoste and Romberg - Scintrex Inc.). Repeat, relative microgravity measurements can record changes in mass and/or density that take place in volcanic areas (e.g., Yokoyama and Tajima, 1957) with corrections made for earth and oceanic tidal loading, instrument calibration issues and drift, and changes in elevation of the survey area over time (see review in Williams-Jones et al., 2008). When

combined with seismic and deformation surveys (e.g., Global Positioning System, Interferometric Synthetic Aperture Radar), microgravity surveys (in both continuous and dynamic/survey mode) can detect and provide an understanding of changes in subsurface mass and or density associated with magmatic activity (e.g., Vigouroux et al., 2008b; see review in Williams-Jones et al., 2008). When combined with estimates of volcanic gas fluxes, microgravity data can provide insight into magma degassing rates and mechanisms as well as changes in conduit permeability (e.g., Williams-Jones et al., 2003).

1.3 Approach

The aim of this study is to track the evolution of volatile species (H_2O , CO_2 , S, Cl and F) from the mantle, through the evolution of a magma in the crust, to the eruption or passive degassing of the magma at the surface and release of the volatiles to the atmosphere, by integrating the numerous geochemical and geophysical methods described above.

This thesis is written in manuscript format with each of the central chapters corresponding to a manuscript that has either been published or is to be submitted. My two field sites are actively degassing volcanoes from two contrasting tectonic settings: 1) the oceanic intra-plate hot spot volcano, Sierra Negra, in the Galápagos archipelago (Chapter 2), and 2) the subduction-related arc volcano, Kawah Ijen, on the island of Java, Indonesia (Chapters 3-5). A discussion of the regional tectonic setting for both localities is given in Chapters 2 and 3 for Sierra Negra and Kawah Ijen, respectively. Both locations offer relatively easy access to the volcano itself and to the fumaroles and volcanic

plume emanating from them. Additionally, both volcanoes have been studied prior to this work, offering a background of knowledge on the petrography, geochemistry and geophysical aspects of each.

The recent activity at Sierra Negra (eruption of 2005 and pre-eruptive activity since 1991) has been described by numerous authors (Chadwick et al., 2006; Yun et al., 2006; Geist et al., 2006; 2008) and the physical volcanology, structural development and petrology of the lavas at Sierra Negra have been described by Reynolds et al. (1995) and Reynolds and Geist (1995). Additionally, two published studies of the fumaroles at Sierra Negra are available (Colony and Nordlie, 1973; Goff et al., 2001); At Kawah Ijen, studies (some dating back to the 1920s when the Dutch still occupied Indonesia) describe the structural and magmatic evolution of Kawah Ijen and the Ijen caldera complex (Sitorus, 1990; Berlo, 2001; van Hinsberg, 2001 and references therein; Handley et al., 2007). The crater lake structure, as well as the geochemistry of the lake waters, acid springs and fumarole gases were studied in the 1990s and 2000s (Delmelle and Bernard, 1994, 2000; Delmelle et al., 2000; van Hinsberg, 2001; Takano et al., 2004; Palmer, 2009; van Hinsberg et al., 2010a,b).

At Sierra Negra, the project focuses on integrating geophysical and geochemical methods to understand the physical process of shallow magma storage, degassing and eruption. My research consisted of 5 field surveys of microgravity (over 2 years). Field work was performed with the collaboration of Andres Gorki Ruiz (University of Idaho), Glyn Williams-Jones (senior supervisor), Bill Chadwick (NOAA-Oregon State University) and Kim Berlo (McGill University).

Samples of basaltic glass from the submarine flanks of Sierra Negra were obtained from Dennis Geist (University of Idaho) and analysed for volatile and major element composition (Appendix A). The microgravity measurements were collected following the 2005 eruption of Sierra Negra and are compared to measurements collected prior to the eruption (Geist et al., 2006; D. Johnson – previously unpublished). Combined with deformation data (continuous and survey GPS data collected and processed by Bill Chadwick, Dennis Geist and Andres Ruiz) and estimates of pre-eruptive and erupted volatile concentrations (Koleszar et al., 2007; Appendix A), these data sets reveal the mechanism by which the latest eruption of Sierra Negra proceeded. The study is published as: *Vigouroux, N., Williams-Jones, G., Chadwick, W., Geist, D., Ruiz, A.G. & Johnson, D. (2008). 4D gravity changes associated with the 2005 eruption of Sierra Negra, Galapagos. Geophysics, 73 (6), WA29-35.* The exact nature of the collaboration is summarized at the beginning of Chapter 2.

At Kawah Ijen, the project focuses on an integrative geochemical study of the transport of volatiles from the mantle, through shallow crustal reservoirs and overlying hydrothermal systems, to the surface. My research was conducted over 3 field seasons and consisted of yearly fumarole gas sampling, MultiGAS plume analysis, SO₂ flux determinations and tephra (pyroclastic rock) sampling for melt inclusion and matrix glass analysis. This field work was done in collaboration with the Kawah Ijen research team composed of scientists from both Simon Fraser University and McGill University, as well as numerous volunteers. Results of the study are presented in collaboration with Glyn Williams-Jones, Paul Wallace

(University of Oregon), Adam Kent (Oregon State University), Katherine Kelly (University of Rhode Island), Vincent van Hinsberg (McGill University), Kim Berlo (McGill University) and A.E. (Willy) Williams-Jones (McGill University) and are reported in Chapters 3-5 with additional material presented in Appendices B-D. The exact nature of the collaborations are summarized at the beginning of each chapter. Chapter 3 uses olivine-hosted melt inclusion major, trace and volatile element compositions to identify the nature of the mantle source for the parental magmas of Kawah Ijen, the nature of the subduction-derived fluid introduced into this mantle and the origin of this fluid within the oceanic lithosphere. Results for Kawah Ijen are compared to another arc-front volcano in Indonesia, Galunggung (unpublished data from Katherine Kelly) and to published data for other arcs worldwide (Kamchatka: Portnyagin et al., 2007; Central America: Sadofsky et al., 2008; Mexico: Johnson et al., 2009). This comparison allows for global trends in subduction zone volatile recycling to be identified and quantification of the mobility of volatile elements during slab subduction. These results will be submitted for publication to the journal *Geochemistry, Geophysics, Geosystems*.

Chapter 4 combines the olivine-hosted melt inclusion record with additional olivine-hosted and orthopyroxene- and plagioclase-hosted melt inclusion data from Kim Berlo to define the magmatic and volatile evolution of the erupted products of Kawah Ijen. Matrix glass compositions from the basaltic tephra, the dacite pumice (from Kim Berlo) and the dome lava (van Hinsberg et al., 2010b) are also combined to obtain a complete magma differentiation and degassing trend. The data suggests that CO₂-rich vapour fluxing through the

plumbing system has been a dominant process at Kawah Ijen in the past. The melt inclusion and glass data are modeled using simple mass balance constraints to generate vapour-melt partition coefficients for the volatile elements S and Cl upon ascent, degassing and crystallization of the magma under different degassing style scenarios and magma compositions. These results are combined with fumarole gas H₂O and CO₂ contents to estimate the magmatic fluid composition currently degassing at Kawah Ijen. This model S-Cl fluid composition is then compared to the composition of fumarole gases, and crater lake and acid spring waters in order to model the effects of ascent and cooling of the magmatic fluid as well as possible interaction with the hydrothermal system. These results will be submitted for publication to the *Journal of Volcanology and Geothermal Research*.

Chapter 5 explores the recent activity at Kawah Ijen and estimates the rate of magma influx into the system required to sustain over 100 years of degassing unaccompanied by a magmatic eruption. The study combines the fumarole gas compositions with those determined in the plume, at various levels of dilution and reaction with air, concluding that there is a very significant depletion of magmatic SO₂ concentrations from the pure magmatic gas phase to the plume (up to 98% loss). This results in large underestimates in volcanic degassing rate (reflected in the low SO₂ flux measured: ~25 tonnes day⁻¹) in large part from S saturation of the magmatic gases and subsequent precipitation of S-bearing compounds in the vent and near-vent area. These results will be submitted for publication to the journal *Geology*.

Finally, the conclusions in Chapter 6 summarize the results of the research presented in this thesis and re-address the two guiding questions, emphasizing the need for integrative research and a multi-disciplinary approach to the understanding of magmatic and volcanic processes.

1.4 References

- Aiuppa, A., Federico, C., Giudice, G., Gurrieri, S., 2005a. Chemical mapping of a fumarolic field: La Fossa Crater, Vulcano Island (Aeolian Islands, Italy). *Geophys. Res. Lett.* 32 (13), L13309.
- Aiuppa, A., Inguaggiato, S., McGonigle, A.J.S., O'Dwyer, M., Oppenheimer, C., Padgett, M.J., Rouwet, D., Valenza, M., 2005b. H₂S fluxes from Mt. Etna, Stromboli, and Vulcano (Italy) and implications for the sulphur budget at volcanoes. *Geochim. Cosmochim. Acta* 69 (7), 1861-1871.
- Anderson, A.T. 1974. Evidence for a picritic, volatile-rich magma beneath Mt. Shasta, California. *J. Petrol.* 15 (2), 243-267.
- Baker, D.R. 2008. The fidelity of melt inclusions as records of melt composition. *Contrib. Mineral. Petrol.* 156 (3), 377-395.
- Barclay, J., Carroll, M.R., Houghton, B.F., Wilson, C.J.N., 1996. Pre-eruptive volatile content and degassing history of an evolving peralkaline volcano. *J. Volcanol. Geotherm. Res.* 74 (1-2), 75-87.
- Berlo, K., 2001. The magmatic evolution of the Ijen caldera, East Java, Indonesia. M.Sc. thesis, University of Utrecht, Netherlands.
- Blundy, J., Cashman, K., 2005. Rapid decompression-driven crystallization recorded by melt inclusions from Mount St. Helens volcano. *Geology* 33 (10), 793-796.
- Chadwick, W.W., Geist, D.J., Jónsson, S., Poland, M., Johnson, D.J., Meertens, C.M., 2006. A volcano bursting at the seams: Inflation, faulting, and eruption at Sierra Negra volcano, Galápagos. *Geology* 34 (12), 1025-1028.
- Colony, W.E., Nordlie, B.E., 1973. Liquid sulphur at Volcan Azufre, Galápagos Islands. *Econ. Geol.* 68 (3), 371-380.
- Crafford, T.C. 1975. SO₂ emission of the 1974 eruption of Volcán Fuego, Guatemala. *Bull. Volcanol.* 39 (4), 536-556.

- Danyushevsky, L.V., Della-Pasqua, F.N., Sokolov, S., 2000. Re-equilibration of melt inclusions trapped by magnesian olivine phenocrysts from subduction-related magmas: petrological implications. *Contrib. Mineral. Petrol.* 138 (1), 68-83.
- Danyushevky, L.V., Leslie, R.A.J., Crawford, A.J., Durance, P., 2004. Melt inclusions in primitive olivine phenocrysts: the role of localized reaction processes in the origin of anomalous compositions. *J.Petrol.* 45 (12), 2531-2553.
- Danyushevsk, L.V., Sokolov, S., Falloon, T.J., 2002. Melt inclusions in olivine phenocrysts: using diffusive re-equilibration to determine the cooling history of a crystal, with implications for the origin of olivine-phyric volcanic rocks. *J.Petrol.* 43 (9), 1651-1671.
- Delmelle, P., Bernard, A., 2000. Downstream composition changes of acidic volcanic waters discharged into the Banyupahit stream, Ijen caldera, Indonesia. *J.Volcanol.Geotherm.Res.* 97 (1-4), 55-75.
- Delmelle, P., Bernard, A., 1994. Geochemistry, mineralogy, and chemical modeling of the acid crater lake of Kawah Ijen volcano, Indonesia. *Geochim. Cosmochim. Acta* 58 (11), 2445-2460.
- Delmelle, P., Bernard, A., Kusakabe, M., Fischer, T.P., Takano, B., 2000. Geochemistry of the magmatic-hydrothermal system of Kawah Ijen volcano, East Java, Indonesia. *J. Volcanol. Geotherm. Res.* 97 (1-4), 31-53.
- Devine, J.D., Gardner, J.E., Brack, H.P., Layne, G.D., Rutherford, M.J., 1995. Comparison of microanalytical methods for estimating H₂O contents of silicic volcanic glasses. *Am. Mineral.* 80 (3-4), 319-328.
- Edmonds, M., Gerlach, T.M., Herd, R.A., 2009. Halogen degassing during ascent and eruption of water-poor basaltic magma. *Chem. Geol.* 263 (1-4), 122-130.
- Edner, H., Ragnarson, P., Svanberg, S., Wallinder, E., Ferrara, R., Cioni, R., Raco, B., Taddeucci, G., 1994. Total fluxes of sulphur dioxide from the Italian volcanoes Etna, Stromboli, and Vulcano measured by differential absorption lidar and passive differential optical absorption spectroscopy. *J. Geophys. Res.* 99 (D9), 18827.
- Eisinger, M., Burrows, J.P., 1998. Tropospheric sulphur dioxide observed by the ERS-2 GOME instrument. *Geophys. Res. Lett.* 25 (22), 4177-4180.
- Fischer, T.P., Giggenbach, W.F., Sano, Y., Williams, S.N., 1998. Fluxes and sources of volatiles discharged from Kudryavy, a subduction zone volcano, Kurile Islands. *Earth Planet. Sci. Lett.* 160 (1-2), 81-96.

- Francis, P., Chaffin, C., Maciejewski, A., Oppenheimer, C., 1996. Remote determination of SiF₄ in volcanic plumes: A new tool for volcano monitoring. *Geophys. Res. Lett.* 23 (3), 249-252.
- Gaetani, G.A., Watson, E.B., 2000. Open system behavior of olivine-hosted melt inclusions. *Earth Planet. Sci. Lett.* 183 (1-2), 27-41.
- Galle, B., Oppenheimer, C., Geyer, A., McGonigle, A.J.S., Edmonds, M., Horrocks, L., 2003. A miniaturised ultraviolet spectrometer for remote sensing of SO₂ fluxes: A new tool for volcano surveillance. *J. Volcanol. Geotherm. Res.* 119 (1-4), 241-254.
- Geist, D., Chadwick, W., Johnson, D., 2006. Results from new GPS and gravity monitoring networks at Fernandina and Sierra Negra volcanoes, Galápagos, 2000-2002. *J. Volcanol. Geotherm. Res.* 150 (1-3), 79-97.
- Geist, D.J., Harpp, K.S., Naumann, T.R., Poland, M., Chadwick, W.W., Hall, M., Rader, E., 2008. The 2005 eruption of Sierra Negra volcano, Galápagos, Ecuador. *Bull. Volcanol.* 70 (6), 655-673.
- Giggenbach, W.F. 1975. A simple method for the collection and analysis of volcanic gas samples. *Bull. Volcanol.* 39 (1), 132-145.
- Giggenbach, W.F., Matsuo, S., 1991. Evaluation of results from second and third IAVCEI field workshops on volcanic gases, Mt Usu, Japan, and White Island, New Zealand. *Appl. Geochem.* 6 (2), 125-141.
- Giggenbach, W.F., Tedesco, D., Sulistiyo, Y., Caprai, A., Cioni, R., Favara, R., Fischer, T.P., Hirabayashi, J.I., Korzhinsky, M., Martini, M., 2001. Evaluation of results from the fourth and fifth IAVCEI field workshops on volcanic gases, Vulcano Island, Italy and Java, Indonesia. *J. Volcanol. Geotherm. Res.* 108 (1-4), 157-172.
- Goff, F., Janik, C.J., Delgado, H., Werner, C., Counce, D., Stimac, J.A., Siebe, C., Love, S.P., Williams, S.N., Fischer, T., 1998. Geochemical surveillance of magmatic volatiles at Popocatepetl volcano, Mexico. *Bull. Geol. Soc. Am.* 110 (6), 695-710.
- Goff, F., McMurtry, G.M., Counce, D., Simac, J.A., Roldán-Manzo, A.R., Hilton, D.R., 2000. Contrasting hydrothermal activity at Sierra Negra and Alcedo volcanoes, Galápagos archipelago, Ecuador. *Bull. Volcanol.* 62 (1), 34-52.
- Gurenko, A.A., Chaussidon, M., 1995. Enriched and depleted primitive melts included in olivine from icelandic tholeiites: origin by continuous melting of a single mantle column. *Geochim. Cosmochim. Acta* 59 (14), 2905-2917.
- Handley, H.K., Macpherson, C.G., Davidson, J.P., Berlo, K., Lowry, D., 2007. Constraining fluid and sediment contributions to subduction-related magmatism in Indonesia: Ijen Volcanic Complex. *J. Petrol.* 48 (6), 1155.

- Hauri, E. 2002. SIMS analysis of volatiles in silicate glasses, 2: Isotopes and abundances in Hawaiian melt inclusions. *Chem. Geol.* 183 (1-4), 115-141.
- Hervig, R.L., Dunbar, N.W., 1992. Cause of chemical zoning in the Bishop (California) and Bandelier (New Mexico) magma chambers. *Earth Planet. Sci. Lett.* 111 (1), 97-108.
- Horton, K.A., Williams-Jones, G., Garbeil, H., Elias, T., Sutton, A.J., Mougini-Mark, P., Porter, J.N., Clegg, S., 2006. Real-time measurement of volcanic SO₂ emissions: Validation of a new UV correlation spectrometer (FLYSPEC). *Bull. Volcanol.* 68 (4), 323-327.
- Jaggard, T.A. 1940. Magmatic gases. *Am. J. Science* 238 (5), 313-353.
- Johnson, E.R., Wallace, P.J., Cashman, K.V., Granados, H.D., Kent, A.J.R., 2008. Magmatic volatile contents and degassing-induced crystallization at Volcán Jorullo, Mexico: Implications for melt evolution and the plumbing systems of monogenetic volcanoes. *Earth Planet. Sci. Lett.* 269 (3-4), 478-487.
- Johnson, E.R., Wallace, P.J., Delgado Granados, H., Manea, V.C., Kent, A.J.R., Bindeman, I., Donegan, C.S., 2009. Subduction-related volatile recycling and magma generation beneath central Mexico: Insights from melt inclusions, oxygen isotopes and geodynamic models. *J. Petrol.* 50 (9), 1729-1764.
- Koleszar, A.M., Saal, A.E., Hauri, E.H., Nagle, A.N., Liang, Y., Kurz, M.D., 2009. The volatile contents of the Galápagos plume; evidence for H₂O and F open system behavior in melt inclusions. *Earth Planet. Sci. Lett.* 287 (3-4), 442-452.
- Lowenstern, J.B. 2003. Melt inclusions come of age: Volatiles, volcanoes, and Sorby's legacy. *Develop. Volcano.* 5, 1-21.
- McGee, K.A., Gerlach, T.M., 1998. Airborne volcanic plume measurements using a FTIR spectrometer, Kilauea volcano, Hawaii. *Geophys. Res. Lett.* 25 (5), 615-618.
- Métrich, N., Clocchiatti, R., 1989. Melt inclusion investigation of the volatile behaviour in historic alkali basaltic magmas of Etna. *Bull. Volcanol.* 51 (3), 185-198.
- Métrich, N., Wallace, P.J., 2008. Volatile abundances in basaltic magmas and their degassing paths tracked by melt inclusions. *Rev. Mineral. Geochem.* 69 (1), 363.
- Montegrossi, G., Tassi, F., Vaselli, O., Bucciatti, A., Garofalo, K., 2001. Sulphur species in volcanic gases. *Anal. Chem.* 73 (15), 3709-3715.

- Nadeau, P.A., Williams-Jones, G., 2008. Beyond COSPEC – Recent advances in SO₂ monitoring technology. In: Williams-Jones, G., Stix, J., Hickson, C. (eds.). *The COSPEC Cookbook: Making SO₂ measurements at active volcanoes*. IAVCEI Methods in Volcanology 1, 219-233.
- Nadeau, P.A., Williams-Jones, G., 2009. Apparent downwind depletion of volcanic SO₂ flux—lessons from Masaya volcano, Nicaragua. *Bull. Volcanol.* 71 (4), 389-400.
- Nielsen, R.L., Crum, J., Bourgeois, R., Hascall, K., Forsythe, L.M., Fisk, M.R., Christie, D.M., 1995. Melt inclusions in high-An plagioclase from the Gorda Ridge: An example of the local diversity of MORB parent magmas. *Contrib. Mineral. Petrol.* 122 (1), 34-50.
- Nielsen, R.L., Michael, P.J., Sours-Page, R., 1998. Chemical and physical indicators of compromised melt inclusions. *Geochim. Cosmochim. Acta* 62 (5), 831-839.
- Palmer, S., 2009. Hydrogeochemistry of the upper Banyu Pahit River valley, Kawah Ijen volcano, Indonesia. M.Sc. Thesis. McGill University, Montréal, Canada, 144 pp.
- Portnyagin, M., Hoernle, K., Plechov, P., Mironov, N., Khubunaya, S., 2007. Constraints on mantle melting and composition and nature of slab components in volcanic arcs from volatiles (H₂O, S, Cl, F) and trace elements in melt inclusions from the Kamchatka arc. *Earth Planet. Sci. Lett.* 255 (1-2), 53-69.
- Reynolds, R.W., Geist, D.J., 1995. Petrology of lavas from sierra negra volcano, isabela island, galápagos archipelago. *J. Geophys. Res.* 100 (B12), 24537.
- Reynolds, R.W., Geist, D., Kurz, M.D., 1995. Physical volcanology and structural development of Sierra Negra volcano, Isabela Island, Galápagos archipelago. *Geol. Soc. Am. Bul.* 107 (12), 1398-1410.
- Roberge, J., Delgado-Granados, H., Wallace, P.J., 2009. Mafic magma recharge supplies high CO₂ and SO₂ gas fluxes from Popocatepetl volcano, Mexico. *Geology* 37 (2), 107.
- Roedder, E., 1979. Silicate liquid immiscibility in magmas. In: Yoder H.S. (ed.). *The evolution of the igneous rocks, fiftieth anniversary perspectives*. Princeton Univ. Press, 15-57.
- Roedder, E., 1984. Fluid Inclusions. *Reviews in Mineralogy*. Mineral. Soc. Amer. 12, 644.
- Roedder, E., Weiblen, P.W., 1970. Silicate liquid immiscibility in lunar magmas, evidenced by melt inclusions in lunar rocks. *Science* 167 (3918), 641-644.

- Roggensack, K., Hervig, R.L., McKnight, S.B., Williams, S.N., 1997. Explosive basaltic volcanism from Cerro Negro volcano: Influence of volatiles on eruptive style. *Science* 277 (5332), 1639-1642.
- Saal, A.E., Hauri, E.H., Langmuir, C.H., Perfit, M.R., 2002. Vapour undersaturation in primitive mid-ocean-ridge basalt and the volatile content of earth's upper mantle. *Nature* 419 (6906), 451-455.
- Sadofsky, S.J., Portnyagin, M., Hoernle, K., van den Bogaard, P., 2008. Subduction cycling of volatiles and trace elements through the Central American volcanic arc: Evidence from melt inclusions. *Contrib. Mineral. Petrol.* 155 (4), 433-456.
- Schiano, P., Clocchiatti, R., Shimizu, N., Weis, D., Mattielli, N., 1994. Cogenetic silica-rich and carbonate-rich melts trapped in mantle minerals in Kerguelen ultramafic xenoliths: Implications for metasomatism in the oceanic upper mantle. *Earth Planet. Sci. Lett.* 123 (1-3), 167-178.
- Shinohara, H. 2005. A new technique to estimate volcanic gas composition: Plume measurements with a portable multi-sensor system. *J. Volcanol. Geotherm. Res.* 143 (4), 319-333.
- Sitorus, K., 1990. Volcanic stratigraphy and geochemistry of the Idjen Caldera Complex, East Java, Indonesia. M.Sc. thesis, University of Wellington, New Zealand.
- Sobolev, A.V., Chaussidon, M., 1996. H₂O concentrations in primary melts from supra-subduction zones and mid-ocean ridges: Implications for H₂O storage and recycling in the mantle. *Earth Planet. Sci. Lett.* 137 (1-4), 45-55.
- Sobolev V. S., Kostyuk V. P., 1975. Magmatic crystallization based on a study of melt inclusions. In: Roedder E., Kozlowski A. (eds.). *Fluid Inclusion Research* 9, 182-253.
- Sobolev, V.S., Bazarova, T.Y., Bakumenko, I.T., 1971. Crystallization temperature and gas phase composition of alkaline effusives as indicated by primary melt inclusions in the phenocrysts. *Bull. Volcanol.* 35 (2), 479-496.
- Sortino, F., Nonell, A., Toutain, J.P., Munoz, M., Valladon, M., Volpicelli, G., 2006. A new method for sampling fumarolic gases: Analysis of major, minor and metallic trace elements with ammonia solutions. *J. Volcanol. Geotherm. Res.* 158 (3-4), 244-256.
- Sperling, R. B. 1975. Evaluation of the correlation spectrometer as an area SO₂ monitor. *Environmental Measurements, Inc.*, PB-249113, 115.

- Spilliaert, N., Allard, P., Métrich, N., Sobolev, A.V., 2006. Melt inclusion record of the conditions of ascent, degassing, and extrusion of volatile-rich alkali basalt during the powerful 2002 flank eruption of Mount Etna (Italy). *J. Geophys. Res.* 111 (B4), B04203.
- Stolper, E. 1982. Water in silicate glasses: An infrared spectroscopic study. *Contrib. Mineral. Petrol.* 81 (1), 1-17.
- Takano, B., Suzuki, K., Sugimori, K., Ohba, T., Fazlullin, S.M., Bernard, A., Sumarti, S., Sukhyar, R., Hirabayashi, M., 2004. Bathymetric and geochemical investigation of Kawah Ijen crater lake, East Java, Indonesia. *J. Volcanol. Geotherm. Res.* 135 (4), 299-329.
- van Hinsberg, V.J., 2001. Water-rock interaction and element fluxes in the Kawah Ijen hyperacid crater lake and the Banyu Pahit river, East Java, Indonesia. M.Sc. thesis, University of Utrecht, Netherlands.
- van Hinsberg, V., Berlo, K., van Bergen, M., Williams-Jones, A.E., 2010a. Extreme alteration by hyperacidic brines at Kawah Ijen volcano, East Java, Indonesia: I. textural and mineralogical imprint. *J. Volcanol. Geotherm. Res.* 198 (1-2), 253-263.
- van Hinsberg, V., Berlo, K., Sumarti, S., van Bergen, M., Williams-Jones, A.E., 2010b. Extreme alteration by hyperacidic brines at Kawah Ijen volcano, East Java, Indonesia: II. metasomatic imprint and element fluxes. *J. Volcanol. Geotherm. Res.* 196 (3-4), 169-184.
- Vigouroux, N., Wallace, P.J., Kent, A.J.R., 2008a. Volatiles in high-K magmas from the western Trans-Mexican volcanic belt: Evidence for fluid fluxing and extreme enrichment of the mantle wedge by subduction processes. *J. Petrol.* 49 (9), 1589-1618.
- Vigouroux, N., Williams-Jones, G., Chadwick, W., Geist, D., Ruiz, A., Johnson, D., 2008b. 4D gravity changes associated with the 2005 eruption of Sierra Negra volcano, galápagos. 73 (6), WA29.
- Vigouroux, N., Williams-Jones, A.E., Wallace, P., Staudacher, T., 2009. The November 2002 eruption of Piton de la Fournaise, Réunion: Tracking the pre-eruptive thermal evolution of magma using melt inclusions. *Bull. Volcanol.* 71 (9), 1077-1089.
- Wallace, P.J. 2005. Volatiles in subduction zone magmas: Concentrations and fluxes based on melt inclusion and volcanic gas data. *J. Volcanol. Geotherm. Res.* 140 (1-3), 217-240.
- Watson, E.B., Sneeringer, M.A., Ross, A., 1982. Diffusion of dissolved carbonate in magmas: Experimental results and applications. *Earth Planet. Sci. Lett.* 61 (2), 346-358.

- Williams-Jones, G., Horton, K.A., Elias, T., Garbeil, H., Mouginis-Mark, P.J., Sutton, A.J., Harris, A.J.L., 2006. Accurately measuring volcanic plume velocity with multiple UV spectrometers. *Bull. Volcanol.* 68 (4), 328-332.
- Williams-Jones, G., Rymer, H., Mauri, G., Gottsmann, J., Poland, M., Carbone, D., 2008. Toward continuous 4D microgravity monitoring of volcanoes. *Geophys.* 73 (6), WA19-WA28.
- Williams-Jones, G., Rymer, H., Rothery, D.A., 2003. Gravity changes and passive SO₂ degassing at the Masaya caldera complex, Nicaragua. *J. Volcanol. Geotherm. Res.* 123 (1-2), 137-160.
- Witter, J.B., Kuehner, S.M., 2004. A simple empirical method for high-quality electron microprobe analysis of fluorine at trace levels in Fe-bearing minerals and glasses. *Am. Mineral.* 89 (1), 57-63.
- Yokoyama, I., Tajima, H., 1957. A gravity survey on volcano Mihara, Ooshima Island by means of a worden gravimeter. *Bull. Earthq. Res. Inst.* 35 23-33.
- Yun, S., Segall, P., Zebker, H., 2006. Constraints on magma chamber geometry at Sierra Negra Volcano, Galápagos Islands, based on InSAR observations. *J. Volcanol. Geotherm. Res.* 150 (1-3), 232-243.

2: 4D GRAVITY CHANGES ASSOCIATED WITH THE 2005 ERUPTION OF SIERRA NEGRA VOLCANO, GALÁPAGOS¹

2.1 Abstract

Sierra Negra volcano, the most voluminous shield volcano in the Galápagos archipelago and one of the largest basaltic calderas in the world, erupted on October 22, 2005 after more than 25 years of quiescence. GPS and InSAR monitoring of the deformation of the caldera floor in the months prior to the eruption documented extraordinary inflation rates (1 cm day^{-1}). The total amount of uplift recorded since monitoring began in 1992 approached 5 m at the centre of the caldera. To gain insight into the nature of the subsurface mass/density changes associated with the inflation leading up to the eruption, gravity measurements performed in 2005, 2006 and 2007 are compared to previous measurements from 2001 and 2002 when the volcano underwent a period of minor deflation and magma withdrawal. The residual gravity decrease between 2001/2002 and 2005 is amongst the largest ever recorded at an active volcano ($-950 \text{ } \mu\text{Gal}$) and suggests that inflation was accompanied by a relative density decrease in the magmatic system. Forward modeling of the residual gravity data

¹ A version of the following chapter has been published as: *Vigouroux, N., Williams-Jones, G., Chadwick, W., Geist, D., Ruiz, A.G. & Johnson, D. (2008). 4D gravity changes associated with the 2005 eruption of Sierra Negra, Galapagos. Geophysics, 73 (6), WA29-35.* The collaboration involved field assistance, discussion of the modeling and manuscript reviews from G. Williams-Jones, W. Chadwick and D. Geist, field assistance and deformation modeling from A. Ruiz and gravity data for 2005 from D. Johnson as well as cross-calibration data for the two gravimeters used in this study.

in 4D (from 2002 to 2005) gives an estimate of the amount of vesiculation in the shallow sill required to explain the observed gravity variations. Geochemical constraints from melt inclusion and satellite remote-sensing data allow us to estimate the pre-eruptive gas content of the magma and place constraints on the thickness of the gas-rich sill necessary to produce the gravity anomalies observed. Results suggest that reasonable sill thicknesses (700-800 m) and gas contents (10-50%) can explain the large decrease in residual gravity prior to eruption. Following the eruption (2006 and 2007), the deformation and gravity patterns suggest re-equilibration of the pressure regime in the shallow magma system perhaps via renewed influx of relatively gas-poor magma into the shallow parts of the system.

2.2 Introduction

Information on mass changes in the subsurface over time can be obtained from microgravity surveys. In volcanic systems, changes in magma supply rate (influx or withdrawal), changes in the vesicularity of magma, and changes in the size or depth of a hydrothermal system can affect the gravity field measured at the surface (e.g. Tiede; Gottsmann et al., 2006). Typically, gravity variations on the order of 100s of μGals are recorded over years to decades and are associated with vertical deformation on the order of a few centimetres to a few meters (e.g., Rymer, 1996; Battaglia et al., 1999). When combined with simultaneous data on elevation change (using GPS or InSAR), microgravity surveys allow us to investigate the causes of ground deformation in active volcanic areas and evaluate the likelihood of an impending eruption (e.g.,

Yokoyama and Tajima, 1957) at a variety of volcanoes, from large silicic calderas (e.g., Campi Flegrei; Berrino et al., 1984) to composite stratovolcanoes (e.g., Merapi; Jousset et al. 2000) to basaltic calderas (e.g., Kilauea; Johnson, 1992). Logistical constraints usually limit the spatial and temporal coverage of the gravity network in remote volcanic areas. However, combined with high precision, continuously recorded ground deformation data, even sparse microgravity data can provide important information on the source of physical unrest at a volcano (e.g. Kauahikaua and Miklius, 2003).

In this contribution, we present gravity data collected prior to and following the October 2005 eruption. In combination with previously published microgravity data on Sierra Negra (Geist et al., 2006), time series analysis of both microgravity and continuous deformation data offers insight into the subsurface processes associated with the 2005 eruption. We use previously published models of the magma reservoir obtained from inversion of deformation data (Amelung et al., 2000; Chadwick et al., 2006; Geist et al., 2006; Yun et al., 2006) to model the changes in subsurface conditions that can reasonably explain the gravity data.

2.3 Geologic Setting and the 2005 Eruption

The Galápagos archipelago is a group of volcanic ocean islands built on the Nazca plate above the Galápagos hot spot, about 200 km south of the Galápagos spreading ridge and 1000 km west of continental Ecuador (Fig. 2-1). The archipelago consists of ~ 15 islands and 20 shield volcanoes along with numerous islets and seamounts, all of which are constructed on a broad and

shallow submarine platform (the Galápagos swell) rising ~ 2000 m above the surrounding ocean floor (Villagómez et al., 2007). Nearly all of the shield volcanoes have been active in the Holocene (Simkin and Siebert, 1994). Although the Nazca plate is moving east relative to the hot spot, volcanism does not clearly evolve from east to west perhaps as a result of spreading of the plume at the base of the lithosphere with little drag effect from the overriding plate (Villagómez et al., 2007).

Sierra Negra volcano is a large shield volcano on Isabela Island (Fig. 2-1). It is the second most active volcano in the Galápagos archipelago (after Fernandina with 12 eruptions since historical recordings began approximately 200 years ago; Smithsonian Institute database) and is by far the most voluminous. Sierra Negra has one of the largest calderas of any basaltic volcano on the planet (10 x 9 km; Wood, 1984). The caldera floor has been uplifted by up to 100 m in the SW corner as a result of repeated slip along a sinuous fault system (Fig. 2-2; Reynolds et al., 1995; Chadwick et al., 2006). The northeast side of the fault block forms a dip slope, resulting in a trapdoor/asymmetric geometry (Lipman, 1997). Located at the base of the western end of the fault scarp is Volcan Azufre, the current center of fumarolic activity. The small fumarole field consists of a main fumarole vent ~ 12 m in diameter, from which the highest gas flux emanates, as well as numerous smaller vents and fissures.

The basaltic lavas of Sierra Negra are phenocryst poor ($\leq 5\%$) Fe-rich tholeiites composed of plagioclase (An_{61-82}) \pm olivine (Fo_{62-88}), clinopyroxene (En_{41-47} , Wo_{35-44} , Fs_{9-22}) and Fe-Ti oxides (Reynolds and Geist, 1995). The lavas

have a very restricted compositional range (4.4 to 6.9 wt% MgO) over an eruptive period of at least 5000 years which suggests a stable plumbing system, high magma supply rates, homogeneous source melting and steady thermal conditions in the crust and lithosphere (Reynolds and Geist, 1995). This is consistent with the large volumes of erupted material (1 km³ in 1979; Reynolds et al., 1995) and the frequency of eruption at Sierra Negra (an eruption every 10-30 years on average in the last 200 years; Smithsonian Institute).

On October 22, 2005, after a 26 year hiatus, Sierra Negra erupted more than 150×10^6 m³ of aphyric (crystal-free) basaltic lava (Geist et al., 2008) from a series of arcuate vents along the northern caldera rim (Fig. 2-2), a common feature of the Galápagos volcanoes (Chadwick and Howard, 1991). Uplift of more than 2 m in the center of the caldera was recorded by continuous GPS over the 3 years preceding the October 2005 eruption (Chadwick et al., 2006). The total inflation (estimated to be 5 m since 1992) prior to eruption is the largest ever recorded at a basaltic caldera (Chadwick et al., 2006).

2.4 Methods

The theory and field practice for microgravity monitoring in volcanic areas has been well described in the literature (e.g., Rymer and Brown, 1989; Rymer, 1996) and therefore will only be summarized briefly here. The gravity network at Sierra Negra is sparse owing to the extremely difficult access to the caldera and rough terrain (at least 10 hours hiking is required to visit 3 gravity stations in the center of the caldera). Our efforts were thus focused on measurements at the center of deformation in the middle of the caldera (Fig. 2-2). Stations were visited

in June 2005, four months prior to the eruption, and in June 2006 and 2007. These data are used in conjunction with earlier gravity surveys in 2001 and 2002 (Geist et al., 2006). All surveys were conducted during the dry season in June. This strategy is designed to limit the effect of water-table fluctuations on the gravity measurements. Although precise water-table effects were not quantified, given the large gravity variations observed, any water-related effects on the order observed at other calderas (e.g., up to 60 μGal at Yellowstone; Battaglia et al., 2003) would fall within the error of our measurements.

Two LaCoste and Romberg model G gravity meters (instrument G-127 and G-209) were used over the course of the surveys at Sierra Negra. The G-209 meter was used for the 2001-2002 (Geist et al., 2006) and June 2005 surveys while the G-127 meter was used during the more recent surveys in 2006 and 2007. The G-209 meter is equipped with a galvanometer and thus the reported microgravity measurements for a given station are taken from at least 2 individual readings. In contrast, the G-127 meter is equipped with an Aliod electrostatic feedback nulling system allowing for repeated in-situ measurements (at 2 Hz) without the need for user input. Both instruments were calibrated on a Palm Desert (California) gravity line and the data presented here are corrected to the G-127 meter.

When time permitted, each station was visited twice during a survey loop and some stations were measured on two different days of the campaign. Our raw gravity measurements are corrected for earth tide, ocean loading and elevation effects: the Bouguer Corrected Free Air Gradient (BCFAG) = a Free Air

Gradient (FAG) of $-308.6 \mu\text{Gal m}^{-1}$ plus an infinite slab Bouguer correction of $117.3 \mu\text{Gal m}^{-1}$, assuming a surrounding rock density of 2.8 g cm^{-3} , were used for these corrections. The resulting, corrected gravity measurement is referred to as the residual gravity. Instrumental drift was negligible over the survey periods. Error in the residual gravity measurements is as follows: The standard deviation (1σ) in the residual gravity averaged over 1 minute and measured over 6-10 minutes at a given station is less than $5 \mu\text{Gal}$ for the G-127 meter. The standard deviation at a given station over the course of one campaign is on the order of $100 \mu\text{Gal}$, due to the difficult conditions experienced by the instruments during transport over rugged terrain. The closure error (difference in the residual gravity measurements made at the base station, SN12, in one day) was also taken into account. Sources of error that factor into the residual gravity measurements include uncertainty in the vertical component of deformation as measured by continuous GPS at most of the gravity benchmarks and uncertainty in the extrapolation of deformation rates to benchmarks where no GPS data are available. We also take into account possible variation in the FAG gradient of up to $\pm 10\%$ (Tsuboi, 1983).

2.5 Gravity and Deformation Results

Deformation data for Sierra Negra extends back to 1992 with satellite radar interferometry (InSAR) studies indicating inflation of 2.5 m from 1992 to 1999, with maximum uplift rates of 60 cm yr^{-1} (Amelung et al., 2000). The InSAR data were inverted to model the magma body and indicated that a 2.1-2.3 km deep sill is located beneath the center of the caldera (Amelung et al., 2000).

In June 2001 and June 2002, GPS campaigns covered a network of 14 to 26 stations at Sierra Negra (Geist et al., 2006). They reported a greatly decreased rate of inflation during the first year, with a maximum uplift rate of 7 cm yr⁻¹, followed by 9 cm of deflation over the next 1.5 years. This period of deflation was accompanied by a 50 μGal decrease (Table 2-1) in the residual gravity observed in the northern part of the caldera (station SN21, relative to SN12 on the caldera rim; Fig. 2-2). Geist et al. (2006) suggested that the combined deflation and decrease in gravity was linked to an episode of magma withdrawal from the shallow magma reservoir, probably into the deeper parts of the plumbing system. From the GPS data, the best-fit geometry for the deflating magma body was found to be a sill with horizontal dimensions of 5.3 x 3.0 km and a depth comparable to that modeled by the InSAR data (2.1-2.3 km). Based on this geometry, the magma body would have contracted in volume by 4.1 x 10⁶ m³ (Geist et al., 2006).

In June 2002, a network of continuous GPS stations was installed on the caldera floor of Sierra Negra, with one station located on its NE rim (Fig. 2-2). The GPS network continued to record the deflation which commenced in 2000-2001 at a rate of -9.1 cm/yr, and then in April 2003 the system switched back to inflation (Chadwick et al., 2006). Between April 2003 and the October 2005 eruption, station GV02, located near the center of the caldera, recorded 2.2 m of uplift. Horizontal N-S extension (GV03-GV06) amounted to 1.4 m over the same time period. A m_b 4.6 earthquake occurred on April 16, 2005 along with 84 cm of vertical slip on the south end of the intra-caldera fault system but this event did

not interrupt the pattern of inflation (Chadwick et al., 2006). This suggests that despite faulting in the roof of the magma reservoir, the internal pressure in the subsurface reservoir was apparently unaffected. Unfortunately, no gravity data was collected between June 2002 and June 2005, but such high inflation rates prior to an eruption are generally associated with continuous magma influx into the shallow reservoir (Johnson, 1992).

Gravity measurements 4 months prior to the October 2005 eruption at the center of the caldera (SN09) show a decrease in residual gravity (relative to the reference station SN12) of up to 950 μGal compared to measurements from 2001 and 2002 (Fig. 2-3). The residual gravity decrease becomes less pronounced towards the caldera rim, with station SN21 recording a 450 μGal decrease relative to 2001/2002. The change in residual gravity on the flank of the caldera (station SN15) is negligible between 2001/2002 and 2005 (Table 2-1; Fig. 2-3). This suggests that the residual gravity anomaly, and hence the area of mass change/density decrease, prior to the eruption, was restricted to the interior of the caldera.

Gravity measurements made 8 and 20 months after the 2005 eruption reveal an increase in residual gravity relative to June 2005 of up to 1000 μGal , again centered on SN09 (Fig. 2-3). For SN09, this represents a slightly higher residual gravity value than the one recorded in 2001 and 2002. For all other stations, the residual gravity measured in June 2007 is lower than the 2001-2002 levels by up to 350 μGal (SN15). Given the error in the measurements, stations SN24 and SN21 show no definite pattern of residual gravity change from

immediately preceding, to after the eruption (June 2005-June 2007). Station SN15, however, shows a clear residual gravity decrease following the 2005 eruption. The change in the relative difference in residual gravity between stations (e.g., SN09-SN24) prior to and following the eruption suggests a shift in the mass distribution at depth as a result of the eruption. Finally, the relative changes in residual gravity measured at SN21 (north edge of the caldera floor) over the entire period, are greater (although within error) than the changes measured at SN24 (station located between SN09 and SN21) indicating that the residual gravity change was radially asymmetric.

2.6 Discussion

The large decrease in residual gravity observed at SN09 and to a lesser extent at SN21 and SN24 preceding the 2005 eruption can be best explained in terms of either a mass or a density decrease in the subsurface. A $\Delta g/\Delta h$ diagram (coupled gravity-elevation variation diagram) allows for better visualization of the processes responsible for the residual gravity changes (Fig. 2-4; Rymer and Williams-Jones, 2000). The maximum $\Delta g/\Delta h$ gradient for the time periods 2002-2005 and 2006-2007 (at station SN09) are plotted along with the theoretical FAG and the calculated BCFAG. The maximum gradient prior to the eruption (2002-2005) plots below both the FAG and BCFAG gradients indicating a decrease in mass and/or a decrease in density. The maximum gradient following the eruption (2006-2007) plots above both the FAG and the BCFAG indicating a mass increase and/or density increase. At the time of the June 2005 gravity survey, the caldera floor was in a period of accelerating inflation (Chadwick et al., 2006). This

rapid increase in elevation of the caldera floor has been interpreted as being caused by an increase in the volume of the subsurface magma chamber due to influx of magma preceding the eruption (Chadwick et al., 2006). Given that magma withdrawal (mass decrease) was not occurring during the time period 2002-2005, the $\Delta g/\Delta h$ gradient observed from 2001 to 2005 is best explained by a density decrease, most likely caused by magma vesiculation.

In order to investigate the role of magma vesiculation in generating the large residual gravity decrease prior to the eruption, we model the shallow magma body using the program Grav3D (Grav3D, 2007) and solve for the density and thickness of the magma body needed to generate the maximum residual gravity change recorded from 2002 to 2005 at SN09. Inverse modeling of the gravity data to solve for the exact density of the causative body was not performed due to the limited spatial coverage of the gravity network.

This approach is made possible because of the good control we have on the geometry of the chamber and its location. Inverse modeling of the deformation data collected at Sierra Negra by both InSAR and GPS since 1992 suggest the deformation is mainly controlled by inflation and deflation of a shallow, sill-like magma body located at 2.1-2.3 km depth (top of the chamber) and having horizontal dimensions of 5.3 x 3.0 km (Fig. 2-5) (Amelung et al., 2000; Chadwick et al., 2006; Geist et al., 2006). However, there is no constraint on the thickness of the body, which could range from 100s of meters to > 1 km (Yun et al., 2006). The chamber geometry is assumed to remain constant between 2002 and 2005. The change in the volume of the chamber of 3.6×10^7

m³ between June 2002 and 2005 (Chadwick et al., 2006) will have an effect on the gravity field but since this volume increase represents << 1% of the total volume of the sill (for any sill thickness from 200 m to > 1 km), the effect is minimal and is therefore ignored.

In order to better constrain the thickness of the sill, we calculate the density of the magma body in the months prior to eruption using estimates of the concentration of volatiles (H₂O, CO₂, S) supplied to the system and using solubility constraints to estimate the amount of exsolved gas in the magma at the pressure and temperature conditions expected in the shallow sill. The lavas erupted in 2005 were essentially aphyric (crystal-free) and as such, preclude melt inclusion studies of the initial melt volatile content. However, melt inclusion data from older eruptions of Sierra Negra and from the neighbouring basaltic shield volcano, Fernandina (Fig. 2-1), can be used to estimate the undegassed concentrations of volatiles feeding the shallow Sierra Negra system. Fernandina erupts lavas of very similar chemical composition to Sierra Negra (c.f. Reynolds et al., 1995; Allan and Simkin, 2000; Geist et al., 2008). Melt inclusions with the highest CO₂ content (up to ~ 7000 ppm) represent the least degassed samples (trapped at ~ 900 MPa, > 30 km depth assuming an average crust density of 2800 kg m⁻³) and have corresponding H₂O contents of 0.8-1 wt% and maximum S contents of ~ 1600 ppm (Koleszar et al., 2007; Table 6-1). The lithostatic pressure at the top of the magma chamber is ~ 58 MPa (2.2 km depth), a minimum for the system in part because we do not take into account the amount of magmatic overpressure (estimated at ≤ 15 MPa in 2005 from the amount of

inflation; Yun et al., 2006). We estimate a magma temperature of 1150 °C based on the geothermometer developed by Montierth et al. (1995) for Mauna Loa basalts and using the composition of the tephra glass from the 2005 eruption (Geist et al., 2008).

The solubility of CO₂ at these conditions is lower than the amount of CO₂ dissolved in the melt phase entering the shallow chamber. Based on the solubility model of Newman and Lowenstern (2002), an input of 7000 ppm CO₂ into the system will degas to 265 ppm, releasing 6735 ppm of CO₂ into the gas phase. In contrast, the concentration of H₂O in the melt is lower than its predicted solubility of 2.4 wt% (Newman and Lowenstern, 2002), and therefore H₂O would mostly remain in solution in a 2.2 km deep sill. Determining the solubility of S in a basaltic magma is more complex, as it involves more parameters, such as the composition of the melt and the oxygen fugacity. Based on the composition of the lava erupted during the 2005 eruption, the average oxygen fugacity of an ocean-island basalt (Fayalite-Magnetite-Quartz buffer, Gerlach, 1993; Ballhaus, 1993), the pressure and temperature estimates mentioned earlier, and the models of Kilinc et al. (1983) and Wallace and Carmichael (1992), we obtain a S solubility of ~ 1600 ppm suggesting that S degassing would have been negligible at Sierra Negra prior to eruption. Based solely on the amount of CO₂ exsolved, the total weight % of exsolved gas in the magma prior to the 2005 eruption is 0.7.

We do not take into account any compositional or temperature changes of the magma during storage in the magma chamber, which could cause H₂O and S to saturate. We also do not take into account the possibility that H₂O partially

degasses with CO₂ in closed-system degassing (Dixon and Stolper, 1995), or that CO₂ is degassing from magma deeper within the system and that this gas is accumulating in the shallow magma chamber (system open to mass flux from below). Consequently, our estimate of the amount of gas exsolved in the sill is a minimum and the resulting estimate of the thickness of the sill is a maximum.

The estimate of the mass fraction of exsolved gas above yields a bulk magma density of 2500 kg m⁻³ calculated using a density of the molten silicate liquid of 2700 kg m⁻³ and a gas density of 200 kg m⁻³ (from the ideal gas law at the P, T of interest). Also note that this calculation is an average density, and the amount of gas could be distributed heterogeneously in the magma reservoir (a possibility which is examined below).

The density of the magma body in 2002 is assumed to be that of the liquid with no exsolved gas or crystals (2700 kg m⁻³), based on evidence that the magma chamber was in a period of deflation and that magma withdrawal was occurring (Geist et al., 2006). The density contrast between June 2002 and 2005 is 200 kg m⁻³. Assuming no change in the planar geometry of the sill, we model the thickness of the sill required to produce the gravity anomaly recorded at SN09 during that time (950 ± 115 μGal). The best fit to the data is a 800-m thick sill, illustrated in Figure 2-6.

We also explore the possibility that the magmatic gases were concentrated in a highly vesicular foam layer progressively accumulated at the top of the magma chamber between 2002 and 2005 (instead of being mixed uniformly in the sill). To get an independent estimate of the volume of this foam

layer, we combine estimates of the total amount of SO₂ gas erupted during October 2005 with estimates of the ratio of H₂O/CO₂/SO₂ in the melt feeding the system, to determine the volume of erupted gas, which we convert to its corresponding volume at depth. Given that a stable foam layer is ≤ 80% bubbles (Wilson et al., 1980), we use a conservative estimate of 50% porosity to calculate a total volume for the foam layer.

The total amount of SO₂ erupted over the 8 days of the eruption is obtained from Ozone Monitoring Instrument (OMI) satellite images and corresponds to ~ 1.9 x 10⁹ kg (Simon Carn, pers. com.). The H₂O/CO₂/S ratios in the undegassed magma are estimated from the melt inclusion data and correspond to an H₂O/S ratio of 5.5 and a maximum CO₂/S ratio of 4.75. If we assume that the ratios of the volatiles at depth prior to degassing are equivalent to the ratios in the eruptive plume, then 45 wt% of the plume gas composition was H₂O, 40 wt% was CO₂, and 15 wt% was SO₂. The total amount of gas erupted equals 11.6 x 10⁹ kg, which translates to a volume of 8.3 x 10⁹ m³ of gas at atmospheric pressure and temperature (calculated from the ideal gas law). Converted to a pressure of 58 MPa (corresponding to 2.2 km depth) at 1150 °C, the pre-eruptive volume of gas in the magma chamber is estimated at 6.8 x 10⁷ m³. Part of this volume will represent volatiles still dissolved in the melt prior to eruption, or exsolved but not accumulated in the foam layer. Therefore the volume of the foam layer is considered a maximum value. Factoring in 50% porosity in the foam layer, the total volume of the layer is 13.6 x 10⁷ m³. This value serves as a rough estimate of the maximum volume of explosively erupted

material. It is approximately equivalent to the volume of effusively erupted lava (Geist et al. 2008).

A 2-layer sill was modeled such that the top of the foam layer was at 2.2 km depth, corresponding to the top of the magma chamber (Fig. 2-5). The foam layer was assigned a density contrast of 850 kg m^{-3} (calculated from the porosity of the foam layer and the density of the erupted gas at the pressure and temperature conditions of the chamber) and the rest of the magma chamber had the same density contrast as in the first model, 200 kg m^{-3} . Since the volume of the foam layer is fixed, the area and thickness of the foam layer were varied along with the thickness of the underlying magma body until the maximum gravity signal produced most closely matched the signal observed between 2002 and 2005. The solution to this model is not unique and a 700 m thick sill with a 50 m thick foam layer (400 x 800 m area) will produce a comparable gravity signal to a thinner sill with a thicker or more extensive foam layer. Figure 2-7 shows the result of one of the configurations found to best fit our measured maximum residual gravity change for 2002-2005.

Although the modeling does not produce unique solutions to the geometry and the density of the shallow body beneath the caldera, it does produce solutions that are realistic and can explain the maximum residual gravity decrease between June 2002 and June 2005. The development of a foam layer with 50% vesiculation above a homogenous vesiculating magma body, or simply a thicker homogenous magma body with 10% vesiculation are both plausible conditions prior to the 2005 eruption, which was explosive in its opening phases.

The development of a foam layer was also put forward by Carbone et al. (2006, 2007) to explain the joint gravity decrease/tremor increase/pause in explosive activity at Mt. Etna during the 2002/2003 eruption, which resulted in a maximum residual gravity decrease of 30 μGal , but no model was developed to quantify the effect. Studies at Masaya volcano have also shown a relationship between an increase in volatile supply and a decrease in residual gravity (Williams-Jones et al., 2003).

The pattern of modeled residual gravity change with distance away from the center of deformation is gradual (Figs. 2-6, 2-7). This pattern suggests that station SN21, 1 km further from the center of the caldera compared to SN24, should have experienced a smaller decrease in residual gravity than was observed. The actual variation in gravity change between 2002 and 2005 at these two stations is similar within error, suggesting that other factors not modeled may be affecting the gravity field on a smaller scale. The location of the 2005 eruptive vents on the NE rim of the caldera (Geist et al., 2008), within ~ 2 km of SN21 (Fig. 2-2), and possible dike propagation from the sill to the surface may have caused localized gravity anomalies. Localized changes in the shallow hydrothermal system also cannot be ruled out. Given these potential complications, only the maximum change in residual gravity (station SN09) was used to fit the models.

Eight and twenty months after the eruption, the gravity signal at SN09 had returned to, and exceeded, the 2001/2002 levels (Fig. 2-3) and was accompanied by a renewal of inflation but at a decelerating rate (Ruiz, 2008).

The maximum $\Delta g/\Delta h$ gradient during this time period plots above both the FAG and BCGAF gradients (Fig. 2-4) suggesting that the change in residual gravity after the eruption is caused by a mass and/or a density increase, both consistent with the loss of the gas-rich, crystal-poor magma during the eruption, leaving behind a denser, perhaps crystal-rich mush and renewed influx of relatively degassed magma from deeper in the system.

2.7 Conclusions

4D microgravity and deformation data at Sierra Negra volcano can be interpreted in terms of the subsurface processes responsible for the largest pre-eruptive inflation ever recorded at a basaltic caldera. The magnitude of maximum residual gravity change prior to the 2005 eruption ($- 950 \mu\text{Gal}$) is also amongst the largest ever recorded. A gravity decrease of similar magnitude ($- 400 \mu\text{Gal}$) was recorded by a permanent gravity station at the summit of Mt. Etna volcano at the onset of the October 2002 eruption (Carbone et al., 2007). The duration of the anomaly was less than 6 hours and was interpreted as reflecting the opening of a dry fracture (not filled with magma) ~ 1 km from the gravity measurement site. The duration of the gravity anomaly at Sierra Negra volcano is unknown because measurements were only performed on 2 consecutive days over periods of 15-20 minutes each time. This problem illustrates the need for continuous 4D gravity monitoring at active volcanoes (Williams-Jones et al., this volume) but the logistical limitations, combined with the current technology available for continuous microgravity recordings, make this unfeasible at Sierra Negra volcano. However, based on the time gap between the gravity measurement in

June 2005 and the onset of the eruption in October 2005, we do not attribute the gravity decrease to the opening of a fracture.

Vesiculation of the magma as the volatiles reached their saturation point can explain the simultaneous uplift of the caldera floor and the decrease in gravity observed between 2001/2002 and June 2005. Although the proposed models do not offer unique solutions, geochemical constraints on the amount of gas present in the magma chamber prior to eruption allow us to model the thickness of the magma body required to produce the observed residual gravity variations. While the error associated with these estimates is large, the models provide a first-order constraint on the third dimension of the shallow magma reservoir at Sierra Negra.

Modeling of the time-series data also offers insight into the time-scales of vesiculation at Sierra Negra and can be used to estimate the volume of gas in the magma chamber prior to eruption. Faulting events at Sierra Negra in the years and months leading up to the 2005 eruption potentially allowed for partial release of pressure in the subsurface magma body and accommodation of subsurface volume expansion. The onset of vesiculation sometime between June 2002 and June 2005 is associated with the accelerating rate of inflation and magma influx recorded from April 2003 to October 2005 (Chadwick et al., 2006), and may have ultimately triggered the eruption. The cause for the onset of vesiculation may have been the influx of volatile-rich magma from depth, combined with chemical evolution of the melt in the chamber (volatile phases

reaching saturation) and perhaps a sudden, partial release of pressure during the 16 April 2005 faulting event.

2.8 Acknowledgments

The authors would like to thank the Galápagos National Park for their permission and assistance in the field as well as the Charles Darwin Research Station for their logistical help. We also thank Ayline Llona for her assistance in providing Dan Johnson's gravity data. Discussions with Paul Wallace helped clarify issues on S solubility. Support was provided by NSF grant [EAR0538205](#) to the University of Idaho and an NSERC Discovery Grant to Glyn Williams-Jones. PMEL contribution number 3193.

2.9 Figures

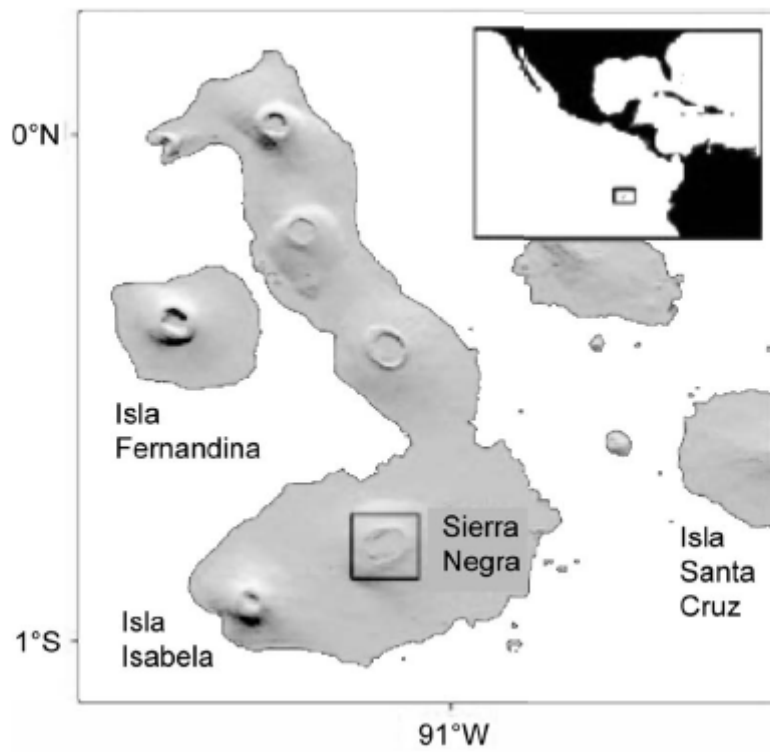


Figure 2-1 Digital Elevation Map of the Galápagos archipelago showing the location of Sierra Negra and Fernandina calderas (modified after Yun et al., 2006).

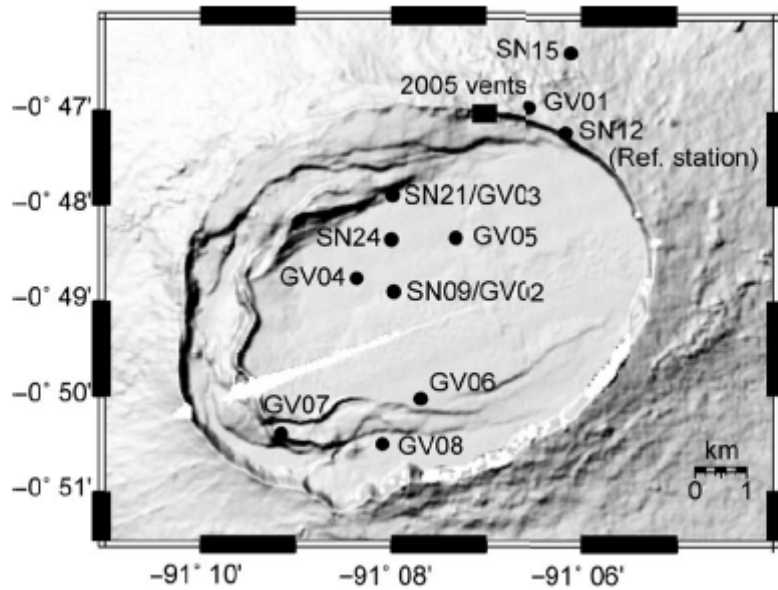


Figure 2-2 Digital Elevation Map of the summit area of Sierra Negra showing the location of the gravity and continuous GPS stations referred to in this study. The eruptive vents from 2005 are also shown.

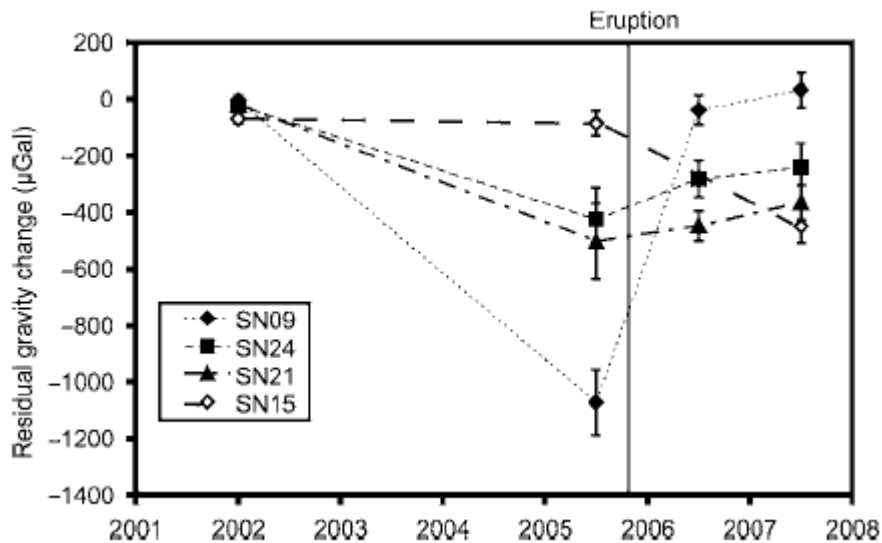


Figure 2-3 Residual gravity change (BCFAG corrected) recorded at all stations referenced to June 2001. The time of the October 2005 eruption is indicated. Error bars represent compounded errors from the sources discussed in the text.

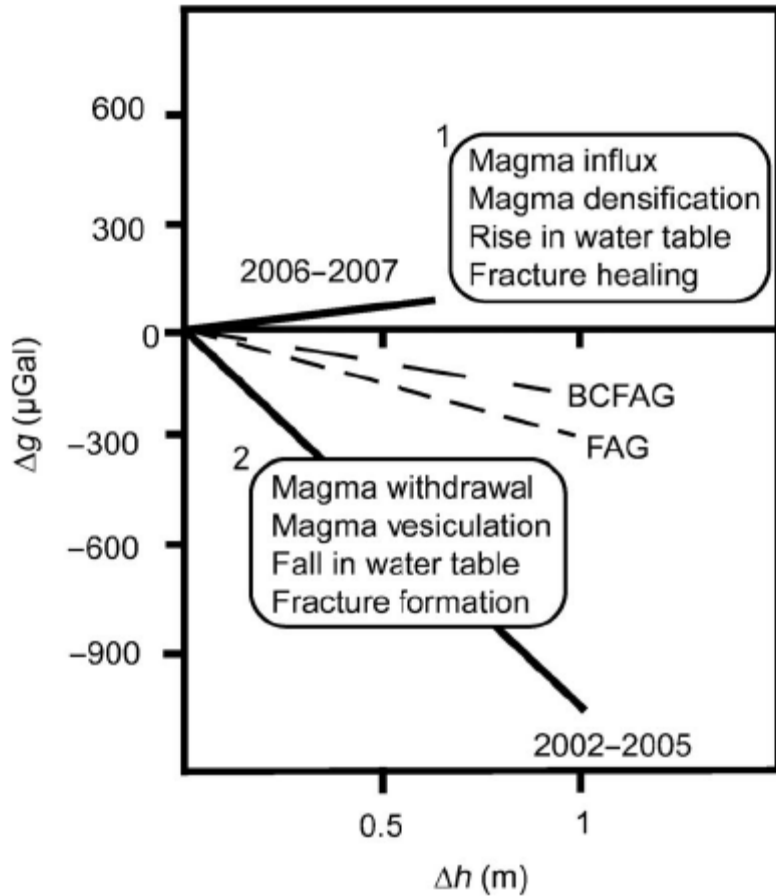


Figure 2-4 Maximum $\Delta g/\Delta h$ gradient for the time period 2002-2005 and 2006-2007 (station SN09) and theoretical FAG (-308.6 $\mu\text{Gal}/\text{m}$) and calculated BCFAG (-191.3 $\mu\text{Gal}/\text{m}$). Scenario boxes 1 and 2 are for gradients that plot above the BCFAG and below the FAG lines respectively.

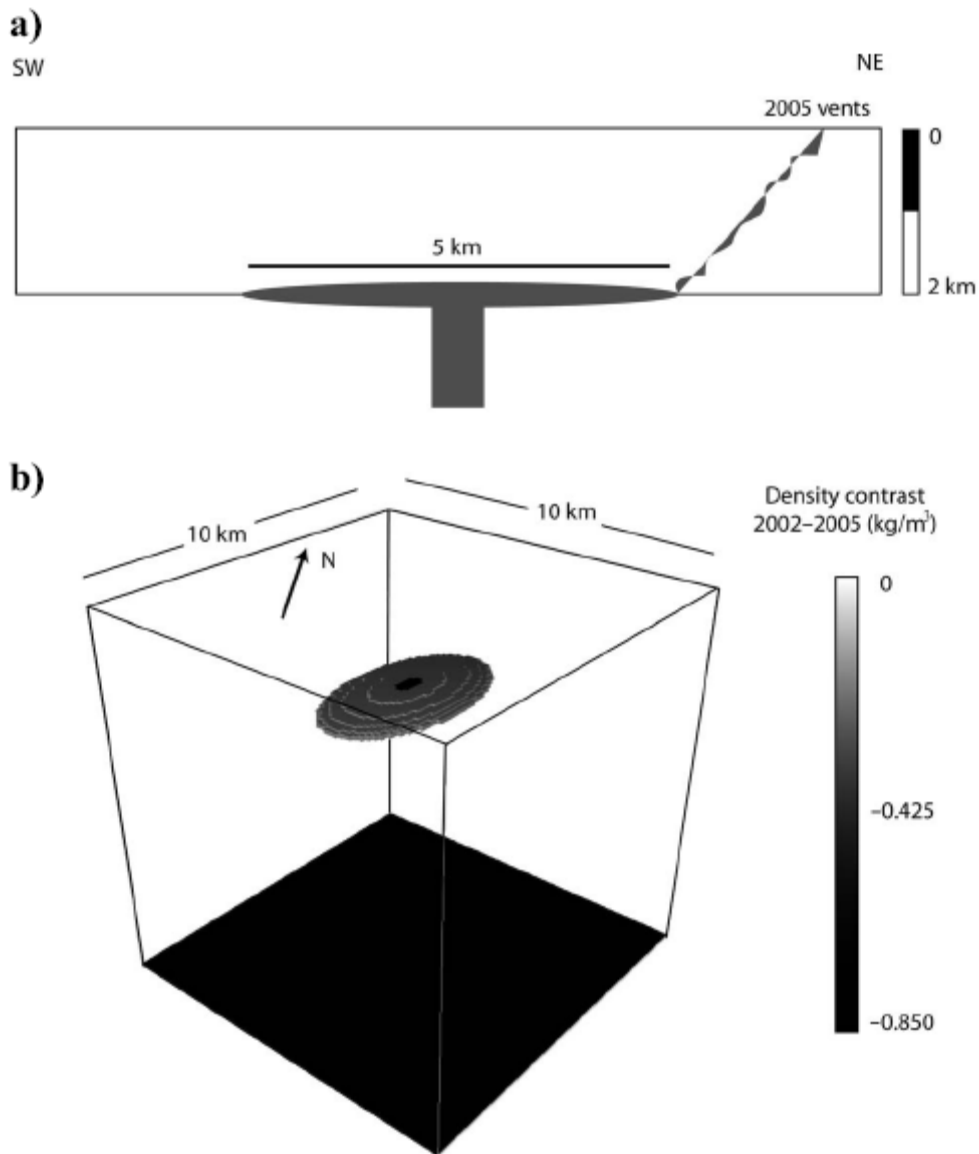


Figure 2-5 Simplified cross-section through the caldera showing the location and geometry of the magma body in 2D (a), and in 3D (b). Part (b) illustrates the geometry of the sill and the foam layer used to generate a maximum gravity anomaly of $-874 \mu\text{Gal}$ (image from Grav3D). The sill is $5000 \times 3000 \times 700$ m and the foam layer is $400 \times 800 \times 50$ m.

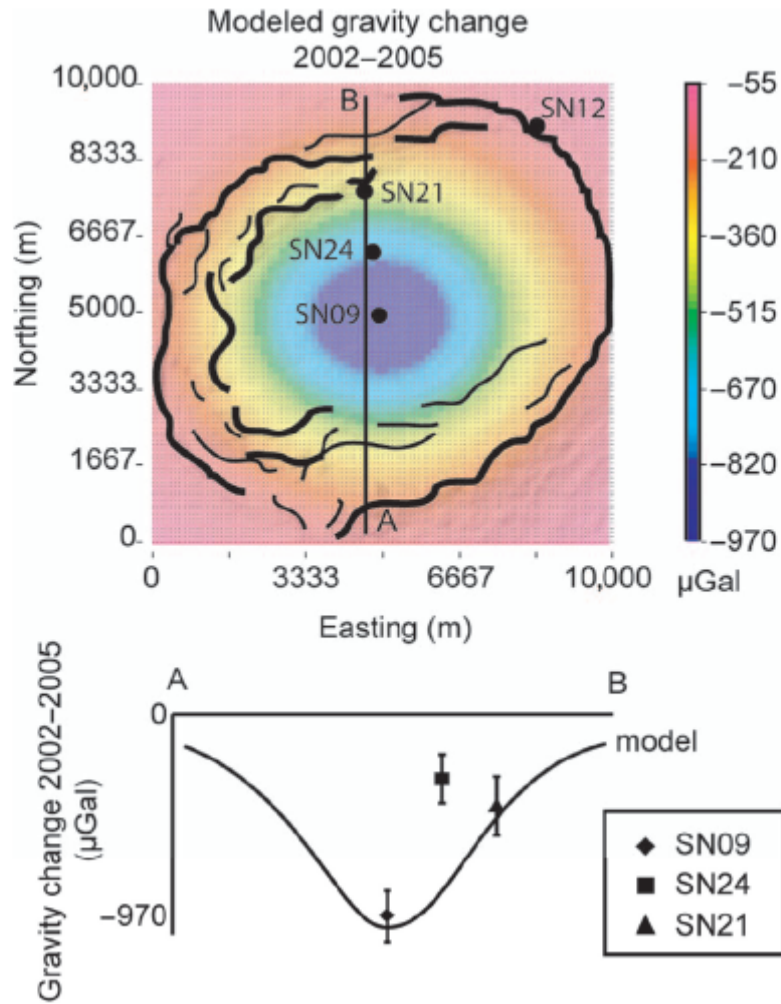


Figure 2-6 Modeled gravity change between June 2002 and 2005 caused by a 800-m thick homogeneous sill with 10% vesiculation.

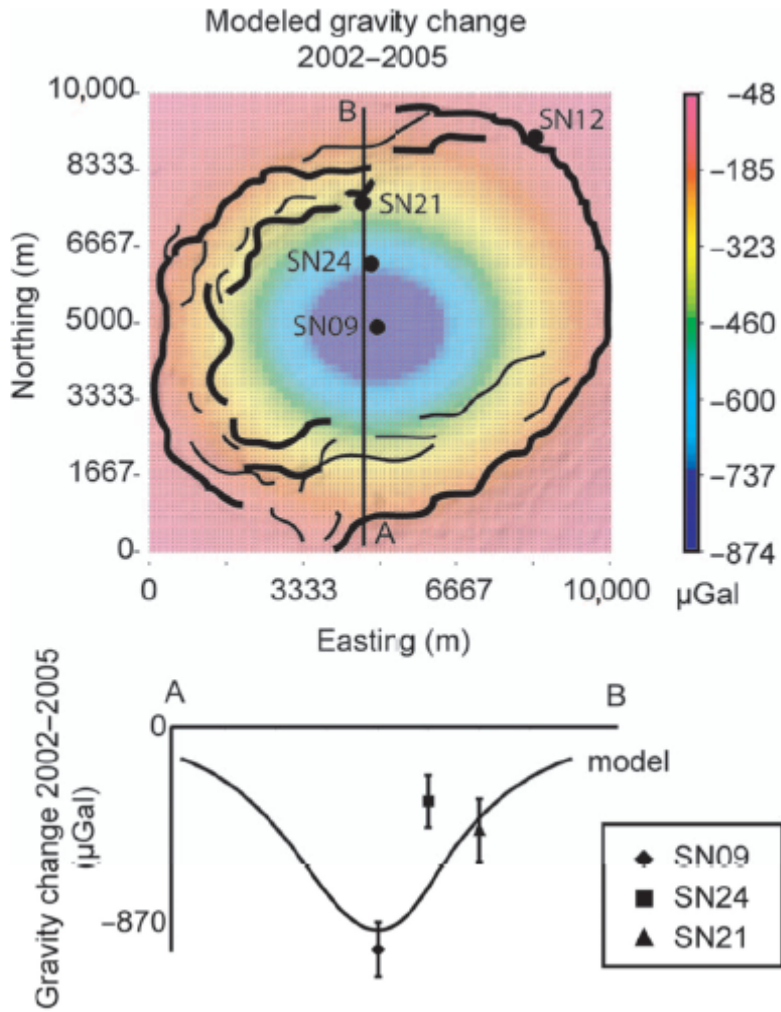


Figure 2-7 Modeled gravity change between June 2002 and 2005 caused by a 700-m thick sill with 10% vesiculation and a 50 m thick foam layer with 50% vesicularity at the top.

2.10 Tables

Table 2-1^a Summary of gravity and deformation data at Sierra Negra

Year	2001 ^b		2002 ^b		2005		2006		2007	
Instrument used ^c	G-209		G-209		G-209		G-127		G-127	
Station	Raw gravity (mGal)									
		Error		Error		Error		Error		Error
SN09	32.89	0.01	32.91	0.01	31.62	0.11	32.90	0.05	32.84	0.06
SN21	34.36	0.01	34.35	0.01	33.78	0.13	33.99	0.05	34.01	0.06
SN24	34.91	0.01	34.90	0.01	34.35	0.11	34.79	0.05	34.74	0.04
SN15	34.03	0.01	33.98	0.01	33.96	0.04	-	-	33.56	0.06
	Elevation (m)									
SN09	952.395	0.013	952.262	0.009	953.407	0.064	952.163	0.016	952.756	0.010
SN21	927.914	0.018	927.860	0.007	928.309	0.039	927.501	0.012	927.808	0.007
SN24	938.492	0.016	938.404	0.009	939.201	0.053	937.675	0.020	938.147	0.010
SN15	797.155	0.013	797.051	0.008	797.075	0.025	797.241	0.017	797.259	0.020
Time period	Δg_{\max}^d	Error	Δh_{\max}	Error	$(\Delta g/\Delta h)_{\max}$					
	(μGal)		(m)		($\mu\text{Gal/m}$)					
2002-2005 (SN09)	-1067	113	1.15	0.06	-931					
2006-2007 (SN09)	71	79	0.59	0.02	119					

^a Raw gravity values are referenced to the base station SN12.

^b Data from Geist et al. (2006).

^c Instruments have been cross-calibrated (referenced to G-127).

^d Corrected for elevation effects (BCFAG= -191.3 $\mu\text{Gal/m}$).

2.11 References

- Allan, J. F., and T. Simkin, 2000, Fernandina volcano's evolved, well-mixed basalts: Mineralogical and petrological constraints on the nature of the Galápagos plume: *Journal of Geophysical Research – Solid Earth*, **105**, 6017-6041.
- Amelung, F., S. Jónsson, H. Zebker, and P. Segall, 2000, Widespread uplift and 'trapdoor' faulting on Galápagos volcanoes observed with radar interferometry: *Nature*, **407**, 993–996.
- Ballhaus, C., 1993, Redox states of lithospheric and asthenospheric upper-mantle: *Contributions to Mineralogy and Petrology*, **114**, 331-348.
- Battaglia, M., C. Roberts, and P. Segall, 1999, Magma intrusion beneath Long Valley caldera confirmed by temporal changes in gravity: *Science*, **285**, 2119-2122.
- Battaglia, M., P. Segall, and C. Roberts, 2003, The mechanics of unrest at Long Valley caldera, California. 2. Constraining the nature of the source using geodetic and micro-gravity data: *Journal of Volcanology and Geothermal Research*, **127**, 219-245.
- Berrino, G., G. Corrado, G. Luongo, and B. Toro, 1984, Ground deformation and gravity changes accompanying the 1982 Pozzuoli uplift: *Bulletin of Volcanology*, **47**, 187-200.
- Carbone, D., G. Budetta, and F. Greco, 2003, Bulk processes prior to the 2001 Mount Etna eruption, highlighted through microgravity studies: *Journal of Geophysical Research - Solid Earth*, **108**, 2556.
- Carbone, D., L. Zuccarillo, G. Saccorotti, and F. Greco, 2006, Analysis of simultaneous gravity and tremor anomalies observed during the 2002-2003 Etna eruption: *Earth and Planetary Science Letters*, **245**, 616-629.
- Carbone, D., G. Budetta, F. Greco, and L. Zuccarello, 2007, A data sequence acquired at Mt. Etna during the 2002-2003 eruption highlights the potential of continuous gravity observations as a tool to monitor and study active volcanoes: *Journal of Geodynamics*, **43**, 320-329.
- Chadwick, W.W. and K.A. Howard, 1991, The pattern of circumferential and radial eruptive fissures on the volcanoes of Fernandina and Isabela islands. *Bulletin of Volcanology*, **53**, 259-275.
- Chadwick, W.W., D. J. Geist, S. Jónsson, M. Poland, D. J. Johnson, and C. M. Meertens, 2006, A volcano bursting at the seams: Inflation, faulting, and eruption at Sierra Negra volcano, Galápagos: *Geology*, **34**, 1025-1028.

- Dixon, J. E., and E. M. Stolper, 1995, An experimental study of water and carbon dioxide solubilities in mid-ocean ridge basaltic liquids. 2. Applications to degassing: *Journal of Petrology*, **36**, 1633-1646.
- Geist, D., W. Chadwick, and D. Johnson, 2006, Results from new GPS and gravity monitoring networks at Fernandina and Sierra Negra Volcanoes, Galápagos, 2000-2002: *Journal of Volcanology and Geothermal Research*, **150**, 79-97.
- Geist, D. J., K. S. Harpp, T. R. Naumann, M. Poland, W. W. Chadwick, M. Hall, and E. Rader, 2008, The 2005 eruption of Sierra Negra volcano, Galápagos, Ecuador: *Bulletin of Volcanology*, **70**, 655-673.
- Gerlach, T. M., 1993, Oxygen buffering of Kilauea volcanic gases and the oxygen fugacity of Kilauea basalt: *Geochimica et Cosmochimica Acta*, **57**, 795-814.
- Gottsmann, J., L. Wooller, J. Martí, J. Fernández, A.G. Camacho, P.J. Gonzalez, A. Garcia, and H. Rymer, 2006, New evidence for the reawakening of Teide volcano: *Geophysical Research Letters*, **33**, L20311.
- GRAV3D; A Program Library for Forward Modeling and Inversion of Gravity Data over 3D Structures, version 20070309, 2007, Developed under the consortium research project *Joint/Cooperative Inversion of Geophysical and Geological Data*, UBC-Geophysical Inversion Facility, Department of Earth and Ocean Sciences, University of British Columbia, Vancouver, British Columbia.
- Johnson, D. J., 1992, Dynamics of magma storage in the summit reservoir of Kilauea volcano, Hawaii: *Journal of Geophysical Research – Solid Earth*, **97**, 1807-1820.
- Jousset, P., S. Dwipa, F. Beauducel, T. Duquesnoy, and M. Diament, 2000, Temporal gravity at Merapi during the 1993-1995 crisis: an insight into the dynamical behavior of volcanoes: *Journal of Volcanology and Geothermal Research*, **100**, 289-320.
- Kauahikaua, J., and A. Miklius, 2003, Long-term trends in microgravity at Kilauea's summit during the Pu'u'ō'ō-Kūpaianaha eruption: *US Geological Survey Professional Paper*, 165-171.
- Kilinc, A., I.S.E. Carmichael, M. L. Rivers, and R.O. Sack, 1983, The ferric-ferrous ratio of natural silicate liquids equilibrated in air: *Contributions to Mineralogy and Petrology*, **83**, 136-140.
- Koleszar, A.M., A. E. Saal, E. H. Hauri, and M. D. Kurz, 2007, Melt inclusions from the Galápagos plume: Mirrors and mirages of the deep: *Geochimica et Cosmochimica Acta*, **71**, A508-A508.

- Lipman, P.W., 1997, Subsidence of ash-flow calderas: relation to caldera size and magma-chamber geometry: *Bulletin of Volcanology*, **59**, 198-218.
- Montierth, C., A. D. Johnston, K. V. Cashman, 1995, An empirical glass-composition-based geothermometer for Mauna Loa lavas, *in* *Mauna Loa revealed: Structure, Composition, History, and Hazards: Geophysical Monograph*, **92**, 207-217
- Newman, S., and J.B. Lowenstern, 2002, VOLATILECALC: a silicate melt-H₂O-CO₂ solution model written in Visual Basic for excel: *Computers & Geosciences*, **28**, 597-604.
- Reynolds, R. and D. Geist, 1995, Petrology of lavas from Sierra Negra volcano, Isabela Island, Galápagos archipelago. *Journal of Geophysical Research* **100**, 24,537-24,553.
- Reynolds, R., D. Geist, and M. Kurz, 1995, Physical volcanology and structural development of Sierra Negra volcano, Galápagos Archipelago: *Geological Society of America Bulletin*, **107**, 1398-1410.
- Ruiz, A., 2008, Inflation and Deflation Modeling at Sierra Negra and Fernandina Volcanoes Based on GPS Measurements, Galapagos Islands, Ecuador. M.Sc. thesis, University of Idaho.
- Rymer, H., 1996, Microgravity monitoring, *in* R. Scarpa, and R. I. Tilling, eds., *Monitoring and Mitigation of Volcano Hazards: Springer-Verlag*, 169-198.
- Rymer, H., and G. Brown, 1989, Gravity changes as a precursor to volcanic-eruption at Poas volcano, Costa-Rica: *Nature*, **342**, 902-905.
- Rymer, H., and G. Williams-Jones, 2000, Volcanic eruption prediction: Magma chamber physics from gravity and deformation measurements: *Geophysical Research Letters*, **27**, 2389-2392.
- Tsuboi, C., 1983, *Gravity: G. Allen and Unwin*.
- Wallace, P., and I. S. E. Carmichael, 1992, Sulphur in basaltic magmas: *Geochimica et Cosmochimica Acta*, **56**, 1863-1874.
- Williams-Jones, G., H. Rymer, and D. A. Rothery, 2003, Gravity changes and passive SO₂ degassing at the Masaya caldera complex, Nicaragua: *Journal of Volcanology and Geothermal Research*, **123**, 137-160.
- Wilson, L., R. S. J. Sparks, and G. P. L. Walker, 1980, Explosive volcanic eruptions—IV. The control of magma chamber and conduit geometry on eruption column behavior: *Geophysical Journal of the Royal Astronomical Society*, **63**, 117–148.
- Wood, C., 1984, Calderas: a planetary perspective: *Journal of Geophysical Research*, **89**, 8391-8406.

- Yokoyama I., and H. Tajima, 1957, A gravity survey on Volcano Mihara, Ooshima Island by means of a Worden gravimeter: Bulletin of the Earthquake Research Institute, **35**, 23–33.
- Yun, S.-H., P. Segall, and H. A. Zebker, 2006, Constraints on magma chamber geometry at Sierra Negra Volcano, Galápagos Islands, based on InSAR observations: Journal of Volcanology and Geothermal Research, **150**, 232–243.

3: THE SOURCE COMPONENTS OF VOLATILE AND FLUID-MOBILE ELEMENTS IN SUBDUCTION ZONES: A MELT INCLUSION STUDY FROM KAWAH IJEN VOLCANO, INDONESIA¹

3.1 Abstract

Subduction zone recycling of H₂O and other volatiles (S, Cl, F) is primarily controlled by the nature of subducted materials (sediment, altered oceanic crust and serpentinized mantle) and the temperature-pressure profile along the top of the slab. These factors vary from one arc to another and even within arc segments. Herein we investigate the variability of volatile and fluid-mobile trace element enrichment in subduction zones using new data for primitive, olivine-hosted melt inclusions from Kawah Ijen volcano, Indonesia, together with similar published data from other arcs worldwide (Central America, Mexico and Kamchatka). Intra-arc variability in Indonesia is assessed by comparing Kawah Ijen to melt inclusion data from Galunggung volcano, located along the same volcanic front, ~ 700 km to the west. Galunggung erupts magmas with distinctly lower H₂O contents (up to ~2 wt%) compared to those of Kawah Ijen (up to 7 wt%).

We observe a global, positive correlation between slab surface temperatures, Sr, H₂O and Cl contents, indicating that these elements are

¹ The following chapter will be submitted to the journal *Geochemistry, Geophysics, Geosystems* under the co-authorship of P. Wallace, G. Williams-Jones, A. Kent and K. Kelley. Extent of the collaboration thus far includes assistance with trace element analysis by A. Kent, reviews by P. Wallace, G. Williams-Jones and A. Kent, and access to data from Galunggung by K. Kelley.

coupled during subduction zone recycling. Arc magma S contents are more variable and F contents generally remain at background mantle values suggesting partial to complete decoupling of these volatile elements from H₂O and Cl during subduction zone recycling. Simple partial melting and dehydration models constrain the source of volatiles and suggest that beneath most arc volcanoes, the altered oceanic crust (AOC) is the main reservoir for the flux of H₂O-rich fluid, in agreement with experimental and thermo-mechanical models. Sediment melt is also an important component in all arcs, but only for the less fluid-mobile elements (e.g., LREE). Our results synthesize the geochemical evidence for the decoupling of volatile and highly fluid-mobile trace elements from the less mobile elements during subduction zone recycling.

Kawah Ijen and Galunggung display different degrees of enrichment in volatile (H₂O, Cl, S) and fluid-mobile elements (Sr), with Kawah Ijen magmas recording higher AOC-derived fluid fluxes (4-5 wt%) compared to Galunggung magmas (~ 1 wt%). The elevated H₂O and Sr contents of the Kawah Ijen magmas are comparable to some of the most fluid-rich arc front magmas in hot slab subduction zones (e.g., Mexico, Central America) and suggest that the eastern Java arc may be one of the wettest cold slab subduction zones in the world.

3.2 Introduction

Recent studies have focussed on obtaining a comprehensive data set of whole rock, glass and/or melt inclusion compositions in order to investigate the nature of the mantle wedge and the added subduction component involved in arc

magma genesis (e.g., Sisson & Bronto, 1998; Wysoczanski et al., 2006; Churikova et al., 2007; Portnyagin et al., 2007; Sadofsky et al., 2008; Johnson et al., 2009; Rowe et al., 2009; Auer et al., 2009; Tollstrup et al., 2010). This study contributes to this growing data set of geochemical data for arc magmas with melt inclusion compositional data from Kawah Ijen volcano in eastern Java. The main aim of this study is to integrate our data with similar data sets from arcs worldwide in order to gain insight into global arc processes that control the recycling of volatile and fluid-mobile elements from the slab to the overriding crust. The data is compared with experimentally determined trace element behaviour in subducting slabs (e.g., Kessel et al., 2005; Klimm et al., 2008, Hermann & Rubatto, 2009) and thermo-mechanical models of slab dehydration (e.g., Rüpke et al., 2002; 2004; Hacker, 2008).

The range of magma compositions erupted in Java and the Sunda arc mirrors the global variability in subduction zone magmas. The presence of coeval tholeiitic, calc-alkaline, shoshonitic and leucitic lavas on Java suggests that a range of magma compositions can be produced via the interplay between different mantle source compositions and the addition of fluids/melts from the slab (Whitford et al., 1979; Nicholls & Whitford, 1983; Wheller et al., 1987; Turner & Foden, 2001). Both decompression melting and fluid-flux melting of the mantle beneath Java have been proposed (Nicholls & Whitford, 1983; Edwards et al., 1991), and the presence of low-H₂O magma at Galunggung on the volcanic front has contributed to the debate on the interplay between melting mechanism and fluxing of subduction-derive fluids in the production of arc magmas (e.g., Sisson

and Bronto, 1998; Kelley et al., 2006; Kohut et al., 2006; Vigouroux et al., 2008; Reagan et al., 2010). These observations highlight the importance of characterizing the exact nature of the mantle wedge, the melting mechanism and the added subduction component in the study of subduction zone element recycling.

The geographic density of volcanoes and the frequency of eruptive activity on Java make it an ideal locality to sample fresh volcanic material for the study of subduction zone processes. Located in eastern Java, Kawah Ijen has erupted H₂O-rich calc-alkaline magmas (this study), whereas in central Java, Galunggung has erupted relatively H₂O-poor calc-alkaline magmas (Sisson & Bronto, 1998; Kelley et al., 2006). The volcanoes are located on the volcanic front but in different arc segments. Galunggung lies much closer to the trench and the top of the slab (Hamilton, 1979; Syracuse & Abers, 2006) compared to Kawah Ijen. In this contribution, we compare Kawah Ijen and Galunggung melt inclusion compositions with dehydration and melting models for the subducting slab beneath Java in order to gain insight into the nature of the subduction component involved at each volcano. The same approach is used to compare the Indonesian volcanoes to other arc volcanoes worldwide (Mexico, Central America, Kamchatka) in an attempt to gain insight into the global variability in volatile and trace element patterns at subduction zones.

3.3 Geologic Setting

Kawah Ijen and the Ijen Caldera Complex are located in eastern Java, Indonesia, along the volcanic front of the Sunda arc. Galunggung volcano is

located ~ 700 km to the west. The mixed continental/oceanic Sunda arc is related to the subduction of the Indo-Australian plate beneath the Eurasian plate along the 1200 km long Java trench (Fig. 3-1).

In Sumatra and the western part of Java, the overriding plate is composed of continental crust with continental lithospheric basement, part of the “Sunda Land” terrane (Hamilton, 1979). Beneath Kawah Ijen, the crust is ~ 20 km thick and is composed of mostly accreted Cretaceous oceanic and Archean continental terranes (Smyth et al., 2007; Clements et al., 2009). Galunggung is located east of the inferred boundary of the continental basement and sits on Cretaceous ophiolites (Clements et al., 2009).

The top of the subducting plate lies 180 km below Kawah Ijen, has an approximate age of 130 Ma at the trench and dips at an angle of 42° (Syracuse & Abers, 2006). Further west on Java, the top of the slab lies 120 km beneath Galunggung, has an age of ~96 Ma at the trench, and dips at an angle of 48° (Syracuse & Abers, 2006).

Within the island of Java, the volcanic front as a whole moved ~50 km north away from the trench, sometime after the Paleogene, which resulted in a pronounced increase in the arc front distance to the trench and depth to the top of the slab near Kawah Ijen in eastern Java (Hamilton, 1979; Syracuse & Abers, 2006), and resulted in a broader distribution of the volcanic arc near Galunggung (Clements et al., 2009).

Convergence of the Australian plate at 7 cm yr⁻¹ is nearly orthogonal near Kawah Ijen (e.g., Tregoning et al., 1994; Syracuse & Abers, 2006) and becomes

more oblique and transpressive further to the west in Sumatra (e.g., Hamilton, 1979). North of Galunggung, major E-W trending regional transcurrent faults are present, whereas to the south a major thrust fault system is present (Harmon & Gerbe, 1992; Clements et al., 2009). Around Kawah Ijen, the crustal tectonics are less well defined, but N-S trending normal faults and E-W trending terrane sutures have been identified (Carn, 2000; Clements et al., 2009).

The sediment package being subducted along the Java trench has been characterized in detail by Plank and Langmuir (1998). An uppermost layer of siliceous ooze (125 m thick) overlies 45 m of sand/clay/silt turbidites, followed by 130 m of pelagic clay. This sediment column is an average for the Java trench determined from two DSDP drill sites located at the eastern and western ends of Java (Fig.3-1). The western end is characterized by the presence of turbidites originating from large off-shore fans transporting sediment from the Himalayan collision zone. The eastern sedimentary sequence contains carbonate-rich turbidites originating from the Australian continent. The thickness of the sedimentary package offshore of the Java trench is relatively uniform (200-400 m) but the amount of sediment in-fill at the trench varies laterally. Offshore of Galunggung, the accretionary margin contains up to 1 km of sediment in-fill, whereas offshore of Kawaj Ijen, the margin is erosional and sedimentary in-fill is nearly absent (Kopp et al., 2006). Seamounts from the Roo Rise are currently being subducted at the Java trench (Clements et al., 2009), and numerous normal and thrust faults are mapped in the oceanic crust at the trench (Masson et al., 1990).

Kawah Ijen is a small, active stratovolcano that sits at the intersection of the Ijen Caldera Complex rim and an intra-caldera lineament of small cinder cones and shields (Fig. 3-1). Kawah Ijen's edifice has been repeatedly built and subsequently destroyed over the last 24,000 years (Sitorus, 1990; Van Hinsberg, 2001), starting with a cone building stage that consists of interbedded layers of basaltic scoria and lava flows. These are overlain (2,500 years B.P.; Sitorus, 1990) by interbedded pyroclastic flow and fall deposits, phreatic deposits, and more felsic and mafic lava flows outcropping on the outer S-SW flank of the edifice and exposed along the inner crater walls and in the river bed of the Banyupahit river (Fig. 3-1). The western flank of the volcano has been progressively destroyed by a series of crater explosions and subsequent collapses. The current configuration is a large (1 km wide) crater, 300 m deep, partly filled with a hyper-acidic lake that drains out via the Banyupahit river. An actively degassing dome, covered in native S precipitates, is located on the SE shore of the lake. Samples of scoria from the lowermost exposed layers of the edifice were collected in order to sample the earliest and most primitive magmas erupted at Kawah Ijen.

3.4 Methodology

The basaltic tephra sampled, the olivine crystals it contains and the olivine-hosted melt inclusions are described in detail in Appendix B, Figure 6-1 and Table 6-3. Olivine-hosted melt inclusions were doubly intersected and polished for H₂O and CO₂ analysis by Fourier Transform Infrared Spectroscopy (FTIR) using a Nicolet Magna 560 FTIR with a Continuum IR microscope and

OMNIC software at the University of Oregon. Absorbance was converted to concentration using the Beer-Lambert law, calculated glass densities using the method of Luhr (2001) and absorbance coefficients from Yamashita et al. (1997), Dixon et al. (1995) and Dixon and Pan (1995). Further details of the methodology can be found in Appendix B. Melt inclusion and olivine host major element compositions (and S, Cl and F contents) as well as sulphur K α wavelength shifts were obtained from electron microprobe analysis using a Cameca SX-100 at the University of Oregon. Details of the analytical conditions and standards used are given in Appendix B. Additional details of the method used for measuring the sulphur K α wavelength shifts have been given by Wallace and Carmichael (1994). Trace element compositions were obtained using Laser Ablation ICP-MS in the W.M. Keck Collaboratory for Plasma Spectrometry at Oregon State University. Details of the technique are summarized in Rowe et al. (2006) and Kent et al. (2004). A 50 μ m laser diameter was used with a 4 Hz pulse rate. ^{43}Ca was used as the internal standard and analyses were calibrated using repeat analysis of BCR-2G glass throughout the analytical session. BVHO-2G glass was analysed as a secondary standard to monitor accuracy and precision, and uncertainties for all elements are generally less than 10%. Due to the average small size of the melt inclusions, only one melt inclusion was sampled twice and results of the reproducibility as well as analysed standards are given in Table 6-2.

3.4.1 Post-entrapment modification correction

Melt inclusion compositions were corrected for post-entrapment crystallization of olivine along the walls of the inclusion (e.g., Sobolev and Danyushevsky, 1994). The correction process involves adding 0.1% increments of equilibrium olivine back into each melt inclusion until the inclusion composition is in equilibrium with the olivine host. The exchange coefficient ($K_D = (\text{Mg}/\text{Fe}^{2+})_{\text{melt}}/(\text{Mg}/\text{Fe}^{2+})_{\text{olivine}}$) was calculated for each melt inclusion using the equation of Toplis (2005) that relates K_D to temperature, pressure, melt composition (including H_2O) and olivine composition. The average pressure (0.3 GPa) and temperature (1100°C) recorded by the melt inclusions were used. Pressures were calculated from Papale et al. (2006), and temperatures are from equation 6a in Sugawara (2000). K_D values ranged from 0.3 to 0.35. We assumed a wt% $\text{FeO}/\text{FeO}_{\text{total}}$ ratio of 0.79, calculated from the $f\text{O}_2$ of the melt inclusions, converted to melt $\text{Fe}^{2+}/\text{Fe}^{3+}$ mole fraction ratio using the method of Kilinc et al. (1983). Oxygen fugacity values were calculated from the S K α measurements on four melt inclusions using a temperature of 1100°C and following the method of Wallace and Carmichael (1994). Extents of post-entrapment crystallization range from 0-8%. Uncertainties in the re-calculated melt inclusion compositions based on uncertainties in $\text{FeO}/\text{FeO}_{\text{total}}$ determination ($\pm 5\%$), K_D (± 0.01) and coexisting olivine host composition ($\pm 0.5 \text{ Fo}$) are $\leq 0.5\%$ for the non-participating oxides and $< 5\%$ for the major participating oxides (FeO , MgO and SiO_2).

Total iron contents in the melt inclusions are comparable to those measured in the bulk rock (Handley et al., 2007) at a given MgO content suggesting that post-entrapment iron loss by diffusion was negligible. The CaO/Al₂O₃ ratios of the melt inclusions lie along the liquid line of descent defined by the whole rock data (Handley et al., 2007). This suggests that the melt inclusion compositions are representative of the bulk melt from which the olivine crystallized and that the melt inclusions were not affected by disequilibrium processes (boundary layer concentration build-up) during entrapment (Faure & Schiano, 2005; Métrich & Wallace, 2008; Kent, 2008).

3.5 Results

Corrected melt inclusion compositions and calculated oxygen fugacities are reported in Table 3-1. Only values corrected for post-entrapment crystallization are described in the text and shown in figures. Uncorrected melt inclusion compositions can be found in Table 6-2. Major, trace and volatile element data for Galunggung are taken from Sisson and Bronto (1998), Kelley et al. (2006), and Kelley and Cottrell (2009) and represent olivine hosted melt inclusions erupted during the latter portion of the 1982-1983 eruption in high-MgO magmas (10-12 wt% MgO; Sisson and Bronto, 1998). The melt inclusion major element compositions are corrected for post-entrapment crystallization of olivine following the method described in Kelley and Cottrell (2009).

Olivine host compositions range from Fo₇₈₋₈₁ for Kawah Ijen whereas they are more primitive for Galunggung, most ranging from Fo₈₈₋₉₀ (Sisson and Bronto, 1998; Kelley and Cottrell, 2009). The Kawah Ijen basaltic melt inclusions (with

the exception of the melt embayment, sample TO-IX) have anhydrous normalized SiO₂ values of 47-49 wt%, Al₂O₃ contents of 19-20 wt%, CaO contents of 11-12 wt% and MgO contents of 5-7 wt%, and can be classified as high-alumina basalt (Kuno, 1960). In comparison, Galunggung magmas have higher and more variable MgO (6-11 wt%) and CaO (11-17 wt%) contents as well as variable SiO₂ contents (44-51 wt%). As discussed in Sisson and Bronto (1998) and Kelley et al. (2006), the Galunggung melt inclusions span a range of compositions between two end-member primitive melts: a high-Mg basalt and a high Ca, silica-undersaturated melt similar in composition to an ankaramite.

Both Kawah Ijen and Galunggung melt inclusions compositions straddle the classification boundary between low-K tholeiitic and medium-K calc-alkaline magmas (Fig. 3-2). For comparison, whole rock data for other volcanoes within Java and the neighbouring island of Bali are shown. They illustrate the range of magma compositions that can erupt in close spatial and temporal proximity (all of the Indonesian volcanoes shown including Kawah Ijen and Galunggung have had historical eruptions, except for Muriah which was active in the Holocene; Siebert & Simkin, 2002).

For comparison to Kawah Ijen and Galunggung, melt inclusions from other arc volcanoes are included: Mexico (Johnson et al., 2009), Central America (Wade et al., 2006; Benjamin et al., 2007; Sadofsky et al., 2008) and Kamchatka (Portnyagin et al., 2007). These datasets were chosen because they report complete major, trace and volatile element compositions in olivine-hosted melt inclusions (Portnyagin et al., 2007 and Sadofsky et al., 2008 do not report CO₂

contents). These melt inclusions also fall within the low-K to medium-K classification. Although this study mainly compares tholeiitic and calc-alkaline basaltic-basaltic andesite magmas, the potassic magmas of Colima, Mexico (Vigouroux et al., 2008) are included to represent the less dominant but ubiquitous magma type present in many arcs (e.g., Muriah volcano, Indonesia).

The trace element pattern of Kawah Ijen magmas are compared to those of Galunggung and volcanoes from the three other arcs in Figure 3-3. On average, the volcanoes display the typical enrichment-depletion pattern of subduction zone magmas with a variable but distinct depletion in the high field-strength elements (HFSE; e.g., Nb, Zr) and a relative enrichment in the large ion lithophile elements (LILE) over the light rare earth elements (LREE) when compared to average mid ocean ridge basalt (MORB) and ocean island basalt (OIB) magmas. The subordinate presence of magmas with an intraplate (“OIB-like”) trace element signature in arcs is represented by Hoya Alvarez, an alkali basaltic maar in the Trans-Mexican Volcanic Belt (Johnson et al., 2009). Within the field for Central America, three volcanoes lack a pronounced Nb depletion and have trace element signatures intermediate between OIB and arc magmas: Nejapa and the high-Nb end member of Granada in Nicaragua, and the high-K end member of Irazú in Costa Rica (Sadofsky et al., 2008). Subsequent discussion of Central American magmas does not include the high-K andesite from Irazú.

Kawah Ijen and Galunggung display very similar trace element patterns except for Sr and the least mobile elements (HFSE). Galunggung magmas have

a relatively flat REE pattern ($\text{La/Yb} = 2.7$ compared to 5.6 for Kawah Ijen), have higher concentrations of the HFSE and lower Sr concentrations relative to the LILE and LREE (e.g., $\text{Ba/Nb} = 50$ and $\text{Sr/Nd} = 25$, compared to 94 and 45 respectively for Kawah Ijen).

In terms of volatile content, the Kawah Ijen and Galunggung melt inclusions are notably different (Fig. 3-4). Kawah Ijen melt inclusions display a wide range of H_2O and CO_2 contents, representing degassing of the magma during ascent and olivine crystallization. In contrast, Galunggung melt inclusions can be sub-divided into two groups: low H_2O with variable CO_2 and moderate H_2O with generally lower CO_2 contents (Kelley et al., 2006). The vapour saturation isobars shown in Figure 3-4 indicate maximum melt inclusion trapping pressures of 0.38 GPa for Kawah Ijen, corresponding to depths of >10 km in the crust, assuming the melts were vapour-saturated. Evidence for vapour saturation of the Kawah Ijen melts includes the presence of vapour bubbles in some melt inclusions and the large range of H_2O and CO_2 contents recorded by the melt inclusions.

For Kawah Ijen, the high CO_2 contents maintained even at low H_2O contents do not correspond to predicted solubilities for degassing of basaltic magmas. The three model curves shown on Figure 3-4 (a) open, b) closed and c) closed system with 5 wt% exsolved vapour) are for a basaltic magma degassing in equilibrium fashion in a system that is either closed to addition or loss of a gas phase, or a system that is open to gas loss only (Newman & Lowenstern, 2002). None of the degassing curves can describe the high $\text{CO}_2/\text{H}_2\text{O}$ ratios of many

Kawah Ijen inclusions. Other volatile-rich arc magmas display a similar range of CO₂/H₂O ratios as Kawah Ijen (e.g., Jorullo, Cerro Negro, Kluchevskoy; Fig. 3-4). These variable and high CO₂/H₂O ratios are best explained by vapour fluxing from deeper in the conduit followed by partial re-equilibration with the magma upon degassing (e.g., Wallace, 2005; Spilliaert et al., 2006; Johnson et al., 2008; Vigouroux et al., 2008; Roberge et al., 2009; Blundy et al., 2010;). Vapour isopleths of 40-70 mol % H₂O bracket most of the Kawah Ijen data (Fig. 3-4).

The low H₂O melt inclusions at Galunggung have been ascribed to decompression melting of relatively dry, yet metasomatized mantle, which would explain the low H₂O contents despite the trace element pattern typical of subduction zones magmas (Sisson and Bronto, 1998; Schiano et al., 2000; Kelley et al., 2006). The moderate H₂O with low CO₂ melt inclusions (Kelley et al., 2006) are more typical of partially degassed melts derived from fluid flux melting of the mantle beneath arcs. In the subsequent discussion of volatiles and trace element mobility in subduction zones, only the moderate-H₂O magma of Galunggung will be included as it shows evidence of H₂O-rich fluid addition from the slab.

3.6 Discussion

In the following discussion, we compare between arc magmas using the average melt inclusion compositions calculated to be in equilibrium with Fo₉₀₋₉₁ as reported in Portnyagin et al. (2007), Sadofsky et al. (2008), Johnson et al. (2009). For Kawah Ijen, we back calculate all melt inclusion composition to be in equilibrium with Fo₉₀ olivine using the same procedure as discussed above for

the correction of post-entrapment crystallization. For Galunggung we back calculate the melt inclusion compositions of Sisson and Bronto (1998) and Kelley et al. (2006) using a K_D of 0.3 and a $\text{FeO}/\text{FeO}_{\text{total}}$ of 0.82 (Kelley and Cottrell, 2009). This procedure does not remove all the effects of differentiation of the primitive melts, especially for melt inclusions hosted in $\text{Fo}_{<85}$ olivine which have likely experienced clinopyroxene, plagioclase and Fe-oxide fractionation, therefore we compare the arc volcanoes using ratios of the trace element composition in equilibrium with Fo_{90-91} olivine. Once ratioed, the trace element signature of each volcano still displays some variability, which is likely related to mantle source variability and/or variability in the amount of partial melting and subduction-derived fluid addition to the mantle source. As such, our discussion of individual arc volcanoes is limited to the average of the trace element ratios for each melt inclusion suite. For ratios involving volatile components, we retain only the highest H_2O values, and the S, Cl and F contents associated with these maximum H_2O contents, thereby minimizing the effects of degassing and any low pressure crystal fractionation effects (e.g., plagioclase, clinopyroxene) which are not accounted for by back calculating to equilibrium with Fo_{90-91} compositions. When ratioed to a non-volatile element (e.g., $\text{H}_2\text{O}/\text{Nd}$) we use the average of the non-volatile trace element in the suite of melt inclusions because not all melt inclusions report a complete volatile and trace element analysis.

3.6.1 Mantle source composition

To quantify the subduction component added to arc mantle sources it is necessary to identify the nature of the mantle wedge prior to the addition of the

subduction component. Recent studies of primitive melt inclusion compositions in arc magmas have used HFSE and HREE, regarded as some of the most conservative or fluid immobile trace elements in subduction zones (Pearce and Peate, 1995), to characterize the mantle wedge (Portnyagin et al., 2007; Johnson et al., 2009). These elements (e.g., Nb, Zr, Ti, Y, Dy, and Yb) are used because they are the least mobile during slab dehydration and melting (e.g., Kessel et al., 2005; Klimm et al., 2008; Hermann & Rubatto, 2009). Previous studies of the Kamchatka and Mexican arc have used Nb/Y and Dy/Yb ratios to characterize the nature of the mantle wedge and the degree of partial melting and previous melt extraction experienced by the mantle (Portnyagin et al., 2007; Johnson et al., 2009).

Figure 3-5 compares the average Nb/Y and Dy/Yb ratios of arc melt compositions with modal batch melting models of various mantle source compositions in both the spinel and garnet lherzolite fields. The Nb/Y ratio is a function of source depletion and degree of partial melting, whereas the Dy/Yb ratio is strongly controlled by the presence or absence of residual garnet in the mantle source. Most arc magmas have Nb/Y ratios varying between N-MORB and E-MORB values, with Irazú and the Mexican magmas trending toward OIB values. Dy/Yb ratios are also variable and range from high values similar to OIB magmas (>2) to values lower than average MORB (<1.5).

Mantle melting curves are modeled using the modal batch melting equation and starting mantle compositions of depleted MORB mantle (DMM; Salters & Stracke, 2004), enriched DMM (E-DMM; Workman & Hart, 2005) and

enriched OIB-like mantle (Hoya Alvarez; Johnson et al., 2009). Partition coefficient (D) values used for modeling melting in the spinel stability field are from Workman and Hart (2005). For melting in the garnet stability field, bulk D values are calculated following the method of Eiler et al. (2005) using garnet D values from Gaetani et al. (2003). The models include partial melting of a mantle that has undergone previous melt extraction (PME) in both the spinel and garnet stability fields following the method of Portnyagin et al. (2007).

Results of these models do not offer a unique solution to the nature of the mantle source beneath these arc volcanoes. Variability between subduction zone magmas in terms of the fluid-immobile HFSE and HREE is likely a combined function of mantle wedge composition, degree of partial melting and degree and nature of PME. The models are also highly sensitive to the D values employed. Nevertheless, a first-order approximation of the mantle source of arc magmas may be assessed from Figure 3-6.

Kawah Ijen magmas have a steeper REE pattern (Fig. 3-3) compared to Galunggung which suggests either a mantle source having undergone smaller extents of partial melting or PME in the garnet stability field. The Nb/Y and Dy/Yb systematics illustrate the relationship between Kawah Ijen and Galunggung. Both plot near the model curves for small degrees of PME in the garnet stability field starting with an enriched depleted MORB mantle source (E-DMM) and the lower Nb/Y ratio of the Galunggung magmas are consistent with larger degrees of partial melting or PME. An MORB-like mantle source component (similar to Indian Ocean MORB; I-MORB) has previously been proposed for some of the

magmas of Java (Turner & Foden, 2001; Gertisser & Keller, 2003; Sendjaja et al., 2008) and Handley et al. (2007) identified an enriched I-MORB component in the magmas of Ijen using Sr, Nd, Hf and O isotopes. Some isotopic studies have found evidence for an OIB mantle components in the magmas of Java (e.g., Edwards et al., 1991; 1994) therefore we do not rule out the possibility of a mantle source containing a mixture of more enriched (OIB-like) and highly depleted mantle components (DMM).

In comparison, the Kamchatka magmas originate from 5-14 wt% partial melting of a DMM-like mantle source having undergone <1 wt% PME in the spinel lherzolite field (Portnyagin et al., 2007). Mexican magmas have highly variable Nb/Y and Dy/Yb ratios, resulting from 0-10.5 wt% PME of an OIB-type mantle source in the garnet stability field, followed by 6-15 wt% partial melting in the spinel stability field (Johnson et al., 2009). Similarly, Central American magmas have highly variable Nb/Y and Dy/Yb ratios, reflecting the overall variability in the isotopic and trace element compositions (Fig. 3-3) of the magmas erupted across the arc (e.g., Carr et al., 1990; Reagan et al., 1994; Leeman et al., 1994; Chan et al., 1999). Partial melting of a DMM mantle source in the spinel lherzolite field at variable temperatures and degrees of melting can reproduce most Central American magmas (Sadofsky et al., 2008). However, the models are non-unique, and similar results could be obtained from melting of a more enriched mantle source or melting in the presence of residual garnet (Sadofsky et al., 2008). The Mexican potassic magmas have similar Nb/Y values as the most enriched Mexican magmas with elevated Dy/Yb ratios, consistent

with PME in the garnet stability field of an enriched mantle source, results that qualitatively agree with the more detailed trace element modeling reported in Vigouroux et al. (2008).

3.6.2 Sediment, crust and serpentinite contributions to arc magmas

3.6.2.1 Source of moderately mobile elements and slab surface temperatures

Although the more conservative elements such as the HFSE and HREE are used to model the mantle source beneath volcanic arcs, the more mobile elements such as the LREE and the actinides (U, Th) are influenced by the addition of fluids or melts from sediment and altered ocean crust (AOC) (e.g., Hermann et al., 2006).

Th and La, both moderately mobile elements during subduction zone recycling, are commonly used to track the addition of sediment melt to arc magmas, as they are most mobile at temperature ≥ 900 and pressures of ~ 4 GPa if allanite and monazite are residual in the slab (Plank, 2005; Kessel et al., 2005; Klimm et al., 2008; Hermann and Rubatto, 2009). Although Th and La are not significantly fractionated from each other during sediment melting (e.g., Hermann & Rubatto, 2009), subducted sediment generally has a higher Th/La ratio compared to MORB and OIB mantle sources, and therefore sediment melt addition leads to elevated Th/La ratios in arc magmas (Plank & Langmuir, 1998; Plank, 2005).

The influence of sediment melt on the Th/La ratio of arc magmas can be evaluated by comparing the Th-La-Sm contents of arc magmas with respect to

starting mantle and sediment melt compositions (Fig. 3-6; Plank, 2005). The mantle source of most arc magmas prior to subduction enrichment has lower Th/La ratios compared to MORB and OIB mantle sources as a result of repeated PME episodes (Portnyagin et al., 2007; Johnson et al., 2009). A field for the composition of the melts produced by melting of this mantle without the added subduction component is plotted. These hypothetical “dry” mantle melts are modeled using modal batch melting in the spinel stability field with D values from Workman and Hart (2005). Fields are also shown for sediment melt at different pressure and temperature conditions in the slab (750-1000 °C, 2.5-4.5 GPa and melt fractions of 20-55%). These fields are calculated using the partitioning data from the experiments of Hermann and Rubatto (2009) and the sediment composition subducted at each trench from Plank and Langmuir (1998).

A field for the composition of fluids derived from the AOC is computed from the average AOC compositions reported by Kelley et al. (2003) and Bach et al. (2003) from two very different DSDP/ODP localities (offshore of the Mariana arc and the northern South American arc, respectively) and partition coefficient data for subducted oceanic basalt at 700-900 °C and 4 GPa from Kessel et al. (2005). A line illustrating the average Th/La ratio of fluids released during the breakdown of antigorite serpentinite during prograde metamorphism is derived from the average composition of olivine-hosted fluid inclusions in the olivine-enstatite rocks of the Betic Cordillera, Spain (Scambelluri et al., 2001). Limited trace element data for these fluid inclusions does not include Sm concentrations. This fluid release may occur in the oceanic peridotite portion of the slab, or above

the slab as the serpentinized forearc mantle wedge gets down-dragged (Straub & Layne, 2003).

Both AOC- and serpentinite-derived fluids have lower Th/La ratios compared to sediment melts. This reflects the slightly higher mobility of La over Th in lower temperature (700-800 °C) AOC-derived fluids (Kessel et al., 2005) and the low Th/La content of average AOC compared to subducted sediment (Plank & Langmuir, 1998; Kelley et al., 2003; Bach et al., 2003). As a result, this ternary diagram allows for some distinction between sediment melt and AOC-derived fluids (Fig. 3-6). In general, the arc magmas plot between N-MORB (and computed dry mantle melts), AOC fluids, and sediment melts, indicating the importance of all three components (e.g., Kawah Ijen, Galunggung, Mexico). Some compositions could be explained using only mantle and AOC-fluid components, but the distinctly elevated Th/La ratios of many compositions require a variable but significant sediment melt component. For the Central American volcanoes, the distinction between AOC-derived fluids and sediment melts is not possible because of the low Th/La of the subducted sediments (Plank & Langmuir, 1998). The potassic magmas of Mexico have high La/Sm and Th/Sm ratios and overlap with the OIB-like magma Hoya Alvarez, consistent with the LREE (and LILE) enriched nature of the magmas (Fig. 3-3; Vigouroux et al., 2008).

The temperature dependence of trace element mobility in subducting slabs is explored using the method of Plank et al. (2009). This method utilizes the temperature dependence of Ce solubility in monazite and allanite-saturated

fluids/melts and the H₂O contents found in experiments of high-pressure fluids/melts from sediment and oceanic basalt at various temperatures (Plank et al., 2009 and references therein). It is important to note that there are several assumptions and uncertainties associated with these geothermometers (see Plank et al., 2009), and as a result we simply use these temperatures to investigate the possible relationship between slab temperature and trace element mobility.

Melt inclusion H₂O/Ce ratios average 3400 for Kawah Ijen, ~1500 for the moderate-H₂O magma of Galunggung, and ~250 for the low-H₂O magma of Galunggung. Corresponding slab surface temperatures are ~800 °C for Kawah Ijen and ~870 °C for the moderate-H₂O magma of Galunggung (Fig. 3-7). The low-H₂O magma of Galunggung does not yield a reliable slab surface temperature estimate because its magma genesis requires little to no involvement of fluids derived from the subducting slab (Kelley et al., 2006). Its H₂O/Ce ratio is therefore representative of its mantle source (average value slightly higher than average MORB; Saal et al., 2002).

In the calculation of slab surface temperatures, it is more accurate to employ the H₂O/Ce ratio of the subduction component as opposed to the final melt composition because the mantle wedge may contribute significant amounts of Ce, thereby imparting a lower H₂O/Ce ratio to the final melt. However, there are a number of assumptions and uncertainties involved in calculating the subduction component of arc magmas (see Portnyagin et al., 2007). Comparison of temperature estimates using both the calculated subduction component from

Portnyagin et al. (2007) and Johnson et al. (2009) and the measured H₂O/Ce ratio in the melt inclusions suggests that slab surface temperatures may be overestimated by up to 60 °C using the latter. Using the subduction component H₂O/Ce ratios (Portnyagin et al., 2007; Johnson et al., 2009), slab surface temperatures are estimated at 755-875 °C for Mexico and 700-860 °C for Kamchatka. No subduction components are calculated for the Central American magmas (Sadofsky et al., 2008) but melt inclusion H₂O/Ce ratios yield slab surface temperatures of 730-950 °C with most values around 850 °C.

Given the uncertainties in calculated slab surface temperatures using both the melt inclusion and subduction component H₂O/Ce ratios, and in order to be consistent in our comparison of the different arc magmas, we examine the relationship of slab surface temperatures with other trace element ratios using only melt inclusion H₂O/Ce ratios. There is a lack of correlation between slab surface temperatures and Th/La ratios ($R^2 = 0.12$; Fig. 3-7a). This agrees with experimental studies that have shown that Th/La ratios in allanite- and monazite-saturated sediment and AOC-derived fluids/melts do not vary significantly as a function of temperature or degree of melting (Kessel et al., 2005; Klimm et al., 2008; Hermann & Rubatto, 2009). The variability is, therefore, a result of variable proportions of sediment melt added to the mantle source of the arc magmas. There is a tendency for melts with lower H₂O/Ce to have somewhat higher Th/La values, which might be interpreted as evidence for increased sediment melting in hotter slabs. However, this is likely an artifact of having few samples from arcs

with cooler slabs, many of which show elevated Th/La as well (e.g., see Figure 3 in Plank, 2005).

Contrary to Th/La, there is a meaningful, positive correlation between slab temperature and Sr/Nd and Cl/Nd ratios (Fig. 3-7b, $R^2 = 0.49$; and 3-7c, $R^2 = 0.58$). Contrary to Th and La, Sr and Cl are both highly fluid-mobile elements, and Nd behaves similarly to La and Ce (moderately mobile at temperatures ≥ 800 °C and pressures ≥ 4 GPa, Kessel et al., 2005; Hermann & Rubatto, 2009). The positive correlation of Sr/Nd with slab temperature agrees with experimental results on sediment and AOC dehydration/melting in which Sr is highly mobile at low temperatures and low fluid/melt fractions compared to the LREE, and Sr/Nd ratios decrease as temperatures increase (Green & Adam, 2003; Kessel et al., 2005; Klimm et al., 2008; Hermann & Rubatto, 2009). Chlorine is also highly mobile as evidenced by its correlation with H₂O contents in arc magmas (Johnson et al., 2009) and from high salinities in subduction zone metamorphic fluids (Philippot et al., 1998; Scambelluri et al., 2004). The similar behaviour of Sr and Cl versus slab temperature suggests that like Sr, Cl mobility is highest at low temperatures and/or low fluid/melt fractions.

3.6.2.2 Source of fluid-mobile elements and volatiles

Fluid-mobile elements

The most mobile trace elements during slab subduction are the LILE (Cs, Rb, Ba, Sr) as well as Pb, B, Be and Li (Kessel et al., 2005; Marschall et al., 2007; Klimm et al., 2008; Hermann & Rubatto, 2009). In melt inclusion studies, not all these elements are routinely analysed due to low concentrations and/or

lack of suitable standards. Some of the most commonly analysed elements, and also those that are measured most accurately, include Sr and Ba because they occur in high concentrations (100s of ppm). We use Ba/Nd and Sr/Nd ratios to constrain the subduction component of these fluid-mobile elements because sediment melt and AOC- and serpentinite-derived fluids have very distinct compositions in Ba-Sr-Nd space (Fig. 3-8).

Sediment melt compositions are calculated for each arc using the same method as described above (Fig. 3-6). The sediment melts define an elongated field with highly variable Sr/Nd ratios that correspond to temperature variations from 750-1000 °C; pressure has only a negligible effect on melt Sr/Nd ratios (Hermann & Rubatto, 2009). The sediment melts also have variable Sr/Ba ratios which are attributed to temperature, pressure and melt fraction variations (Hermann & Rubatto, 2009).

AOC- and serpentinite-derived fluids are also calculated as described above except that this time Nd values are reported for the serpentinite-derived fluids. AOC-derived fluids have similar Sr/Nd ratios compared to sediment melt but lower Ba/Nd and higher Sr/Ba ratios (Fig. 3-8). This reflects the composition of subducted sediments and AOC despite the fact that Ba is slightly more mobile than Sr in AOC-derived fluids, and the opposite is true for sediment melt (Kessel et al., 2005; Hermann & Rubatto, 2009).

Magmas from Kawah Ijen, Mexico and Kamchatka have Sr/Ba ratios that are higher than expected for simple mixing between sediment melt and MORB mantle sources prior to subduction zone enrichment. These magmas span the

range of compositions between sediment melt and AOC/serpentinite fluids and in some cases, AOC/serpentinite fluids appear to dominate the fluid-mobile element signature. The Mexican potassic magmas have Sr/Nd and Ba/Nd ratios at the upper end of the range for the calc-alkaline and tholeiitic arc magmas, consistent with the extreme subduction zone enrichment signature observed from the trace element pattern (Fig. 3-3).

Kawah Ijen and Galunggung have different Sr/Ba ratios with Kawah Ijen magmas being richer in Sr (and H₂O) compared to Galunggung magmas. This is consistent with a greater proportion of AOC- or serpentine-derived fluid component for Kawah Ijen. Isotopic studies have suggested an important role for AOC-derived fluids in all the magmas of Java with a smaller proportion of a sediment-derived component on average (Edwards et al., 1993; Alves et al., 1999; Turner & Foden, 2001). Handley et al. (2007) conducted a detailed trace element and isotope study of the lavas of the Ijen Caldera Complex. They suggest that a fertile MORB-like mantle source was first fluxed with 3% AOC-derived fluid followed by the addition of <1% of bulk sediment. Our estimates of AOC-derived fluid addition based on H₂O-Sr-Nd systematics are very similar (4%; see Fig. 3-9 and discussion below).

In the Michoacan-Guanujato Volcanic Field (MGVF) of the Mexican arc (Johnson et al., 2009), the volcanoes with the highest Sr/Ba ratio are La Loma, Jorullo, Paricutin and San Miguel. These magmas also have the lowest δO^{18} values for the amount of H₂O-rich subduction component added to their sources, consistent with a greater role for AOC-derived fluids compared to other studied

volcanoes in this region (Johnson et al., 2009). For the other volcanoes (e.g., San Juan), the importance of sediment melt is clearly discernable from the Ba-Sr-Nd systematics.

Kamchatkan magmas vary systematically from low to high Sr/Ba ratios with Ksudach volcano having the highest Sr/Ba ratio. All volcanoes plot within the AOC fluid field which agrees with isotopic studies that reveal little to no sediment component but a distinct AOC-derived fluid signature in the mantle source of these volcanoes (Kersting & Arculus, 1995; Kepezhinskis et al., 1997; Ishikawa et al., 2001). This is at odds with the slightly elevated Th/La ratios of the Kamchatka magmas compared to background mantle wedge compositions (Fig. 3-6; Plank, 2005) and the range of Ba/Sr ratios which would suggest variable degrees of sediment melt influence. However, given the low Ba, Sr, Pb and Nd concentrations in North Pacific sediments (Plank & Langmuir, 1998), the isotopic signature of low degrees of sediment melt addition may be masked by the more dominant reservoirs (depleted mantle and the AOC; Kersting & Arculus, 1995).

In Central America, the Nicaraguan volcanoes (along with Arenal in Costa Rica) have the highest Sr/Ba ratios. However, the subducted sediment also has high Sr/Ba, and low temperature melts derived from this sediment will be particularly enriched in Sr over Ba. This masks the contribution from the AOC- and serpentinite-derived fluids. Nonetheless, other studies offer insight into the nature of the subduction component beneath Central America. Rüpke et al. (2002) used a 2-D thermo-mechanical model to explain the variation in certain trace element ratios (e.g., B/La and Ba/La) across the arc. On the basis of

modeled water retention patterns for the slab, they suggested that the fluid signature of the Nicaraguan magmas originates mainly from the serpentinized lithosphere of the subducting slab, whereas the fluid added to the Costa Rican magmas originates mainly from the metamorphosed basaltic crust. They support their results with arguments based on B and Be concentrations and isotope ratios. For both arc segments however, they find only a small contribution from the subducted sediment based on the high concentration of B and δB^{11} values. Other researchers have suggested that sediment melt (Carr et al., 1990; Feigenson et al., 2004), as well as AOC- and serpentinite-derived fluids, are involved across the arc. The uniqueness of Nicaragua appears to be related to a greater fluid flux beneath that portion of the arc (e.g., Feigenson & Carr, 1986; Patino et al., 2000; Abers et al., 2003; Sadofsky et al., 2008), dominated by AOC- and serpentinite-derived fluids (Rüpke et al., 2002; Eiler et al., 2005). The steep subduction angle beneath Nicaragua ($\sim 60^\circ$, Syracuse & Abers, 2006), resulting in extensive flexural faulting of the oceanic lithosphere at the outer rise (Ranero et al., 2001), perhaps coupled with up-slab fluid flow, likely accentuates the hydration of the Nicaraguan slab (Abers et al., 2003). Our analysis supports the hypothesis that the mantle wedge beneath Nicaraguan volcanoes (with the exception of Masaya and Nejapa) is fluxed dominantly with fluids derived from either the AOC or the serpentinized mantle (high Sr/Ba, high H_2O/Ce and low Th/La) and that the overall subduction-derived flux is highest beneath Nicaragua (highest Ba/Nd and Sr/Nd).

Volatile elements

Information on the mobility and partitioning of the volatile elements other than H₂O during slab dehydration and melting is scarce. In order to relate the volatile elements (H₂O, S, Cl and F) to their source subduction components, we consider their relationship with Sr (Fig. 3-9). Sr contents are correlated to H₂O ($R^2 = 0.61$ when the low H₂O magma of Galunggung is left out) and Cl contents ($R^2 = 0.51$), whereas the trend with S is more scattered ($R^2 = 0.35$). Fluorine contents do not appear to correlate with Sr contents and remain mostly near background mantle values (MORB and OIB).

The global correlation between the volatiles and other fluid-mobile elements such as Ba and Pb is more scattered than for Sr and needs to be examined on the scale of individual arcs. The poor correlation between Ba and H₂O ($R^2 = 0.06$), Cl ($R^2 = 0.06$) and S ($R^2 = 0$) may be a result of the more complex behaviour of Ba compared to Sr during sediment melting (Fig. 6-2). The concentration of Ba in fluids/melts varies with temperature, pressure, and degree of melting, and residual phengite plays a role in buffering Ba concentrations (Kessel et al., 2005, Klimm et al., 2008, Hermann & Rubatto, 2009). Conversely, no residual phases retain Sr in the slab at sub-arc depths and temperatures $\geq 700^\circ\text{C}$ (Feineman et al., 2007; Schmidt & Poli, 1998). Its concentration in the fluid/melt phase is governed by the fraction of fluid/melt produced, which in turn is a function of temperature (Hermann & Rubatto, 2009). Although Pb is highly mobile during both dehydration and melting processes in the slab (Tenthorey & Hermann, 2004; Kessel et al., 2005; Hermann & Rubatto, 2009), its concentration only correlates roughly with Cl contents globally ($R^2 = 0.24$; not

shown). Good correlations for H₂O ($R^2 = 0.83$), Cl ($R^2 = 0.72$) and S ($R^2 = 0.56$) are only seen within the Mexican data (not shown). Only Central America shows a clear positive correlation between Ba/La and Pb/Ce ($R^2 = 0.6$), and data from Mexico and Java actually have uniform Ba/La contents over variable Pb/Ce contents.

Given that Sr, Ba and Pb are all very mobile during slab dehydration and melting, regardless of temperature, pressure and degree of melting, their contrasting behaviour is intriguing. The main reservoir for Ba and Pb is the sediment (Plank & Langmuir, 1998). Therefore, the total flux of Ba and Pb from the slab at sub-arc depths is likely to come dominantly from the sediment melt, not the dehydrating AOC or the serpentinized mantle, which are the main reservoirs for Sr. Given that the main dehydrating reservoirs at sub-arc depths is the AOC (and in some arcs the serpentinized mantle; Rüpke et al., 2004; Johnson et al., 2009; this study), and that Ba and Pb have a more complex behaviour than Sr during sediment melting (Hermann & Rubatto, 2009), this could explain the lack of correlation between Ba, Pb and the volatile elements in most arcs.

Mobility of H₂O

For the calc-alkaline arc basalts, H₂O and Sr contents are variably elevated above background mantle values (except for the low-H₂O of Galunggung), and their positive correlation implies that they are coupled during slab dehydration at sub-arc depths (80-180 km for the arcs described in this study). Kawah Ijen magmas have some of the highest H₂O/Nd (5800) and Sr/Nd

(46) ratios of the arc magmas compared in this study, whereas the moderate-H₂O magma of Galunggung plots at the low end of the range (H₂O/Nd = 2000; Sr/Nd = 25). The low-H₂O magma of Galunggung has a similar average H₂O/Nd ratio to MORB and OIB magmas (< 500) and an average Sr/Nd ratio similar to that of the moderate-H₂O magma. Low H₂O/Nd ratios and Sr/Nd ratios variably elevated above mantle values are also characteristic of the potassic magmas of western Mexico (Vigouroux et al., 2008) and the picrites and ankaramites of the southern Marianas arc (Kohut et al., 2006). The potassic magmas have low H₂O/Nd ratios despite having high H₂O contents (up to 6 wt% H₂O) as a result of elevated concentrations of all trace elements, and are thought to originate from fluid-fluxing of a highly metasomatized mantle source (Vigouroux et al., 2008). The picrites and ankaramites of the southern Marianas have very low H₂O contents and have been interpreted as the result of dry, decompression melting of a metasomatized mantle source (Kohut et al., 2006). These magmas are similar to the low-H₂O Galunggung magmas in composition and trace element pattern and may share a common magma genesis.

Addition of fluids/melts from the slab and to the mantle wedge after PME is modeled in Figure 3-9a. We used a starting mantle composition with Sr/Nd and H₂O/Nd ratios of 20 and 200, respectively (Portnyagin et al., 2007; Johnson et al., 2009). Simple binary mixing of this mantle source with AOC-derived fluids and sediment melt, both at 800°C, produces trends of constant H₂O/Sr ratios (very little fractionation of H₂O-Sr-Nd occurs during mantle peridotite melting). Sediment melts, with the exception of Central America, have a higher H₂O/Sr

ratio compared to AOC-derived fluids calculated from the average composition reported in Bach et al. (2003). The mixing line for AOC-derived fluids best replicates the slope of the data from the arc magmas, whereas mixtures with sediment melt result in H₂O/Sr ratios that are too high to explain most of the arc data (with the exception of Central America for which the ratio is too low). Sediment melt compositions at different pressures and temperatures have very similar H₂O/Sr ratios (230-300 for 750-900 °C and 2.5-4.5 GPa; Hermann & Rubatto, 2009), therefore the results will remain the same regardless of the conditions in the slab at sub-arc depths. AOC-derived fluids, however, have higher H₂O/Sr ratios at higher temperatures (900°C, 2.5 GPa; Klimm et al., 2008) and may have lower H₂O/Sr ratios at lower temperatures however no complete compositional data is available for the lower temperature experiments. Since temperatures \leq 800 °C are expected to predominate in the interior portions of the slab at sub-arc depths (Rüpke et al., 2002; Johnson et al., 2009) and most of the data plots on the AOC mixing line or at slightly lower H₂O/Sr ratios, this reinforces our interpretation that the H₂O/Sr ratio of arc magmas is best explained by AOC-derived fluids.

From these models, we can estimate the proportion of AOC-derived fluids added to the source regions of arc magmas. Kawah Ijen magmas appear to contain 4-5 wt% AOC fluids, whereas Galunggung magmas contain ~ 1 wt% AOC-derived fluids. Within the Mexican arc, the H₂O/Sr ratios correspond to <1-6 wt% AOC-derived fluid with Paricutin and La Loma containing the highest proportion of AOC-derived fluid and San Juan the lowest. These results agree

quantitatively with those found by Johnson et al. (2009) although our estimates of fluid addition range to higher values compared to their estimates (0.5 – 1.2% of H₂O-rich subduction component). For Kamchatka magmas, our model estimates 1-2 wt% AOC-derived fluid addition, which is also higher compared to the 0.2-0.4 wt% estimates for H₂O-rich subduction component reported in Portnyagin et al. (2007). Qualitatively, our results agree with those from Portnyagin et al. (2007) whereby the mantle source of Ksudach magmas contain the highest proportion of subduction component (highest Sr/Ba, Sr/Nd, H₂O/Nd and Cl/Nd; Figs. 3-8, 3-9). In Central America, our model suggests that Cerro Negro receives the highest amount of AOC-derived fluid (7-8 wt%) and volcanoes such as Nejapa, Masaya and Atitlan receive the lowest amount (≤ 1 wt%). This agrees quantitatively with estimates of H₂O contents in the mantle source of the Central American magmas (Sadofsky et al., 2008). Our estimate of fluid addition for Cerro Negro (7-8 wt%) is again higher than estimates of slab component (3.4-4 wt%) from Eiler et al. (2005) and Sadofsky et al. (2008). At this time, our method of estimating % fluid addition should only be used as a first order approximation because it lacks data for Sr and Nd solubility in AOC-derived fluids at temperatures < 800 °C. Given that H₂O and Sr are increasingly mobile in fluids and melts as slab temperature decreases (Kessel et al., 2005; Hermann and Spandler, 2008; Hermann and Rubatto, 2009), the estimated percentage of AOC-derived fluids released from the slab at temperatures < 800 °C should be lower than those reported in our model for a temperature of 800 °C.

The halogen-rich andesites (HRA) of the Izu arc are compared to the basaltic arc magmas because their high concentrations of H₂O and halogens are interpreted to reflect the dehydration of forearc serpentinitized mantle (Straub & Layne, 2003). The composition of fluids released during the dehydration of serpentinite (Fig. 3-9a, b, path B) through antigorite-serpentinite (Fig. 3-9a, b, path A) to harzburgite (Scambelluri et al., 2001; 2004) are also shown. The addition of some H₂O and Sr from the serpentinitized oceanic lithosphere cannot be ruled out since the arc data falls within the range of serpentinite-derived fluid compositions, however no magmas apart from the Izu HRA plot close to path A, the fluid composition most likely to be present at sub-arc pressures and temperatures (Scambelluri et al., 2004).

Mobility of Cl

As with H₂O, Cl contents correlate with Sr contents ($R^2 = 0.51$ and $R^2 = 0.6$ if the Galunggung magmas are left out). The positive correlation between Cl and H₂O (Johnson et al., 2009), Cl and slab temperature (Fig. 3-7c), and Cl and Sr (Fig. 3-9b) suggests that these elements are not significantly fractionated from each other at sub-arc depths. Their concentrations correlate directly with slab temperatures and the fraction of hydrous fluid/melt produced. Kawah Ijen magmas have moderate Cl/Sr ratios compared to other arc magmas, some of which have similar Sr/Nd ratios but trend to higher Cl/Nd ratios (e.g., some of the Mexican magmas). Galunggung magmas (both the high- and low-H₂O magmas), have elevated Cl/Sr ratios and trend towards the basalts and HRA of the Izu arc

although Cl/Nd ratios remain well below the HRA levels (~ 1000 ; Straub and Layne, 2003).

Straub and Layne (2003) suggested that partial decoupling between H_2O , the halogens (Cl, F) and the LILE (Sr) may occur beneath the forearc region where mantle wedge peridotites are serpentinized by the shallow release of sediment pore fluids rich in halogens but poor in structurally bound H_2O , LILE and other trace elements. The resulting fluids have high Cl/Sr and Cl/ H_2O as exhibited by the HRA of the Izu arc (Straub and Layne, 2003). Even fluids produced from the dehydration of oceanic serpentinite in the deeper parts of the slab (Scambelluri et al., 2001; 2004; Fig. 3-9b paths A and B) have lower Cl/Sr ratios compared to the HRA of the Izu arc (Fig. 3-9b). This suggests that the composition of the fluid phase involved in the hydration of the slab peridotites may differ from that of the mantle wedge peridotites.

The Cl/Sr ratios of most arc magmas fall within the range of modeled mixtures of AOC-derived fluid and depleted mantle. The AOC-derived fluids were calculated using three different average Cl contents in the AOC: 50 ppm (Ito et al., 1983), 200 ppm (Phillipot et al., 1998) and 500 ppm (Marschall et al., 2009). We estimate fluid-solid bulk D values for Cl in the dehydrating meta-igneous crust to be 5-10 based on whole rock Cl contents determined in coexisting blueschist and eclogite rocks from Syros, Greece (Marschall et al., 2009). Peak metamorphic conditions for these rocks are estimated at ~ 2 GPa and 500°C . Fluid-solid bulk D values for Nd and Sr are from the lowest temperature and

pressure experiments of Kessel et al. (2005) and the average Sr and Nd contents of AOC from Bach et al. (2003).

Based on these Cl models, the Cl/Sr ratio of arc magmas appears to correspond most closely to AOC-derived fluids with a starting bulk Cl content of 200-500 ppm. The estimated amount of AOC-derived fluid added to the mantle source of the arc magmas varies from < 1 to 8 wt% which is in excellent agreement with our estimates using H₂O/Sr ratios (Fig. 3-9a). Galunggung magmas can be modeled with ~ 2 wt% AOC-derived fluid addition, in agreement with the estimates in Figure 3-9a, but Cl contents in the AOC required to fit the data would be higher than for Kawah Ijen (500 versus 200 ppm). The picrites and ankaramites from the Marianas mainly have low Cl/Nd ratios (< 100) but some melt inclusions record Cl/Nd ratios > 200, similar to the melt inclusions from ankaramites in Lombok, Indonesia (Elburg et al., 2007). These highly variable Cl/Nd ratios may reflect the heterogeneity of the metasomatized mantle. The potassic magmas of Mexico have more uniform Cl/Sr ratios, which are lower than the calc-alkaline magmas due to high Sr contents and despite elevated Cl contents (~ 2000 ppm; Vigouroux et al., 2008).

Fluids released from the dehydration of oceanic serpentinites in the slab also bracket most of the arc magmas (Fig. 3-9b, paths A and B), however, as argued above for the H₂O/Sr data, the mixing lines for AOC-derived fluids best approximate the slope of the data from the arc magmas suggesting that the AOC is the dominant source component for the solute-poor, H₂O-, Sr- and Cl-rich fluids at sub-arc depths.

Although there is no obvious global correlation between the moderately-mobile elements (e.g., Th, LREE) and Cl, S and F contents (not shown), a rough correlation is seen between Cl and the LREE in some arcs (e.g., Central America; Sadofsky et al., 2008). This has been interpreted as a reflection of the coupled mobility of Cl (and S, F) with the LREE in the higher temperature melt phase coming off the slab (Sadofsky et al., 2008). As illustrated in Figure 3-7a, H₂O contents are decoupled from moderately-mobile elements such as Th. This would suggest that in some arcs, Cl (and S, F) may be partly decoupled from H₂O and the hydrous fluid phase released from the slab.

Mobility of S and F

Sulphur contents also appear to correlate broadly with Sr contents although there is more scatter than for Cl and H₂O ($R^2 = 0.35$; Fig. 3-9c). Global variability in mantle S/REE ratios (Saal et al., 2002; Workman et al., 2006) and the complexity of S solubility in melts/fluids (e.g., Mavrogenes & O'Neill, 1999; Jugo et al., 2005) may account for some of this variability. Most of the arc magmas have S contents in excess of the sulphide-saturation limit for basaltic magmas, consistent with the high oxidation state of subduction zone magmas (e.g., Carmichael et al., 2006; Vigouroux et al., 2008). Sulphide globules have been reported in some of the melt inclusions from Central America only (Sadofsky et al., 2008), but their presence at some stage in the evolution of magmas from other arc volcanoes cannot be ruled out. Kawah Ijen magmas have S/Sr ratios that fall within the average for other calc-alkaline magmas, whereas Galunggung magmas, along with Kamchatka magmas, have variable

S/Sr ratios which extend to values above average for the calc-alkaline magmas. The ankaramites from the southern Marianas have highly variable S/Nd ratios (not shown) which extend to ~ 350 (Kohut et al., 2006). The highly variable S and Cl contents may be a result of variable concentrations in the metasomatized mantle source or the influence from residual metasomatic minerals such as apatite and sulphides/sulphates.

Apart from the issue of S solubility in arc magmas, fluid sources of S may be highly variable depending on the amount of S subducted in sediment and AOC. Average S contents in the AOC are ~ 1300 ppm (Alt et al., 1989; Bach et al., 2003), but concentrations in sediment packages can vary greatly depending on the nature of the sediment (Alt & Burdett, 1982). Pelagic clays and cherts are generally most enriched in S (1000s of ppm) whereas volcanoclastics usually have very low S contents (100s ppm; Alt & Burdett, 1982). No S contents are reported in the sediment analyses of Plank and Langmuir (1998), but based on the variability of sediment compositions subducted beneath arcs, highly variable S/Sr is expected in the subduction fluids/melts. Sediments subducted offshore of Kamchatka are particularly rich in pelagic clays and oozes, whereas sediments subducted offshore of Mexico have a high proportion of clastic turbidites. Average sediment subducted at the Java trench contains a mix of these sediment types. This may help explain the higher S/Sr of the Kamchatka magmas compared to the magmas of Mexico and Java.

Fluorine contents do not correlate with Sr contents (Fig. 3-9d). Most arc magmas have F/Nd ratios similar to or slightly greater than MORB and OIB

values (e.g., Galunggung). However, we cannot discount the possibility that in some studies, analytical difficulties in analysing F contents results in their underestimation. Some arc magmas are enriched in F above mantle values, including Kawah Ijen and the Mexican magmas. These magmas have F/Nd ratios similar to the HRA of the Izu arc and the potassic magmas of Mexico. High F contents in basaltic magmas have been linked to the presence of F-rich minerals in the melting source region of these magmas (e.g., F-phlogopite; Sigvaldason & Oskarsson, 1986; Vigouroux et al., 2008). The F/Sr ratio of F-phlogopite and apatite from the Colima potassic magmas (Luhr & Carmichael, 1981) are shown on Figure 3-9d. The elevated F/Sr ratio of these minerals may contribute to the source of high-F in some arc magmas. Phosphoritic sediments, rich in fluoro-apatite (e.g., Burnett, 1977), and F-rich aragonite and high-Mg calcite in calcareous sediments (e.g., Kitano & Okumura, 1973; Wei et al., 2005) can also contribute to F-rich fluids/melts from the slab.

3.6.2.3 Link to subduction zone physical parameters

The previous section has illustrated the correlation between slab surface temperature and the mobility of the most volatile and fluid-mobile trace elements in subduction zones. The release from the slab of Sr, H₂O, Cl and to a lesser extent S, is coupled at sub-arc depths and appears to be controlled mainly by fluid release from the AOC. The minor presence of magmas with highly enriched (potassic) and depleted (ankaramite) trace element compositions, which retain the trace element pattern typical of subduction zone magmas, attests to the variability in subduction zone processes. These magmas do not fall along the

trend produced by the calc-alkaline magmas and do not share the same magma genesis or mantle source (Kohut et al., 2006; Vigouroux et al., 2008).

Experimental studies combined with thermo-mechanical models support the melt inclusion results and suggest that up to 85% of sediment H₂O is released by 100 km depth such that the AOC is the main dehydrating reservoir at sub-arc depths (Schmidt & Poli, 1998; Rüpke et al., 2004; Hacker, 2008; Johnson et al., 2009). For hot subduction zones (e.g., young plates ≤ 40 Ma), the amount of H₂O released from the AOC and the sediment in the slab will reach a maximum at less than 100 km depth, then the overall flux of H₂O will decrease (Schmidt & Poli, 1998; Rüpke et al., 2004; Hacker, 2008). Therefore for young plates, such as those subducting beneath Mexico and Central America, decreasing magmatic H₂O contents with distance from the trench would be expected. In the MGVF of Mexico, this pattern is obscured by the fact that the dip of the slab has shifted in the last 3 Ma (Johnson et al., 2009). In Central America, estimates of primitive, undegassed magmatic H₂O contents are difficult to make (Sadofsky et al., 2008) and any patterns with subduction zone physical parameters are harder to constrain. Nevertheless, rear-arc volcanoes from Guatemala have lower estimated primitive magma H₂O contents compared to arc-front volcanoes (Sadofsky et al., 2008), as would be expected for a progressively dehydrating slab.

For colder and older slabs (> 40 Ma), like the ones subducting beneath Java and Kamchatka (Syracuse and Abers, 2006), the amount of H₂O released from the AOC and the sediment in the slab should remain almost constant at all

sub-arc depths (80-180 km) and will be lower than for younger slabs (Rüpke et al., 2004; Hacker, 2008). As such, for cold slabs, we would expect to see nearly constant magmatic H₂O contents across the arc as is seen in Kamchatka (Portnyagin et al., 2007). In Java, Galunggung and Kawah Ijen are both located on the volcanic front, yet Galunggung magmas have distinctly lower H₂O/Nd and Sr/Nd ratios compared to Kawah Ijen magmas. The volcanoes are located in different arc segments, with H₂O-rich Kawah Ijen being much further from the trench (200 km versus 100 km) and the top of the slab (175 km versus 120 km) compared to Galunggung. Kelley et al. (2006) compared Galunggung with melt inclusions from Tambora, located on the island of Sumbawa east of Java in the Sunda arc. Tambora is located ~ 130 km from the trench and more than 150 km from the top of the slab (Syracuse and Abers, 2006). As with Galunggung, Tambora melt inclusions have low H₂O contents, leading Kelley et al. (2006) to suggest that the Indonesian arc is water-poor. However the data presented here for Kawah Ijen volcano suggests that H₂O contents in the arc are highly variable. Based on only three volcanoes (Kawah Ijen, Galunggung and Tambora), no clear pattern of H₂O content with distance from the trench or to the top of the slab emerges. More complete melt inclusion studies from additional Indonesian volcanoes, combined with geodynamic models of the pressure-temperature conditions of the mantle and slab beneath each volcano, are needed to map out and understand the along-arc and across-arc pattern of H₂O release beneath the Sunda arc.

Despite this current limitation, the study of melt inclusions at Kawah Ijen volcano has allowed for preliminary assessment of slab surface temperatures and amount of fluid release beneath eastern Java (Figs. 3-7, 3-9). Although the Sunda arc is considered a cold subduction zone, Kawah Ijen has some of the highest H₂O, Sr and Cl contents of the arc magmas compared in this study, and our estimate of the AOC-derived fluid flux beneath Kawah Ijen (4-5 wt%) is comparable to estimates for volcanic fronts in hotter slabs (e.g., Mexico). This suggests that the volcanic front in eastern Java may be unusually wet for a cold subduction zone.

3.7 Conclusions

From the relationship between Sr, volatile elements (H₂O, S, Cl, F), and the predicted compositions of sediment melt, AOC- and serpentinite-derived fluids at sub-arc depths, the sources of volatiles in arc front magmas can be constrained. The positive correlations between slab surface temperature, H₂O, Cl and Sr, coupled with the high Sr/Ba ratio of most arc magmas, suggest that most of the H₂O and Cl content of arc front magmas originates from the dehydration of the AOC. The serpentinitized mantle is likely to be an important source of H₂O-rich fluids only in arc segments with hot slab geotherms and steep slab dips such as Nicaragua. Our results suggest that the involvement of H₂O and Cl derived from sediment melt is secondary to the AOC in most arc front magmas, although sediment melt does contribute to Ba, Pb, and LREE contents.

The source of sulphur and fluorine in arc magmas is not as easily discerned although the moderate correlation between Sr and S contents

suggests that either some S is supplied by the dehydrating AOC, or S is efficiently scavenged from the overlying meta-sediment layer. Highly variable S and F contents in subducted sediment (e.g., Wei et al., 2005; Alt et al., 1989), complex and poorly understood solubility mechanisms for S and F, respectively, and the lack of experimental studies on the mobility of S and F in subducted materials makes it difficult to evaluate the source of these volatiles. More F analyses in melt inclusions from arc magmas and better constraints on S and F in slab and mantle components will improve our understanding of S and F recycling in subduction zones.

Results from this study agree with thermo-mechanical models of fluid release in subduction zones and reinforce the role of melt inclusion studies as a complementary method of estimating the nature and amount of fluid release beneath arc volcanoes.

Kawah Ijen and Galunggung display different degrees of enrichment in volatile (H_2O , Cl, S) and fluid-mobile elements (Sr), with Kawah Ijen magmas recording higher AOC-derived fluid fluxes (4-5 wt%) compared to Galunggung magmas (~ 1 wt%). The elevated H_2O and Sr contents of the Kawah Ijen magmas are comparable to some of the wettest volcanic front magmas worldwide (e.g., Mexico, Central America). This would suggest that the eastern Java arc may be one of the wettest cold slab subduction zones in the world.

3.8 Acknowledgement

The authors would like to thank the Kawah Ijen Park service and particularly Tom Mulja and Niken Widyastuti of East Asia Minerals for their help. The Kawah Ijen research team, namely Guillaume Mauri, Stephanie Palmer, Samantha Scher, as well numerous other volunteers, offered valuable help in the field. We acknowledge John Donovan (University of Oregon) for assistance with the microprobe analyses. Funding for this work was provided by an NSERC-CRD grant to G. Williams-Jones.

3.9 Figures

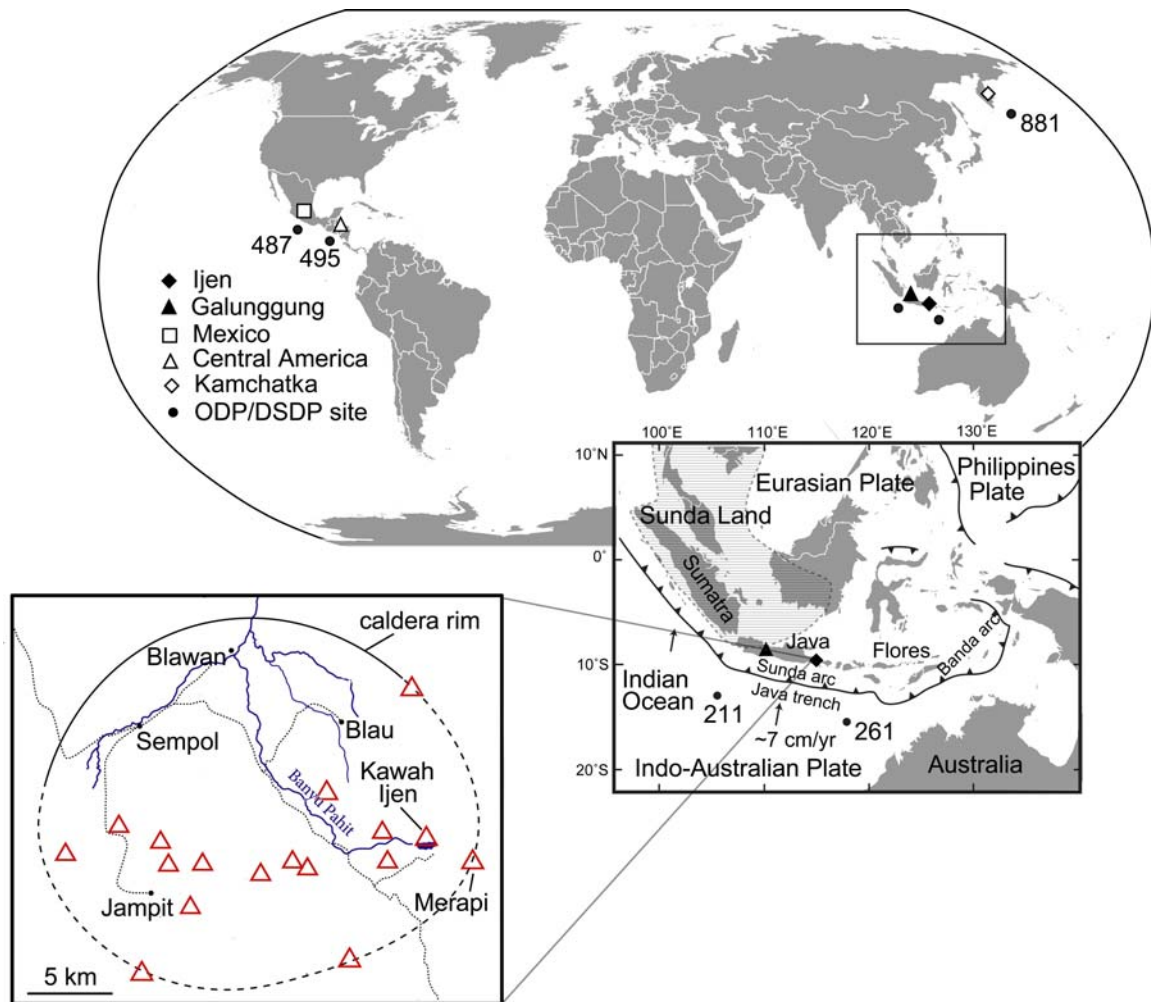


Figure 3-1 Map showing the locations of the volcanic arcs discussed in this study. Also shown are drill core recovery sites from either the Ocean Drilling Program (ODP) or the Deep Sea Drilling Project (DSDP) as discussed in Plank and Langmuir (1998). Inset: the location of the Sunda arc and Kawah Ijen (filled diamond) and Galunggung (filled triangle) volcanoes on the island of Java, Indonesia. The thatched region labeled Sunda Land delineates the inferred extent of the continental lithosphere beneath the arc (Hamilton, 1979). Arrows indicate relative plate motions (Tregoning et al., 1994) and convergence rate (Syracuse & Abers, 2006). The location of Kawah Ijen within the Ijen Caldera Complex is shown in the zoom-in (map modified from Van Hinsberg et al., 2008).

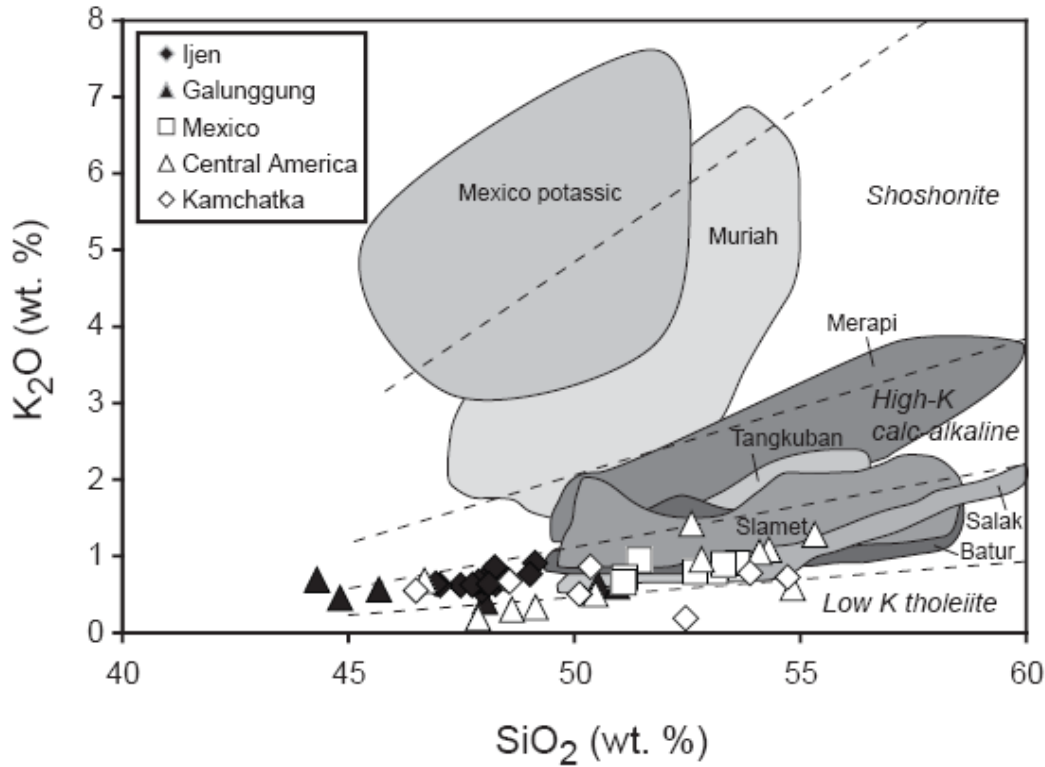


Figure 3-2 Major element composition, K_2O versus SiO_2 (wt%), of the Sunda arc magmas compared to other arcs discussed in this study. Shaded fields represent whole rock data for Sunda arc volcanoes other than Kawah Ijen and Galunggung (Muriah: Calanchi et al., 1983; Edwards et al., 1991, Merapi: Camus et al., 2000; Gertisser et al., 2003, Nadeau et al., 2010, Tangkuban: Sendjaja et al., 2008, Slamet: Vukadinovic & Sutawidjaja, 1995; Reubi et al., 2002, Salak: Handley et al., 2008, Batur: Reubi & Nicholls, 2004). Data for Kawah Ijen, Galunggung and the other arcs are olivine-hosted melt inclusion compositions calculated to be in equilibrium with their host olivine. Individual melt inclusions are plotted from Kawah Ijen (this study) and Galunggung (Sisson & Bronto, 1998; Kelley & Cottrell, 2009). Averages for each volcano are plotted for the other arcs (Mexico: Johnson et al., 2009, Central America: Wade et al., 2006; Benjamin et al., 2007; Sadofsky et al., 2008, Kamchatka: Portnyagin et al., 2007). Data from the melt inclusions of the potassic magmas of Colima, Mexico are shown as a shaded field (Vigouroux et al., 2008). Error bars (standard deviation for a given volcano) are smaller than symbol size. Diagram classification scheme is from Peccerillo and Taylor (1976).

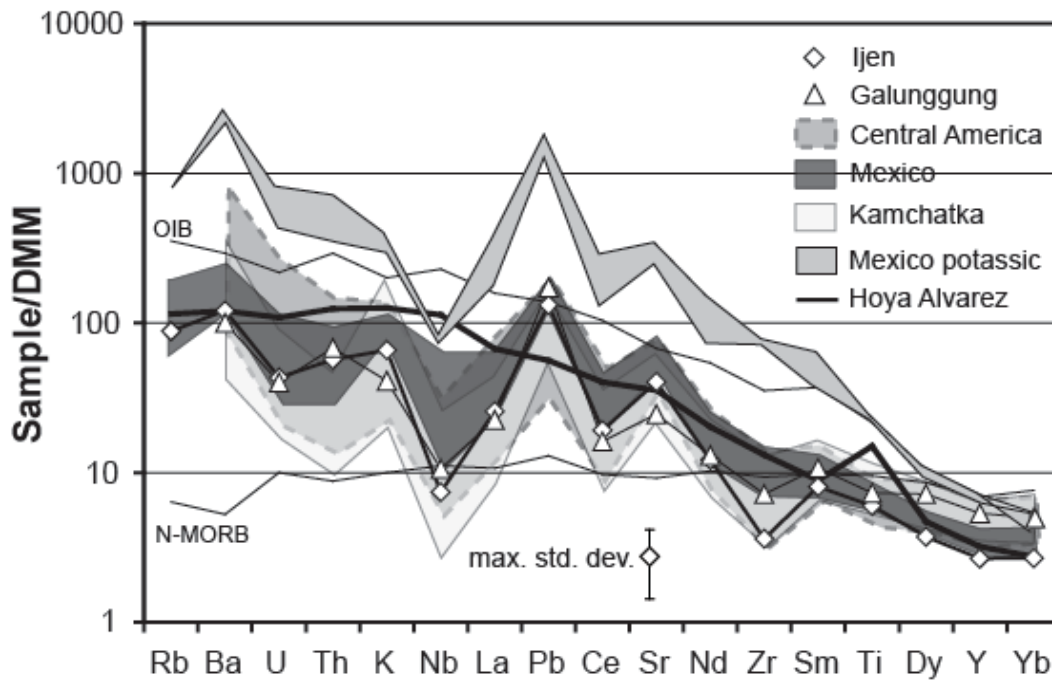


Figure 3-3 Multi-element spider diagram normalized to depleted MORB mantle (DMM; Salters & Stracke, 2004). Shaded fields are shown for the melt inclusion data of Mexico, Central America and Kamchatka (including data from Churikova et al., 2007) and average values for Kawah Ijen, Galunggung and Hoya Alvarez (Mexico; Johnson et al., 2009) are shown. The maximum standard deviation for a given volcano is shown. Also shown for comparison are data from the potassic melt inclusions of Colima, Mexico (Vigouroux et al., 2008) and average ocean island basalt (OIB) and normal MORB (N-MORB), both from Sun and McDonough (1989).

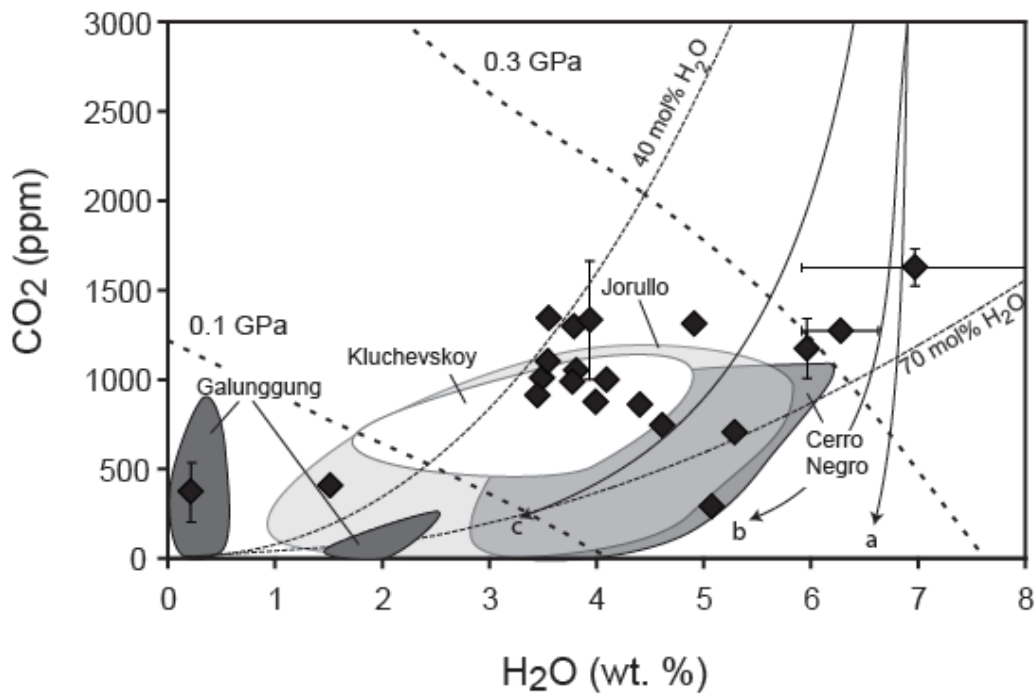


Figure 3-4 CO₂ versus H₂O contents of melt inclusions from Kawah Ijen (filled diamonds). Compositions are in equilibrium with their host olivine. Error bars are standard deviation for a given melt inclusion. Also shown are shaded fields for melt inclusions from Galunggung, which separates into two groups, high and low H₂O contents (Sisson & Bronto, 1998; Kelley et al., 2006); Jorullo from the Mexican arc (Johnson et al., 2009); Cerro Negro from Central America (Roggensack et al., 1997); and Kluchevskoy in Kamchatka (Auer et al., 2009). Widely dashed curves are isobars from Papale et al. (2006). Solid curves are calculated degassing paths (a = open system, b = closed and c = closed with 5 wt% exsolved vapour). Closely dashed curves are isopleths of constant vapour composition. Both are calculated using VolatileCalc (Newman & Lowenstern, 2002). The starting melt composition was chosen to have the highest H₂O found in the melt inclusions with a total of 6000 ppm CO₂ based on the assumption that there has been > 50 % CO₂ degassed by 0.3 GPa (Wallace, 2005; Blundy et al., 2010).

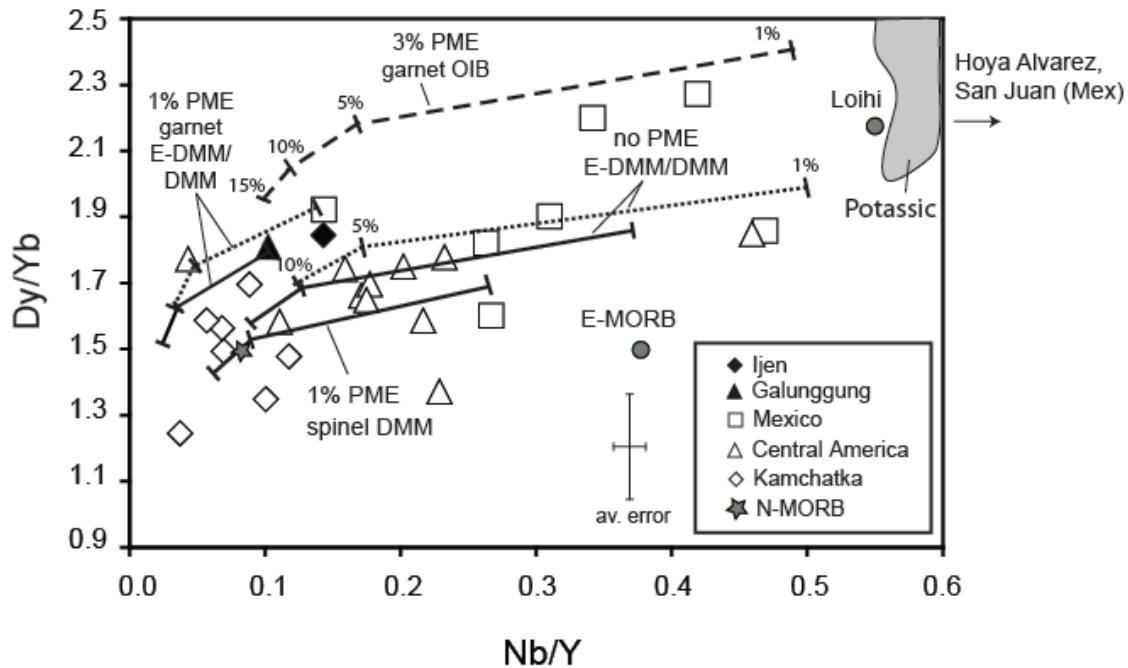


Figure 3-5 Dy/Yb versus Nb/Y of average melt inclusion compositions from each arc volcano along with a field for the potassic magmas of Colima, Mexico (Vigouroux et al., 2008) and average MORB and OIB-type magmas. N-MORB and E-MORB are from Sun and McDonough (1989) and the Loihi sample is a tholeiitic basalt (KK16-1) from Dixon and Clague (2001). The average standard deviation for each volcano is shown. The curves represent modal batch melting of a depleted MORB mantle (DMM from Salters & Stracke, 2004; solid lines), an enriched DMM (E-DMM from Workman & Hart, 2005; thin dashed lines) and an enriched OIB-like mantle (Hoya Alvarez mantle source from Johnson et al., 2009; thick dashed lines) in the spinel stability field (percent partial melting indicated). The mantle source has either undergone no episode of previous melt extraction (PME) or 1% PME in the garnet and spinel ilherzolite stability fields. See text for details of the modeling.

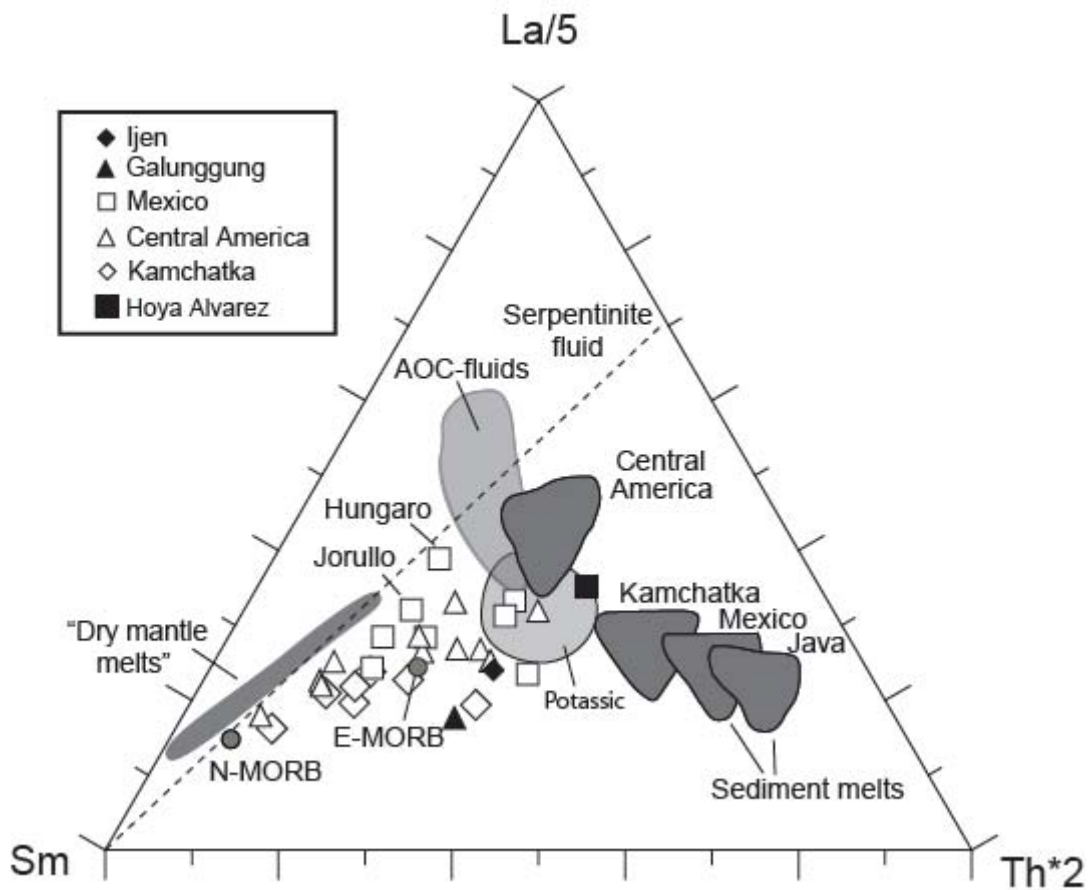


Figure 3-6 Th-La-Sm ternary showing the composition of arc magmas compared to Hoya Alvarez, the potassic magmas of Mexico, average N-MORB and E-MORB (data sources same as in previous figures) and “Dry mantle melts” (5-10 % partial melts in the spinel stability field of the mantle sources of Java, Mexico and Kamchatka after PME and without the addition of a subduction component). Fields labeled “Sediment melt” represent the range of sediment melt produced at each arc and the field labeled “AOC fluids” represents the range of fluids derived from the AOC (see text for details). No Sm values are reported for serpentinite-derived fluid (Scambelluri et al., 2001) therefore a dashed line shows the Th/La ratio of the fluids (~23).

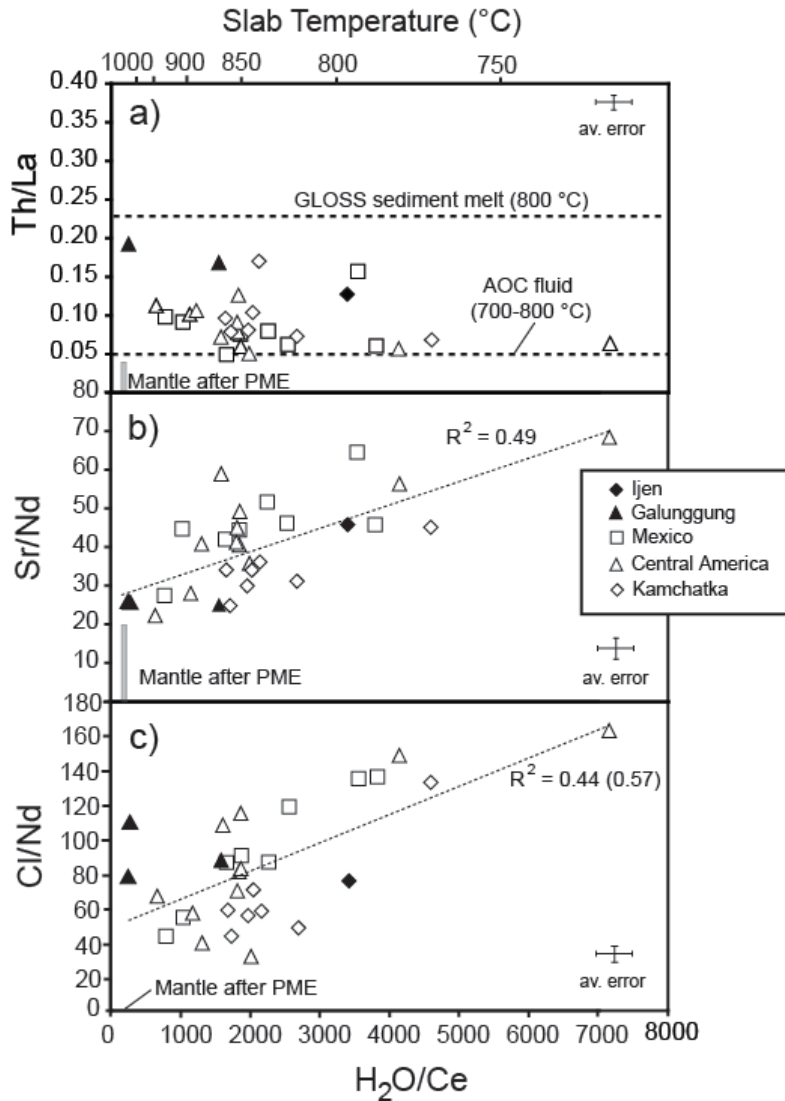


Figure 3-7 a) Th/La, b) Sr/Nd and c) Cl/Nd versus H_2O/Ce of arc magmas. Thick dashed lines in a) represent the minimum Th/La in a sediment melt (bulk global subducted sediment: GLOSS; Plank & Langmuir, 1998) at temperatures ≥ 800 $^{\circ}C$ and the maximum Th/La in an AOC-derived fluid at 700-800 $^{\circ}C$ (using bulk AOC from Bach et al., 2003). Modeling procedures are the same as for Figure 3-6. Shaded field labeled “Mantle after PME” is derived as in Figure 3-6. Slab surface temperatures are calculated from the H_2O/Ce ratio of the melt inclusions using the method of Plank et al. (2009). Average error is calculated from the average reported standard deviation for H_2O and Cl contents in a given melt inclusion (Johnson et al., 2009; this study) and from the average standard deviation of primitive Th, La, Ce, Nd and Sr contents at a given volcano (Portnyagin et al., 2007; Sadofsky et al., 2008; Johnson et al., 2009; this study). Linear regression lines (thin dashed lines) and correlation coefficients are given in panels b) and c). In panel c), the correlation coefficient increases to 0.57 if the low H_2O magma of Galunggung is excluded.

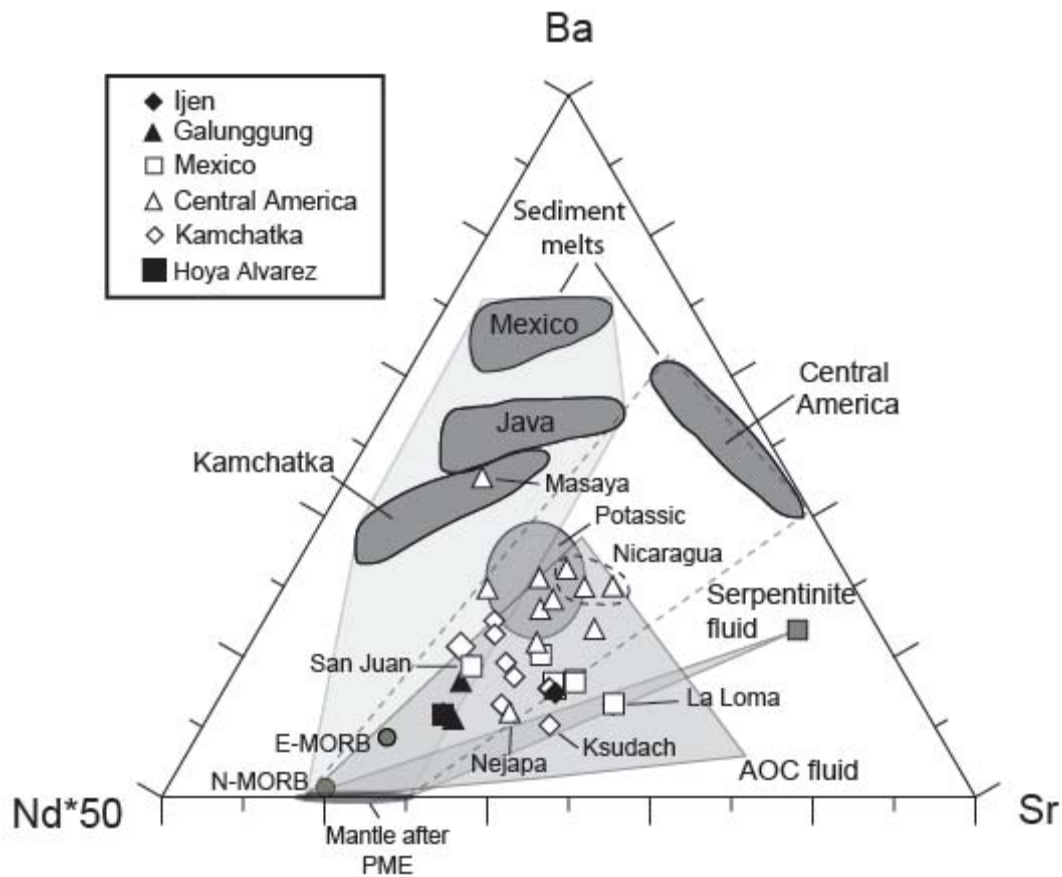


Figure 3-8 Ternary diagram Sr-Nd-Ba illustrating the role of the three subduction component reservoirs: sediment melt, AOC-derived fluid and serpentinite-derived fluid. Details of the fluid/melt composition modeling are described in the text. Data sources are the same as in Figure 3-7.

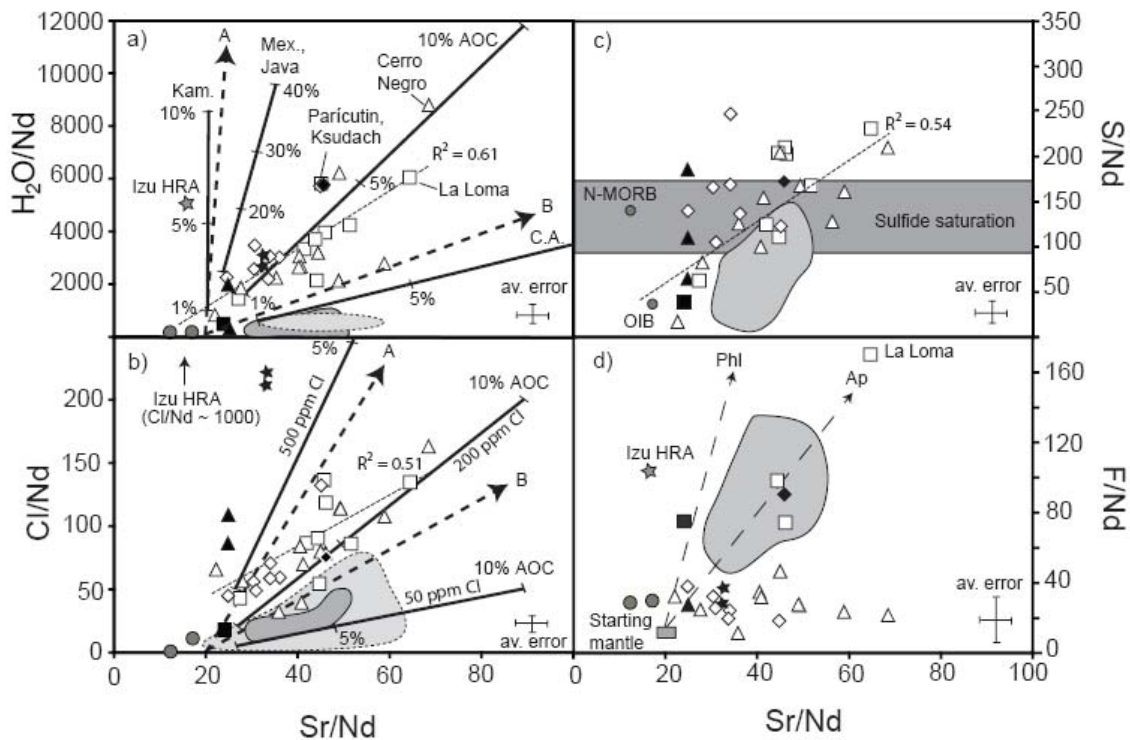


Figure 3-9 Variations in volatile content (a) H₂O; b) Cl; c) S and d) F of parental subduction zone magmas with respect to Sr (normalized to Nd to remove the effects of mantle source variability). Data sources and symbols are the same as in previous figures except for N-MORB and OIB. N-MORB composition is calculated from the H₂O/Ce, S/Dy and Cl/K ratios reported in Saal et al., 2002 and the average N-MORB composition, including F content, reported in Sun and McDonough (1989). OIB is calculated in a similar fashion but element ratios are from Dixon et al. (2002), Stroncik and Haase (2004) and Workman et al. (2006). Average error bars are calculated as in Fig. 3-7 (S/Nd and F/Nd are calculated like Cl/Nd). The solid shaded field represents primitive shoshonitic and leucitic magmas from the western Mexican arc (Vigouroux et al., 2008). The dotted shaded field represents picrites and ankaramites from the southern Mariannas arc (Kohut et al., 2006). Also shown for comparison are data for basalts (black stars) and halogen-rich andesites (HRA) from the Izu arc (grey stars; Straub & Layne, 2003). In a), the solid lines represent mixing between mantle wedge compositions after PME and sediment melt for each arc (Plank & Lamguir, 1998) and AOC fluid (from Bach et al., 2003), all at 800 °C. Modeling procedures for Sr/Nd are the same as in Figure 3-8. H₂O/Nd ratios for sediment melt and AOC-derived fluid are from Hermann and Rubatto (2009) and Klimm et al. (2008) respectively. The % of sediment melt and AOC fluid added is indicated. In a) and b), the Cl/Sr ratio of fluids released during the breakdown of serpentinite (path B, fluid with 6 wt% NaCl) and antigorite (path A, fluid with 0.4 wt% NaCl) are taken from fluid inclusion data (Scambelluri et al., 2001; 2004). In c), limits for sulphide saturation in basaltic magmas at T=1100-1300 °C and P=0.3-1.0 GPa are calculated from Liu et al. (2007) for an average Kawah Ijen magma (lower limit) and taken from Jugo et al. (2005) for a dry magma (upper limit). In d), the F/Sr ratio of fluoro-phlogopite and fluoro-apatite is from Luhr and Carmichael (1981).

3.10 Tables

Table 3-1 Kawah Ijen melt inclusions (corrected for post-entrapment modifications). Major and volatile elements in wt%, trace elements in ppm.

	OT-1-1	OT-1-2	OT-1-3	OT-1-4	OT-1-6	OT-1-8	TO-I	TO-VIII	TO-IX	TO-XI	TO-XIV	TO-XV	TO-XVI	TO-XVII
SiO ₂	46.4	44.9	45.1	45.4	45.6	46.1	45.7	45.5	47.7	45.4	45.3	46.5	44.6	45.5
TiO ₂	1.33	0.75	1.09	1.04	1.00	0.97	1.06	1.03	1.17	1.03	1.04	0.97	1.00	0.99
Al ₂ O ₃	17.8	18.8	17.5	18.4	18.1	18.1	18.3	18.4	15.7	17.6	17.7	18.8	18.3	18.8
FeO ^T	9.4	10.0	9.8	9.8	10.1	10.0	10.1	10.0	11.9	10.2	10.5	9.7	10.1	9.8
MnO	0.18	0.20	0.18	0.16	0.15	0.18	0.17	0.18	0.19	0.16	0.17	0.16	0.19	0.17
MgO	5.1	5.9	5.3	5.6	5.8	6.3	5.4	5.8	6.9	5.6	5.9	5.8	6.6	5.8
CaO	10.5	10.4	11.0	11.0	10.7	10.4	10.5	10.7	9.5	10.3	10.2	10.4	10.7	10.6
Na ₂ O	1.98	1.83	1.82	1.89	2.52	2.64	1.93	2.08	2.86	1.64	1.59	1.43	1.69	1.46
K ₂ O	0.62	0.49	0.61	0.63	0.60	0.58	0.64	0.63	0.86	0.61	0.60	0.70	0.56	0.64
P ₂ O ₅	0.44	0.35	0.32	0.34	0.32	0.30	0.33	0.34	0.34	0.32	0.30	0.26	0.24	0.28
S	0.185	0.111	0.204	0.203	0.190	0.159	0.221	0.198	0.135	0.219	0.212	0.196	0.200	0.200
Cl	0.081	0.069	0.094	0.099	0.088	0.087	0.097	0.091	0.095	0.100	0.092	0.101	0.099	0.103
F	0.080	0.125	0.101	0.105	0.102	0.146	0.131	0.100	0.111	0.116	0.111	0.082	0.100	0.099
H ₂ O	3.58	5.09	4.12	6.02	3.94	3.56	4.21	5.29	1.52	6.38	7.09	4.44	4.62	3.81
CO ₂	0.112	0.029	0.100	0.119	0.133	0.135	0.100	0.070	0.040	0.129	0.166	0.087	0.074	0.130
Host Fo ^a	78.7	78.2	78.3	78.5	78.7	79.6	78.4	78.3	79.8	78.0	78.1	79.2	79.7	79.5
Fo equil. ^b	77.7	79.8	78.3	74.7	80.1	81.6	77.7	79.8	72.5	77.0	76.3	76.2	81.4	77.2

^a Forsterite content of the olivine host located ~ 100 μm from melt inclusion.

^b Forsterite content calculated to be in equilibrium with the uncorrected melt inclusion composition assuming a FeO/FeO_{total} ratio of 0.79 and a calculated K_D (see text for details).

P (Gpa) ^c	0.20	0.17	0.20	0.30	0.23	0.22	0.21	0.22	0.11	0.33	0.39	0.20	0.19	0.21
T (°C) ^d	1096	1089	1090	1073	1106	1122	1093	1086	1163	1072	1071	1096	1108	1106
X olivine add. ^e	1.00	0.00	0.10	4.00	0.00	0.00	0.70	0.00	8.40	1.10	2.20	3.40	0.00	2.70
K _D ^f	0.33	0.34	0.33	0.34	0.32	0.32	0.33	0.33	0.32	0.35	0.35	0.35	0.33	0.34
fO ₂ (ΔNNO) ^g				0.97	0.7				0.5		1.31			

^c Pressure of melt inclusion entrapment based on the partial pressures of H₂O and CO₂, calculated using the program of Papale et al. (2006).

^d Temperature of melt inclusion entrapment calculated using eq. 6a from Sugawara (2000).

^e Weight % olivine added back into the composition of the melt inclusions to attain equilibrium between the two phases.

^f K_D values are calculated using the method of Toplis (2005) and the pressure and temperature calculated for each melt inclusion.

^g Oxygen fugacity values are calculated from the S Kα peak position data and are given as log units relative to the nickel-nickel oxide (NNO) buffer at a temperature of 1100 °C.

	TO-XVIII	TO-XIX	TO-XX	TO-XXII	TO-XXIII	TO-XXIV	TO-XXV
SiO ₂	47.1	45.3	44.9	44.4	45.6	43.5	45.7
TiO ₂	1.22	1.05	1.02	1.02	1.09	1.04	1.02
Al ₂ O ₃	19.0	19.1	18.8	19.1	18.5	19.0	19.0
FeO ^T	8.9	10.0	9.6	10.3	10.1	9.8	9.6
MnO	0.14	0.17	0.17	0.17	0.18	0.16	0.17
MgO	4.6	5.7	6.6	5.7	5.6	5.5	5.8
CaO	11.9	10.6	10.5	11.0	11.2	11.0	10.8
Na ₂ O	3.52	1.63	1.60	1.75	1.92	1.75	2.04
K ₂ O	0.81	0.61	0.56	0.57	0.58	0.57	0.58
P ₂ O ₅	0.33	0.26	0.26	0.26	0.27	0.27	0.26
S	0.206	0.213	0.205	0.216	0.213	0.203	0.204
Cl	0.125	0.107	0.100	0.102	0.107	0.134	0.101
F	0.126	0.145	0.151	0.139	0.162	0.150	0.133
H ₂ O	0.23	4.02	4.91	3.51	-	3.84	3.44
CO ₂	0.037	0.088	0.131	0.101	-	0.106	0.091
Host Fo	79.7	79.4	80.1	79.2	79.2	79.2	80.0
Fo equil.	76.6	79.0	82.2	78.3	79.1	76.4	80.6
P (Gpa)	0.03	0.18	0.25	0.17		0.19	0.16
T (°C)	1130	1101	1108	1108	1113	1100	1109
X olivine add.	2.60	0.60	0.00	1.10	0.20	3.00	0.00
K _D	0.3	0.33	0.34	0.33	0.33	0.33	0.33
$f_{O_2}(\Delta NNO)$							

	OT-1-1	OT-1-2	OT-1-3	OT-1-4	OT-1-6	OT-1-8	TO-I	TO-VIII	TO-IX	TO-XI	TO-XIV	TO-XV	TO-XVI	TO-XVII
Rb	9.15	7.60	10.47	11.94	9.98	8.05	11.34	12.08	17.17	9.60	9.95	12.24	8.60	11.79
Ba	212	146	215	201	198	200	191	216	259	193	188	202	172	187
Th	0.85	0.87	0.87	1.04	1.09	0.72	1.06	1.10	1.82	0.90	0.93	1.38	0.90	1.24
U	0.22	0.14	0.23	0.18	0.28	0.21	0.31	0.36	0.52	0.27	0.24	0.47	0.18	0.33
Nb	2.00	1.36	2.58	1.97	2.19	1.95	2.44	2.45	2.91	2.05	1.88	2.49	1.79	2.19
Ta	0.07	0.04	0.14	0.07	0.13	0.11	0.10	0.04	0.20	0.07	0.06	0.11	bdl	0.07
La	8.56	6.15	8.19	7.42	7.21	6.19	7.94	8.21	10.84	8.21	8.46	8.96	6.55	8.17
Pb	4.34	2.81	3.87	3.96	3.43	3.50	3.75	4.76	6.22	3.99	4.40	4.29	4.06	3.92
Ce	20.45	14.20	19.26	21.80	19.15	18.02	20.76	23.11	26.62	20.54	19.54	20.25	16.21	19.50
Sr	570	573	530	546	527	532	507	549	477	538	525	501	466	508
Pr	2.84	1.97	2.54	2.53	2.62	2.14	2.74	2.74	3.36	2.65	2.42	2.51	1.94	2.32
Nd	13.25	8.31	11.53	11.90	10.23	9.08	11.82	10.62	15.73	12.76	12.83	11.74	9.45	11.77
Zr	37	28	40	35	35	30	45	35	54	36	36	44	31	39
Hf	0.67	0.92	0.97	1.07	1.23	0.90	1.12	1.26	1.51	1.19	1.04	0.95	1.12	0.99
Sm	3.06	2.20	2.87	2.91	2.98	2.74	3.16	2.53	3.50	2.67	3.07	3.08	1.79	3.14
Eu	1.32	0.77	1.05	1.16	1.04	0.91	1.19	1.23	1.26	1.06	0.99	1.05	0.88	0.91
Gd	2.66	1.97	3.57	3.26	3.01	2.34	3.42	1.88	3.33	2.74	2.18	2.61	1.38	1.93
Ti	8489	4735	7178	6310	5972	6146	6092	6487	7418	6282	6477	5863	6016	6042
Dy	2.92	1.87	2.62	2.60	2.75	2.34	3.10	2.42	3.29	2.92	2.86	2.30	2.22	2.17
Li	7.45	7.76	6.83	7.78	6.34	6.68	7.72	6.68	12.00	6.81	7.76	6.45	7.21	7.65
Y	14.90	11.39	15.06	12.75	14.01	12.59	17.35	12.34	16.84	13.35	14.40	14.66	13.29	13.35
Yb	1.01	1.17	1.47	1.19	1.36	1.32	1.68	1.62	2.33	1.46	1.05	1.40	1.32	1.45

	TO-XVIII	TO-XIX	TO-XX	TO-XXII	TO-XXIII	TO-XXIV	TO-XXV
Rb	10.48	9.20	8.25	8.41	9.83	7.82	9.78
Ba	198	175	171	160	185	164	171
Th	1.04	1.06	0.99	1.04	0.89	0.73	0.92
U	0.30	0.23	0.17	0.25	0.27	0.18	0.23
Nb	1.96	1.84	1.66	1.71	1.91	1.72	1.73
Ta	bdl	0.09	bdl	0.08	0.13	0.07	bdl
La	8.88	8.06	7.69	7.90	7.60	6.96	7.36
Pb	4.14	3.54	3.51	3.52	4.19	4.30	3.84
Ce	20.00	16.85	16.79	17.16	19.82	18.35	18.78
Sr	576	500	488	482	509	488	488
Pr	2.69	2.48	2.07	2.11	2.50	2.31	2.63
Nd	13.75	10.01	11.73	11.00	12.13	10.85	8.57
Zr	48	40	39	36	37	32	34
Hf	1.19	1.03	1.08	1.19	0.97	1.06	0.99
Sm	2.62	2.94	2.54	3.48	3.26	2.70	2.62
Eu	1.26	0.95	1.03	0.94	1.20	0.89	1.06
Gd	3.33	2.97	2.38	2.39	2.47	2.52	1.67
Ti	6519	6001	5959	5831	6213	5981	5964
Dy	2.64	3.15	2.39	2.46	2.40	2.54	2.64
Li	6.54	4.87	6.02	5.63	7.98	6.84	7.78
Y	17.34	14.71	14.93	15.53	13.44	13.14	13.45
Yb	1.98	1.23	1.34	1.35	1.11	1.30	1.41

3.11 References

- Abers, G.A., Plank, T., Hacker, B.R., 2003. The wet Nicaraguan slab. *Geophys. Res. Lett.* 30 (2), 1098.
- Alt, J.C., Anderson, T.F., Bonnell, L., 1989. The geochemistry of sulfur in a 1.3 km section of hydrothermally altered oceanic crust, DSDP hole 504B. *Geochim. Cosmochim. Acta* 53 (5), 1011-1023.
- Alt, J.C., Burdett, J.W., 1982. Sulfur in pacific deep-sea sediments (leg 129) and implications for cycling of sediment in subduction zones. *Proc. Ocean Drill. Prog.* 129 283-294.
- Alves, S., Schiano, P., Allègre, C.J., 1999. Rhenium-osmium isotopic investigation of Java subduction zone lavas. *Earth Planet. Sci. Lett.* 168 (1-2), 65-77.
- Auer, S., Bindeman, I., Wallace, P.J., Ponomareva, V., Portnyagin, M., 2009. The origin of hydrous, high- $\delta^{18}\text{O}$ voluminous volcanism: Diverse oxygen isotope values and high magmatic water contents within the volcanic record of Klyuchevskoy volcano, Kamchatka, Russia. *Contrib. Mineral. Petrol.* 157 (2), 209-230.
- Bach, W., Peucker-Ehrenbrink, B., Hart, S. R., Blusztajn, J. S., 2003. Geochemistry of hydrothermally altered oceanic crust: DSDP/ODP Hole 504B—Implications for seawater-crust exchange budgets and Sr-and Pb-isotopic evolution of the mantle. *Geochem. Geophys. Geosyst.* 4 (3), 8904. doi:10.1029/2002GC000419.
- Benjamin, E.R., Plank, T., Wade, J.A., Kelley, K.A., Hauri, E.H., Alvarado, G.E., 2007. High water contents in basaltic magmas from Irazú volcano, Costa Rica. *J. Volcanol. Geotherm. Res.* 168 (1-4), 68-92.
- Blundy, J., Cashman, K.V., Rust, A., Witham, F., 2010. A case for CO_2 -rich arc magmas. *Earth Planet. Sci. Lett.* 290 (3-4), 289-301.
- Bureau, H., Métrich, N., Semet, M.P., Staudacher, T., 1999. Fluid–magma decoupling in a hot–spot volcano. *Geophys. Res. Lett.* 26 (23), 3501-3504.
- Burnett, W.C. 1977. Geochemistry and origin of phosphorite deposits from off Peru and Chile. *Geol. Soc. Am. Bul.* 88 (6), 813-823.
- Calanchi, N., Lucchini, F., Rossi, P.L., 1983. Considerations on the high-K volcanic rocks of the volcanoes Muriah and Lasem (Java). *Mineral. Petrog. Acta* 27 15-34.

- Camus, G., Gourgaud, A., Mossand-Berthommier, P.C., Vincent, P.M., 2000. Merapi (Central Java, Indonesia): An outline of the structural and magmatological evolution, with a special emphasis to the major pyroclastic events. *J. Volcanol. Geotherm. Res.* 100 (1-4), 139-163.
- Carmichael, I.S.E., Frey, H.M., Lange, R.A., Hall, C.M., 2006. The Pleistocene cinder cones surrounding Volcán Colima, Mexico re-visited: Eruption ages and volumes, oxidation states, and sulfur content. *Bull. Volcanol.* 68 (5), 407-419.
- Carn, S.A. 2000. The Lamongan volcanic field, East Java, Indonesia: physical volcanology, historic activity and hazards. *J. Volcanol. Geotherm. Res.* 95 (1-4), 81-108.
- Carr, M.J., Feigenson, M.D., Bennett, E.A., 1990. Incompatible element and isotopic evidence for tectonic control of source mixing and melt extraction along the Central American arc. *Contrib. Mineral. Petrol.* 105 (4), 369-380.
- Colabella, A., Kelley, K., 2006. The effects of slab composition and mantle processes in magma generation at the Indonesian subduction zone. GSO technical report, 2006-02, 5-10.
- Chan, L.H., Leeman, W.P., You, C.F., 1999. Lithium isotopic composition of Central American Volcanic Arc lavas: implications for modification of subarc mantle by slab-derived fluids. *Chem. Geol.* 160 (4), 255-280.
- Churikova, T., Worner, G., Mironov, N., Kronz, A., Volatile (S, Cl and F) and fluid mobile trace element compositions in melt inclusions: Implications for variable fluid sources across the Kamchatka arc. *Contrib. Mineral. Petrol.* 154 (2), 217-239.
- Clements, B., Hall, R., Smyth, H.R., Cottam, M.A., 2009. Thrusting of a volcanic arc: A new structural model for Java. *Pet. Geosci.* 15 (2), 159-174.
- Danyushevsky, L.V., Della-Pasqua, F.N., Sokolov, S., 2000. Re-equilibration of melt inclusions trapped by magnesian olivine phenocrysts from subduction-related magmas: petrological implications. *Contrib. Mineral. Petrol.* 138 (1), 68-83.
- Davis, E.E., Chapman, D.S., Forster, C.B., Villinger, H., 1989. Heat-flow variations correlated with buried basement topography on the Juan de Fuca ridge flank. *Nature* 342, 533-537.
- Dixon, J.E., Clague, D.A., 2001. Volatiles in basaltic glasses from Loihi seamount, Hawaii: Evidence for a relatively dry plume component. *J. Petrol.* 42 (3), 627-654.
- Dixon, J.E., Leist, L., Langmuir, C., Schilling, J.G., 2002. Recycled dehydrated lithosphere observed in plume-influenced mid-ocean-ridge basalt. *Nature* 420 (6914), 385-389.

- Edwards, C., Menzies, M., Thirlwall, M., 1991. Evidence from Muriah, Indonesia, for the interplay of supra-subduction zone and intraplate processes in the genesis of potassic alkaline magmas. *J. Petrol.* 32 (3), 555-592.
- Edwards, C.M.H., Menzies, M.A., Thirlwall, M.F., Morris, J.D., Leeman, W.P., Harmon, R.S., 1994. The transition to potassic alkaline volcanism in island arcs: The Ringgit-Beser Complex, East Java, Indonesia. *J. Petrol.* 35 (6), 1557-1595.
- Edwards, C.M.H., Morris, J.D., Thirlwall, M.F., 1993. Separating mantle from slab signatures in arc lavas using B/Be and radiogenic isotope systematics. *Nature* 362 530-533.
- Edwards, C., Menzies, M., Thirlwall, M., 1991. Evidence from Muriah, Indonesia, for the interplay of supra-subduction zone and intraplate processes in the genesis of potassic alkaline magmas. *J. Petrol.* 32 (3), 555-592.
- Eiler, J. M., Carr, M. J., Reagan, M., Stolper, E., 2005. Oxygen isotope constraints on the sources of Central American arc lavas. *Geochem. Geophys. Geosyst.* 6 (7), Q07007, doi:10.1029/2004GC000804.
- Faure, F., Schiano, P., 2005. Experimental investigation of equilibration conditions during forsterite growth and melt inclusion formation. *Earth Planet. Sci. Lett.* 236 (3-4), 882-898.
- Feigenson, M.D., Carr, M.J., 1986. Positively correlated Nd and Sr isotope ratios of lavas from the Central American volcanic front. *Geology* 14 (1), 79-82.
- Feigenson, M. D., Carr, M. J., Maharaj, S. V., Juliano, S., Bolge, L. L., 2004. Lead isotope composition of Central American volcanoes: Influence of the Galápagos plume. *Geochem. Geophys. Geosyst.* 5 (6), Q06001, doi:10.1029/2003GC000621.
- Feineman, M.D., Ryerson, F.J., DePaolo, D.J., Plank, T., 2007. Zoisite-aqueous fluid trace element partitioning with implications for subduction zone fluid composition. *Chem. Geol.* 239 (3-4), 250-265.
- Gaetani, G.A., Kent, A.J.R., Grove, T.L., Hutcheon, I.D., Stolper, E.M., 2003. Mineral/melt partitioning of trace elements during hydrous peridotite partial melting. *Contrib. Mineral. Petrol.* 145 (4), 391-405.
- Gertisser, R., Keller, J., 2003. Trace element and Sr, Nd, Pb and O isotope variations in medium-K and high-K volcanic rocks from Merapi Volcano, Central Java, Indonesia: evidence for the involvement of subducted sediments in Sunda arc magma genesis. *J. Petrol.* 44 (3), 457-489.
- Green, T.H., Adam, J., 2003. Experimentally-determined trace element characteristics of aqueous fluid from partially dehydrated mafic oceanic crust at 3.0 GPa, 650–700 C. *Eur. J. Mineral.* 15 815-830.

- Hamilton, W., 1974. Sedimentary basins of the Indonesia region. U.S. Geol. Survey, Map 1-875-B.
- Hamilton, W. 1979. Tectonics of the Indonesian region. USGS Prof. Paper 1078 345.
- Handley, H.K., Davidson, J.P., Macpherson, C.G., Stimac, J.A., 2008. Untangling differentiation in arc lavas: Constraints from unusual minor and trace element variations at Salak Volcano, Indonesia. *Chem. Geol.* 255 (3-4), 360-376.
- Handley, H.K., Macpherson, C.G., Davidson, J.P., Berlo, K., Lowry, D., 2007. Constraining fluid and sediment contributions to subduction-related magmatism in Indonesia: Ijen Volcanic Complex. *J. Petrol.* 48 (6), 1155.
- Harmon, R.S., Gerbe, M., 1992. The 1982–83 eruption at Galunggung volcano, Java (Indonesia): Oxygen isotope geochemistry of a chemically zoned magma chamber. *J. Petrol.* 33 (3), 585-609.
- Hauri, E. 2002. SIMS analysis of volatiles in silicate glasses, 2: isotopes and abundances in Hawaiian melt inclusions. *Chem. Geol.* 183 (1-4), 115-141.
- Hermann, J., Spandler, C.J., 2008. Sediment melts at sub-arc depths: an experimental study. *J. Petrol.* 49 (4), 717-740.
- Hermann, J., Rubatto, D., 2009. Accessory phase control on the trace element signature of sediment melts in subduction zones. *Chem. Geol.* 265 (3-4), 512-526.
- Hermann, J., Spandler, C., Hack, A., Korsakov, A.V., 2006. Aqueous fluids and hydrous melts in high-pressure and ultra-high pressure rocks: Implications for element transfer in subduction zones. *Lithos* 92 (3-4), 399-417.
- Ishikawa, T., Tera, F., Nakazawa, T., 2001. Boron isotope and trace element systematics of the three volcanic zones in the Kamchatka arc. *Geochim. Cosmochim. Acta* 65 (24), 4523-4537.
- Ito, E., Harris, D.M., Anderson, A.T., 1983. Alteration of oceanic crust and geologic cycling of chlorine and water. *Geochim. Cosmochim. Acta* 47 (9), 1613-1624.
- Johnson, E.R., Wallace, P.J., Cashman, K.V., Granados, H.D., Kent, A.J.R., 2008. Magmatic volatile contents and degassing-induced crystallization at Volcán Jorullo, Mexico: Implications for melt evolution and the plumbing systems of monogenetic volcanoes. *Earth Planet. Sci. Lett.* 269 (3-4), 478-487.

- Johnson, E.R., Wallace, P.J., Delgado Granados, H., Manea, V.C., Kent, A.J.R., Bindeman, I., Donegan, C.S., 2009. Subduction-related volatile recycling and magma generation beneath central Mexico: Insights from melt inclusions, oxygen isotopes and geodynamic models. *J. Petrol.* 50 (9), 1729-1764.
- Jugo, P.J., Luth, R.W., Richards, J.P., 2005. An experimental study of the sulfur content in basaltic melts saturated with immiscible sulfide or sulfate liquids at 1300 °C and 1.0 GPa. *J. Petrol.* 46 (4), 783-798.
- Kelley, K.A., Cottrell, E., 2009. Water and the oxidation state of subduction zone magmas. *Science* 325 (5940), 605-607.
- Kelley, K. A., Plank, T., Ludden, J., Staudigel, H., 2003. Composition of altered oceanic crust at ODP Sites 801 and 1149. *Geochem. Geophys. Geosyst.* 4 (6), 8910, doi:10.1029/2002GC000435.
- Kelley, K. A., Colabella, A., Sisson, T. W., Hauri, E. H., Sigurdsson, H., 2006. Decompression melting beneath the Indonesian volcanic front. *Eos Trans. AGU* 87 (52) Fall Meet. Suppl. Abstract V54A-03.
- Kent, A.J.R. 2008. Melt inclusions in basaltic and related volcanic rocks. *Rev. Mineral. Geochem.* 69 (1), 273-331.
- Kent, A. J. R., Stöpler, E. M., Francis, D., Woodhead, J., Frei, R., Eiler, J., 2004. Mantle heterogeneity during the formation of the North Atlantic Igneous Province: Constraints from trace element and Sr-Nd-Os-O isotope systematics of Baffin Island picrites. *Geochem. Geophys. Geosyst.* 5 (11), Q11004, doi:10.1029/2004GC000743.
- Kepezhinskas, P., McDermott, F., Defant, M.J., Hochstaedter, A., Drummond, M.S., Hawkesworth, C.J., Koloskov, A., Maury, R.C., Bellon, H., 1997. Trace element and Sr-Nd-Pb isotopic constraints on a three-component model of Kamchatka arc petrogenesis. *Geochim. Cosmochim. Acta* 61 (3), 577-600.
- Kersting, A.B., Arculus, R.J., 1995. Pb isotope composition of Klyuchevskoy volcano, Kamchatka and North Pacific sediments: implications for magma genesis and crustal recycling in the Kamchatkan arc. *Earth Planet. Sci. Lett.* 136 (3-4), 133-148.
- Kessel, R., Schmidt, M.W., Ulmer, P., Pettke, T., 2005. Trace element signature of subduction-zone fluids, melts and supercritical liquids at 120–180 km depth. *Nature* 437 724-727.
- Kilinc, A., Carmichael, I.S.E., Rivers, M.L., Sack, R.O., 1983. The ferric-ferrous ratio of natural silicate liquids equilibrated in air. *Contrib. Mineral. Petrol.* 83 (1), 136-140.

- Kitano, Y., Okumura, M., 1973. Coprecipitation of fluoride with calcium carbonate. *Geochem. J.* 7 37-49.
- Klimm, K., Blundy, J.D., Green, T.H., 2008. Trace element partitioning and accessory phase saturation during H₂O-saturated melting of basalt with implications for subduction zone chemical fluxes. *J. Petrol.* 49 (3), 523-553.
- Kohut, E.J., Stern, R.J., Kent, A.J.R., Nielsen, R.L., Bloomer, S.H., Leybourne, M., 2006. Evidence for adiabatic decompression melting in the southern Mariana arc from high-Mg lavas and melt inclusions. *Contrib. Mineral. Petrol.* 152 (2), 201-221.
- Kopp, H., Flueh, E.R., Petersen, C.J., Weinrebe, W., Wittwer, A., Meramex Scientists, 2006. The Java margin revisited: Evidence for subduction erosion off Java. *Earth Planet. Sci. Lett.* 242 (1-2), 130-142.
- Kuno, H. 1960. High-alumina basalt. *J. Petrol.* 1 (2), 121-145.
- Leeman, W.P., Carr, M.J., Morris, J.D., 1994. Boron geochemistry of the Central American volcanic arc: constraints on the genesis of subduction-related magmas. *Geochim. Cosmochim. Acta* 58 (1), 149-168.
- Liu, Y., Samaha, N.T., Baker, D.R., 2007. Sulfur concentration at sulfide saturation (SCSS) in magmatic silicate melts. *Geochim. Cosmochim. Acta* 71 (7), 1783-1799.
- Luhr, J.F. 1997. Extensional tectonics and the diverse primitive volcanic rocks in the western Mexican Volcanic Belt. *Can. Mineral.* 35 (2), 473-500.
- Luhr, J.F., Carmichael, I.S.E., 1981. The Colima volcanic complex, Mexico: Part II. Late-quaternary cinder cones. *Contrib. Mineral. Petrol.* 76 (2), 127-147.
- Macpherson, C.G., Chiang, K.K., Hall, R., Nowell, G.M., Castillo, P.R., Thirlwall, M.F., 2009. Plio-pleistocene intra-plate magmatism from the southern Sulu arc, Semporna peninsula, Sabah, Borneo: Implications for high-Nb basalt in subduction zones. *J. Volcanol. Geotherm. Res.* 190 (1-2), 25-38.
- Manea, V.C., Manea, M., Kostoglodov, V., Sewell, G., Thermo-mechanical model of the mantle wedge in Central Mexican subduction zone and a blob tracing approach for the magma transport. *Phys. Earth Planet. Inter.* 149 (1-2), 165-186.
- Marschall, H.R., Altherr, R., Rüpke, L., 2007. Squeezing out the slab-modeling the release of Li, Be and B during progressive high-pressure metamorphism. *Chem. Geol.* 239 (3-4), 323-335.
- Marschall, H.R., Altherr, R., Gméling, K., Kasztovszky, Z., 2009. Lithium, boron and chlorine as tracers for metasomatism in high-pressure metamorphic rocks: A case study from Syros (Greece). *Mineral. Petrol.* 95 (3), 291-302.

- Masson, D.G., Parson, L.M., Milsom, J., Nichols, G., Sikumbang, N., Dwiyanto, B., Kallagher, H., 1990. Subduction of seamounts at the Java trench: A view with long-range sidescan sonar. *Tectonophysics* 185 (1-2), 51-65.
- Mavrogenes, J.A., O'Neill, H.S.C., 1999. The relative effects of pressure, temperature and oxygen fugacity on the solubility of sulphide in mafic magmas. *Geochim. Cosmochim. Acta* 63 (7-8), 1173-1180.
- Métrich, N., Wallace, P.J., 2008. Volatile abundances in basaltic magmas and their degassing paths tracked by melt inclusions. *Rev. Mineral. Geochem.* 69 (1), 363.
- Nadeau, O., Williams-Jones, A.E., Stix, J., 2010. Sulphide magma as a source of metals in arc-related magmatic hydrothermal ore fluids. *Nature Geosci.* 3, 501-505.
- Newman, S., Lowenstern, J.B., 2002. VolatileCalc: A silicate melt-H₂O-CO₂ solution model written in Visual Basic for excel. *Comput. Geosci.* 28, 597-604.
- Nicholls, I.A., Whitford, D.J., 1983. Potassium-rich volcanic rocks of the Muriah complex, Java, Indonesia: Products of multiple magma sources? *J. Volcanol. Geotherm. Res.* 18 (1-4), 337-359.
- Papale, P., David, M., 2006. The compositional dependence of the saturation surface of H₂O+CO₂ fluids in silicate melts. *Chem. Geol.* 229 (1-3), 78-95.
- Patino, L.C., Carr, M.J., Feigenson, M.D., 2000. Local and regional variations in Central American arc lavas controlled by variations in subducted sediment input. *Contrib. Mineral. Petrol.* 138 (3), 265-283.
- Peccerillo, A., Taylor, S.R., 1976. Geochemistry of Eocene calc-alkaline volcanic rocks from the Kastamonu area, northern Turkey. *Contrib. Mineral. Petrol.* 58 (1), 63-81.
- Philippot, P., Agrinier, P., Scambelluri, M., 1998. Chlorine cycling during subduction of altered oceanic crust. *Earth Planet. Sci. Lett.* 161 (1-4), 33-44.
- Plank, T. 2005. Constraints from thorium/lanthanum on sediment recycling at subduction zones and the evolution of the continents. *J. Petrol.* 46 (5), 921-944.
- Plank, T., Cooper, L.B., Manning, C.E., 2009. Emerging geothermometers for estimating slab surface temperatures. *Nature Geosci.* 2 (9), 611-615.
- Plank, T., Langmuir, C.H., 1998. The chemical composition of subducting sediment and its consequences for the crust and mantle. *Chem. Geol.* 145 (3-4), 325-394.

- Portnyagin, M., Almeev, R., Matveev, S., Holtz, F., 2008. Experimental evidence for rapid water exchange between melt inclusions in olivine and host magma. *Earth Planet. Sci. Lett.* 272 (3-4), 541-552.
- Portnyagin, M., Hoernle, K., Plechov, P., Mironov, N., Khubunaya, S., 2007. Constraints on mantle melting and composition and nature of slab components in volcanic arcs from volatiles (H₂O, S, Cl, F) and trace elements in melt inclusions from the Kamchatka Arc. *Earth Planet. Sci. Lett.* 255 (1-2), 53-69.
- Ranero, C. R., Morgan, J. P., McIntosh, K. D., Reichert, C., 2001. Flexural faulting and mantle serpentinization at the Middle America Trench. *Eos Trans. AGU* 82 (47) Fall Meet. Suppl. Abstract T22D-04.
- Reagan, M.K., Morris, D., Herrstrom, E.A., Murrell, M.T., 1994. Uranium series and beryllium isotope evidence for an extended history of subduction modification of the mantle below Nicaragua. *Geochim. Cosmochim. Acta* 58 (19), 4199-4212.
- Reagan, M.K., Ishizuka, O., Stern, R.J., Kelley, K.A., Ohara, Y., Blichert-Toft, J., Bloomer, S.H., Cash, J., Fryer, P., Hanan, B.B., 2010. Fore-arc basalts and subduction initiation in the Izu-Bonin-Mariana system. *Geochem. Geophys. Geosyst.* 11 (3), Q03X12, doi:10.1029/2009GC002871.
- Reubi, O., Nicholls, I.A., 2004. Magmatic evolution at Batur volcanic field, Bali, Indonesia: petrological evidence for polybaric fractional crystallization and implications for caldera-forming eruptions. *J. Volcanol. Geotherm. Res.* 138 (3-4), 345-369.
- Reubi, O., Nicholls, I.A., Kamenetsky, V.S., 2003. Early mixing and mingling in the evolution of basaltic magmas: evidence from phenocryst assemblages, Slamet Volcano, Java, Indonesia. *J. Volcanol. Geotherm. Res.* 119 (1-4), 255-274.
- Roberge, J., Delgado-Granados, H., Wallace, P.J., 2009. Mafic magma recharge supplies high CO₂ and SO₂ gas fluxes from Popocatepetl volcano, Mexico. *Geology* 37 (2), 107.
- Roggensack, K., Hervig, R.L., McKnight, S.B., Williams, S.N., 1997. Explosive basaltic volcanism from Cerro Negro volcano: Influence of volatiles on eruptive style. *Science* 277 (5332), 1639.
- Rowe, M.C., Nielsen, R.L., Kent, A.J.R., 2006. Anomalously high Fe contents in rehomogenized olivine-hosted melt inclusions from oxidized magmas. *Am. Mineral.* 91 (1), 82.
- Rowe, M.C., Kent, A.J.R., Nielsen, R.L., 2009. Subduction influence on oxygen fugacity and trace and volatile elements in basalts across the Cascade volcanic arc. *J. Petrol.* 50 (1), 61-91.

- Rüpke, L.H., Morgan, J.P., Hort, M., Connolly, J.A.D., 2004. Serpentine and the subduction zone water cycle. *Earth Planet. Sci. Lett.* 223 (1-2), 17-34.
- Rüpke, L.H., Morgan, J.P., Hort, M., Connolly, J.A.D., 2002. Are the regional variations in Central American arc lavas due to differing basaltic versus peridotitic slab sources of fluids? *Geology* 30 (11), 1035-1038.
- Saal, A.E., Hauri, E.H., Langmuir, C.H., Perfit, M.R., 2002. Vapour undersaturation in primitive mid-ocean-ridge basalt and the volatile content of earth's upper mantle. *Nature* 419 (6906), 451-455.
- Sadofsky, S.J., Portnyagin, M., Hoernle, K., van den Bogaard, P., 2008. Subduction cycling of volatiles and trace elements through the Central American volcanic arc: evidence from melt inclusions. *Contrib. Mineral. Petrol.* 155 (4), 433-456.
- Salter, V. J. M., Stracke, A., 2004. Composition of the depleted mantle. *Geochem. Geophys. Geosyst.* 5 (5), Q05B07, doi:10.1029/2003GC000597.
- Scambelluri, M., Bottazzi, P., Trommsdorff, V., Vannucci, R., Hermann, J., Gómez-Pugnaire, M.T., López-Sánchez Vizcaíno, V., 2001. Incompatible element-rich fluids released by antigorite breakdown in deeply subducted mantle. *Earth Planet. Sci. Lett.* 192 (3), 457-470.
- Scambelluri, M., Müntener, O., Ottolini, L., Pettke, T.T., Vannucci, R., 2004. The fate of B, Cl and Li in the subducted oceanic mantle and in the antigorite breakdown fluids. *Earth Planet. Sci. Lett.* 222 (1), 217-234.
- Schiano, P., Eiler, J.M., Hutcheon, I.D., Stolper, E.M., 2000. Primitive CaO-rich, silica-undersaturated melts in island arcs: Evidence for the involvement of clinopyroxene-rich lithologies in the petrogenesis of arc magmas. *Geochem. Geophys. Geosyst.* 1 (5), 1018, doi:10.1029/1999GC000032.
- Schmidt, M.W., Poli, S., 1998. Experimentally based water budgets for dehydrating slabs and consequences for arc magma generation. *Earth Planet. Sci. Lett.* 163 (1-4), 361-379.
- Sendjaja, Y.A., Kimura, J.I., Sunardi, E., 2008. Across-arc geochemical variation of Quaternary lavas in West Java, Indonesia: Mass-balance elucidation using arc basalt simulator model. *Island Arc* 18 (1), 201-224.
- Siebert L, Simkin T (2002-). *Volcanoes of the World: an Illustrated Catalog of Holocene Volcanoes and their Eruptions*. Smithsonian Institution, Global Volcanism Program Digital Information Series, GVP-3, (<http://www.volcano.si.edu/world/>).
- Sigvaldason, G.E., Óskarsson, N., 1986. Fluorine in basalts from Iceland. *Contrib. Mineral. Petrol.* 94 (3), 263-271.

- Sisson, T.W., Bronto, S., 1998. Evidence for pressure-release melting beneath arcs from basalt at Galunggung, Indonesia. *Nature* 391 883-886.
- Sitorus, K., 1990. Volcanic stratigraphy and geochemistry of the Idjen Caldera Complex, East Java, Indonesia. M.Sc. thesis, University of Wellington, New Zealand.
- Smyth, H.R., Hamilton, P.J., Hall, R., Kinny, P.D., 2007. The deep crust beneath island arcs: Inherited zircons reveal a Gondwana continental fragment beneath east Java, Indonesia. *Earth Planet. Sci. Lett.* 258 (1-2), 269-282.
- Sobolev, A.V., Danyushevsky, L.V., 1994. Petrology and geochemistry of boninites from the north termination of the Tonga Trench: Constraints on the generation conditions of primary high-Ca boninite magmas. *J. Petrol.* 35 (5), 1183-1211.
- Spilliaert, N., Métrich, N., Allard, P., 2006. S-Cl-F degassing pattern of water-rich alkali basalt: Modeling and relationship with eruption styles on Mount Etna volcano. *Earth Planet. Sci. Lett.* 248 (3-4), 772-786.
- Straub, S. M., Layne, G. D., 2003. Decoupling of fluids and fluid-mobile elements during shallow subduction: Evidence from halogen-rich andesite melt inclusions from the Izu arc volcanic front. *Geochem. Geophys. Geosyst.* 4 (7), 9004. doi:10.1029/2002GC000349.
- Stroncik, N.A., Haase, K.M., 2004. Chlorine in oceanic intraplate basalts: Constraints on mantle sources and recycling processes. *Geology* 32 (11), 945-948.
- Sugawara, T. 2000. Empirical relationships between temperature, pressure, and MgO content in olivine and pyroxene saturated liquid. *J. Geophys. Res.* 105 (B4), 8457-8472.
- Sun, S.S., McDonough, W.F., 1989. Chemical and isotopic systematics of oceanic basalts: Implications for mantle composition and processes. *Geol. Soc. Lond. Spec. Pub.* 42 (1), 313-345.
- Syracuse, E. M., Abers, G. A., 2006. Global compilation of variations in slab depth beneath arc volcanoes and implications. *Geochem. Geophys. Geosyst.* 7 (5), Q05017. doi:10.1029/2005GC001045.
- Tenthorey, E., Hermann, J., 2004. Composition of fluids during serpentinite breakdown in subduction zones: Evidence for limited boron mobility. *Geology* 32 (10), 865-868.
- Tollstrup, D., Gill, J., Kent, A. J. R., Prinkey, D., Williams, R., Tamura, Y., Ishizuka, O., 2010. Across-arc geochemical trends in the Izu-Bonin arc: Contributions from the subducting slab, revisited. *Geochem. Geophys. Geosyst.* 11 (1), Q01X10. doi:10.1029/2009GC002847.

- Toplis, M.J. 2005. The thermodynamics of iron and magnesium partitioning between olivine and liquid: Criteria for assessing and predicting equilibrium in natural and experimental systems. *Contrib. Mineral. Petrol.* 149 (1), 22-39.
- Tregoning, P., Brunner, F.K., Bock, Y., Puntodewo, S.S.O., McCaffrey, R., Genrich, J.F., Calais, E., Rais, J., Subarya, C., 1994. First geodetic measurement of convergence across the Java trench. *Geophys. Res. Lett.* 21 (19), 2135-2138.
- Turner, S., Foden, J.D., 2001. U, Th and Ra disequilibria, Sr, Nd and Pb isotope and trace element variations in Sunda arc lavas: Predominance of a subducted sediment component. *Contrib. Mineral. Petrol.* 142 (1), 43-57.
- van Hinsberg, V.J., 2001. Water-rock interaction and element fluxes in the Kawah Ijen hyperacid crater lake and the Banyu Pahit river, East Java, Indonesia. M.Sc. thesis, University of Utrecht, Netherlands.
- van Hinsberg, V.J., Williams-Jones, A.E., Mauri, G., Vigouroux, N., Williams-Jones, G., McKenzie, J., Palmer, S., Nasution A., 2008. Studying the Kawah Ijen volcano-hydrothermal system - merits of an interdisciplinary approach. IAVCEI, Reykjavik, Iceland, Abstract 2-b P29.
- Vigouroux, N., Wallace, P.J., Kent, A.J.R., 2008. Volatiles in high-K magmas from the Western trans-Mexican volcanic belt: Evidence for fluid fluxing and extreme enrichment of the mantle wedge by subduction processes. *J. Petrol.* 49 (9), 1589-1618.
- Vukadinovic, D., Sutawidjaja, I., 1995. Geology, mineralogy and magma evolution of Gunung Slamet volcano, Java, Indonesia. *J. Southeast Asian Earth Sci.* 11 (2), 135-164.
- Wade, J.A., Plank, T., Melson, W.G., Soto, G.J., Hauri, E.H., 2006. The volatile content of magmas from Arenal volcano, Costa Rica. *J. Volcanol. Geotherm. Res.* 157 (1-3), 94-120.
- Wallace, P.J. 2005. Volatiles in subduction zone magmas: Concentrations and fluxes based on melt inclusion and volcanic gas data. *J. Volcanol. Geotherm. Res.* 140 (1-3), 217-240.
- Wallace, P.J., Carmichael, I.S.E., 1994. S speciation in submarine basaltic glasses as determined by measurements of SK α X-ray wavelength shifts. *Am. Mineral.* 79 (1-2), 161-167.
- Wei, W., Kastner, M., Deyhle, A., Spivack, A.J., 2005. Geochemical cycling of fluorine, chlorine, bromine, and boron and implications for fluid-rock reactions in Mariana forearc, South Chamorro seamount, ODP leg 195. *Proc. Ocean Drill. Prog.* 195 1-23.

- Wheller, G.E., Varne, R., Foden, J.D., Abbott, M.J., 1987. Geochemistry of Quaternary volcanism in the Sunda-Banda arc, Indonesia, and three-component genesis of island-arc basaltic magmas. *J. Volcanol. Geotherm. Res.* 32 (1-3), 137-160.
- Whitford, D.J., Nicholls, I.A., Taylor, R.S., 1979. Spatial variations in the geochemistry of quaternary lavas across the Sunda arc in Java and Bali. *Contrib. Mineral. Petrol.* 70 (3), 341-356.
- Workman, R.K., Hart, S.R., 2005. Major and trace element composition of the depleted MORB mantle (DMM). *Earth Planet. Sci. Lett.* 231 (1-2), 53-72.
- Workman, R.K., Hauri, E., Hart, S.R., Wang, J., Blusztajn, J., 2006. Volatile and trace elements in basaltic glasses from Samoa: Implications for water distribution in the mantle. *Earth Planet. Sci. Lett.* 241 (3-4), 932-951.
- Wysoczanski, R.J., Wright, I.C., Gamble, J.A., Hauri, E.H., Luhr, J.F., Eggins, S.M., Handler, M.R., 2006. Volatile contents of Kermadec Arc-Havre Trough pillow glasses: Fingerprinting slab-derived aqueous fluids in the mantle sources of arc and back-arc lavas. *J. Volcanol. Geotherm. Res.* 152 (1-2), 51-73.

4: INTEGRATED GEOCHEMICAL MODELING OF MAGMATIC DEGASSING AND HYDROTHERMAL INTERACTION: A CASE STUDY FROM KAWAH IJEN VOLCANO, INDONESIA¹

4.1 Abstract

Monitoring active volcanoes requires an understanding of magmatic degassing in relation to magma depth, temperature, composition, style of degassing (open vs. closed) and interactions with hydrothermal systems. This study combines results of subsurface degassing interpreted from melt inclusions with measurements of fumarole gases and acid spring waters from Kawah Ijen volcano, Indonesia. Kawah Ijen is a stratovolcano with a growing rhyolite dome on the shore of a hyperacidic crater lake. The dome is emitting sulphur-rich gases from high temperature fumaroles (350-450°C).

Matrix glass and melt inclusion compositions (including H₂O, CO₂, S, Cl and F) were measured for basaltic, dacitic and rhyolitic magmas. The behaviour of the volatile species ($D^{\text{vap-melt}}$) during ascent, degassing and crystallization were modeled for an open system (including vapour fluxing) assuming Rayleigh fractionation, and for closed system processes assuming batch degassing and crystallization. The variable H₂O-CO₂ contents of the melt inclusions suggest that

¹ The following chapter will be submitted to the *Journal of Volcanology and Geothermal Research* under the co-authorship of G. Williams-Jones, K. Berlo, V. van Hinsberg, A.E. Williams-Jones and P. Wallace. The extent of the collaboration thus far includes assistance with field sampling from V. van Hinsberg, G. Williams-Jones and A.E. Williams-Jones, some sample analysis by K. Berlo and V. van Hinsberg, modeling assistance by P. Wallace and manuscript review by G. Williams-Jones.

open system vapour fluxing ($X_{\text{H}_2\text{O}_{\text{vapour}}} = 0.25\text{-}0.95$ for basalt; $0.9\text{-}0.95$ for dacite) is the dominant degassing style. The modeled $S D^{\text{vap-melt}}$ values for basalt remain low (2-10) as the melt ascends ($P = 400$ to 100 MPa), then increase sharply to 200 at pressures < 100 MPa. As the melt evolves from basalt to dacite, $S D^{\text{vap-melt}}$ values are high (100-300) and independent of pressure. Evolution from dacite to rhyolite is characterized by a constant $D^{\text{vap-melt}}$ value of 35. Chlorine behavior is strongly affected by crystallization of Cl-rich apatite in the basaltic magma. In dacite and rhyolite, Cl is mostly dissolved in the melt. The $D^{\text{vap-melt}}$ values range from 7-9 as basalt evolves to dacite and reach 5 for dacite to rhyolite at low pressures. Fluorine contents are highly variable due to crystallization of F-rich apatite, especially in the more evolved rocks. This precludes meaningful modeling of F release to the vapour.

The best-fit modeled gas compositions (mass ratio) are: $\text{CO}_2/\text{H}_2\text{O} = 0.13\text{-}0.27$, $\text{CO}_2/S_{(\text{total})} = 2.9\text{-}5.7$, $\text{H}_2\text{O}/S_{(\text{total})} = 21\text{-}22$ and $\text{CO}_2/\text{HCl} = 8\text{-}16$; fumarole gas compositions are: $\text{CO}_2/\text{H}_2\text{O} = 0.25\text{-}0.3$, $\text{CO}_2/S_{(\text{total})} = 4\text{-}5$, $\text{H}_2\text{O}/S_{(\text{total})} = 12\text{-}20$ and $\text{CO}_2/\text{HCl} = 230\text{-}420$. The latter represent some of the most S- and CO_2 -rich and Cl-poor compositions recorded for arc volcanoes. Partly, the vapour data are interpreted to reflect the important drop in S solubility between the basaltic and more evolved magmas, and the low Cl content a result of apatite crystallization. In part, they are interpreted to reflect condensation of the magmatic vapour upon ascent. S and C are concentrated in the residual vapour and Cl and F are lost to the liquid. As a result, fumarole gases precipitate large quantities of native S at the surface and acid spring waters are enriched in Cl and F ($\text{SO}_4^{2-}/\text{Cl} \approx 3$; $\text{SO}_4^{2-}/\text{F}$

≤ 70). The lack of S scrubbing by the hydrothermal system beneath the dome implies that the gas C/S ratio at Kawah Ijen is an important parameter for the monitoring of magmatic activity. This study illustrates the importance of integrating melt inclusion data with surface gas compositions in evaluating the effects of magmatic and hydrothermal processes on surface degassing patterns at active volcanoes.

4.2 Introduction

Recent integrative studies of magmatic degassing have broadened our understanding of the link between subsurface exsolution of volatiles and surface gas emissions at active, open vent volcanoes (Aiuppa et al., 2004; 2007; 2010; Wallace, 2005; Spilliaert et al., 2006; Roberge et al., 2009; Edmonds et al., 2009; 2010). Melt inclusions provide quantitative characterization of the melt volatile content during ascent, degassing and crystallization of magma (e.g., Métrich and Clocchiatti, 1989; Johnson et al., 2008; Vigouroux et al., 2008). In counterpart, the composition of gases at the surface can be measured either directly, using an evacuated flask (e.g., Giggenbach, 1975; Giggenbach and Goguel, 1989) or indirectly in the plume using remote sensing methods such as Open-Path FTIR (e.g., Oppenheimer et al., 1998; Oppenheimer and Kyle, 2008) and in-situ measurements using the MultiGAS sensor (e.g., Shinohara, 2005; Chapter 5). Combining melt inclusion volatile data with mass balance constraints and solubility models (e.g., H₂O-CO₂: Newman and Lowenstern, 2002; Papale et al., 2006, S: Scaillet and Pichavant, 2005) allows for the characterization of the magmatic fluid, which can be directly compared with measured surface

emissions (e.g., Spilliaert et al., 2006; Roberge et al., 2009; Johnson et al., 2010; Edmonds et al., 2010; Aiuppa et al., 2010).

Models that link subsurface degassing to measured surface gas compositions need to include the evaluation of the effects of cooling, decompression and interaction with hydrothermal fluids on the gas composition. Thermodynamic modeling is used to offer insight into the chemical reactions taking place at equilibrium between a cooling magmatic gas, groundwater and host rock (e.g., Symonds et al., 2001; Marini and Gambardella, 2005). However, use of these models in a quantitative fashion is often limited by incomplete information regarding the water/gas and water/rock ratios as well as the input magmatic fluid composition at a given volcano. Other studies have focussed on the changes recorded in the measured surface gas and water compositions to infer changes in the magmatic-hydrothermal system (e.g., Giggenbach, 1987; Giggenbach et al., 1990; Christenson, 2000; Edmonds et al., 2003; Caracausi et al., 2005) but again, estimates of the initial, unaffected magmatic fluid component are rarely available.

This study combines estimates of the magmatic fluid composition derived from melt inclusion data with measured surface fumarole and acid sulphate-chloride waters at Kawah Ijen volcano in order to gain insight into possible scrubbing of magmatic gases by the hydrothermal system. A large hyper-acidic crater lake and acid stream runoff attests to the presence of this hydrothermal system. Any effects of the hydrothermal system on degassing are quantified by

comparing the gas specie ratios in the modeled magmatic fluid with those measured in both the fumarole gases and the acidic waters.

4.3 Geologic Setting

4.3.1 Kawah Ijen volcano

Kawah Ijen and the Ijen Caldera Complex are located in eastern Java, Indonesia, along the volcanic front of the Sunda arc (Fig. 4-1). Beneath Kawah Ijen, subduction of the 130 Ma Indo-Australian plate occurs at $\sim 7 \text{ cm yr}^{-1}$, making it one of the fastest and oldest subducting plates (Syracuse and Abers, 2006). Water-rich fluid release from the subducting plate to the volcanic front is amongst the highest documented at arcs worldwide (Chapter 3) and results in volatile-rich magmas such as those found at Kawah Ijen.

Kawah Ijen is a small, active stratovolcano that sits on the eroded flank of the inactive Merapi volcano, at the intersection of the Ijen Caldera Complex rim and an intra-caldera lineament of small cinder cones and shields (Fig. 4-1). Kawah Ijen's edifice has been repeatedly built and subsequently destroyed over the last 24,000 years (Sitorus, 1990; van Hinsberg, 2001), starting with a cone building stage that consists of interbedded layers of basaltic to dacitic lava and pyroclasts (ash to bomb size) exposed within the crater walls and on the outer flanks of the volcano. Large lava flows can be seen extending from the crater to the distal flanks of the volcano, exposed mainly on the south-western flank of the volcano and delimiting active drainages. The most prominent of these lava flows is a thick dacitic flow outcropping on the outer S-SW flank of the edifice and

exposed along the inner crater walls and in the river bed of the Banyu Pahit river. These early deposits are discordantly overlain by interbedded dacitic pyroclastic flow and fall deposits, ballistics, phreato-magmatic, phreatic and hydrothermal deposits. The Banyu Pahit river valley exposes most of the pyroclastic flow and fall deposits. The western flank of the volcano has been progressively destroyed by a series of crater explosions and subsequent collapses (van Hinsberg, 2001). The current configuration is a large (1 km wide) crater, ~ 300 m deep, partly filled with a hyper-acidic lake that drains into the Banyu Pahit river. The presence of both effusive and explosive eruptive material within the exposed stratigraphy of Kawah Ijen suggests alternating periods of edifice building and periods of explosive, destructive activity.

On the SE shore of the lake is a vigorously degassing magmatic dome whose surface is covered in native sulphur deposits. Pipes have been installed to divert the flow of gas from most of the fumaroles to the base of the dome, allowing the vapours to cool from $> 350\text{ }^{\circ}\text{C}$ to $< 200\text{ }^{\circ}\text{C}$ and native S to condense into the liquid phase, pooling and crystallizing at the base for local miners to extract. From 2006 to 2010, the size and morphology of the dome appears to have varied (Smithsonian Institute, 2007, 2009) but due to the presence of the miners and the pipes, we are unable to confirm whether the dome has indeed been growing. Gravity and self-potential surveys around the S flank of Kawah Ijen have imaged remnants of a shallow hydrothermal system in the S-SE part of the edifice, likely located within the top 1 km (Mauri, 2009). Shallow hydrothermal activity within the crater is evidenced by the crater lake, degassing dome and

hydrothermally altered sections through older dome rocks (van Hinsberg et al., 2010a).

4.3.2 Crater lake and Banyu Pahit river

A recent bathymetric survey of the lake reveals that the crater extends 180 m below the surface of the water although competing sediment deposition, alteration and hydrothermal explosions are constantly altering the lake profile (Takano et al., 2004). The lake is filled with an oxidized hyperacidic brine with $> 100 \text{ g kg}^{-1}$ of dissolved solids (Delmelle et al., 2000; van Hinsberg et al., 2010a). Acidity levels measured sporadically in the last 50 years have been consistently high (pH=0-0.4; as reported in Delmelle and Bernard, 1994; Delmelle et al., 2000; Palmer, 2009; van Hinsberg et al., 2010a). The lake waters seep out through the Banyu Pahit river and become progressively diluted and neutralized downstream. Rock alteration by these hyperacidic waters is evident in the lake shore sediment and the altered bedrock of the Banyu Pahit river. Near-complete leaching of all elements results in a silica-rich matrix typical of silicic alteration in high-sulphidation mineralization environments (van Hinsberg et al., 2010a). Near the currently active dome, exposure through a section of the crater floor has revealed the presence of an extinct hydrothermal zone believed to be the remnants of the magmatic dome at an early time (van Hinsberg et al., 2010a) The pervasively altered rock material consists of alunite, vuggy silica, pyrite and native sulphur, a mineral assemblage typical of low pH, near surface, intense advanced argillic alteration in high-sulphidation hydrothermal zones (e.g., Chouinard et al., 2005).

4.4 Methodology

4.4.1 Petrological sampling and analysis

Samples of scoria from the lowermost exposed layers of the edifice were collected in order to sample the earliest and most primitive magmas erupted at Kawah Ijen (Chapter 3 and additional samples reported in Table 4-1). These data are compared to younger samples of more felsic pyroclastic bombs sampled from the western crater rim (Table 4-1; Berlo et al., in prep.). One sample of dome material containing a glassy interstitial melt globule (sample KV08-702; van Hinsberg et al., 2010b) is also compared.

The basaltic scoria deposits (layers TO and OT; Chapter 3) are well sorted and overall clast size grades from ash to lapilli. They contain abundant, loose crystals of olivine up to 2 mm in length, along with trace amounts of plagioclase (≤ 0.5 mm in length) both as loose crystals and within the scoria clasts. Rare clinopyroxene is also present. The olivine lack any mineral inclusions (e.g., spinel) but contain abundant glassy melt inclusions suitable for analysis. Most of the glassy melt inclusions contain a small shrinkage bubble formed upon cooling and contraction of the melt. A few melt inclusions contain larger (≥ 20 vol %) vapour bubbles (not analysed), suggesting that the magma was vapour saturated during melt inclusion entrapment. Details of the morphologies, dimensions and other characteristics of the olivine-hosted melt inclusions as well as details of the sample preparation for Fourier Transform Infrared Spectroscopy (FTIR) and electron microprobe analysis can be found in Chapter 3 (Appendix B).

Descriptions of the melt inclusions presented in Table 4-1 are given in Berlo et al. (in prep.).

FTIR analyses were performed using a Nicolet Magna 560 FTIR with a Continuum IR microscope and OMNIC software at the University of Oregon. Absorbance was converted to concentration using the Beer-Lambert law, calculated glass densities using the method of Luhr (2001) and absorbance coefficients from Yamashita et al. (1997), Dixon et al. (1995) and Dixon and Pan (1995) for the olivine- and clinopyroxene-hosted melt inclusions and from Okumura (2003) and Behrens (2004) for the orthopyroxene- and plagioclase-hosted melt inclusions and felsic matrix glass. Further details of the methodology can be found in Chapter 3 (Appendix B).

Melt inclusion, mineral host and matrix glass major element compositions (and S, Cl and F contents) as well as sulphur $K\alpha$ wavelength shifts were obtained from electron microprobe analysis using a Cameca SX-100 at the University of Oregon and a JEOL 8900 at McGill University. Details of the analytical conditions and standards used at the University of Oregon are reported in Appendix B. Details of the analyses performed at McGill, are given in Berlo et al. (in prep). Measurements of sulphur $K\alpha$ wavelengths were obtained following the method described in Wallace and Carmichael (1994). Additional details on the method and the analytical conditions are given in Chapter 3. Peak positions were converted to sulphur speciation using the linear relationship $S^{6+}/S_{\text{total}} = (\Delta SK\alpha_{\text{unknown}} / \Delta SK\alpha_{\text{anhydrite}}) \times 100$ defined by Carroll & Rutherford (1988).

Olivine-hosted melt inclusion compositions were corrected for post-entrapment crystallization of olivine along the walls of the inclusion (e.g., Sobolev and Danyushevsky, 1994). The correction process involves adding 0.1% increments of equilibrium olivine back into each melt inclusion until the inclusion composition is in equilibrium with the olivine host. The exchange coefficient ($K_D = (\text{Mg}/\text{Fe}^{2+})_{\text{melt}} / (\text{Mg}/\text{Fe}^{2+})_{\text{olivine}}$) was calculated for each melt inclusion using the equation of Toplis (2005) that relates K_D to temperature, pressure, melt composition (including H_2O) and olivine composition. The average pressure (0.3 GPa) and temperature (1100°C) recorded by the melt inclusions were used. Saturation pressures based on partial pressures of the H_2O and CO_2 in the basaltic melt inclusions were calculated from the model of Papale et al. (2006) using a melt temperature calculated from equation 6a of Sugawara (2000). This process was performed iteratively due to the co-dependence of volatile saturation pressure on melt temperature. K_D values ranged from 0.3 to 0.35. We assumed a $\text{FeO}/\text{FeO}_{\text{total}}$ weight ratio of 0.77, calculated from the $f\text{O}_2$ of the melt inclusions, converted to melt $\text{Fe}^{2+}/\text{Fe}^{3+}$ mole fraction ratio using the method of Kilinc et al. (1983). Oxygen fugacity values were calculated from the S $K\alpha$ measurements on seven melt inclusions using a temperature of 1100°C and following the method of Wallace and Carmichael (1994) (Table 4-1). Extents of post-entrapment crystallization range from 0-8%. Uncertainties in the re-calculated melt inclusion compositions based on uncertainties in $\text{FeO}/\text{FeO}_{\text{total}}$ determination ($\pm 5\%$), K_D (± 0.01) and coexisting olivine host composition ($\pm \text{Fo } 0.5$) are $\leq 0.5\%$ for the non-

participating oxides and < 5 % for the major participating oxides (FeO, MgO and SiO₂).

Saturation pressures and melt inclusion trapping temperatures for the clinopyroxene-, plagioclase- and orthopyroxene-hosted melt inclusions were calculated as for the olivine-hosted melt inclusions, using the models of Papale et al. (2006) and Sugawara (2000), respectively.

Total iron contents in the melt inclusions (Table 4-1) are comparable to those measured in the bulk rock (Handley et al., 2007) at a given MgO content suggesting that post-entrapment iron loss by diffusion was negligible. The CaO/Al₂O₃ ratios of the melt inclusions lie along the liquid line of descent defined by the whole rock data (Handley et al., 2007). This suggests that the melt inclusion compositions are representative of the bulk melt from which the olivine crystallized and that the melt inclusions were not affected by disequilibrium processes (boundary layer concentration build-up) during entrapment (Faure & Schiano, 2005; Métrich & Wallace, 2008; Kent, 2008).

4.4.2 Fumarole gas sampling and analysis

Fumaroles on the active dome were sampled in 2007 and 2008 following the method of Giggenbach (1975), using an evacuated glass flask filled with 80 ml of 3.5 M NaOH solution. The NaOH is trace metal grade and diluted with nano-pure water. Exit temperatures of the fumaroles were > 350 °C and the hottest fumaroles were selected for sampling. The sampling points were located on the top of the dome directly into the natural fumaroles and not from the exit of

the pipes at the base of the dome. A thin (0.8 cm) quartz tube (≤ 1 m in length) was inserted into the fumarole and linked to the sampling flask via high temperature Teflon tubing whose length was kept as short as possible to avoid large temperature drops and vapour condensation. The tubing was purged with gas prior to sampling. Samples were collected for 5-15 minutes ensuring that the flow rate did not exceed ~ 1 bubble s^{-1} to avoid air contamination. Samples were analysed at the Analytical Chemistry Lab at the University of New Mexico. Insoluble gas species (e.g., CO_2 , CO) were measured using gas chromatography and the soluble gas species (e.g., SO_2 , H_2S , HCl, HF) were analysed using wet chemistry following the method of Giggenbach and Goguel (1989). H_2O contents were determined using the weight difference of the flask prior to and following sampling (weighted to 0.1g).

4.5 Results

4.5.1 Melt inclusion and matrix glass major and volatile element composition

Table 4-1 reports the major element composition of the melt inclusions and the matrix glasses including H_2O , CO_2 , S, Cl and F contents, host compositions (olivine only), oxygen fugacities from S peak shift measurements (select melt inclusions only) and volatile saturation pressures and melt temperatures (for previously reported basaltic melt inclusion compositions refer to Chapter 3). Olivine-hosted compositions have been corrected for post-entrapment crystallization (Table 4-1). Analysed values can be found in Appendix

C. Melt inclusions hosted in other phases: clinopyroxene, orthopyroxene and plagioclase are reported as analysed.

Olivine hosts have compositions of Fo₇₈₋₈₁ (Fo = forsterite %) and a more faylite-rich rim of Fo₇₆₋₇₇, up to 20 µm wide, visible in back-scattered electron imaging. Some olivine crystals have Cr-rich oxides present as inclusions in the rim only. Two profiles, one length-wise and one width-wise were performed on a euhedral olivine phenocryst (Fig. 4-2). The profiles (2.3 and 1.3 mm long) display a normal zoning pattern overprinted by a small-scale reverse zoning trend from the rim inward from Fo₇₉ to Fo_{79.5}.

Olivine-hosted melt inclusions are basaltic in composition (Fig. 4-3) with (normalized on an anhydrous basis) 47-50 wt% SiO₂, 5-7 wt% MgO, FeO_{total} contents of 10-12 wt% (excluding the embayment glass sample TO-XVIII; Chapter 3), a CaO/Al₂O₃ ratio of 0.55-0.63 and a total alkali content of 2.2-4.1 wt% (NaO + K₂O). The basaltic melt inclusions classify as medium-K calc-alkaline magmas as is typical of arc magmas in eastern Java and Bali (Chapter 3). The matrix glass of the basaltic tephra has 53-54 wt% SiO₂, 3.5-4 wt% MgO and elevated FeO contents of 13-15 wt% (anhydrous normalized values). The CaO/Al₂O₃ ratio is 0.58-0.70, extending to higher values than the melt inclusions. Total alkali content of the matrix glass overlaps with that of the melt inclusions (3.3-4 wt% NaO + K₂O).

One clinopyroxene- and one plagioclase-hosted melt inclusion have been analysed for major element and S, Cl and F content (Table 4-1; mountpx1 and plmi1, respectively). H₂O and CO₂ contents are available for a second

clinopyroxene-hosted melt inclusion (ijenbas2; Table 4-1). Sample mountpx1 is a basaltic andesite (Fig. 4-3). It has a lower MgO content (3.9 wt%), higher SiO₂ and alkalis (52 and 5.1 wt%, respectively) and a similar FeO_{total} content compared to the basaltic melt inclusions (normalized on an anhydrous basis; Fig. 4-4). It has a slightly lower CaO/Al₂O₃ ratio of 0.47 compared to the basalts, which agrees with the presence of a clinopyroxene host. The plagioclase- and orthopyroxene-hosted melt inclusions are more evolved (65-69 wt% SiO₂) and have a total alkali content that places them on the border of the dacite and trachydacite classifications (8.3-9.6 wt%) (Figs. 4-3, -4). The glass globule from the dome material is rhyolitic in composition with 71 wt% SiO₂ and a total alkali content of 9.7 wt%.

K₂O content in the melt inclusions, whole rock (van Hinsberg et al., 2010b) and matrix glass covaries with SiO₂ content and behaves as an incompatible element throughout the evolution of the magmatic series (Fig. 4-3). Variation of FeO and TiO₂ contents with MgO suggests that fractionation of Ti-Fe-oxides is suppressed in the basaltic sequence but is a fractionating phase in the more evolved magmas (Fig. 4-4b,c). Crystallization of clinopyroxene is minor compared to plagioclase in the basaltic sequence as evidenced by the elevated CaO/Al₂O₃ ratio of the basaltic matrix glass (Fig. 4-4a). Petrographic observation and qualitative Energy Dispersive X-ray Spectroscopy analysis on the basaltic matrix reveals the presence of plagioclase, olivine and minor clinopyroxene (augite) microphenocrysts as well as an oxide phase, in agreement with the chemical trend within the basaltic sequence. As the system evolves towards

dacite and rhyolite, $\text{CaO}/\text{Al}_2\text{O}_3$ ratios decrease, attesting to the dominant presence of clinopyroxene in the whole rock samples (van Hinsberg et al., 2010b). Na_2O behaves as an incompatible element in the basaltic sequence but decreases as differentiation proceeds within the dacitic sequence suggesting the evolution of plagioclase composition from Ca-rich anorthite to more Na-rich albite.

P_2O_5 contents are more variable than K_2O contents in the basaltic melt. Variation of P_2O_5 content with MgO and SiO_2 contents reveals a broad trend of increasing P_2O_5 values as differentiation proceeds, with the matrix glass displaying the highest values (Fig. 4-5). This trend is not continuous towards more evolved compositions. Dacitic melt inclusions have lower P_2O_5 concentrations and the opposite trend of decreasing P_2O_5 content with increasing differentiation suggesting the fractionation of a P_2O_5 -bearing phase. Whole rock data spans the gap between the basaltic and dacitic melt compositions. A similar pattern can be seen when comparing K_2O and P_2O_5 contents (Fig. 4-13).

Maximum H_2O , CO_2 , S and Cl contents in the Kawah Ijen basalts are typical of arc basalts worldwide (Chapter 3). Both basaltic and dacitic H_2O and CO_2 contents are variable (H_2O : 7.1-0.23 wt%, CO_2 : 3500-20 ppm for basaltic; H_2O : 6.7-1.3 wt%, CO_2 : 100 to below detection limit for dacitic; Table 4-1, Fig. 4-6). Sulphur in the basaltic melt inclusions varies from 430 to 2200 ppm although most values are within the range 1900-2200 ppm (Table 4-1; Fig. 4-7a). In contrast, the basaltic matrix glass contains only 10-45 ppm S. The clinopyroxene-hosted melt inclusion (basaltic andesite) has a S content of 270 ppm. Lower S

contents are also found in the dacitic melt inclusions, ranging from 90 to 300 ppm. Dacitic matrix glass S contents overlap at 80-170 ppm (Fig. 4-7a). The interstitial glass globule from the dome rock (rhyolitic glass) contains 130 ppm S. The basaltic melt inclusions display nearly constant S content with decreasing H₂O content until 1.5 wt% H₂O, then decrease to < 50 ppm in the matrix glass (Fig. 4-7a). The variability in S content at H₂O contents > 3 wt% may be attributed to the presence of S-saturated globules in some of the melt inclusions, mainly from tephra layer OT (Fig. 4-7a). In the more evolved samples, S contents remain nearly constant throughout the range of H₂O contents (6.7-0 wt%). No primary magmatic S-saturated globules have been found in the evolved samples.

Chlorine contents in the basaltic melt inclusions vary between 700-1300 ppm and are higher in the matrix glass (1500-1800 ppm; Table 4-1; Fig. 4-7b). Chlorine contents of 760 ppm are found in the basaltic andesite melt inclusion. The dacitic melt inclusions have 1800-2300 ppm Cl whereas the dacitic matrix glass has slightly lower concentrations (1500-1600 ppm) and the rhyolitic glass even lower Cl contents (1385 ppm). Within the basaltic sequence, Cl contents remain approximately constant as H₂O contents decrease with more elevated values in the matrix glasses (Fig. 4-7b). In the dacitic-rhyolitic sequence the opposite trend is seen with decreasing Cl contents as H₂O decreases.

Fluorine contents range from 780-1600 ppm in the basaltic melt inclusions (Table 4-1, Fig. 4-7c) and are some of the highest concentrations reported for arc basalts (Chapter 3). F contents are only slightly lower on average in the basaltic matrix glass (600-1070 ppm). As H₂O contents decrease, F contents remain

variable but relatively elevated until eruption (Fig. 4-7c). Fluorine contents in the dacitic melt inclusions and matrix glass are highly variable (200-1300 ppm and 200-1000 ppm, respectively) and no trend is seen with H₂O content (Fig. 4-7c). No F content is reported for the basaltic andesite or the rhyolitic glass.

4.5.2 Sulphur speciation and oxygen fugacity

The ratio of oxidized sulphur species to total S (S^{6+}/S_{total}) in the basaltic melt is 0.16-0.88 which corresponds to a $\log fO_2$ of -7.5 to -9 bars at a temperature of 1100 °C. The one dacitic melt inclusion analysed for S K α peak position has a $\log fO_2$ of -10.1 bars at 1000 °C. These fugacities correspond to 0.5 to 2 units above the Faylite-Magnetite-Quartz (FMQ) buffer (Table 4-1). This relatively large range in melt fO_2 correlates with melt H₂O content and pressure (Fig. 4-8).

4.5.3 Fumarole gas chemistry

Fumarole gas compositions from 2007 and 2008 and their sampling temperatures are reported in Table 4-2. As for most arc magmas, H₂O is the dominant gas specie followed by CO₂ > S_{total} (SO₂+H₂S) > N₂ ≥ HCl > HF > minor species. It should be noted that prior to this study, samples were collected at the exit of the pipes as opposed to directly from the fumaroles (Delmelle et al., 2000). As a result, those samples will have experienced variable amounts of S_{total} loss as evidenced by the low S_{total} concentrations (Fig. 4-9), lower sampling temperatures (< 250 °C compared to > 350 °C in 2007 and 2008) and the liquid sulphur that condenses out of the gas phase as it cools through the pipes. In

2007, gas samples have higher H_2O/CO_2 and H_2O/S_{total} weight ratios compared to 2008 samples (Fig. 4-9). These samples also have H_2-N_2-Ar contents that reflect the addition of air-saturated water (Fig. 4-10). These same systematics reveal that the 2008 samples have experienced variable degrees of air contamination (sample 2008-3 in particular; Table 4-2). Compared to other arc volcanoes, Kawah Ijen gases (2008) have low H_2O/S_{total} and CO_2/S_{total} weight ratios as well as low H_2O/CO_2 (Fig. 4-9). The 2008 gases have a lower SO_2/H_2S weight ratio as well as lower average CO_2/S_{total} compared to the 2007 samples (Fig. 4-9). The 2007 samples have lower S_{total}/HCl and S_{total}/HF weight ratios compared to 2008 and all Kawah Ijen gases have relatively low HCl and HF concentrations compared to other arc volcanoes (Fig. 4-11).

4.6 Discussion

4.6.1 Magma evolution

The melt inclusion oxide variation diagrams show evidence of both crystal fractionation and magma mixing in the generation of the Kawah Ijen magmatic series (Figs. 4-3, -4 and -5). The mafic magma series (basalt to basaltic andesite) is characterized by the suppression of Ti- and Fe-oxide fractionation, variable degrees of late clinopyroxene fractionation and only minor apatite fractionation. In contrast, the felsic magma series (dacite to rhyolite) is characterized by extensive fractionation of Na-rich plagioclase, apatite and pyroxene. The whole rock compositions bridge the compositional gap between the basaltic and dacitic melt inclusions and some oxides (e.g., FeO , TiO_2 , Na_2O , P_2O_5) reflect mixing processes between the two end member melt compositions

(Figs. 4-4 and 4-5). In contrast, K_2O , which remains incompatible throughout the differentiation sequence, does not reflect this mixing process as well. Handley et al. (2007) noted similar trends within the whole rock data from Kawah Ijen and other volcanoes within the Ijen Caldera Complex. Low-Ca and Al magmas, having experienced significant plagioclase fractionation, appear to originate from the shallower, central parts of the caldera, and also feed the intra-caldera lineament volcanoes (Fig. 4-1b). High-Ca and Al magmas characterize the caldera rim volcanoes and represent deeper level fractionation of mostly olivine and clinopyroxene. Handley et al. (2007) noted that Kawah Ijen lavas represented mixing of these two end-member magma series, a conclusion that is supported by our melt inclusion data. These plagioclase-dominated intra-caldera magmas are also more enriched in P_2O_5 and K_2O , on average, compared to the caldera rim magmas (Handley et al., 2007). This would explain the saturation of apatite in the more evolved samples at Kawah Ijen and the presence of phlogopite in some of the lavas from the intra-caldera vents (Berlo, 2001).

4.6.2 Volatile evolution

4.6.2.1 H_2O and CO_2 systematics

H_2O and CO_2 solubility, which is strongly pressure dependent (e.g., Dixon et al., 1995), results in fluid saturation early on during magma ascent from the mantle to the upper crust, especially in hydrous mafic magma (e.g., Métrich and Wallace, 2008). At Kawah Ijen, the range of H_2O and CO_2 contents in the basaltic magma reflects in part variable degrees of degassing as the magma ascends from > 14 km depth to the surface (Fig. 4-6a). However, the variation in H_2O and

CO₂ contents cannot be explained by a single degassing model regardless of the degassing mechanism invoked (open vs. closed system). In particular, the variable CO₂/H₂O ratios at a given pressure and the retention of high CO₂ concentrations even at low H₂O contents, suggests melt/fluid equilibrium under variable fluid compositions. The concept of gas fluxing of magma by a vapour phase and partial to complete re-equilibration of the melt with this vapour has previously been proposed for volatile-saturated magmas in an “open system” where gas is allowed to flux through a magma from deeper depths (e.g., Rust et al., 2004). This process has been invoked to explain the H₂O-CO₂ patterns observed in other melt inclusions from hydrous arc magmas (e.g., Johnson et al., 2008; Vigouroux et al., 2008; Wallace and Métrich, 2008; Roberge et al., 2009; Blundy et al., 2010). For the Kawah Ijen basaltic magma, H₂O and CO₂ contents can be explained by open system gas fluxing of the melt with vapours ranging in composition from XH₂O = 0.95 to 0.25 (mole fraction H₂O). This process may be combined with open or closed system degassing of the magma body itself resulting in H₂O-CO₂ contents intermediate between the vapour isopleths and the open/closed system degassing curves (Fig. 4-6a). Similar vapour compositions have been invoked to explain the H₂O-CO₂ contents of melt inclusions from arc volcanoes (XH₂O = 0.25-0.6; Spilliaert et al., 2006; Johnson et al., 2008; Vigouroux et al., 2008; Roberge et al., 2009; Johnson et al., 2010).

The dacitic melt inclusions and matrix glass have highly variable H₂O contents but a more restricted range of CO₂ contents which, as with the basalt, cannot be related via a single degassing model (Fig. 4-6b). The H₂O-CO₂

contents of the dacitic melt inclusions can also be best explained by a combination of gas fluxing with a vapour phase of $X_{H_2O} = 0.9-0.95$ and open/closed system degassing.

4.6.2.2 S systematics

Melt volatile content will evolve during ascent and cooling of magma as a result of degassing and differentiation. Using K_2O as an index of differentiation and the partial pressures of H_2O and CO_2 as an index of pressure/depth, the relative effects of decompression and cooling on melt S, Cl and F content can be evaluated (Fig. 4-12). Sulphur contents in the basaltic magma remain nearly constant at 2000-2200 ppm and a S/ K_2O ratio of 0.35 as the magma ascends from 14 to 8 km depth (Fig. 4-12b). Below 200 MPa (< 8 km) the melt is variably depleted in S with the matrix glass exhibiting the greatest amount of S loss. In the dacitic and rhyolitic samples, S contents are variable in the melt inclusions but overlap with concentrations in the matrix glasses. Similarly S/ K_2O ratios remain nearly constant (0.002-0.004) as the felsic magma ascends to the surface. As the melt evolves from basalt to rhyolite, the solubility of S decreases (Fig. 4-12b), independently of pressure and most likely associated with a drop in magma temperature, fractionation of Fe^{2+} -bearing phases (Fe-oxides) from the melt phase and a drop in oxygen fugacity (Fig. 4-8).

Saturation of the melt with respect to S implies that S partitions either into the fluid phase or into a sulphate- or sulphide-saturated phase (anhydrite and pyrrhotite crystalline phases or sulphide and sulphate immiscible melts).

Sulphate saturation of a basaltic melt requires elevated oxygen fugacities (\geq

$\Delta\text{FMQ} + 2.32$) and very high S contents ($> 1 \text{ wt}\%$; Jugo et al., 2005b; Jugo, 2009) which are not found at Kawah Ijen (maximum $f\text{O}_2$ is $\Delta\text{FMQ} + 2$; S contents are $\leq 2200 \text{ ppm}$; Table 4-1, Fig. 4-8). At oxygen fugacities $< \Delta\text{FMQ} + 2.32$, basaltic melt may saturate with a sulphide-phase if its S content reaches the solubility limit. This limit has been shown to vary with melt composition, H_2O content, pressure and temperature (Liu et al., 2007). Figure 8a shows the results of calculated S solubility limits at sulphide saturation (SCSS) using the equation of Liu et al. (2007) for an average Kawah Ijen basalt composition at variable pressures (and consequently H_2O contents). As the magma ascends from 400 MPa to 10 MPa and H_2O degasses from 7 wt% to $< 1 \text{ wt}\%$ (calculated from the model of Papale et al., 2006 assuming a constant vapour composition of $\text{XH}_2\text{O} = 0.75$), the SCSS increases from 300 ppm to 1500 ppm at $f\text{O}_2$ conditions $\leq \Delta\text{FMQ} = 0$ and from 3300 to 8700 ppm at the 'critical $f\text{O}_2$ ' of $\Delta\text{FMQ} = +2.32$, which corresponds to the maximum S solubility of the system when both sulphide- and sulphate-saturation coexists (Jugo, 2009). At intermediate $f\text{O}_2$ conditions ($\Delta\text{FMQ} = 0-2$) which correspond to those determined for the Kawah Ijen basalt, the SCSS limit increases exponentially and is therefore very sensitive to oxygen fugacity variations. At Kawah Ijen, oxygen fugacity co-varies with the H_2O content/pressure of the basaltic melt (Fig. 4-8b). As H_2O degasses, the speciation of S in the melt shifts to lower $\text{S}^{6+}/\text{S}^{2-}$ ratios reflecting a decrease in oxygen fugacity. If the melt phase were initially sulphide-undersaturated, a decrease in $f\text{O}_2$ would result in sulphide-saturation. However, decreasing H_2O content in the melt phase shifts the SCSS limit to higher values thereby creating

an interplay between the shifting SCSS limit and the fO_2 . S contents in Kawah Ijen basaltic melt remain elevated over a range of fO_2 conditions ($\Delta FMQ = 1.5-2$). However, determining whether or not the Kawah Ijen basalt is sulphide-saturated as it ascends from 400 MPa to 200 MPa is currently limited by the uncertainties in both the SCSS determination (Liu et al., 2007) and the uncertainty associated with the fO_2 determination from the S K α peak shift. At pressures lower than 200 MPa, S contents are decreasing and significantly lower than the associated SCSS implying that the melt is sulphide-undersaturated and that degassing of S into the fluid phase is the dominant process. The dacitic melt inclusion falls along the trend of pressure versus fO_2 defined by the basalt (Fig. 4-8b). At an oxygen fugacity of $\Delta FMQ = + 0.9$, the dacite has a S content (300 ppm) lower than its SCSS implying that it is sulphide undersaturated.

4.6.2.3 Cl and F systematics and apatite fractionation

Chlorine and fluorine contents are variable in the basaltic samples and F is also highly variable in the dacitic melt inclusions and matrix glasses (Fig. 4-12c,d). In the basaltic samples, Cl/K₂O ratios are highly variable but do not appear to decrease as pressure decreases suggesting that although Cl contents in the melt are variable, they remain dissolved to shallow depths. In the dacitic samples, Cl/K₂O ratios are less variable and remain constant until pressures < 50 MPa at which point Cl exsolves from the melt phase. As the melt evolves from basalt to rhyolite, the solubility of Cl in the melt phase decreases, independent of pressure but likely associated with a drop in magma temperature (1150-1000 °C) and change in melt and fluid phase composition ($X_{H_2O} = 0.25-0.95$ to $X_{H_2O} =$

0.9-0.95). Similarly to Cl, the F/K₂O ratios are highly variable in the basaltic and dacitic melt inclusions and matrix glass samples (Fig. 4-12d). Unlike Cl however, F/K₂O ratios appear to decrease slightly at pressures < 50 MPa in the basaltic samples and conversely do not decrease in the low pressure dacitic samples. As the melt evolves from basalt to dacite, the solubility of F in the melt phase decreases, again independently of pressure.

The presence of apatite as mineral inclusions and in the matrix of the more evolved samples, combined with the co-variation of melt P₂O₅, Cl and F contents (Fig. 4-13) suggests that apatite controls the Cl and F content of the melt phase. The P₂O₅/Cl ratio of the basaltic samples are compatible with fractionation of apatite containing 2000 ppm to 1.5 wt% Cl; common concentrations of Cl in apatite from subduction-zone basalts (e.g., Luhr and Carmichael, 1981; Boyce and Hervig, 2009; Fig. 4-13b). Conversely, the P₂O₅/F ratio of the basaltic samples is lower than would be expected from the crystallization of either Cl-apatite or F-apatite due to overprinting by F degassing (decreasing K₂O/F ratio at nearly constant K₂O/ P₂O₅; Fig. 13c). In the more evolved samples, the fractionation of Cl-apatite is replaced by F-apatite and K₂O/Cl ratios become nearly constant as neither Cl degasses or is taken up by apatite. Only the dacitic matrix glass shows evidence of degassing. The K₂O/F ratio of the evolved melt is more variable and indicates a combination of uptake by F-apatite and degassing of F (Fig. 4-13c).

4.6.3 Degassing modeling

Following the method described in Johnson et al. (2010), we model the evolution of the gas phase as magma ascends, cools and evolves chemically by combining information on the variation of S, Cl and F contents with H₂O and K₂O contents (Figs. 4-7 and 4-12) with equations of mass balance. After establishing the initial (undegassed) magmatic compositions, the volatile element partition coefficients between the melt and vapour fraction ($D^{\text{vap-melt}}$) are calculated for each melt inclusion (see Appendix C for details of the modeling procedure). Mass balance constraints are used to model: 1) open system degassing where the gas is continuously removed from the magma as it is produced. For this scenario we use the equation for Rayleigh fractionation; 2) closed system degassing where the gas remains in equilibrium with the melt phase during its production. In this scenario we employ equations for batch processes; and 3) open system vapour fluxing where the melt is re-equilibrated with a fluid phase introduced into the system from depth.

When modeling the melt inclusion and matrix glass data, not all degassing scenarios are realistic or appropriate. For the basaltic and dacitic melt inclusions, which have trapped variably degassed melt at various levels within the magmatic plumbing system, H₂O and CO₂ contents suggest the degassing style is dominantly vapour fluxing and that simple open or closed system degassing cannot account for the elevated melt CO₂ contents. As such, we evaluate the $D^{\text{vap-melt}}$ values for the vapour fluxing scenario with 1 wt% and 5 wt% initial vapour present (range of values proposed at other arc volcanoes; Johnson et al.,

2010). Given that a combination of vapour fluxing and open or closed system degassing may have occurred (Rust et al., 2004), we also modeled the melt inclusions for open and closed system degassing only and found that resulting $D^{\text{vap-melt}}$ values are within error of the uncertainties associated with calculating the $D^{\text{vap-melt}}$ values in any given model (Johnson et al., 2010; Appendix C). The basaltic and dacitic matrix glasses are evaluated assuming open system degassing (most likely scenario given rapid vesiculation upon eruption). Finally, the intermediate case of a basaltic magma evolving to a dacitic magma is the least constrained, given the limited H₂O and CO₂ contents for this compositional range. Given that vapour fluxing is the dominant degassing style for the basaltic and dacitic melt inclusions, we assume that the same process also dominates during the evolution of basalt to dacite. In fact, one clinopyroxene-hosted melt inclusion does show evidence of vapour fluxing, with elevated CO₂ contents at relatively low H₂O contents (0.16 wt% CO₂ at 4.6 wt% H₂O; Fig. 4-6a).

H₂O can be used as a tracer of degassing and K₂O as an index of magma differentiation (e.g., Blundy and Cashman, 2005; Johnson et al., 2010). The two are inter-related as the degassing of H₂O-saturated magmas promotes melt crystallization and melt crystallization of anhydrous minerals promotes H₂O saturation. As a result, a rough correlation between H₂O contents and degree of crystallization is often observed at arc volcanoes (e.g., Blundy and Cashman, 2005). At Kawah Ijen, the correlation between H₂O and K₂O content in the basalts is markedly scattered around 200 MPa (Fig. 4-12a), corresponding to the depth range where melt inclusion formation, CO₂ –rich vapour fluxing and

variability in melt composition and Cl and F content is the most pronounced (Figs. 4-6a and 4-12c,d). Olivine crystallization under H₂O-undersaturated conditions may occur if the melt is fluxed with a CO₂-rich vapour such as at Kawah Ijen (e.g., Johnson et al., 2008). Re-equilibration of the melt with the CO₂-rich vapour will draw H₂O out of the melt phase causing the melt to crystallize even though the melt remains H₂O undersaturated. Consequently, the relationship between crystallization and melt H₂O content is likely to be more complex under gas fluxing conditions.

Establishing the initial H₂O-K₂O content of the basaltic magma giving rise to each melt inclusion is non-trivial, therefore, we simplify the problem by assuming that the variations in the H₂O/K₂O ratio of the melt inclusions (Fig. 4-12a) are inherited during degassing, crystallization and interaction with CO₂-rich fluids, and are not inherent to the parental mantle melt. As such, we define the initial K₂O content of the system from the basaltic melt inclusion with the lowest K₂O concentration (OT-1-2; 0.52 wt% K₂O on an anhydrous basis; see Chapter 3 and Fig. 4-3). Increasing the parental magma K₂O content up to 0.60 wt% on an anhydrous basis (corresponding to sample TO-XXIV; see Chapter 3 and Fig. 4-3) does not change the conclusions of this study, it simply decreases the amount of crystallization estimated for each melt inclusion, thereby decreasing the calculated $D^{\text{vap-melt}}$ values by up to 10 units (therefore making some $D^{\text{vap-melt}}$ values negative and inducing large errors in samples with melt fractions approaching a value of 1; Johnson et al., 2010). Melt inclusion OT-1-2 has H₂O and CO₂ contents typical of melts that have partially degassed but are unaffected

by CO₂-rich vapour fluxing (Fig. 4-6a; H₂O = 5.1 wt%, CO₂ = 286 ppm). Its low CO₂ content places it along the closed system degassing path for a melt starting with 7.1 wt% H₂O and 2000 ppm CO₂, values corresponding to the high pressure (390 MPa), melt inclusion (TO-XIV; Fig. 4-6a) with the highest H₂O content.

As such we define the initial H₂O content of the system to be 7.1 wt%. Subsequent loss of H₂O from the melt phase is, therefore, a combination of H₂O saturation of the melt phase and H₂O degassing due to CO₂-fluxing. Within the dacitic system, the initial H₂O and K₂O contents are taken as the highest and lowest value recorded by the melt inclusions, respectively (6.7 wt% H₂O, 3.4 wt% K₂O). We also model the evolution of basalt to dacite using the same starting conditions as in the basalt-only system but final melt compositions as determined by the dacitic melt inclusions. As discussed earlier, K₂O behaves incompatibly in the crystallizing assemblage from basalt to rhyolite. As a result, variations in K₂O alone cannot differentiate between evolution of the magma via crystal fractionation or via magma mixing. However, the effect both these processes have on the resulting melt volatile content is the same; S, Cl and F will degas or be removed via the crystallization of apatite or the precipitation of a sulphide phase in response to changes in external parameters such as melt composition and temperature and not specifically to the mechanism that brings about these changes.

Initial (undegassed) S contents are estimated from the highest S/K₂O ratios of the basaltic and dacitic melt inclusions (sample TO-XXII at 0.38 and sample rhyo2y at 0.008, respectively; Table 4-1, Fig. 4-12b) combined with the

least evolved K_2O contents of 0.49 and 3.4 wt%, respectively. This yields an initial S content of ~1860 ppm for the basaltic magma and ~270 ppm for the dacitic magma. Chlorine $D^{vap-melt}$ values are not modeled for the basaltic system due to evidence of Cl-apatite fractionation (Fig. 4-13). However, for the modeling of basaltic to dacitic magma, we assume that Cl-apatite fractionation does not persist across the compositional gap and establish the initial basaltic Cl content to be ~1180 ppm (using a maximum Cl/ K_2O ratio of 0.24; Fig. 4-12c). For the dacitic melt inclusions, given that Cl does not appear to partition into apatite (Fig. 4-13), we establish initial Cl contents from the highest Cl/ K_2O ratio (0.05; Fig. 4-12c) with an initial K_2O content of 3.4 wt% to yield a value of 1700 ppm. Fluorine $D^{vap-melt}$ values are obscured by the fractionation of apatite in the dacitic samples (Fig. 4-13). In the basaltic samples, a combination of degassing and apatite fractionation is likely occurring. Modeling of the F $D^{vap-melt}$ values in the basalt is further complicated by the the highly variable F/ K_2O contents that do not correlate with either the index of degassing (H_2O or pressure, Fig. 4-12d) or differentiation (K_2O). As such, we exclude F from our modeling.

Results of the modeled $D^{vap-melt}$ values are presented in Table 4-3. Average S $D^{vap-melt}$ values remain low (2-9) as the basaltic magma ascends, degasses and crystallizes under vapour fluxing conditions (Fig. 4-14). Only at pressures < 100 MPa is there a sharp increase in the partitioning of S into the vapour phase ($D^{vap-melt} > 40$). These results are consistent with modeled S $D^{vap-melt}$ values at other arc basaltic systems (e.g., Jorullo, Mexico, Johnson et al., 2010; Stromboli, Italy, Scaillet and Pichavant, 2005; Etna, Italy, Spilliaert et al.,

2006). The evolution of basalt to dacite is associated with a marked decrease in magma temperature (Table 4-1) and the fractionation of Fe-Ti oxides (Fig. 4-4), both contributing to a decrease in the solubility of S (e.g., Scaillet & Pichavant, 2005). Given that there is no evidence of sulphide saturation in the erupted dacites, the large S $D^{\text{vap-melt}}$ values modeled for the transition from basalt to dacite (average of 70-225; Fig. 4-14) likely reflects large degrees of S degassing, independent of changes in pressure. Calculated S $D^{\text{vap-melt}}$ values for ascent and evolution of dacitic melt are scattered around an average of 20 and show no clear trend with decreasing pressure (not shown). These $D^{\text{vap-melt}}$ values are similar to those obtained experimentally on a sulphide-saturated rhyodacite at 200 MPa and 850 °C under similar fluid compositions (~20; Botcharnikov et al., 2004). The saturation of pyrrhotite does not preclude the fractionation of S into the vapour phase and in fact, there is a positive correlation between mole fraction of pyrrhotite and S $D^{\text{vap-melt}}$ values, likely related to the concomitant decrease in melt FeO content and S solubility (Botcharnikov et al., 2004).

As mentioned above, Cl $D^{\text{vap-melt}}$ values cannot be modeled in the same fashion for the basaltic system due to evidence of Cl-apatite fractionation. However, they can be estimated based on the composition of the apatites themselves. Mathez and Webster (2005) showed that for fluid- and apatite-saturated basalts at 200 MPa and temperatures between 1066-1150 °C (with a composition similar to Kawah Ijen basalts), Cl $D^{\text{vap-melt}}$ values vary with apatite Cl content but will remain low (~1) for apatite Cl contents typical of subduction zone basalts (< 2 wt%; Luhr and Carmichael, 1981; Boyce and Hervig, 2008). This

suggests that minimal Cl degassing is expected from the apatite-saturated basalts, which agrees with the K_2O -Cl- P_2O_5 systematics of the basalts (Fig. 4-13). For the dacitic melt inclusions, we obtain $D^{vap-melt}$ values of 0-2 at pressures > 100 MPa and slightly higher values of 4 at low pressures (< 50 MPa) suggesting shallow degassing of Cl (Fig. 4-15). Cl $D^{vap-melt}$ values associated with the evolution of basalt to dacite are slightly higher (4-6) than for the dacite-only case and do not vary significantly with pressure (Fig. 4-15).

4.6.4 Model magmatic fluid composition and comparison with measured fumarole compositions

We derive a model magmatic fluid composition by combining the S and Cl $D^{vap-melt}$ values calculated as a function of pressure and melt composition with H_2O and CO_2 fluid compositions derived from the melt inclusion data (see Appendix C for more details). H_2O - CO_2 fluid compositions are constrained by the vapour isopleths that bracket the melt inclusion data (Figs. 4-6 and 4-7). The composition of these fluids range from mole fraction H_2O values of 0.25-0.95 for the basaltic system and 0.9-0.99 for the dacitic system. For the intermediate case of a basalt evolving to a dacite, given the limited number of melt inclusion data in this compositional range, we model the H_2O - CO_2 fluid for a relatively wide range of fluid compositions ($X_{H_2O} = 0.5$ -0.95). As discussed earlier, open (no vapour fluxing) and closed system degassing are not likely to dominate at Kawah Ijen (in the past and currently), therefore, model fluid compositions are not presented for these scenarios.

Results of the modeled magmatic fluid compositions are summarized in Table 4-3. The fluid compositions either have H₂O as the most abundant component or CO₂ depending on the nature of the fluid fluxing the system, followed by SO_{2 (total)} (all S expressed as SO₂) then HCl, in agreement with the order of abundance commonly found in magmatic gas samples from arc volcanoes worldwide (e.g., Symonds et al., 1994 for review). In all model compositions, HCl contents in the fluid are very low (XHCl = 0.001-0.005) and are highest during the evolution of basalt to dacite. SO_{2 (total)} contents are also highest in the basalt-dacite scenario (XSO_{2 (total)} = 0.017). Fluid S contents in the basaltic scenario increase as pressure decreases (XSO_{2 (total)} = 0.003 at P = 400 MPa to XSO₂ = 0.007 at P < 10 MPa). They are lowest in the dacite scenario with XSO_{2 (total)} = 0.002 at all pressures.

In order to determine the model composition that best represents the current Kawah Ijen system, we compare the H₂O and CO₂ model fluid compositions with the analysed fumarole compositions. As mentioned earlier, the chemistry of the 2007 fumarole samples shows evidence for the incorporation of external water and as a consequence, its H₂O/CO₂ weight ratio is much higher than the modeled fluid compositions (Fig. 4-9). The 2008 fumarole samples are more representative of the magmatic component currently degassing at Kawah Ijen, with H₂O, CO₂ and S_{total} ratios that fall within the range reported for high temperature fumaroles (showing no signs of water contamination) at other arc volcanoes (Fig. 4-9). As a first order approximation, we assume that the H₂O/CO₂ ratio of the 2008 gas samples has not been affected by shallow hydrothermal

processes. This ratio corresponds to a X_{H_2O} of 0.9, which is within the range of fluxing vapour compositions determined from the dacitic melt inclusion data ($X_{H_2O} = 0.9-0.99$). The presence of mafic, CO_2 -rich magma degassing at depth is required to explain the high CO_2 contents measured at the surface of the rhyolitic dome and recorded in the melt inclusions. This mafic magma may be a ponded body at > 10 km, degassing in an open conduit (gas is free to escape through the shallower plumbing system). This minimum depth estimate arises from the intersection of the most H_2O -rich open system degassing curve in the basaltic system with the vapour isopleth corresponding to a X_{H_2O} of 0.9 (Fig. 4-6a). Alternatively, basaltic magma may be present at a variety of depths and the combined fluid composition approximates a X_{H_2O} of 0.9. In either case, a plumbing system open to gas (and magma) flux from a variety of levels is required.

It is not trivial to distinguish between a single degassing mafic magma body at > 10 km depth and mafic magma present at a variety of depths. Potential-field surveys (e.g., Bouguer gravity) and geodetic models based on deformation (e.g., continuous GPS) can offer insight into the presence of a deep magma chamber beneath Kawah Ijen. Unfortunately, access to the area surrounding the crater is limited by steep terrain and thick vegetation and the presence of a large crater lake obscures gravity signals originating from the deeper parts of the system (Mauri, 2009).

By setting the magmatic fluid composition to a constant $X_{H_2O} = 0.9$, regardless of pressure, the S and Cl contents can now be constrained. In reality,

these S and Cl concentrations do not change if the X_{H_2O} content of the gas is set to 0.95 or 0.50 because the concentration of these two species relative to H_2O and CO_2 is low. The main factor affecting S and Cl contents in the gas phase is not the nature of the fluid phase, the style of degassing (i.e., the H_2O and CO_2 proportions) or the depth of degassing, but rather the composition of the magma that is degassing. The largest difference in S and Cl solubility is seen between the basaltic and dacitic melt inclusions (Fig. 4-12b,c) and the highest D values are modeled for a magma evolving from a basalt to a dacite (Figs. 4-13 and 4-14). Consequently, maximum fluid $X_{SO_2 (total)}$ values of 0.023 and X_{HCl} values of 0.006-0.008 correspond to a differentiating magma body (basalt-dacite).

Comparing the modeled $X_{SO_2 (total)}$ and X_{HCl} values with the 2008 fumarole gas samples is the next step in evaluating the modeled fluid composition. Model SO_2 fluid concentrations are significantly lower than those actually measured for all models except the basalt-dacite scenario (Table 4-3). Combining this $SO_2 (total)$ content with a mole fraction of water of 0.90 generates a model fluid composition that corresponds closely to the 2008 fumarole gas samples (Fig. 4-9) with slightly higher proportions of CO_2 and $SO_2 (total)$ in the measured gas samples compared to the model. The good agreement between the model and measured gas composition adds validation to our model and implies that magma evolution, whether it occurs via crystal fractionation, magma mixing or crustal assimilation is required to explain the high S contents of the gas measured at the surface.

Figure 4-11 compares the SO_2 (total), HCl and HF contents of the measured gases with the model fluid and the crater lake and acid spring fluids (Delmelle et al., 2000; Palmer, 2009). No HF values are calculated for the model fluid composition which thus plots on the SO_2 (total)-HCl line. The crater lake and acid spring waters are highly acidic (pH = -0.01-0.4 crater lake; 0.11-0.5 acid springs) and have $\text{SO}_4^{2-}/\text{Cl}$ ratios of 2.6-3.3, typical of acid sulphate-chloride waters at other Indonesia volcanoes (e.g., Keli Mutu, Flores, Varekamp and Kreulen, 2000; Papandayan, Java, Mazot et al., 2008). These acid sulphate-chloride waters are likely the result of condensation of volcanic gases into groundwaters (e.g., Kiyosu and Kurahashi, 1983; Rowe et al., 1992; Delmelle and Bernard, 1994). Palmer (2009) estimated that magmatic/hydrothermal fluids contribute up to 50% of the acid sulphate-chloride waters discharged at Kawah Ijen. Compared to the measured 2008 gas composition, this magmatic/hydrothermal component (as recorded by the springs and crater lake waters) is enriched in Cl and F and heavily depleted in S (Fig. 4-11). Similarly, when compared to the model magmatic fluid composition (S/Cl ratio only), the acid spring component is also enriched in Cl relative to S although to a much lesser extent. The 2007 gases form a linear series between the Cl- and F-rich acid waters and the S-enriched 2008 vapours (Fig. 4-11). This suggests that mixing of the two fluid compositions may have occurred in 2007, supported by the H_2O and He-Ar-N systematics which indicate addition of air-saturated waters (Figs. 4-9, -10). This mixing series suggests that the acid waters and the gas samples are related to each other via the addition or removal of a Cl- and F-enriched (and S-depleted) component.

Given that the fumarole gases represent the uncondensed portion of the magmatic fluid and that the acid waters likely represent the condensed portion, this suggests that fractionation of S from Cl and F is occurring in the subsurface and that S is preferentially retained in the vapour phase while Cl and F are enriched in the liquid phase. Consequently, a line linking the acid waters and the 2008 gases can be interpreted as both a mixing line (when boiling of acid waters is mixed with magmatic vapours as in 2007) and an unmixing line (when condensation of the magmatic fluid results in a Cl- and F-enriched liquid and a S-enriched vapour). The extension of a line from the S/Cl ratio of the model magmatic fluid to the F apex will intersect the mixing/unmixing line at a point which represents the original magmatic fluid S-Cl-F composition (Fig. 4-11).

With the original magmatic fluid composition established in terms of all major components (H_2O , CO_2 , S_{total} , HCl, HF), the 2008 fumarole gas data can be summarized as follows: 1) H_2O - CO_2 - S_{total} systematics suggest that the vapour phase is slightly enriched in S_{total} assuming the $\text{H}_2\text{O}/\text{CO}_2$ ratio remains constant as the magmatic fluid evolves to the surface (therefore setting the magmatic fluid composition at $X_{\text{H}_2\text{O}} = 0.9$; Fig. 4-9). This assumption is based on the low solubility of CO_2 in meteoric and hydrothermal waters and the buffering capacity of these waters for H_2O (Symonds et al., 2001). This buffering results in constant H_2O contents in the gas phase (and nearly constant $\text{H}_2\text{O}/\text{CO}_2$ with CO_2 being affected only by dilution) for gas/water ratios > 1 and temperatures $> 250^\circ\text{C}$ (Symonds et al., 2001). 2) S_{total} -Cl-F systematics suggest that the vapour phase

is relatively enriched in S_{total} and a residual liquid phase is enriched in Cl and F (Fig. 4-11).

Delmelle et al. (2000) measured the S isotopic composition of the crater lake and acid spring waters, native S globules in lake sediment and pyroclastic material, as well as fumarole gases. They noted that the enriched $\delta^{34}\text{S}$ composition of the acid waters is best explained by the disproportionation of magmatic SO_2 to SO_4^{2-} during interaction of the magmatic gases with groundwater. This observation agrees with the higher solubility of SO_2 over H_2S in groundwaters across a range of magmatic gas compositions, temperatures, gas-water and water-rock ratios (Symonds et al., 2001). This would lead to a relative enrichment in H_2S over SO_2 in the uncondensed magmatic vapour but also to a decrease in S_{total} concentration. Molar $\text{H}_2\text{S}/\text{SO}_2$ ratios in the 2008 fumaroles vary from 1.9-3, values that are higher than many high temperature fumarole gases from other arc volcanoes (Symonds et al., 1994 compilation). This lends support to the conclusion of Delmelle et al. (2000) that Kawah Ijen fumarole gases have experienced SO_2 disproportionation in the subsurface hydrothermal system. However, the Kawah Ijen fumarole gases have S_{total} contents typical of arc volcanoes (unaffected by H_2O contamination) and even slightly higher than the model fluid composition (Fig. 4-9), which is contrary to what would be expected if significant SO_2 was being dissolved in groundwater. Furthermore, thermodynamic models of magmatic gas-water interaction suggest that HCl and HF tend to be less soluble in air-saturated water compared to SO_2 , especially in low pH waters (Symonds et al., 2001), which would result in

relatively S-rich but Cl- and F-poor waters (acid spring waters at Kawah Ijen are relatively Cl- and F-rich). Finally, at temperatures > 250°C, gas/water ratios are likely to be greater than 1 which would limit the loss of SO₂ (and HCl and HF) to the groundwater (Symonds et al., 2001).

An alternate explanation for the high-S vapour phase and the high-Cl and F acid spring waters is that unmixing of the magmatic fluid upon ascent and cooling in the shallow plumbing system results in the formation of a Cl- and F-enriched liquid and a S-enriched vapour. Equilibrium cooling of the gas phase from 800-900 °C to 400 °C leads to a 3-fold increase in the H₂S/SO₂ molar ratio due to conversion of SO₂ to H₂S (Symonds et al., 2001) and could explain the high H₂S/SO₂ ratio of the fumarole gases. Subsequent flow and dilution of the Cl-F-rich liquid with meteoric water may lead to the formation of acidic chloride-rich waters. Diffuse magmatic degassing, away from the dome, may introduce lower temperature gases into the groundwater mixing at gas/water ratios <1 and temperatures < 250°C. These would be ideal conditions for the disproportionation of SO₂ into the acidic waters and perhaps further scrubbing of HCl and HF, creating highly acidic sulphate-chloride waters equivalent to the acid spring waters seeping out of the flanks of Kawah Ijen (Delmelle et al., 2000; Palmer, 2009).

4.7 Summary and Conclusions

Kawah Ijen is an actively degassing volcano emitting CO₂- and S-rich vapours as well as Cl- and F-enriched acid waters. Melt inclusion H₂O, CO₂, S, Cl and F contents for melts spanning the range basalt to rhyolite indicate that the

magmatic system at Kawah Ijen is fluxed by CO₂-rich fluids originating from mafic magma at depth and that open system gas fluxing is the dominant degassing style. Evolution of mafic magma to dacite and rhyolite is accompanied by a large drop in the solubility of S and Cl in the melt phase and exsolution of these volatiles. There is no evidence for sulphide-saturation in the more evolved magmas at Kawah Ijen (dacite and rhyolite) suggesting that the net transfer of S from the basaltic magma occurs in the fluid phase. Apatite fractionation over the entire range of magma compositions affects the Cl and F content of the melt and fluid phase. Cl-rich apatite fractionation occurs in the basalts whereas F-rich apatite fractionation dominates in the more evolved magmas. As such, little to no F is degassed from the magma at Kawah Ijen. However, the remaining Cl in the melt may exsolve into the fluid phase as the magma composition evolves from basalt to dacite.

Magmatic fluid compositions are modeled for various initial and final melt compositions and H₂O-CO₂ fluids fluxing the system using mass balance equations. Model outputs are partition coefficients for S and Cl between the melt and vapour phase at various pressures and for various melt compositions. The model that generates the highest $D^{\text{vap-melt}}$ values for S and Cl and the most realistic magmatic fluid composition is a basaltic magma evolving to a dacitic/rhyolitic magma with the system being fluxed with a fluid of composition $X_{\text{H}_2\text{O}} = 0.9$ originating (at least in part) from deeper mafic magma. Comparison of this model fluid with measured fumarole gas compositions suggests that the surface vapours are relatively enriched in S compared to the model fluid.

Additionally, acid sulphate-chloride waters at Kawah Ijen are relatively depleted in S and enriched in Cl- and F- compared to the model fluid composition. This suggests that upon ascent and cooling of the magmatic fluid, unmixing into a S-rich vapour and Cl- and F-rich acidic liquid occurs. Further cooling of the liquid phase and mixing with air-saturated groundwater and diffuse magmatic gases leads to the formation of highly acidic sulphate-chloride waters. High degassing fluxes recorded at the surface of the dome ($2\text{-}14 \text{ kg s}^{-1}$ of SO_2 ; see Chapter 5) suggest rapid fluid rise rates within the shallow plumbing system beneath the dome, limiting cooling and interaction with groundwater. As a result, the elevated S contents of the magmatic fluid are mostly conserved until they are degassed at the surface (and through the crater lake bottom). The presence of high concentrations of both H_2S and SO_2 in these gases leads to extensive native S precipitation at the surface upon cooling with ambient air (Giggenbach, 1987).

The combination of initially elevated magmatic S contents ($> 2000 \text{ ppm}$), highly efficient exsolution of S during the evolution of basaltic to dacitic/rhyolitic magma and the limited scrubbing of fluid phase S by the hydrothermal system beneath the dome contribute to making Kawah Ijen one of the most productive active volcanic sulphur mines in the world. The high CO_2 content of the fumarole gases suggests that mafic material is present beneath the rhyolitic dome and actively degassing. The open system degassing style at Kawah Ijen currently precludes the build-up of fluid overpressures within the conduits. Studies such as this one, which offer insight into magmatic fluid-groundwater-rock interactions, are crucial for understanding the formation of hydrothermal fluids, their evolution,

and their effects on important physical parameters such as conduit permeability and rock strength.

4.8 Acknowledgments

The authors would like to thank the Kawah Ijen Park service and particularly Tom Mulja and Niken Widyastuti of East Asia Minerals for their help. The Kawah Ijen research team, namely Guillaume Mauri, Stephanie Palmer, Samantha Scher, as well numerous other volunteers, offered valuable help in the field. Local miners Pa Im and Jumanto were invaluable for their assistance in the field, especially with dome fumarole sampling. We acknowledge Tobias Fischer (University of New Mexico) for analysis of the fumarole gas samples, as well as John Donovan (University of Oregon) and Lang Shi (McGill University) for assistance with the microprobe analyses. Funding for this work was provided by an NSERC-CRD grant to A.E. Williams-Jones and G. Williams-Jones.

4.9 Figures

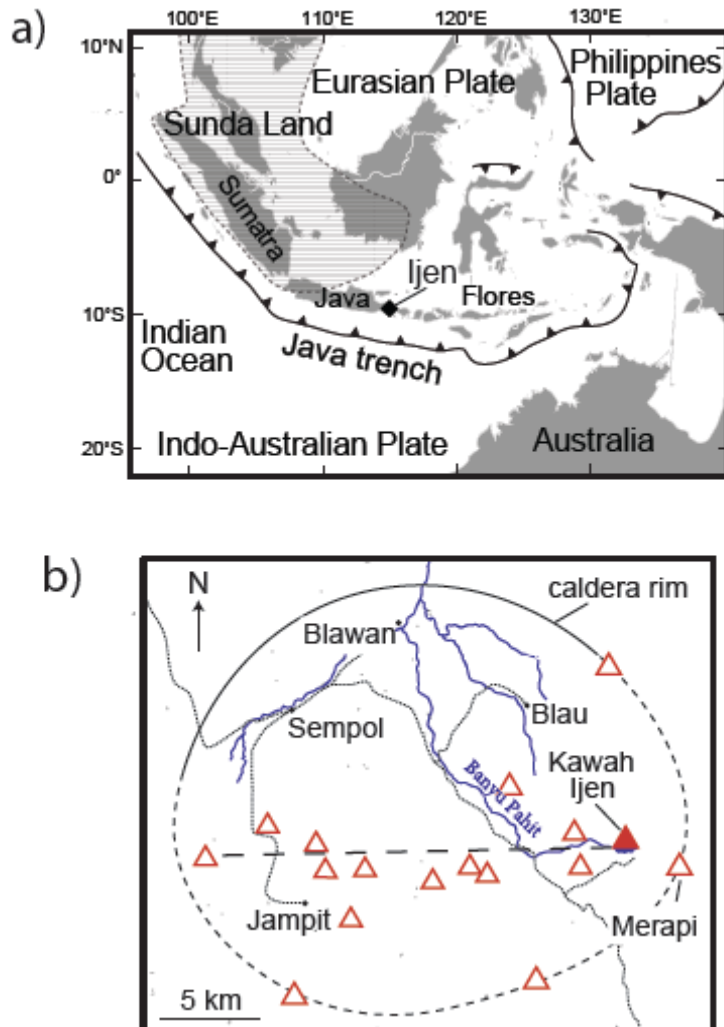


Figure 4-1 a) The location of the Ijen Caldera Complex on the island of Java, Indonesia. The thatched region labeled Sunda Land delineates the inferred extent of the continental lithosphere beneath the arc (Hamilton, 1979), b) The location of Kawah Ijen volcano within the Ijen Caldera Complex, as well as the intra-caldera lineament (dashed line) of volcanoes running E-W. Map modified from van Hinsberg et al., 2010a.

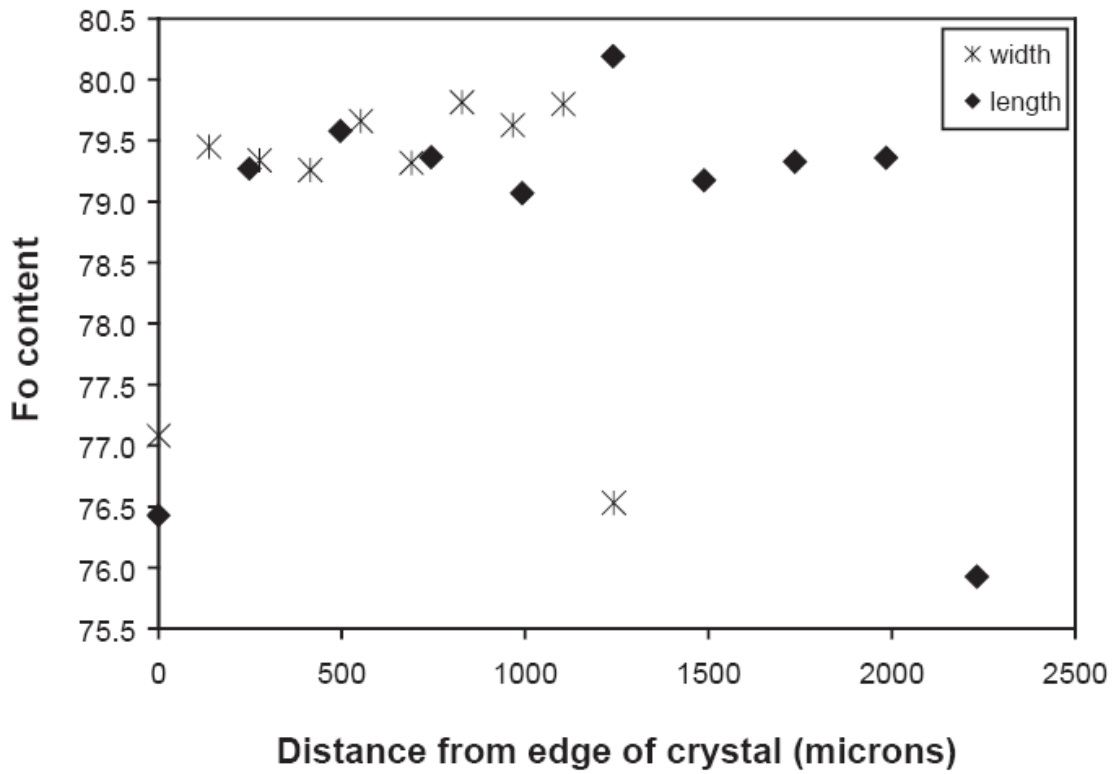


Figure 4-2 Compositional (forsterite mole fraction; $Fo = 100 \cdot (\text{moles Mg}) / (\text{moles Mg} + \text{moles Fe})$) profiles (length and width) through an olivine phenocryst showing a overall normal zoning pattern with a small reverse zoning pattern outwards of the core.

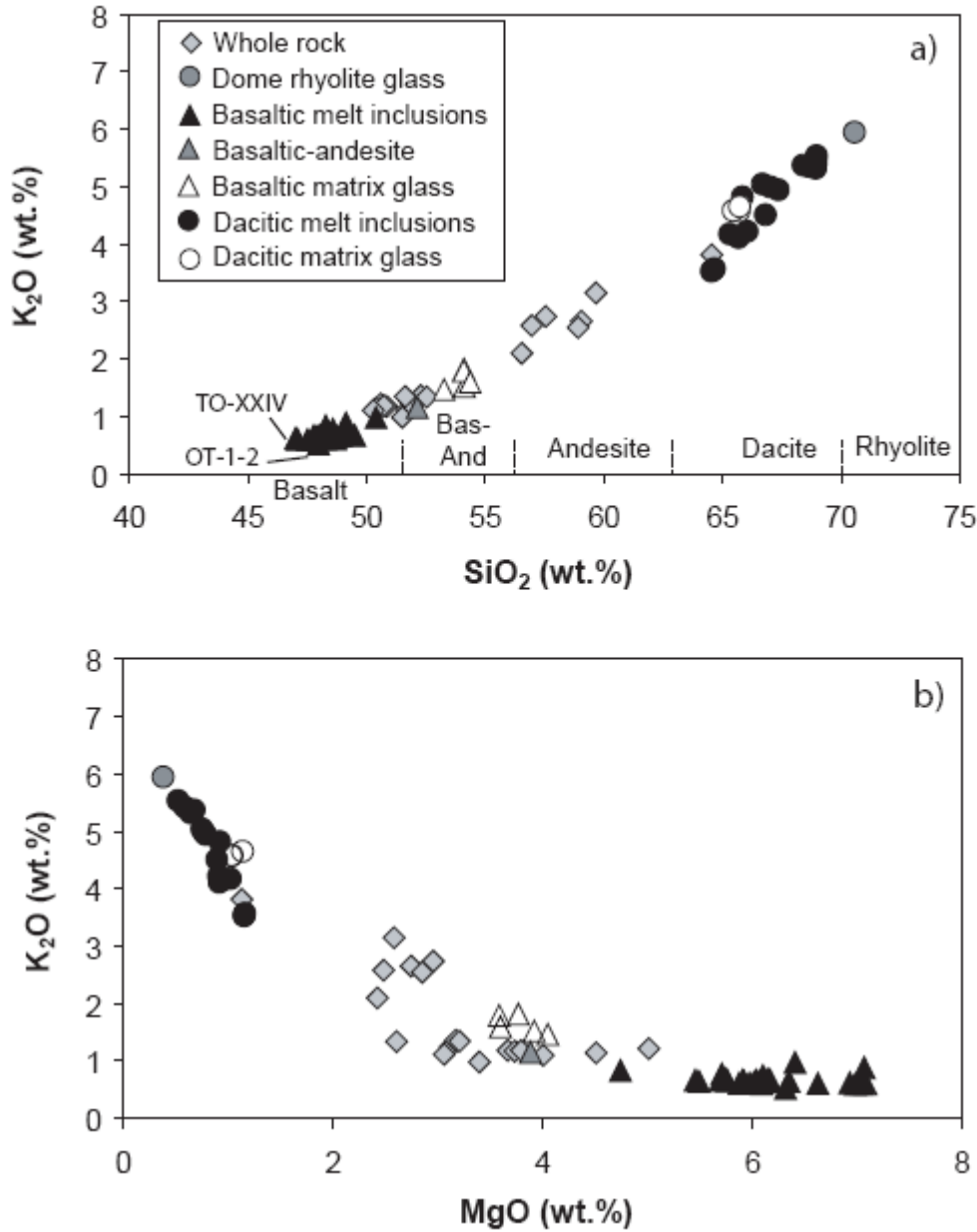


Figure 4-3 K₂O variation diagrams versus: a) SiO₂ and b) MgO (all in weight % normalized on an anhydrous basis). Dome rhyolite glass corresponds to sample KV08-702 (Table 4-1) and represents interstitial melt within the dome rock. The basaltic melt inclusions are olivine-hosted from tephra layers TO and OT (Chapter 3; Table 4-1). The basaltic-andesite corresponds to sample mountpx1 (Table 4-1) from layer TO and is clinopyroxene-hosted. Basaltic matrix glasses are from tephra layer TO (Chapter 3). Dacitic melt inclusions are orthopyroxene-hosted and the corresponding matrix glasses are from pumice bombs (Table 4-1). Samples OT-1-2 and TO-XXIV are labeled with reference to the discussion on degassing modeling (see text). Whole rock data is from van Hinsberg et al. (2010b).

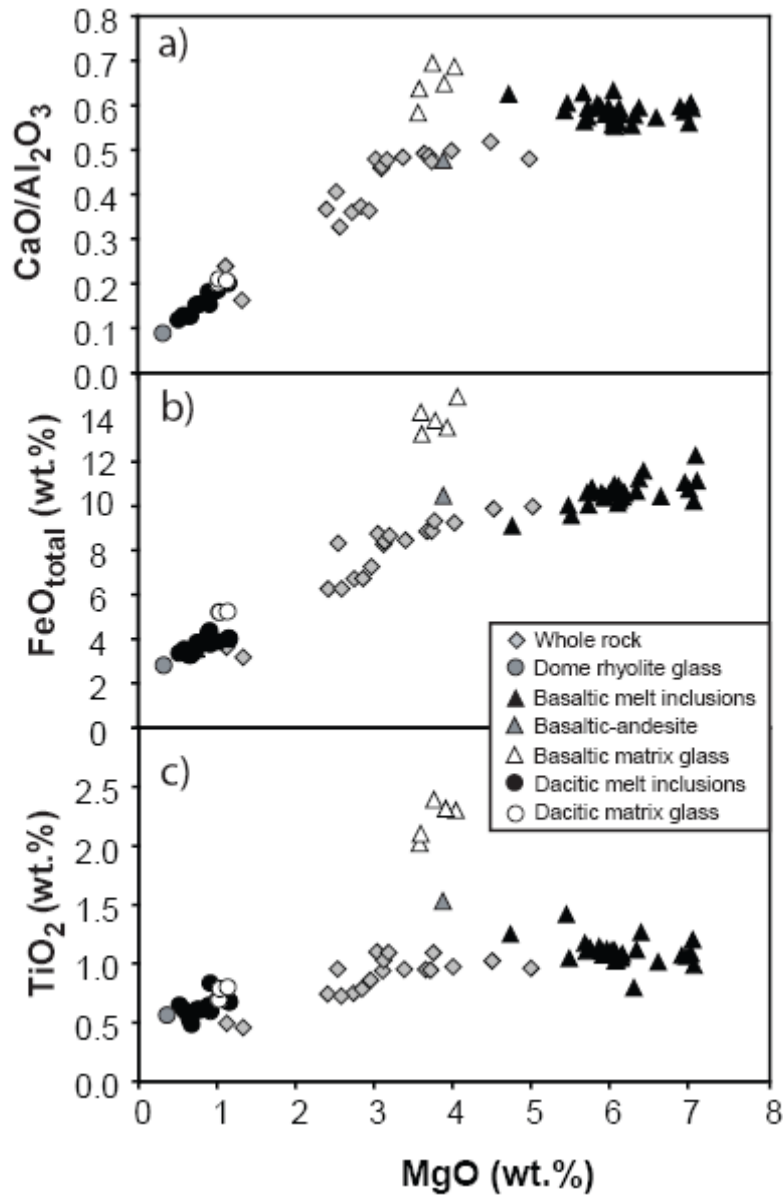


Figure 4-4 MgO variation diagrams versus: a) CaO/Al₂O₃ ratio, b) FeO_{total} (all iron is reported as FeO) and c) TiO₂ (all in weight % normalized on an anhydrous basis). Data sources as in Figure 4-3.

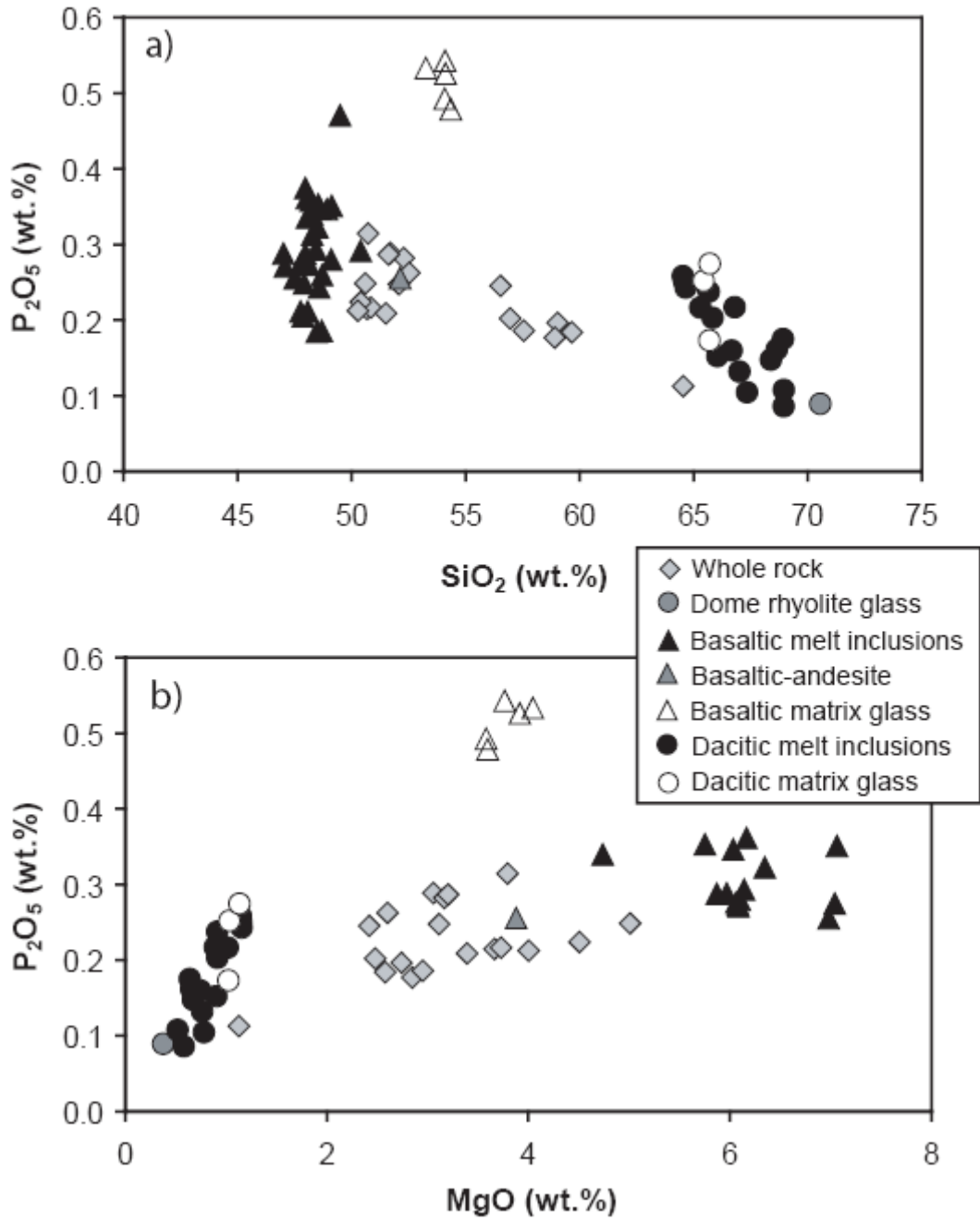


Figure 4-5 Variation in P_2O_5 content versus a) SiO_2 and b) MgO (all in weight % normalized on an anhydrous basis). Data sources as in Figure 4-3.

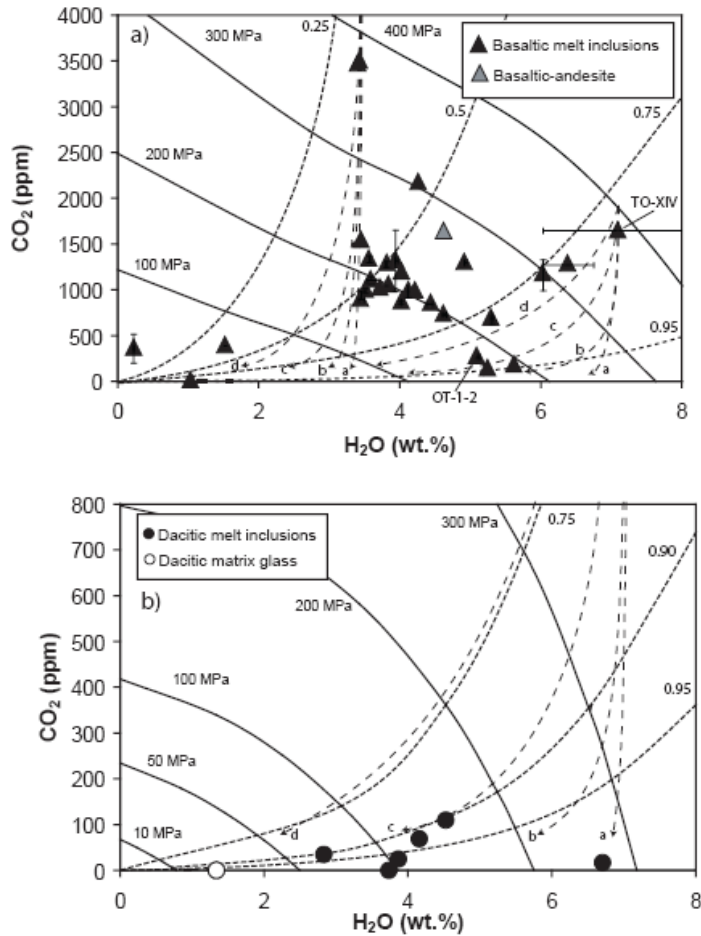


Figure 4-6 H₂O (weight %) versus CO₂ (ppm) content of: a) the mafic melt inclusions (basaltic and basaltic-andesite) and b) the dacitic melt inclusions and matrix glasses. Error bars are standard deviation for a given melt inclusion. Solid curves are isobars from Papale et al. (2006). Dashed curves in a) are calculated degassing paths (a = open system, b = closed and c = closed with 1 wt% exsolved vapour and d = closed with 5 wt% exsolved vapour) for an average Kawah Ijen basaltic melt at 1100 °C with two different starting volatile contents: a high H₂O, low CO₂ melt with 7.1 wt% H₂O and 2000 ppm CO₂, and a low H₂O, high CO₂ melt with 3.45 wt% H₂O and 4000 ppm CO₂. These starting compositions were chosen from the highest and lowest H₂O contents found in the high pressure mafic melt inclusions (P > 300 MPa) with CO₂ contents slightly in excess of those measured, based on the assumption that there has been > 50 % CO₂ degassed by 300 MPa (Wallace, 2005; Blundy et al., 2010). Dashed curves in b) are calculated degassing paths for an average Kawah Ijen dacitic melt at 1000 °C with the same starting volatile content as the high H₂O mafic melt inclusions. Closely dashed curves are isopleths of constant vapour composition (XH₂O) calculated for a) an average Kawah Ijen basalt at 1100 °C and b) an average Kawah Ijen dacite at 1000 °C. Both degassing paths and isopleths are calculated using VolatileCalc (Newman & Lowenstern, 2002). Data sources as in Figure 4-3.

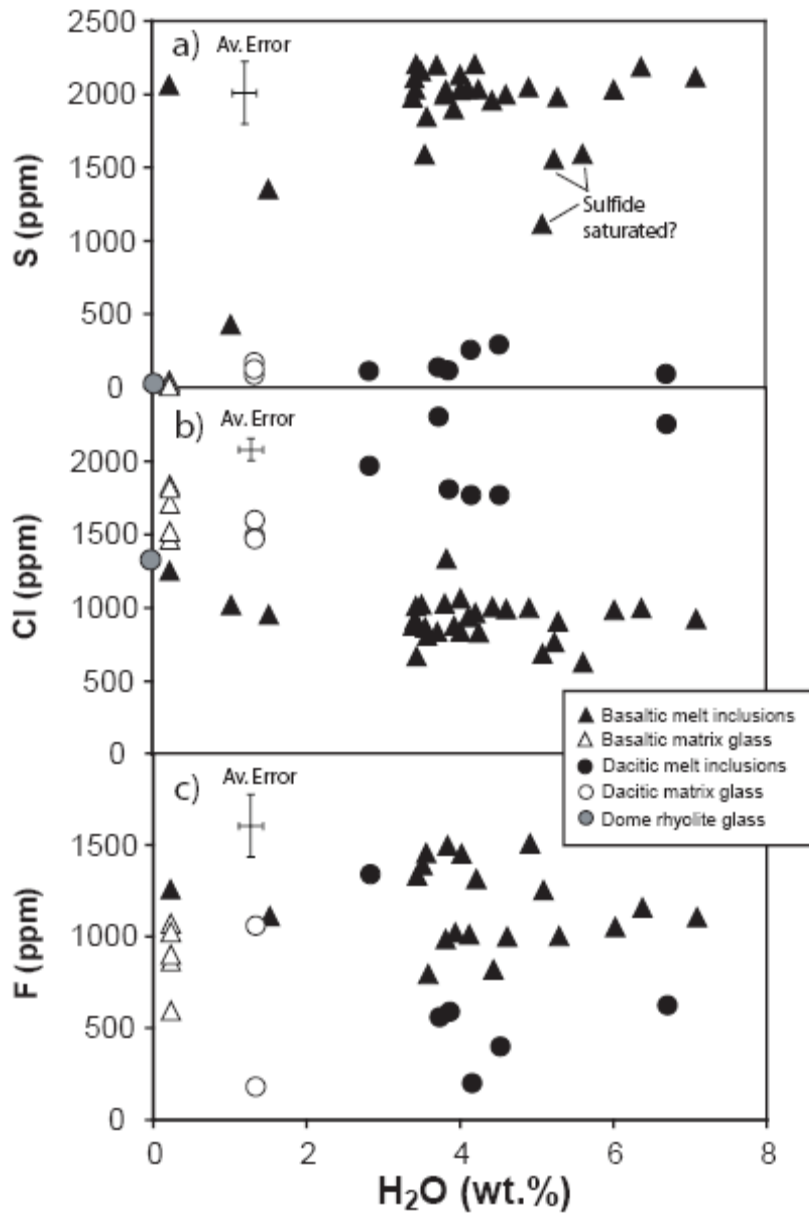


Figure 4-7 Variation of H₂O content (weight %) with a) S, b) Cl, and c) F contents (ppm) in the melt inclusions and matrix glasses. Basaltic matrix glasses and the dome rhyolite glass were not analysed for H₂O content. The basaltic matrix glasses are arbitrarily assigned the same H₂O content as the olivine-hosted glass embayment (sample TO-XVIII; Table 1) and the rhyolitic glass is assigned an H₂O content of zero (based on its analysis total of 100) for graphing purposes only. Error bars represent the average standard deviation of 2 analyses on each melt inclusion. Data sources as in Figure 4-3.

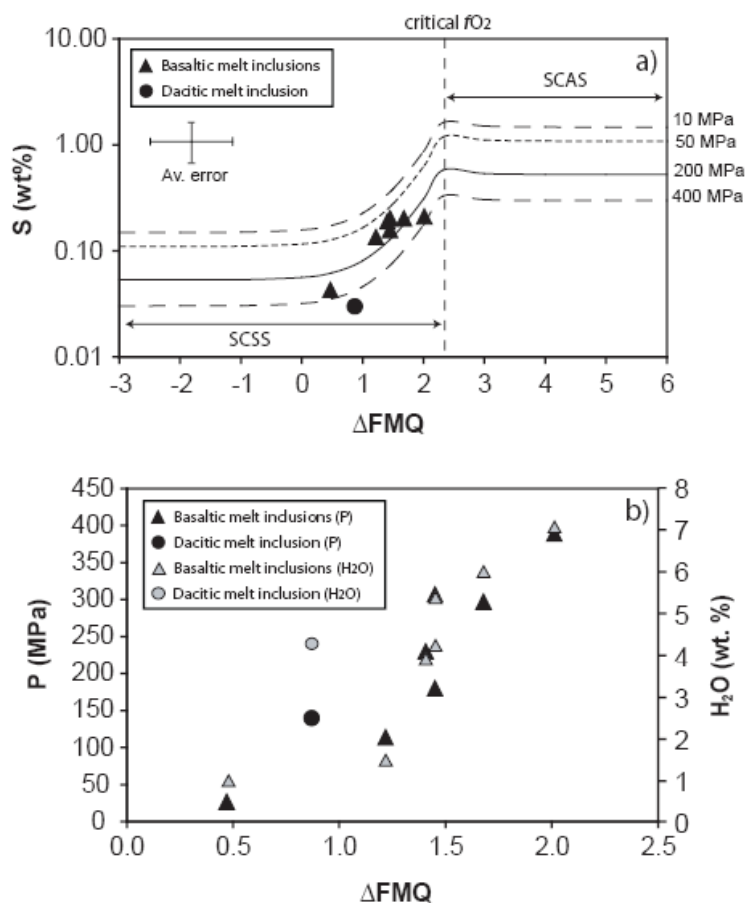


Figure 4-8 a) Sulphur contents in the basaltic and dacitic melt inclusions (log scale) versus oxygen fugacity (represented as log units relative to the Faylite-Magnetite-Quartz buffer, FMQ), calculated from the S K α peak positions and converted to oxygen fugacity at a temperature of 1100 °C and 1000 °C for the basaltic and dacitic melt inclusions, respectively (see text for details). Error bars represent the average standard error (1 sigma) on the oxygen fugacity value, propagated throughout the calculation process and including the standard deviation in measured S K α peak positions between spectrometers. Also shown are sulphur contents at sulphide-saturation (SCSS) for an average Kawah Ijen basalt at 1100 °C, calculated using the method of Liu et al. (2007), at different pressures (400, 200, 50 and 10 MPa corresponding to 7, 5, 2.2 and 0.75 wt% H₂O, respectively). Pressures are computed from Papale et al., 2006 for an average Kawah Ijen basalt in equilibrium with a vapour phase composition of XH₂O = 0.75). The transition from sulphide- to sulphate-saturation and the critical fO_2 value are defined by equations 7, 8 and 9 from Jugo (2009). Experimental data from dry basalt at 1300 °C and 1 GPa (Jugo et al., 2005a) is used to derive the absolute value of change in S solubility from sulphide- to sulphate-saturated conditions, a value which is then applied to the SCSS calculated for Kawah Ijen basalt in order to derive the sulphur content at anhydrite- (sulphate-) saturation (SCAS). This assumes that melt composition, temperature and pressure do not affect the relationship between the SCSS, the SCAS and the critical fO_2 , only the absolute values of each (Jugo, 2009). No SCSS or SCAS curves are shown for the dacitic melt inclusion but similar calculations were performed as for the basaltic case and results suggest that the dacitic melt inclusion has S contents significantly below its SCSS limit at the fO_2 , pressure and temperature conditions it exhibits. In panel b) melt inclusion H₂O content and calculated trapping pressure is plotted versus calculated fO_2 .

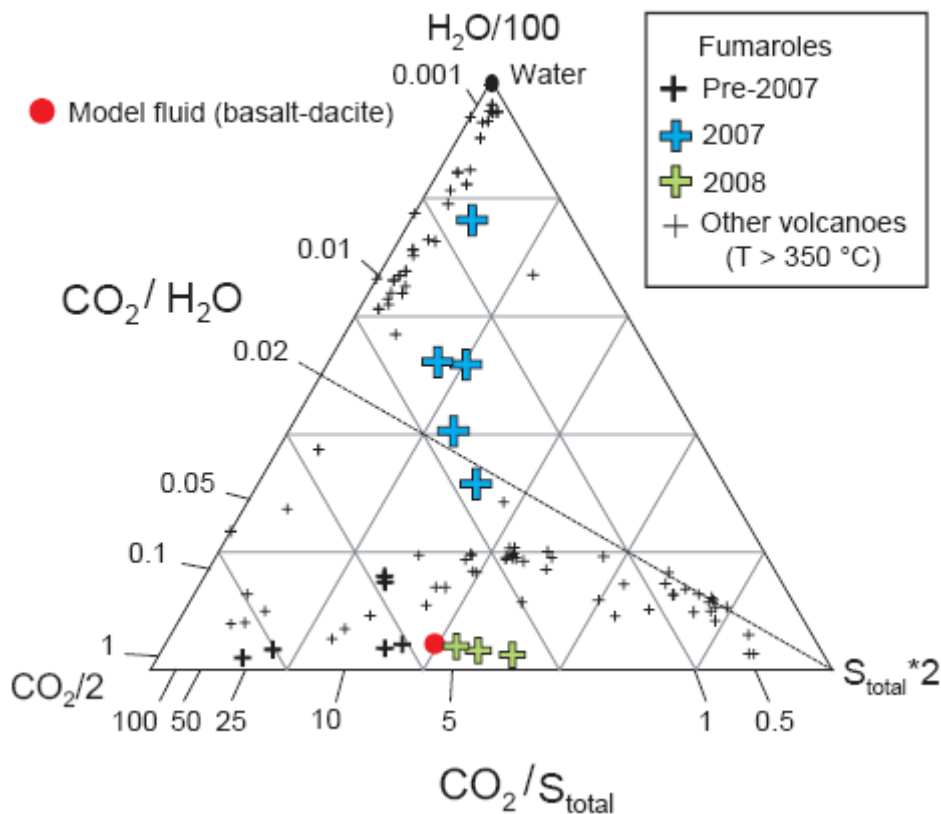


Figure 4-9 H₂O-CO₂-S_{total} ternary diagram (on a weight basis) comparing the Kawah Ijen fumarole gases (compilation from Delmelle et al., 2000 plus data from this study: Table 4-2) with high temperature (> 350 °C) fumarole gases from other arc volcanoes: Unzen volcano (Ohba et al., 2008) Usu volcano (compiled in Symonds et al., 1994) and Showa-Shinzan dome on the flank of Usu (Symonds et al., 1996) in Japan; Colima volcano (Taran et al., 2002) in Mexico; Poás (compiled in Symonds et al., 1994), Mombacho (Garofalo et al., 2007) and Momotombo (Menyailov et al., 1986) volcanoes in Central America; Kudryavy (Fischer et al., 1998) and Klyuchevskoy (Taran et al., 1991) volcanoes in Kamchatka; Augustine volcano (compiled in Symonds et al., 1994) in the Aleutians and Papandayan volcano (compiled in Mazot et al., 2008) in Indonesia. The dashed line, at a CO₂/H₂O weight ratio of 0.02, represents a lower limit of realistic magmatic vapour compositions at arc volcanoes (equivalent to a vapour XH₂O of 0.99). Vapour compositions that lie above this line are at risk of containing a meteoric water component (e.g., 2007 gas samples from Kawah Ijen and Usu and Showa-Shinzan, Symonds et al., 1996; see also Figure 4-10). Also shown is the best-fit model magmatic fluid composition derived from the melt inclusion data (see text for details; Table 4-3).

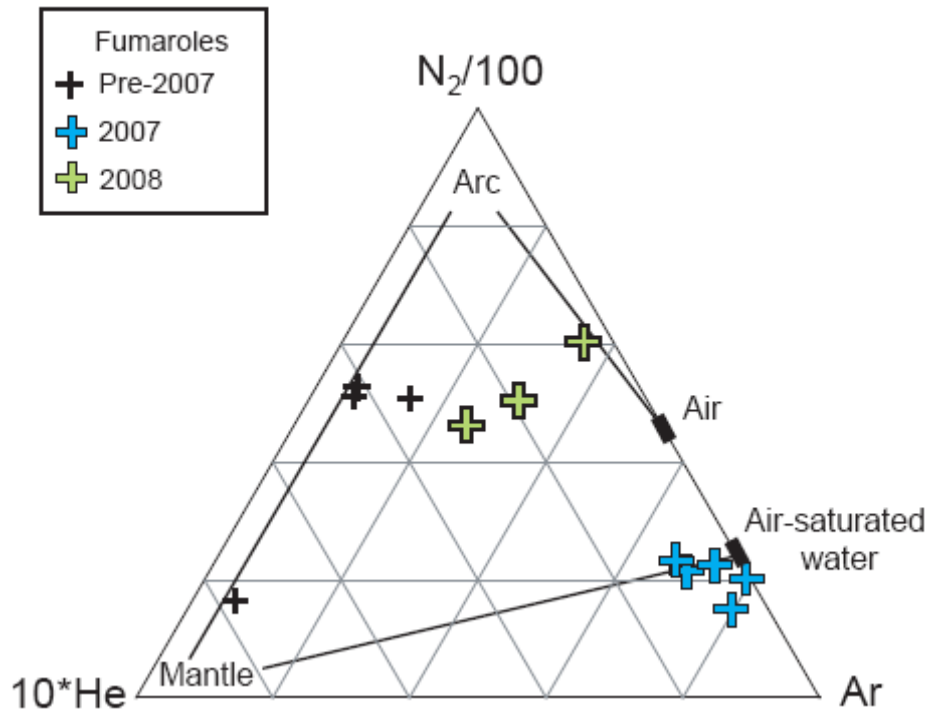


Figure 4-10 He-N₂-Ar ternary diagram (on a molar basis) comparing the Kawah Ijen fumarole gases with air and air-saturated water (e.g., Giggenbach, 1987). “Arc-type” gases are enriched in N₂ and “Mantle-type” gases are enriched in He (Giggenbach and Matsuo, 1991). Data sources are the same as in Figure 4-9.

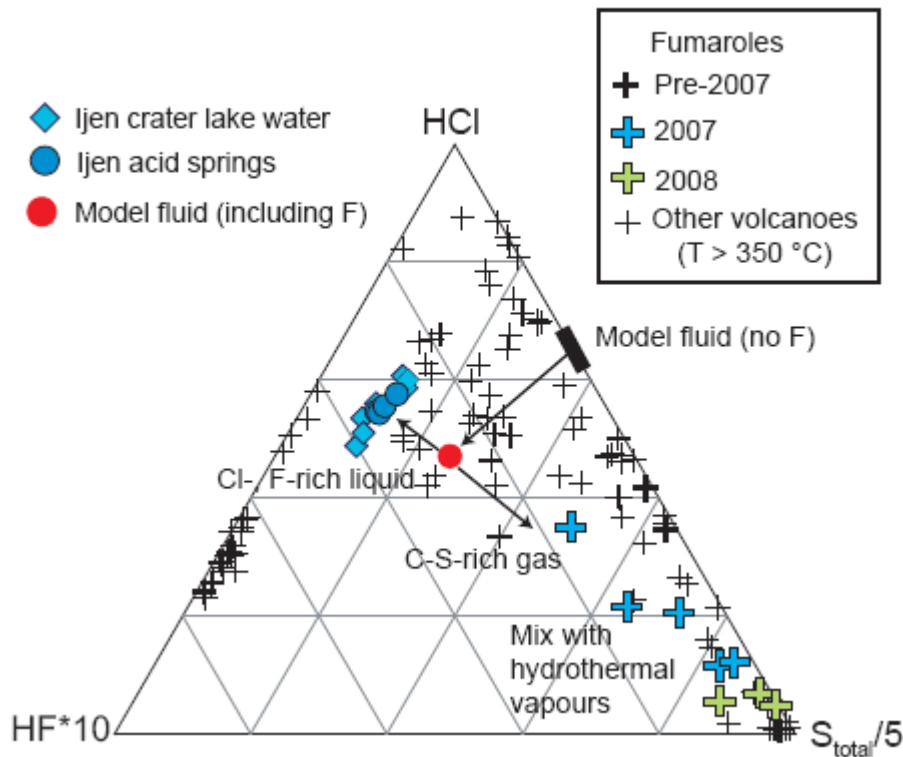


Figure 4-11 HF-HCl-S_{total} ternary diagram (on a weight basis) comparing the Kawah Ijen fumarole gases with high temperature (> 350 °C) fumarole gases from other arc volcanoes. Also shown are crater lake and acid spring waters from Kawah Ijen (Delmelle et al., 2000; Palmer, 2009) and the best-fit model magmatic fluid composition (S-Cl only) derived from the melt inclusion data (see text for details; Table 4-3). The original magmatic fluid (including F) is inferred from the intersection of the linear series relating the acidic waters and the fumarole gases with the line relating the model fluid composition and the F apex. Data sources are the same as in Figure 4-9.

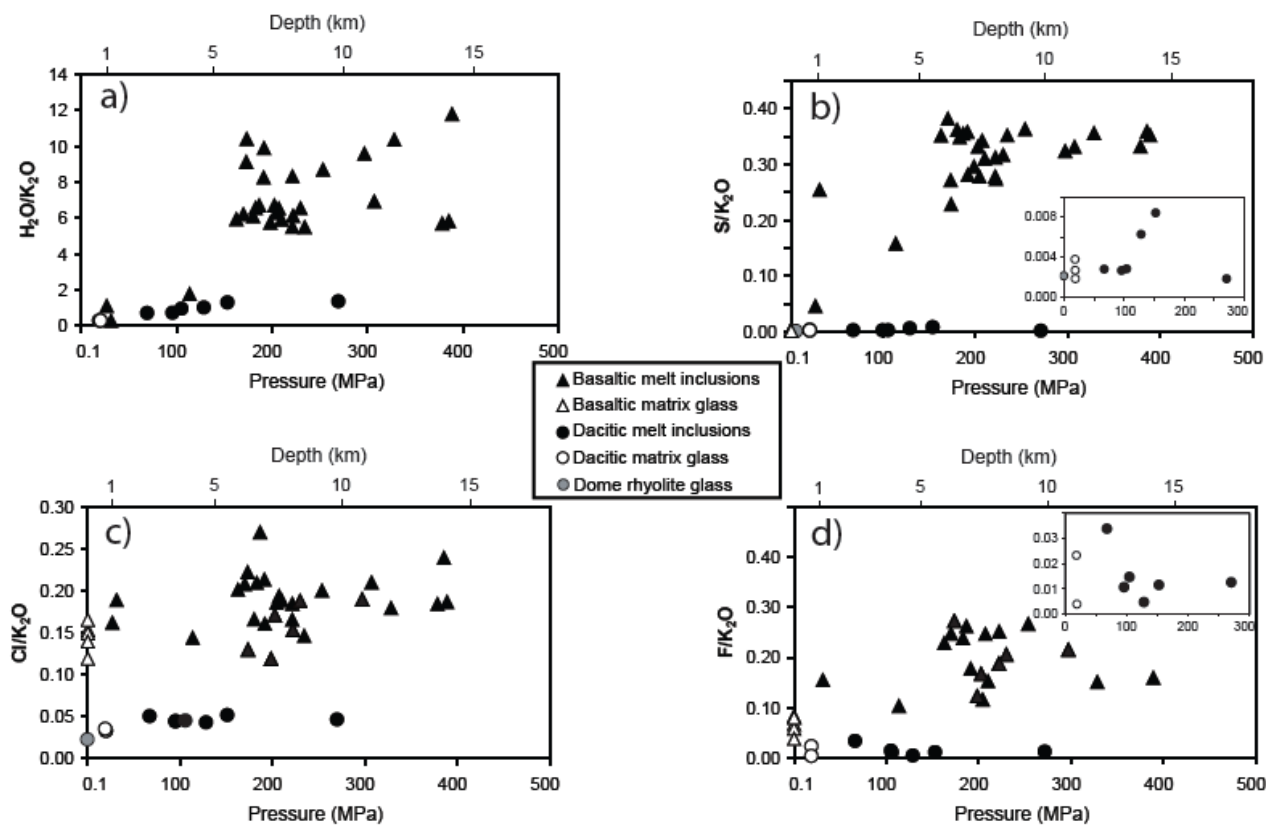


Figure 4-12 Variation in the ratio of a) H_2O , b) S, c) Cl and d) F over K_2O contents as a function of melt inclusion trapping pressure and depth. Basaltic matrix glass and dome rhyolite glass samples have not been analysed for H_2O and CO_2 , therefore, an arbitrary pressure of 0.1 MPa has been assigned to them for graphing purposes only. Insets in b) and d) show a zoom-in of the dacitic and rhyolitic samples. Data sources are the same as in Figure 4-3.

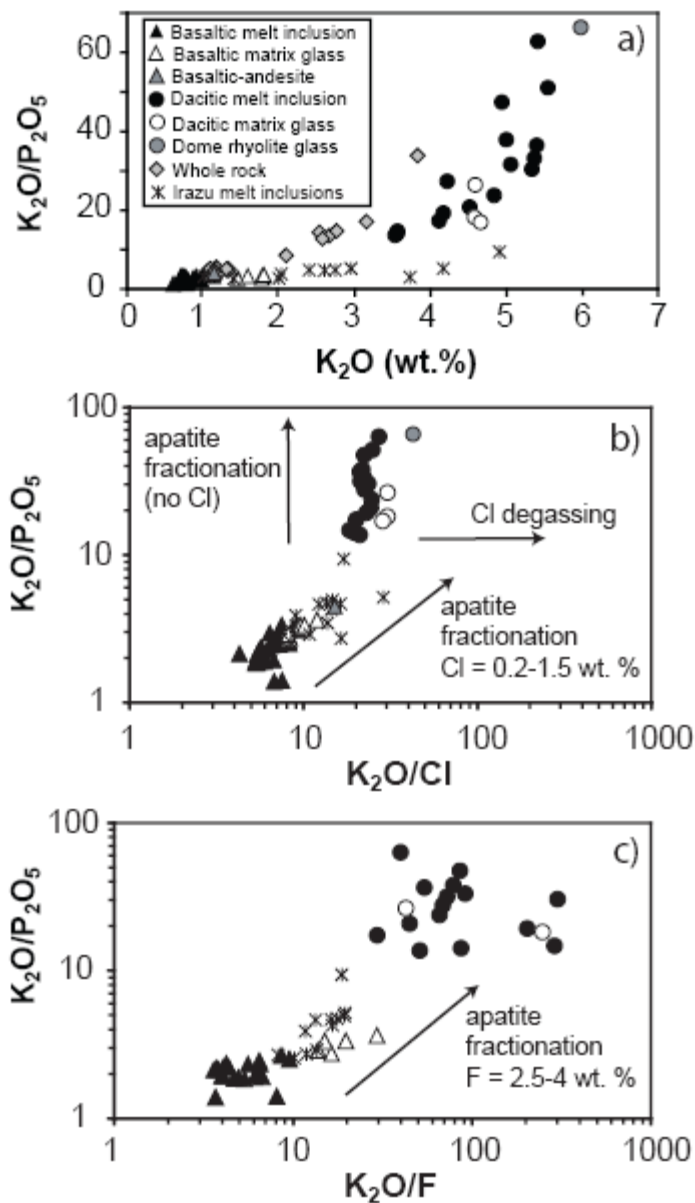


Figure 4-13 Variation of the K_2O/P_2O_5 ratio with a) K_2O content (wt%), b) K_2O/Cl ratio and c) K_2O/F ratio. Data sources are the same as in Figure 4-3 with the addition of melt inclusions from Irazú volcano, Costa Rica (Benjamin et al., 2007; Sadofsky et al., 2008) shown for comparison. Irazú has erupted lavas and pyroclastic material containing apatite phenocrysts. Combined with apatite compositions from mafic magmas near Colima volcano, Mexico (0.18 wt% Cl, 2.86-3.02 wt% F; Luhr and Carmichael, 1981), the Irazú apatite compositions (0.54-1.5 wt% Cl, 2.5-4 wt% F; Boyce and Hervig, 2009) define the P_2O_5/Cl and P_2O_5/F ratios of a liquid fractionating apatite.

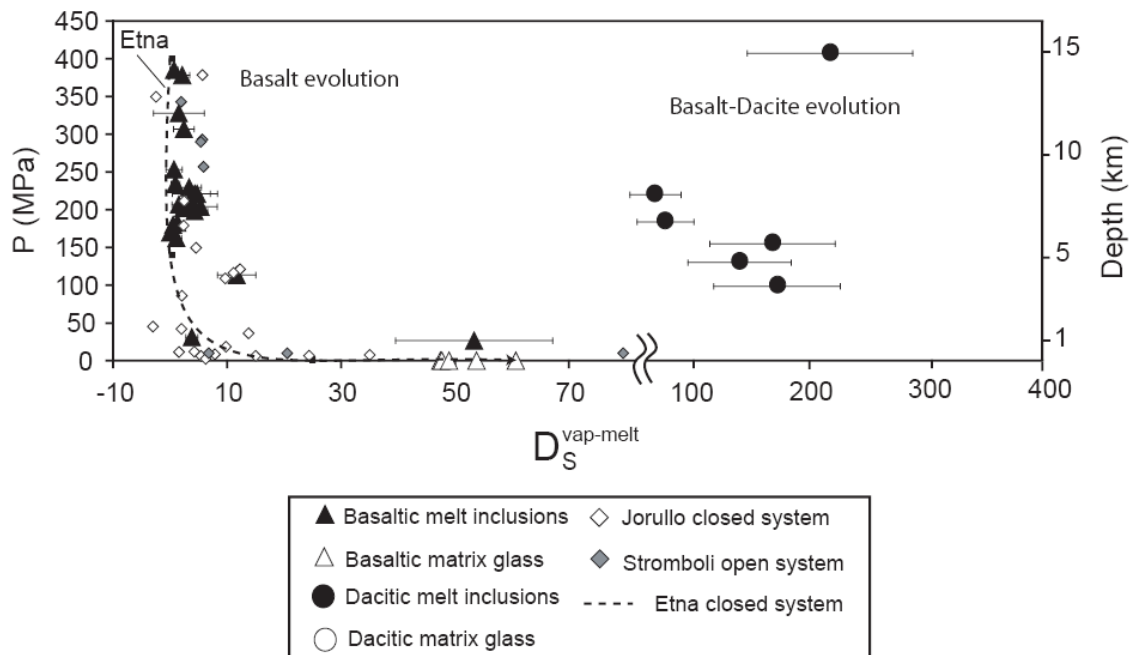


Figure 4-14 Pressure (and depth) versus modeled $D_S^{\text{vap-melt}}$ values for S within the Kawah Ijen basaltic magma and for the evolution of basaltic to dacitic compositions (see text for details of the modeling procedure; Table 4-3). Model values are for vapour fluxing conditions (average between 1 and 5 wt% vapour) and open system degassing for the melt inclusions and basaltic matrix glasses, respectively. Melt inclusion error bars represent the standard deviation between the model results for 1 and 5 wt% vapour fluxing. Shown for comparison are S $D_S^{\text{vap-melt}}$ values for the basaltic melt inclusions of Jorullo volcano, Mexico, under closed system degassing constraints (Johnson et al., 2010) and Stromboli volcano, Italy, under open system degassing constraints (Scaillet and Pichavant, 2005). The dashed curve represents the best-fit through $D_S^{\text{vap-melt}}$ values obtained for Etna volcano, Italy (Spilliaert et al., 2006), under closed system degassing constraints.

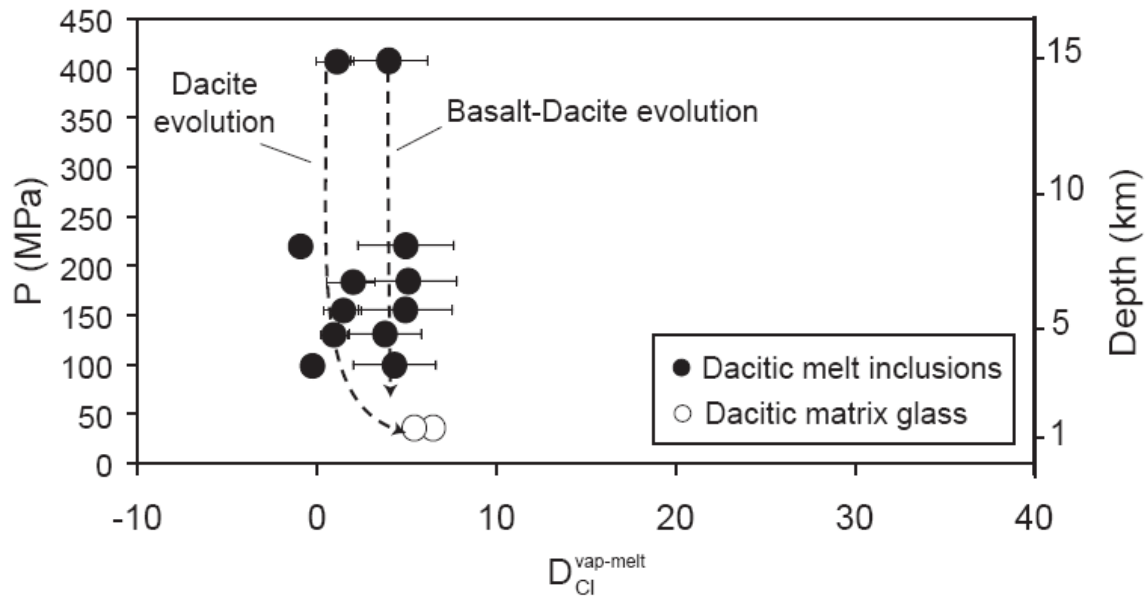


Figure 4-15 Pressure (and depth) versus modeled $D_{Cl}^{vap-melt}$ values for Cl within the dacitic magma and for a system where basaltic magma is evolving to dacitic compositions (see text for details of the modeling procedure; Table 4-3). Model values are for vapour fluxing conditions (average between 1 and 5 wt% vapour) and open system degassing for the melt inclusions and dacitic matrix glasses, respectively. Melt inclusion error bars represent the standard deviation between the model results for 1 and 5 wt% vapour fluxing. Solid curves highlight the trend within the data.

4.10 Tables

Table 4-1 Kawah Ijen melt inclusion and matrix glass compositions (wt%)^a

	ijenbas9	ijenbas3	ijenbas11	ijenbas5	ijenbas12x	ijenbas12ya	ijenbas1	ijenbas8	ijenbas7
Host phase ^b	olivine	olivine	olivine	olivine	olivine	olivine	olivine	olivine	olivine
SiO ₂	45.4	45.5	45.3	48.2	45.0	45.6	45.7	45.4	46.1
TiO ₂	1.02	1.02	0.97	1.21	1.00	0.92	1.04	1.08	0.99
Al ₂ O ₃	18.4	18.3	17.6	15.5	16.8	16.8	18.4	18.5	18.5
FeO ^T	9.8	10.1	10.0	11.1	10.3	10.4	9.4	10.3	9.1
MnO	0.19	0.19	0.16	0.15	0.18	0.24	0.16	0.16	0.17
MgO	5.6	5.7	5.7	6.1	6.4	6.6	5.4	5.5	5.2
CaO	10.9	10.9	11.1	9.2	10.1	10.0	10.4	11.0	11.2
Na ₂ O	2.59	2.45	2.57	3.00	2.33	2.31	2.64	2.43	2.59
K ₂ O	0.61	0.60	0.59	0.93	0.57	0.57	0.73	0.63	0.61
P ₂ O ₅	0.19	0.24	0.20	0.28	0.17	0.17	0.23	0.20	0.25
S	0.203	0.198	0.211	0.043	0.156	0.159	0.203	0.220	0.220
Cl	0.083	0.088	0.092	0.102	0.077	0.063	0.084	0.067	0.084
F	b.d.l.	b.d.l.	b.d.l.	b.d.l.	b.d.l.	b.d.l.	b.d.l.	0.056	0.050
H ₂ O	4.26	3.40	3.43	1.03	5.24	5.62	4.02	3.45	3.72
CO ₂ (ppm)	2184	3478	3509	19	151	189	1204	1552	1030
Host Fo ^c	79.9	79.9	80.1	80.1	80.9	80.9	80.0	78.6	79.6
P (MPa) ^d	307	378	385	27	173	192	221	234	180

^a Details of the electron microprobe analytical conditions can be found in van Hinsberg et al. (2010a) and Berlo et al. (in prep.)

^b Only olivine-hosted melt inclusions have been corrected for post-entrapment modifications.

^c Forsterite content of the olivine host located ~ 50 μm from melt inclusion.

T (°C) ^e	1093	1108	1107	1160	1097	1095	1094	1103	1092
X olivine add. ^f	0.80	2.20	3.10	5.90	2.40	3.60	0.10	3.00	5.10
K _D ^g	0.32	0.32	0.32	0.3	0.33	0.33	0.32	0.32	0.32
fO ₂ (ΔFMQ) ^h	1.45	-	-	0.47	1.45	1.45	-	-	-

^d Minimum pressure of melt inclusion entrapment based on the partial pressures of H₂O and CO₂, calculated from Papale et al. (2006).

^e Temperature of melt inclusion entrapment calculated using eq. 6a from Sugawara (2000).

^f Weight % olivine added back into the composition of the melt inclusions to attain equilibrium between the two phases.

^g K_D values are calculated using the method of Toplis (2005) and the pressure and temperature calculated for each melt inclusion.

^h Oxygen fugacity values are calculated from the S Kα peak position data and are given as log units relative to the faylite-magnetite-quartz (FMQ) buffer at a temperature of 1100 °C for the basalt and 1000 °C for the dacite. Variations in temperature of ± 75 °C have no effect on the calculated fO₂.

	gg1	gg2	gg3	gg4	gg5	mountpx1	ijenbas2	plmi1	rhyo4	rhyo4b	rhyo4	rhyo3
Host phase	glass	glass	glass	glass	glass	cpx	cpx	plag	opx	opx	opx	opx
SiO ₂	51.6	52.9	52.5	52.8	52.4	51.2	-	66.0	66.2	65.4	65.8	66.4
TiO ₂	2.23	2.34	2.24	1.97	2.03	1.53	-	0.62	0.52	0.47	0.49	0.60
Al ₂ O ₃	12.2	12.3	12.8	13.1	13.0	17.7	-	14.3	14.7	15.0	14.8	15.8
FeO ^T	14.5	13.6	13.1	13.9	12.8	10.2	-	3.2	3.2	3.1	3.1	3.7
MnO	0.38	0.34	0.34	0.32	0.28	0.17	-	0.13	0.08	0.06	0.07	0.09
MgO	3.9	3.7	3.8	3.5	3.5	3.8	-	0.5	0.6	0.6	0.6	0.8
CaO	8.4	8.6	8.3	7.7	8.3	8.4	-	1.7	1.9	1.9	1.9	2.4
Na ₂ O	1.83	1.78	1.84	2.15	2.19	3.84	-	3.84	3.66	3.73	3.70	3.88
K ₂ O	1.42	1.78	1.47	1.75	1.54	1.13	-	5.30	5.11	5.14	5.13	4.88
P ₂ O ₅	0.52	0.53	0.51	0.48	0.46	0.25	-	0.10	0.17	0.14	0.15	0.10
S	0.004	0.003	0.004	0.002	0.001	0.027	-	0.010	0.014	0.014	0.014	0.012
Cl	0.171	0.184	0.182	0.147	0.152	0.076	-	0.213	0.217	0.244	0.231	0.219
F	0.087	0.090	0.107	0.060	0.103	b.d.l.	-	b.d.l.	0.017	0.095	0.056	0.057
H ₂ O	-	-	-	-	-	-	4.63	-	-	-	3.73	-
CO ₂ (ppm)	-	-	-	-	-	-	1612	-	-	-	b.d.l.	-
Host Fo	-	-	-	-	-	-	-	-	-	-	-	-
P (MPa)	-	-	-	-	-	-	329*	-	-	-	96	-
T (°C)	-	-	-	-	-	-	-	-	-	-	1020	-
X olivine add.	-	-	-	-	-	-	-	-	-	-	-	-
K _D	-	-	-	-	-	-	-	-	-	-	-	-
fO ₂ (ΔFMQ)	-	-	-	-	-	-	-	-	-	-	-	-

* Saturation pressure is calculated using the composition and temperature of sample mountpx1.

	rhyo3b	rhyo3	rhyo3crim	rhyo2a	rhyo2ab	rhyo2y	rhyo2b	rhyo2c	rhyo1	rhyo5	rhyo100	gm1	gm2	gm3	KV08-702
Host phase	opx	opx	opx	opx	opx	opx	opx	opx	opx	opx	opx	glass	glass	glass	glass
SiO ₂	65.1	65.8	65.8	62.8	63.5	63.2	63.6	64.6	63.1	63.3	65.6	64.9	63.7	64.4	71.2
TiO ₂	0.60	0.60	0.58	0.66	0.67	0.66	0.69	0.59	0.80	0.62	0.63	0.69	0.77	0.79	0.58
Al ₂ O ₃	15.8	15.8	14.3	16.9	17.1	17.0	16.4	16.2	15.9	15.7	15.7	15.3	15.1	14.9	14.4
FeO ^T	3.8	3.7	3.4	3.9	4.0	3.9	3.8	3.9	3.6	4.2	4.2	5.2	5.1	5.1	2.8
MnO	0.08	0.08	0.09	0.09	0.11	0.10	0.13	0.15	0.13	0.13	0.05	0.11	0.13	0.10	0.06
MgO	0.7	0.7	0.6	1.1	1.1	1.1	1.0	0.9	0.9	0.9	0.9	1.0	1.0	1.1	0.4
CaO	2.4	2.4	1.8	3.4	3.5	3.4	3.0	2.5	2.8	2.9	2.5	3.1	3.2	3.1	1.3
Na ₂ O	4.06	3.97	3.69	4.60	4.74	4.67	4.48	4.45	4.65	3.99	4.03	3.89	3.65	3.67	3.80
K ₂ O	4.93	4.91	5.18	3.47	3.47	3.47	4.07	4.73	3.95	4.05	4.43	4.52	4.46	4.56	6.00
P ₂ O ₅	0.16	0.13	0.08	0.24	0.25	0.25	0.21	0.20	0.23	0.15	0.21	0.17	0.25	0.27	0.09
S	0.006	0.009	0.009	0.033	0.025	0.029	0.026	0.025	0.011	0.012	0.014	0.017	0.008	0.012	0.013
Cl	0.232	0.226	0.191	0.189	0.165	0.177	0.177	0.192	0.197	0.181	0.182	0.149	0.147	0.160	0.139
F	0.068	0.063	0.130	0.012	0.068	0.040	0.020	0.072	0.134	0.059	0.099	0.106	0.018	b.d.l.	-
H ₂ O	-	6.71	-	-	-	4.53	4.16	-	2.83	3.87	-	1.34	1.34	1.34	-
CO ₂	-	17	-	-	-	110	69	-	35	25	-	b.d.l.	b.d.l.	b.d.l.	-
Host Fo	-	-	-	-	-	-	-	-	-	-	-	-	-	-	-
P (MPa)	-	270	-	-	-	153	128	-	67	104	-	19	19	19	-
T (°C)	-	989	-	-	-	1019	1022	-	1037	1022	-	-	-	-	-
X olivine add.	-	-	-	-	-	-	-	-	-	-	-	-	-	-	-
K _D	-	-	-	-	-	-	-	-	-	-	-	-	-	-	-
fO ₂ (ΔFMQ)	-	-	-	-	-	0.87	-	-	-	-	-	-	-	-	-

Table 4-2 Fumarole gas compositions and sampling temperatures (2007 & 2008) in molar and mass units

Sample	Date	Temp. (°C)	H ₂ O mmol/mol	CO ₂	SO ₂	H ₂ S	HCl	HF	H ₂	Ar	O ₂	N ₂	CH ₄	CO
401	2007	>452	997	1.8	0.38	b.d.l.	0.022	0.003	0.0002	0.032	<0.001	0.81	< 0.00001	< 0.00001
404	2007	>370	994	5.0	1.02	0.15	0.145	0.012	0.0008	0.006	<0.001	0.12	< 0.00001	< 0.00001
412	2007	371	986	10.5	3.13	b.d.l.	0.077	0.007	0.0016	0.003	0.002	0.10	< 0.00001	< 0.00001
423	2007	461	993	5.5	0.84	0.11	0.047	0.003	0.0009	0.004	<0.001	0.12	< 0.00001	< 0.00001
424	2007	461	990	7.9	1.86	b.d.l.	0.047	0.002	0.0012	0.002	<0.001	0.08	< 0.00001	< 0.00001
3	2008	489	881	87.7	8.37	15.89	0.272	0.075	0.0118	0.038	0.001	6.43	0.00009	0.00001
10	2008	450	852	105.0	12.15	28.70	0.539	0.024	0.0111	0.007	<0.001	1.15	0.00001	0.00001
14	2008	450	866	100.7	8.09	23.92	0.288	0.004	0.0137	0.005	0.001	0.88	0.00014	0.00016
			wt%											
401	"	"	99	0.4	0.12	0.00	0.004	0.000	<0.00001	0.006	<0.0001	0.108	<0.00001	<0.00001
404	"	"	98	1.1	0.31	0.02	0.025	0.001	<0.00001	0.001	<0.0001	0.016	<0.00001	<0.00001
412	"	"	96	2.2	0.95	0.00	0.013	0.001	<0.00001	0.001	0.00034	0.014	<0.00001	<0.00001
423	"	"	98	1.2	0.26	0.02	0.008	0.000	<0.00001	0.001	<0.0001	0.016	<0.00001	<0.00001
424	"	"	97	1.7	0.57	0.00	0.008	0.000	<0.00001	0.000	<0.0001	0.011	<0.00001	<0.00001
3	"	"	76	18.4	2.55	2.57	0.047	0.007	<0.00001	0.007	0.00015	0.858	<0.00001	<0.00001
10	"	"	70	21.2	3.57	4.48	0.090	0.002	<0.00001	0.001	<0.0001	0.147	<0.00001	<0.00001
14	"	"	73	20.7	2.42	3.80	0.049	0.000	<0.00001	0.001	0.00018	0.115	<0.00001	<0.00001

Table 4-3 Model magmatic fluid compositions

P (MPa)	Model $D_S^{\text{vap-melt a}}$	Model $D_{Cl}^{\text{vap-melt b}}$	H ₂ O	CO ₂	SO _{2 (total) c}	HCl	H ₂ O	CO ₂	SO _{2 (total)}	HCl
			Mole fraction				wt%			
Basalt										
400	1		0.25-0.90	0.10-0.75	0.003	-	12-78	21-88	0.3-0.5	-
300	2		0.25-0.90	0.10-0.75	0.003	-	12-78	21-87	0.4-0.8	-
200	3		0.25-0.90	0.10-0.75	0.004	-	12-77	21-87	0.7-1.3	-
100	8		0.25-0.90	0.10-0.75	0.004	-	12-76	21-86	1.7-3.1	-
50	20		0.25-0.90	0.10-0.75	0.005	-	11-72	20-84	4.3-7.5	-
10	157		0.25-0.90	0.10-0.75	0.007	-	12-75	20-86	2.3-4.1	-
			Basalt-Dacite							
400	150	5	0.49-0.93	0.05-0.49	0.017	0.005	28-83	11-68	3.5-5.4	0.6-1.0
300	150	5	0.49-0.93	0.05-0.49	0.017	0.005	28-83	11-68	3.5-5.4	0.6-1.0
200	150	5	0.49-0.93	0.05-0.49	0.017	0.005	28-83	11-68	3.5-5.4	0.6-1.0
100	150	5	0.49-0.93	0.05-0.49	0.017	0.005	28-83	11-68	3.5-5.4	0.6-1.0
50	150	5	0.49-0.93	0.05-0.49	0.017	0.004	28-83	11-68	3.5-5.4	0.5-0.7
10	150	5	0.49-0.93	0.05-0.49	0.017	0.004	28-83	11-68	3.5-5.4	0.5-0.7
			Dacite							
400	20	1	0.90-0.99	0.01-0.10	0.002	0.001	78-97	2-21	0.7-0.8	0.2
300	20	1	0.90-0.99	0.01-0.10	0.002	0.001	78-97	2-21	0.7-0.8	0.2
200	20	1	0.90-0.99	0.01-0.10	0.002	0.001	78-97	2-21	0.7-0.8	0.2
100	20	1	0.90-0.99	0.01-0.10	0.002	0.001	78-97	2-21	0.7-0.8	0.2
50	20	4	0.90-0.99	0.01-0.10	0.002	0.003	78-96	2-21	0.7-0.8	0.5-0.6
10	20	4	0.90-0.99	0.01-0.10	0.002	0.003	78-96	2-21	0.7-0.8	0.5-0.6

^a Values are fitted using a best-fit power law equation regressed through the data (Fig. 4-14) for the basalt. Average values independent of pressure are reported for the basalt-dacite and dacite scenarios.

^b Average values, independent of pressure.

^c Total S contents are reported as SO₂.

4.11 References

- Aiuppa, A., Federico, C., Giudice, G., Gurrieri, S., Paonita, A., Valenza, M., 2004. Plume chemistry provides insights into mechanisms of sulphur and halogen degassing in basaltic volcanoes. *Earth Planet. Sci. Lett.* 222 (2), 469-483.
- Aiuppa, A., Moretti, R., Federico, C., Giudice, G., Gurrieri, S., Liuzzo, M., Papale, P., Shinohara, H., Valenza, M., 2007. Forecasting Etna eruptions by real-time observation of volcanic gas composition. *Geology* 35 (12), 1115-1118.
- Aiuppa, A., Bertagnini, A., Métrich, N., Moretti, R., Di Muro, A., Liuzzo, M., Tamburello, G., 2010. A model of degassing for Stromboli volcano. *Earth Planet. Sci. Lett.* 295 (1-2), 195-204.
- Behrens, H., Tamic, N., Holtz, F., 2004. Determination of the molar absorption coefficient for the infrared absorption band of CO₂ in rhyolitic glasses. *Am. Mineral.* 89 (2-3), 301-306.
- Benjamin, E. R., Plank, T., Wade, J. A., Kelley, K. A., Hauri, E. H., Alvarado, G. E., 2007. High water contents in basaltic magmas from Irazú Volcano, Costa Rica. *J. Volcanol. Geotherm. Res.* 168 (1-4), 68-92.
- Blundy, J., Cashman, K., 2005. Rapid decompression-driven crystallization recorded by melt inclusions from Mount St. Helens volcano. *Geology* 33 (10), 793-796.
- Blundy, J., Cashman, K. V., Rust, A., Witham, F., 2010. A case for CO₂-rich arc magmas. *Earth Planet. Sci. Lett.* 290 (3-4), 289-301.
- Botcharnikov, R. E., Behrens, H., Holtz, F., Koepke, J., Sato, H., 2004. Sulfur and chlorine solubility in Mt. Unzen rhyodacitic melt at 850 °C and 200 MPa. *Chem. Geol.* 213 (1-3), 207-225.
- Boyce, J. W., Hervig, R. L., 2009. Apatite as a monitor of late-stage magmatic processes at Volcán Irazú, Costa Rica. *Contrib. Mineral. Petrol.* 157 (2), 135-145.
- Caracausi, A., Ditta, M., Italiano, F., Longo, M., Nuccio, P. M., Paonita, A., Rizzo, A., 2005. Changes in fluid geochemistry and physico-chemical conditions of geothermal systems caused by magmatic input: The recent abrupt outgassing off the island of Panarea (Aeolian Islands, Italy). *Geochim. Cosmochim. Acta* 69 (12), 3045-3059.
- Carroll, M. K., Rutherford, M. J., 1988. Sulfur speciation in hydrous experimental glasses of varying oxidation state--results from measured wavelength shifts of sulphur X-rays. *Am. Mineral.* 73 (7), 845-849.

- Chouinard, A., Williams-Jones, A. E., Leonardson, R. W., Hodgson, C. J., Silva, P., Tellez, C., Vega, J., Rojas, F., 2005. Geology and genesis of the multistage high-sulfidation epithermal Pascua Au-Ag-Cu deposit, Chile and Argentina. *Econ. Geol.* 100 (3), 463-490.
- Christenson, B. W., 2000. Geochemistry of fluids associated with the 1995-1996 eruption of Mt. Ruapehu, New Zealand: signatures and processes in the magmatic-hydrothermal system. *J. Volcanol. Geotherm. Res.* 97 (1-4), 1-30.
- Delmelle, P., Bernard, A., 1994. Geochemistry, mineralogy, and chemical modeling of the acid crater lake of Kawah Ijen Volcano, Indonesia. *Geochim. Cosmochim. Acta* 58 (11), 2445-2460.
- Delmelle, P., Bernard, A., Kusakabe, M., Fischer, T. P., Takano, B., 2000. Geochemistry of the magmatic-hydrothermal system of Kawah Ijen volcano, East Java, Indonesia. *J. Volcanol. Geotherm. Res.* 97 (1-4), 31-53.
- Dixon, J. E., Pan, V., 1995. Determination of the molar absorptivity of dissolved carbonate in basaltic glass. *Am. Mineral.* 80 (11-12), 1339-1342.
- Dixon, J. E., Stolper, E. M., Holloway, J. R., 1995. An experimental study of water and carbon dioxide solubilities in mid-ocean ridge basaltic liquids. Part I: Calibration and solubility models. *J. Petrol.* 36 (6), 1607-1631.
- Edmonds, M., Oppenheimer, C., Pyle, D. M., Herd, R. A., Thompson, G., 2003. SO₂ emissions from Soufriere Hills Volcano and their relationship to conduit permeability, hydrothermal interaction and degassing regime. *J. Volcanol. Geotherm. Res.* 124 (1-2), 23-43.
- Edmonds, M., Gerlach, T. M., Herd, R. A., 2009. Halogen degassing during ascent and eruption of water-poor basaltic magma. *Chem. Geol.* 263 (1-4), 122-130.
- Edmonds, M., Aiuppa, A., Humphreys, M., Moretti, R., Giudice, G., Martin, R. S., Herd, R. A., Christopher, T., 2010. Excess volatiles supplied by mingling of mafic magma at an andesite arc volcano. *Geochem. Geophys. Geosyst.* 11 (4), Q04005.
- Faure, F., Schiano, P., 2005. Experimental investigation of equilibration conditions during forsterite growth and melt inclusion formation. *Earth Planet. Sci. Lett.* 236 (3-4), 882-898.
- Fischer, T. P., Giggenbach, W. F., Sano, Y., Williams, S. N., 1998. Fluxes and sources of volatiles discharged from Kudryavy, a subduction zone volcano, Kurile Islands. *Earth Planet. Sci. Lett.* 160 (1-2), 81-96.

- Garofalo, K., Tassi, F., Vaselli, O., Delgado-Huertas, A., Tedesco, D., Frische, M., Hansteen, T. H., Poreda, R. J., Strauch, W., 2007. Fumarolic gases at Mombacho volcano (Nicaragua): presence of magmatic gas species and implications for volcanic surveillance. *Bull. Volcanol.* 69 (7), 785-795.
- Giggenbach, W. F., 1975. A simple method for the collection and analysis of volcanic gas samples. *Bull. Volcanol.* 39 (1), 132-145.
- Giggenbach, W. F., 1987. Redox processes governing the chemistry of fumarolic gas discharges from White Island, New Zealand. *Appl. Geochem.* 2 (2), 143-161.
- Giggenbach, W. F., Goguel, R. L., 1989. Collection and analysis of geothermal and volcanic water and gas discharges. New Zealand DSIR Chemistry Division Report 2401, 81.
- Giggenbach, W. F., Matsuo, S., 1991. Evaluation of results from Second and Third IAVCEI field workshops on volcanic gases, Mt Usu, Japan, and White Island, New Zealand. *Appl. Geochem.* 6 (2), 125-141.
- Giggenbach, W. F., Garcia, P., Londoño C., A., Rodriguez V., L., Rojas G., N., Calvache V., M. L., 1990. The chemistry of fumarolic vapour and thermal-spring discharges from the Nevado del Ruiz volcanic-magmatic-hydrothermal system, Colombia. *J. Volcanol. Geotherm. Res.* 42 (1-2), 13-39.
- Handley, H. K., Macpherson, C. G., Davidson, J. P., Berlo, K., Lowry, D., 2007. Constraining fluid and sediment contributions to subduction-related magmatism in Indonesia: Ijen Volcanic Complex. *J. Petrol.* 48 (6), 1155.
- Hamilton, W. 1979. Tectonics of the Indonesian region. USGS Prof. Paper 1078 345.
- Johnson, E. R., Wallace, P. J., Cashman, K. V., Granados, H. D., Kent, A. J. R., 2008. Magmatic volatile contents and degassing-induced crystallization at Volcán Jorullo, Mexico: implications for melt evolution and the plumbing systems of monogenetic volcanoes. *Earth Planet. Sci. Lett.* 269 (3-4), 478-487.
- Johnson, E. R., Wallace, P. J., Cashman, K. V., Granados, H. D., 2010. Degassing of volatiles (H₂O, CO₂, S, Cl) during ascent, crystallization, and eruption at mafic monogenetic volcanoes in central Mexico. *J. Volcanol. Geotherm. Res.* 197 (1-4), 225-238.
- Jugo, P. J., 2009. Sulfur content at sulfide saturation in oxidized magmas. *Geology* 37 (5), 415-418.
- Jugo, P. J., Luth, R. W., Richards, J. P., 2005a. An experimental study of the sulfur content in basaltic melts saturated with immiscible sulfide or sulfate liquids at 1300 °C and 1.0 GPa. *J. Petrol.* 46 (4), 783-798.

- Jugo, P. J., Luth, R. W., Richards, J. P., 2005b. Experimental data on the speciation of sulfur as a function of oxygen fugacity in basaltic melts. *Geochim. Cosmochim. Acta* 69 (2), 497-503.
- Kent, A. J. R., 2008. Melt inclusions in basaltic and related volcanic rocks. *Rev. Mineral. Geochem.* 69 (1), 273-331.
- Kilinc, A., Carmichael, I. S. E., Rivers, M. L., Sack, R. O., 1983. The ferric-ferrous ratio of natural silicate liquids equilibrated in air. *Contrib. Mineral. Petrol.* 83 (1), 136-140.
- Kiyosu, Y., Kurahashi, M., 1983. Origin of sulphur species in acid sulfate-chloride thermal waters, northeastern Japan. *Geochim. Cosmochim. Acta* 47 (7), 1237-1245.
- Liu, Y., Samaha, N. T., Baker, D. R., 2007. Sulfur concentration at sulfide saturation (SCSS) in magmatic silicate melts. *Geochim. Cosmochim. Acta* 71 (7), 1783-1799.
- Luhr, J. F., 2001. Glass inclusions and melt volatile contents at Parícutin Volcano, Mexico. *Contrib. Mineral. Petrol.* 142 (3), 261-283.
- Luhr, J. F., Carmichael, I. S. E., 1981. The Colima volcanic complex, Mexico: Part II. Late-Quaternary cinder cones. *Contrib. Mineral. Petrol.* 76 (2), 127-147.
- Marini, L., Gambardella, B., 2005. Geochemical modeling of magmatic gas scrubbing. *Annal. Geophys.* 48 (4-5), 739-753.
- Mathez, E. A., Webster, J. D., 2005. Partitioning behaviour of chlorine and fluorine in the system apatite-silicate melt-fluid. *Geochim. Cosmochim. Acta* 69 (5), 1275-1286.
- Mauri, G., 2009. Multi-scale analysis of multiparameter geophysical and geochemical data from active volcanic systems. Ph. D. Thesis, Simon Fraser Univ. Burnaby, Canada, 436 pp.
- Mazot, A., Bernard, A., Fischer, T., Inguaggiato, S., Sutawidjaja, I. S., 2008. Chemical evolution of thermal waters and changes in the hydrothermal system of Papandayan volcano (West Java, Indonesia) after the November 2002 eruption. *J. Volcanol. Geotherm. Res.* 178 (2), 276-286.
- Menyailov, I. A., Nikitina, L. P., Shapar, V. N., Pilipenko, V. P., 1986. Temperature increase and chemical change of fumarolic gases at Momotombo volcano, Nicaragua, in 1982-1985: are these indicators of a possible eruption? *J. Geophys. Res.* 91 (B12), 12199-12214.
- Métrich, N., Clocchiatti, R., 1989. Melt inclusion investigation of the volatile behaviour in historic alkali basaltic magmas of Etna. *Bull. Volcanol.* 51 (3), 185-198.

- Métrich, N., Wallace, P. J., 2008. Volatile abundances in basaltic magmas and their degassing paths tracked by melt inclusions. *Rev. Mineral. Geochem.* 69 (1), 363-402.
- Newman, S., Lowenstern, J. B., 2002. VolatileCalc: a silicate melt-H₂O-CO₂ solution model written in Visual Basic for Excel. *Comput. Geosci.* 28, 597-604.
- Ohba, T., Hirabayashi, J., Nogami, K., Kusakabe, M., Yoshida, M., 2008. Magma degassing process during the eruption of Mt. Unzen, Japan in 1991 to 1995: Modeling with the chemical composition of volcanic gas. *J. Volcanol. Geotherm. Res.* 175 (1-2), 120-132.
- Okumura, S., Nakamura, M., Nakashima, S., 2003. Determination of molar absorptivity of IR fundamental OH-stretching vibration in rhyolitic glasses. *Am. Mineral.* 88 (11-12), 1657-1662.
- Oppenheimer, C., Francis, P., Burton, M., Maciejewski, A. J. H., Boardman, L., 1998. Remote measurement of volcanic gases by Fourier transform infrared spectroscopy. *Appl. Phys. B* 67 (4), 505-515.
- Oppenheimer, C., Kyle, P. R., 2008. Probing the magma plumbing of Erebus volcano, Antarctica, by open-path FTIR spectroscopy of gas emissions. *J. Volcanol. Geotherm. Res.* 177 (3), 743-754.
- Palmer, S., 2009. Hydrogeochemistry of the upper Banyu Pahit River valley, Kawah Ijen volcano, Indonesia. M.Sc. Thesis. McGill University, Montréal, Canada, 144 pp.
- Papale, P., Moretti, R., Barbato, D., 2006. The compositional dependence of the saturation surface of H₂O+CO₂ fluids in silicate melts. *Chem. Geol.* 229 (1-3), 78-95.
- Roberge, J., Delgado-Granados, H., Wallace, P. J., 2009. Mafic magma recharge supplies high CO₂ and SO₂ gas fluxes from Popocatepetl volcano, Mexico. *Geology* 37 (2), 107.
- Rowe Jr, G. L., Brantley, S. L., Fernandez, M., Fernandez, J. F., Borgia, A., Barquero, J., 1992. Fluid-volcano interaction in an active stratovolcano: the crater lake system of Poas volcano, Costa Rica. *J. Volcanol. Geotherm. Res.* 49 (1-2), 23-51.
- Rust, A. C., Cashman, K. V., Wallace, P. J., 2004. Magma degassing buffered by vapor flow through brecciated conduit margins. *Geology* 32 (4), 349-352.
- Sadofsky, S. J., Portnyagin, M., Hoernle, K., van den Bogaard, P., 2008. Subduction cycling of volatiles and trace elements through the Central American volcanic arc: evidence from melt inclusions. *Contrib. Mineral. Petrol.* 155 (4), 433-456.

- Scaillet, B., Pichavant, M., 2005. A model of sulphur solubility for hydrous mafic melts: application to the determination of magmatic fluid compositions of Italian volcanoes. *Annal. Geophys.* 48 (4-5), 671-698.
- Shinohara, H., 2005. A new technique to estimate volcanic gas composition: plume measurements with a portable multi-sensor system. *J. Volcanol. Geotherm. Res.* 143 (4), 319-333.
- Sitorus, K., 1990. Volcanic stratigraphy and geochemistry of the Ijen Caldera Complex, East Java, Indonesia. M. Sc. Thesis. University of Wellington, Wellington, New Zealand.
- Smithsonian Institute, 2007. *Ijen. Bull. Glob. Volcan. Network* 32 (02-09).
- Smithsonian Institute, 2009. *Ijen. Bull. Glob. Volcan. Network* 34 (02).
- Sobolev, A. V., Danyushevsky, L. V., 1994. Petrology and geochemistry of boninites from the north termination of the Tonga Trench: constraints on the generation conditions of primary high-Ca boninite magmas. *J. Petrol.* 35 (5), 1183.
- Spilliaert, N., Métrich, N., Allard, P., 2006. S-Cl-F degassing pattern of water-rich alkali basalt: modeling and relationship with eruption styles on Mount Etna volcano. *Earth Planet. Sci. Lett.* 248 (3-4), 772-786.
- Sugawara, T., 2000. Empirical relationships between temperature, pressure, and MgO content in olivine and pyroxene saturated liquid. *J. Geophys. Res.* 105 (B4), 8457-8472.
- Symonds, R. B., Gerlach, T. M., Reed, M. H., 2001. Magmatic gas scrubbing: implications for volcano monitoring. *J. Volcanol. Geotherm. Res.* 108 (1-4), 303-341.
- Symonds, R. B., Rose, W. I., Bluth, G. J. S., Gerlach, T. M., 1994. Volcanic-gas studies; methods, results, and applications. *Rev. Mineral. Geochem.* 30 (1), 65-66.
- Syracuse, E. M., Abers, G. A., 2006. Global compilation of variations in slab depth beneath arc volcanoes and implications. *Geochem. Geophys. Geosyst.* 7 (5), Q05017.
- Takano, B., Suzuki, K., Sugimori, K., Ohba, T., Fazlullin, S. M., Bernard, A., Sumarti, S., Sukhyar, R., Hirabayashi, M., 2004. Bathymetric and geochemical investigation of Kawah Ijen Crater Lake, East Java, Indonesia. *J. Volcanol. Geotherm. Res.* 135 (4), 299-329.
- Taran, Y. A., Rozhkov, A. M., Serafimova, E. K., Esikov, A. D., 1991. Chemical and isotopic composition of magmatic gases from the 1988 eruption of Klyuchevskoy volcano, Kamchatka. *J. Volcanol. Geotherm. Res.* 46 (3-4), 255-263.

- Taran, Y., Gavilanes, J. C., Cortés, A., 2002. Chemical and isotopic composition of fumarolic gases and the SO₂ flux from Volcan de Colima, Mexico, between the 1994 and 1998 eruptions. *J. Volcanol. Geotherm. Res.* 117 (1-2), 105-119.
- van Hinsberg, V. 2001. Water-rock interaction and element fluxes in the Kawah Ijen Hyperacidic Crater Lake and the Banyu Pait river, east Java, Indonesia. M. Sc. Thesis. University of Utrecht, Netherlands, 299 pp.
- van Hinsberg, V., Berlo, K., van Bergen, M., Williams-Jones, A. E., 2010a. Extreme alteration by hyperacidic brines at Kawah Ijen volcano, East Java, Indonesia: I. Textural and mineralogical imprint. *J. Volcanol. Geotherm. Res.* 198, 253-263.
- van Hinsberg, V., Berlo, K., Sumarti, S., van Bergen, M., Williams-Jones, A.E., 2010b. Extreme alteration by hyperacidic brines at Kawah Ijen volcano, East Java, Indonesia: II. Metasomatic imprint and element fluxes. *J. Volcanol. Geotherm. Res.* 196, 169-184.
- Varekamp, J. C., Kreulen, R., 2000. The stable isotope geochemistry of volcanic lakes, with examples from Indonesia. *J. Volcanol. Geotherm. Res.* 97 (1-4), 309-327.
- Vigouroux, N., Wallace, P. J., Kent, A. J. R., 2008. Volatiles in high-K magmas from the Western trans-Mexican volcanic belt: Evidence for fluid fluxing and extreme enrichment of the mantle wedge by subduction processes. *J. Petrol.* 49 (9), 1589-1618.
- Wallace, P. J., 2005. Volatiles in subduction zone magmas: concentrations and fluxes based on melt inclusion and volcanic gas data. *J. Volcanol. Geotherm. Res.* 140 (1-3), 217-240.
- Wallace, P. J., Carmichael, I. S. E., 1994. S speciation in submarine basaltic glasses as determined by measurements of SK α X-ray wavelength shifts. *Am. Mineral.* 79 (1-2), 161-167.
- Yamashita, S., Kitamura, T., Kusakabe, M., 1997. Infrared spectroscopy of hydrous glasses of arc magma compositions. *Geochem. J.* 31 (3), 169–174.

5: UNDERESTIMATING VOLCANIC DEGASSING: THE CASE OF KAWAH IJEN VOLCANO, INDONESIA¹

5.1 Abstract

FLYSPEC measurements of SO₂ gas emissions from the rhyolite dome at Kawah Ijen volcano over 5 years reveal a constant flux of $\sim 0.3 \pm 0.1 \text{ kg s}^{-1}$. This relatively low SO₂ flux is accompanied by visible deposition of native S on the surface. MultiGAS plume composition measurements (2008, 2009) as well as direct fumarole samples (2007, 2008) constrain the total volatile budget of the plume. Plume compositions have H₂O/SO₂ ratios of 400-1000 and CO₂/SO₂ ratios of 100-200 (by weight) and are highly depleted in SO₂ compared to fumarole compositions (H₂O/SO₂ ratios of 20-30, CO₂/SO₂ ratios of 6-9 and H₂S/SO₂ ratios of 1-1.5 (by weight)). This extensive loss of SO₂ ($\sim 82\text{-}98\%$) is associated with the deposition of S-bearing sublimates and oxidation of S to SO₃ and SO₄²⁻ as the volcanic gases cool and mix with ambient air. An unquantified amount of S is also lost to the crater lake, via precipitation of native S and disproportionation to form dissolved sulphates. Minimum restored SO_{2(total)} fluxes are 2-14 ($\pm 30\%$) kg s⁻¹ (SO_{2(total)} = SO₂ + H₂S reported as SO₂) and total volatile fluxes from the dome are 15-200 kg s⁻¹. Melt inclusion data suggests that S degasses efficiently (up to 2000 ppm) as mafic and felsic magmas mix and

¹ The following chapter will be submitted to the journal *Geology* under the co-authorship of G. Williams-Jones, V. van Hinsberg and A.E. Williams-Jones. The collaboration so far includes assistance in field sample collection from all co-authors as well as discussion and review by G. Williams-Jones.

differentiate at depth. Total magma mass flux is therefore estimated at 260-2400 kg s⁻¹ (equivalent to a total volume flux of ~0.1-0.9 m³ s⁻¹). Over the 5 year sampling period, the total volume of degassed magma is estimated to be at least 0.02-0.14 km³. Given that no significant magmatic eruption has occurred in the last 100 years (only minor phreatic eruptions have been recorded), the total volume of unerupted, degassing magma is ~ 0.3-2.9 km³. This implies large volumes of stored magma, and without evidence for significant deformation in the area, sub-surface accommodation/drainback of degassed magma must be occurring beneath the Ijen caldera. Compared to other open vent arc volcanoes, Kawah Ijen is a small yet important S emitter not previously recognized due to massive S deposition and fluxing through the crater lake, leading to a disproportionately low SO₂ flux at the surface.

5.2 Introduction

Open vent degassing at arc volcanoes is typically characterized by continuous release of large volumes of gas, often without eruption of magmatic material, which has led authors to suggest several mechanisms by which large volumes of magma can efficiently degas at depth without extrusion. Release of gas during magma overturn in the conduit and return flow of dense degassed magma to depth has been proposed for various volcanoes (e.g., Izu-Oshima: Kazahaya et al., 1994; Satsuma-Iwojima: Kazahaya et al., 2002; Stromboli: Stevenson and Blake, 1998; Villarica: Witter et al., 2004; Masaya: Stix, 2007). For arc volcanoes with deep seated, CO₂-rich mafic magma degassing beneath open vents, large volumes of SO₂ may also be released without requiring shallow

conduit convection (e.g., Popocatépetl, Roberge et al., 2009). In both cases, large volumes of magma are required to supply the gas flux measured at the surface and effective monitoring of these volcanoes requires knowledge of both the degassing mechanism and the volumes of magma involved. Oxidation of SO₂ to form SO₃ and sulphate species in tropospheric volcanic plumes may also contribute to large underestimates of the SO₂ flux (e.g., Oppenheimer et al., 1998; Porter et al., 2002). The presence of large amounts of native S deposition at volcanic vents can have a significant effect on the estimated total volatile fluxes at open vent volcanoes and, therefore, on the estimated magma fluxes. Using the example of Kawah Ijen, this study illustrates the importance of characterizing plume versus fumarole compositions when estimating total volatile and magmatic fluxes at open vent volcanoes. Similarly, other open vent volcanoes with visible S precipitation at the surface may have significantly underestimated magmatic fluxes.

5.3 Geologic Setting and Magmatic History

Kawah Ijen and the Ijen Caldera Complex are located in eastern Java, Indonesia, along the volcanic front of the Sunda arc (Fig. 5-1). Beneath Kawah Ijen, subduction of the 130 Ma Indo-Australian plate occurs at $\sim 7 \text{ cm yr}^{-1}$ (Syracuse and Abers, 2006) and water-rich fluid release from the subducting plate to the volcanic front is amongst the highest documented at arcs worldwide (Chapter 3). Kawah Ijen is a small, active stratovolcano that sits at the intersection of the Ijen Caldera Complex rim and an intra-caldera lineament of small cinder cones and shields (Fig. 5-1). Kawah Ijen has erupted a range of

magma compositions during its history, starting with a cone building stage consisting of alternating basaltic to andesitic lava flows and pyroclasts (ash to scoria; van Hinsberg et al., 2010b). These are discordantly overlain by interbedded pyroclastic flow and fall deposits of dominantly dacitic composition, dacitic lava flows, balistics, phreato-magmatic, phreatic and hydrothermal deposits associated with the partial destruction of the volcanic edifice and formation of a crater lake (van Hinsberg, 2001). The current configuration is a large (1 km wide), ~300 m deep crater, partly filled with a hyper-acidic lake that drains into the Banyu Pahit river. An active rhyolitic dome extrudes on the SE shore of the crater lake. The dome is currently 10 x 10 x 100 m in size and is actively degassing, with the dome surface and nearby crater walls covered in native S precipitates. Pipes have been installed by local miners to divert the flow of gas from most of the fumaroles to the base of the dome, allowing the vapours to cool from > 350 °C to < 200 °C and native S to condense into the liquid phase, pooling and crystallizing at the base for subsequent extraction.

The oldest recorded eruption of Kawah Ijen is in 1796 during which the crater lake boiled off and its morphology changed (see van Hinsberg, 2001 for references). In 1817, large earthquakes were felt in eastern Java and nearby Bali followed by a large phreato-magmatic eruption that ejected ash, bombs and sulphur and was accompanied by lahars on the outer flanks. The presence of a crater lake is reported again in 1820 (van Hinsberg, 2001). During the 20th century, one minor ash eruption as well as fluctuating lake levels, boiling of the lake waters and numerous phreatic explosions have occurred, the latest one as

recently as 2002 (van Hinsberg, 2001; Smithsonian Institute, 2002). During a 5 year campaign at Kawah Ijen (2006-2010), activity was restricted to degassing from the dome and acid spring runoff in the Banyu Pahit river (Smithsonian Institute, 2007, 2009). Maximum recorded fumarole temperatures are 600 °C on the top of the dome and up to 270 °C at the exit of the pipes. Crater lake temperatures have remained in the range 30-45 °C, and lake levels varied by no more than 1 m (Smithsonian Institute, 2007; 2009).

5.4 Sample Description and Methods

This study combines plume gas chemistry with fumarole gas compositions (Chapter 4) and plume SO₂ flux measurements in order to fully characterize the flux of volatiles at Kawah Ijen. Fumarole gas samples were collected in 2007 and 2008 from the top of the dome following the method of Giggenbach (1975) and Giggenbach and Goguel (1989). Details of the sampling technique and analysis of the fumarole gas samples can be found in Chapter 4. Fumarole temperatures at the time of sampling were 350-490 °C. The gases in 2008 are rich in CO₂ and S_{total} but have compositions comparable to other high temperature fumaroles from arc volcanoes (Table 5-3, Fig. 5-2; Chapter 4). Gases sampled in 2007 are contaminated by air-saturated waters as evidenced by their elevated H₂O, N₂ and Ar contents (Fig. 5-2; Chapter 4).

Near-simultaneous plume compositions were obtained using a portable multi-gas sensor unit (MultiGAS; Shinohara, 2005) in 2008 and 2009 (Table 5-1). The MultiGAS sensor consists of temperature, pressure and relative humidity sensors (to calculate H₂O contents), a LICOR IR CO₂ detector (20,000 ppm CO₂

saturation limit) and Interscan Corp. and Alphasense Ltd. SO₂ electrochemical cells (100 and 500 ppm saturation limits, respectively). Particle and desiccant filters (at the front of the line) and in-line gas scrubbers (to remove H₂S) are used to eliminate contamination or interferences. Plume gases were sampled at ambient temperature (20-30°C) and at varying distances from the dome (< 1m to > 100 m on the crater rim) in order to detect variations in plume composition as dilution progresses. Maximum/peak volcanic gas concentrations in the plume are recorded over a sampling period of 20-30 minutes and ratioed (e.g., H₂O/CO₂, CO₂/SO₂). This technique was favoured because obtaining ratios of the species by linear regression through all of the data was hampered by the variable sampling rates of the sensors.

SO₂ flux measurements were obtained in 2006-2010 with a FLYSPEC UV spectrometer (Horton et al., 2006) and walking traverses under the plume along the S-SE crater rim (Table 5-2). Relatively strong winds generally blew the plume directly over the edge of the crater, allowing us to obtain flux measurements and wind speeds (using a hand held anemometer) at close proximity to the plume height (< 10 m overhead); this significantly reduced the uncertainties (< 10 %; Mori et al., 2006; Williams-Jones et al., 2006; Nadeau and Williams-Jones, 2009). Wind direction is obtained from the line of sight relating the dome and the point on the rim at which maximum plume concentrations are recorded. Due to the lateral motion of the plume over the rim, spectra for each traverse represent different “puffs” of plume as the FLYSPEC line of site intersected the plume at various points along the crater rim (see Appendix D for additional details). As

such, each spectra was carefully evaluated and flux values were determined for each individual “puff”, representing the plume at a given moment in time. Overall variability in SO₂ flux over the 5 years is within range of the daily variability recorded.

5.5 Effects of Dilution, Reaction with Air and Precipitation of Native S on Plume Compositions

MultiGAS plume measurements represent mixtures of volcanic gas and ambient air, and as such, cooling, dilution and high temperature reactions need to be considered (e.g., Symonds and Reed, 1993; Gerlach, 2004; Martin et al., 2006; 2009). The plume compositions are highly variable when compared to the 2008 fumarole gases (with negligible air or air-saturated water contamination; Fig. 5-2). A tie-line linking the composition of ambient air (measured prior to and following each plume sample) to the plume compositions can be extended until it intersects the field of fumarole gas samples collected by earlier workers at the exit of the pipes at a temperature of < 250 °C (Delmelle et al., 2000). These pipe gases are variably depleted in SO₂ (confirmed by the liquid sulphur draining from the pipes; Fig. 5-4) compared to the 2008 samples collected directly from fumaroles on the top of the dome. The plume samples represent mixtures of ambient air and volcanic gases that are variably depleted in SO₂ as a result of native S deposition. High temperature, near-vent oxidation of SO₂ and H₂S to form SO₃ and H₂SO₄ (Allen et al., 2002; Gerlach, 2004; Mather et al., 2006; Martin et al., 2006), combined with ambient temperature conversion of plume

SO₂ to aerosol downwind, will also lead to a depletion in SO₂ as recorded in the plume measurements (e.g., Oppenheimer et al., 1998).

In order to quantify the effects of dilution only, the plume H₂O and CO₂ contents are compared to the 2008 gas compositions assuming both species remain nonreactive (e.g., Martin et al., 2006), and simple mass balance constraints are used to estimate the % dilution for each sample (calculated range is 20-98%; Table 5-1). H₂O/CO₂ ratios in the plume track the effects of dilution back to the 2008 fumarole compositions (Fig. 5-3a), a trend which is an artefact of the procedure used to calculate the % dilution. Comparing the H₂O/SO₂ and CO₂/SO₂ dilution trends with measured fumarole compositions suggests that simple dilution of inert gas species is not occurring (Fig. 5-3b,c). Plume H₂O/SO₂ ratios are highly variable but remain constant, on average, as dilution progresses from 20 to 98%. Given simple dilution, which assumes all species behave conservatively, H₂O/SO₂ ratios should increase as dilution progresses, however they remain constant. This implies that SO₂ concentrations, between 20 and 98% dilution and at ambient temperatures, are being buffered by the reaction and oxidation of reduced S species to produce more SO₂ as the plume mixes with air. This also implies that no further oxidation of SO₂ to form SO₃ or sulphates is occurring in the short time scales of plume-air interaction prior to sampling (e.g., Oppenheimer et al., 1998). A calculated dilution trend, starting with the 2008 fumarole gas composition and assuming a constant SO₂ concentration regardless of the fraction of air in the mixture, reproduces the plume trend but at lower H₂O/SO₂ ratios (Fig. 5-3b). The plume H₂O/SO₂ ratios track back to a

restored near-vent composition (hereafter defined as $\ll 20\%$ dilution, when the volcanic gas first encounters air and temperatures drop very rapidly from > 350 °C to ambient values) that approximates (although still overestimates) the gas samples collected at the exit of the pipes (Delmelle et al., 2000). We can quantify the loss of SO_2 from the volcanic gas fraction in the near-vent area by comparing the restored near-vent $\text{H}_2\text{O}/\text{SO}_2$ ratio of the plume with the 2008 fumarole ratios. The result is an 88 to 98 % loss of SO_2 from the volcanic gas fraction. An equivalent estimate is obtained from the CO_2/SO_2 systematics (82-97%; Fig. 5-3c). Similarly, comparison of the gas samples collected at the exit of the pipes with those collected in 2008 from the fumaroles at the top of the dome yields SO_2 loss estimates that range from 12-88% (from $\text{H}_2\text{O}/\text{SO}_2$ ratios) and 23-90% (from CO_2/SO_2 ratios).

5.6 Discussion

S deposition, visible on the surface of the dome and at the exit of the pipes (Fig. 5-4) and oxidation of gaseous SO_2 at relatively high temperatures (> 350 °C) (e.g., Mather et al., 2006; Martin et al., 2006) are both likely causes for loss of SO_2 from the plume in the near-vent area and underestimation of total SO_2 flux at Kawah Ijen. Underestimation of the SO_2 flux will be even higher if S disproportionation in the crater lake and pyritization of the dome rock can be quantified. SO_2 flux underestimates due to S deposition (e.g., Aiuppa et al., 2005a) and conversion of H_2S and SO_2 to sulphate aerosols (e.g., Oppenheimer et al., 1998) have been recognized previously but the degree of flux underestimation has not been fully quantified (Williams-Jones et al., 2006). Near-

vent deposition of native S is typically observed in low temperature fumaroles (< 200 °C; Giggenbach, 1987) and most open-vent volcanoes degas dominantly at higher temperatures, thereby quenching the gas phase before S saturation can be reached (e.g., Aiuppa et al., 2005a,b). Kawah Ijen gases have elevated SO₂ and H₂S contents that promote native S saturation at elevated temperatures (Fig. 5-4). Furthermore, enhanced oxidation of H₂S and SO₂ by heterogeneous reaction in the presence of particulate S in the plume (e.g., Oppenheimer et al., 1998), especially at high temperatures in the near-vent area (e.g., Mather et al., 2006), may also contribute to the underestimate in SO₂ flux as measured downwind.

Given the range of SO₂ loss estimated from the comparison of fumarole gases and near-vent plume data (82-98%), the SO₂ flux measured with the FLYSPEC on the crater rim (~150 m above the dome) will also be underestimated. Without quantitative constraint of the conversion of H₂S to SO₂ in the plume as it mixes with air, we can only assume that such a process is occurring because absolute SO₂ concentrations in the plume are not affected by dilution (Fig. 5-3b,c). Given our assumption that the SO₂ concentration in the plume as it crosses over the crater rim (at > 98% dilution with air) corresponds to near-vent SO₂ concentrations plus oxidized H₂S, the measured flux of 0.3 (± 0.1) kg s⁻¹ therefore represents the flux of SO_{2(total)} (where SO_{2(total)} = SO₂ + H₂S). Taking into account 82 to 98% loss of SO₂ in the near-vent area, this translates to an actual SO_{2(total)} flux (at the exit of the dome fumaroles) of 2-14 kg s⁻¹, values which approach daily SO₂ flux estimates (during quiescent degassing) from some

of the world's largest volcanic S emitters (e.g., $\sim 23 \text{ kg s}^{-1}$ at Popocatepetl, Mexico: Goff et al., 1998; $\sim 12\text{-}58 \text{ kg s}^{-1}$ at Etna, Italy: Caltabiano et al., 1994; Bruno et al., 1999).

The total volatile flux at Kawah Ijen can be estimated from the fumarole $\text{H}_2\text{O}/\text{SO}_{2(\text{total})}$ and $\text{CO}_2/\text{SO}_{2(\text{total})}$ ratios (by weight; Table 5-3) and the restored $\text{SO}_{2(\text{total})}$ flux. The range in fumarole $\text{H}_2\text{O}/\text{SO}_{2(\text{total})}$ and $\text{CO}_2/\text{SO}_{2(\text{total})}$ ratios, combined with the range in $\text{SO}_{2(\text{total})}$ flux yields a total volatile flux of $\sim 15\text{-}200 \text{ kg s}^{-1}$ ($10\text{-}145 \text{ kg s}^{-1} \text{ H}_2\text{O}$, $3\text{-}36 \text{ kg s}^{-1} \text{ CO}_2$). This very large range reflects the variability in the fumarole and plume compositions, a common feature of fumarole fields (e.g., Giggenbach, 1987; Fischer et al., 1996; Aiuppa et al., 2005b). Additional uncertainties in quantifying the total SO_2 flux at the rim (values have an average standard deviation of 30%) leads us to place less emphasis on the restored volatile flux values and more on the observation that these restored fluxes are up to 98% higher than the directly measured fluxes.

Maximum S loss of 2000 ppm from the melt due to degassing of a magma body at depth (Chapter 4) yields a calculated magma mass flux rate of $260\text{-}2400 \text{ kg s}^{-1}$, which corresponds to a volume flux of $\sim 0.1\text{-}0.9 \text{ m}^3 \text{ s}^{-1}$ of degassing magma (using an average magma density of 2600 kg m^{-3}). These values are at the low end of the range reported for other open-vent degassing arc volcanoes ($\sim 2.2 \text{ m}^3 \text{ s}^{-1}$ at Villarica, Witter et al., 2004; $\sim 4 \text{ m}^3 \text{ s}^{-1}$ at Izu-Oshima, Kazahaya et al., 1994; $10 \text{ m}^3 \text{ s}^{-1}$ at Satsuma-Iwojima, Kazahaya et al., 2002). In the five years of survey at Kawah Ijen, SO_2 flux measurements have remained virtually constant suggesting that $0.02\text{-}0.14 \text{ km}^3$ of magma must have degassed without

eruption. Given that no significant magmatic eruption has occurred in over 100 years, $\sim 0.3\text{-}2.9\text{ km}^3$ of magma must have degassed before being recycled to or stored in the deeper parts of the plumbing system. Without evidence for significant deformation in the area (Mauri, 2009), sub-surface accommodation and/or drainback of degassed magma must be occurring beneath the Ijen caldera.

This study reveals the potential for large underestimates in total SO_2 flux emitted from open-vent degassing arc volcanoes when S deposition and near-vent oxidation of S species are important factors. High total S concentrations in the fumarole gases at Kawah Ijen lead to high temperature precipitation of native S in the plume, which may enhance heterogeneous oxidation of SO_2 and H_2S by atmosphere-derived OH radicals (Oppenheimer et al., 1998). Evidence of near-vent, high temperature conversion of S species to aerosol compounds (e.g., Mather et al., 2006) and high temperature S deposition from S-rich magmas at arc volcanoes (e.g., Satsuma-Iwojima, Japan, Kazahaya et al., 2002) can lead to very large underestimates of total gas and unerupted magma fluxes. This has important implications for modeling of convective overturn of degassed magma and storage/accommodation of unerupted magma in the mid- to upper-crust. Furthermore, compared to other open vent arc volcanoes, Kawah Ijen ranks as a small edifice yet a very important S emitter not previously recognized due to significant S deposition and degassing through its crater lake.

5.7 Acknowledgments

The authors would like to thank the Kawah Ijen Park service and particularly T. Mulja and N. Widyastuti of East Asia Minerals for their assistance. The Kawah Ijen research team, namely G. Mauri, S. Palmer, S. Scher, as well as numerous other volunteers, offered valuable help in the field. Local miners Pa Im and Jumanto were invaluable in their assistance in the field, especially with dome fumarole sampling. We acknowledge T. Fischer (University of New Mexico) for analysis of the fumarole gas samples. Funding for this work was provided by an NSERC-CRD grant to A.E. Williams-Jones and G. Williams-Jones.

5.8 Figures

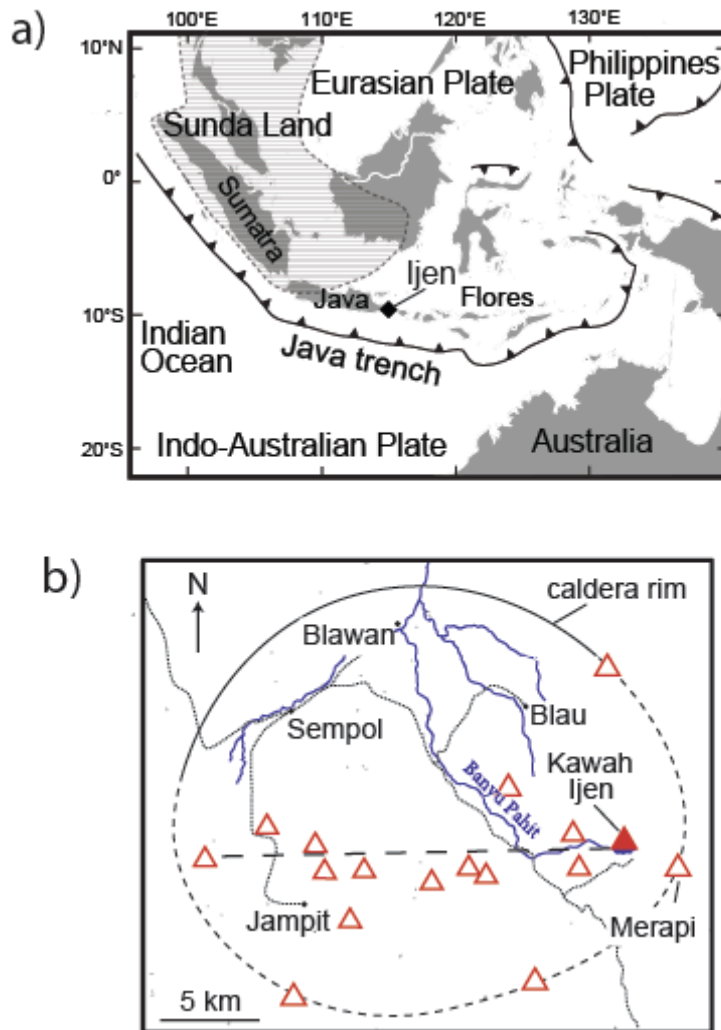


Figure 5-1 a) The location of the Ijen Caldera Complex on the island of Java, Indonesia. The thatched region, labeled Sunda Land, delineates the inferred extent of the continental lithosphere beneath the arc (Hamilton, 1979), b) The location of Kawah Ijen volcano within the Ijen Caldera Complex, as well as the intra-caldera lineament (dashed line) of volcanoes running E-W. Map modified from van Hinsberg et al., 2010a.

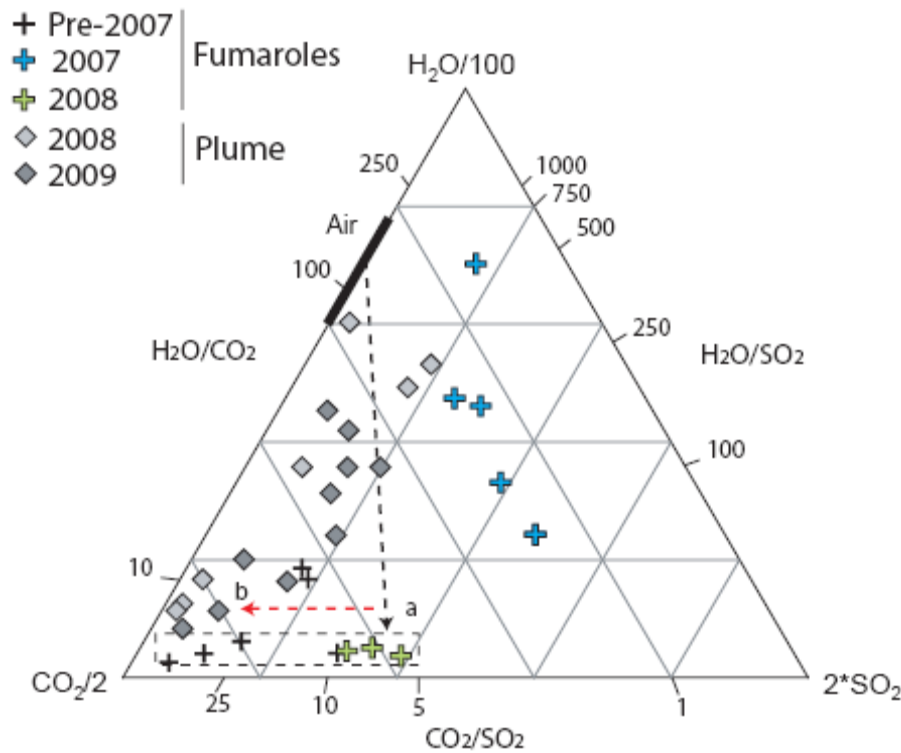


Figure 5-2 $\text{H}_2\text{O}-\text{CO}_2-\text{SO}_2$ ternary diagram comparing the fumarole and plume compositions. Fumarole samples collected prior to this study (Pre-2007) were collected at the exit of the pipes and have experienced variable loss of SO_2 from the condensation of liquid S (Delmelle et al., 2000). Fumarole samples in 2007 have experienced contamination from meteoric H_2O . The 2008 fumarole samples are the most representative of the uncontaminated magmatic gas phase at Kawah Ijen (Chapter 4). The plume samples have variable compositions representing both a) dilution of the magmatic gas with air and b) loss of SO_2 due to oxidation and S precipitation (in the pipes, on the surface of the dome and as particulate S in the plume, deposited downwind).

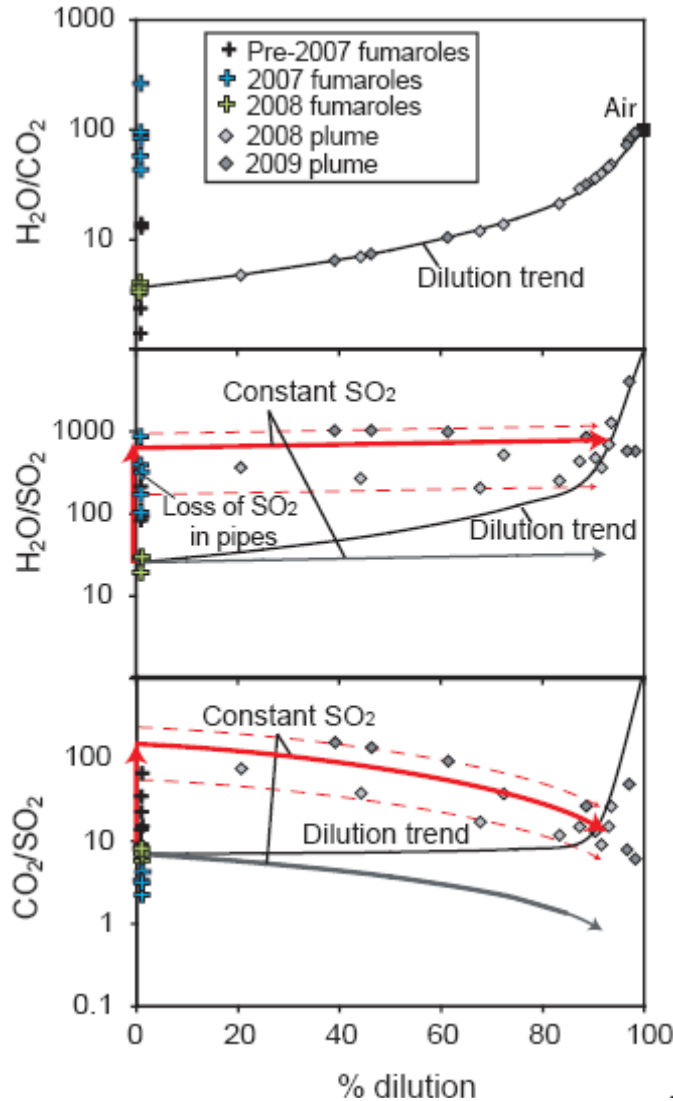


Figure 5-3 Volatile ratios a) $\text{H}_2\text{O}/\text{CO}_2$, b) $\text{H}_2\text{O}/\text{SO}_2$ and c) CO_2/SO_2 versus the % dilution by air calculated for each plume sample. Fumarole gas volatile ratios are also plotted at 0% dilution by air. The dilution trend in a) is calculated assuming H_2O and CO_2 are unreactive species in the plume and relates the average of the 2008 fumarole samples to the average composition of air. The dilution trend in b) is calculated in the same manner as in a), assuming H_2O and SO_2 are unreactive species and their concentrations are effected only by dilution. The plume data does not follow this simple dilution trend and $\text{H}_2\text{O}/\text{SO}_2$ ratios appear to remain approximately constant as dilution progresses. This trend (labeled as Constant SO_2) can be reproduced if H_2O remains unreactive but SO_2 contents are buffered by the continuous oxidation of more reduced S species (H_2S , S^0). This trend runs through the average of the plume compositions and the two dotted trends bracket the variability in plume compositions. The constant SO_2 trend tracking back to the average 2008 fumarole compositions represents the plume trend expected if no near-vent SO_2 was occurring. The same pattern is seen with the CO_2/SO_2 ratios of the plume samples in c). Pre-2007 data is from Delmelle et al. (2000).

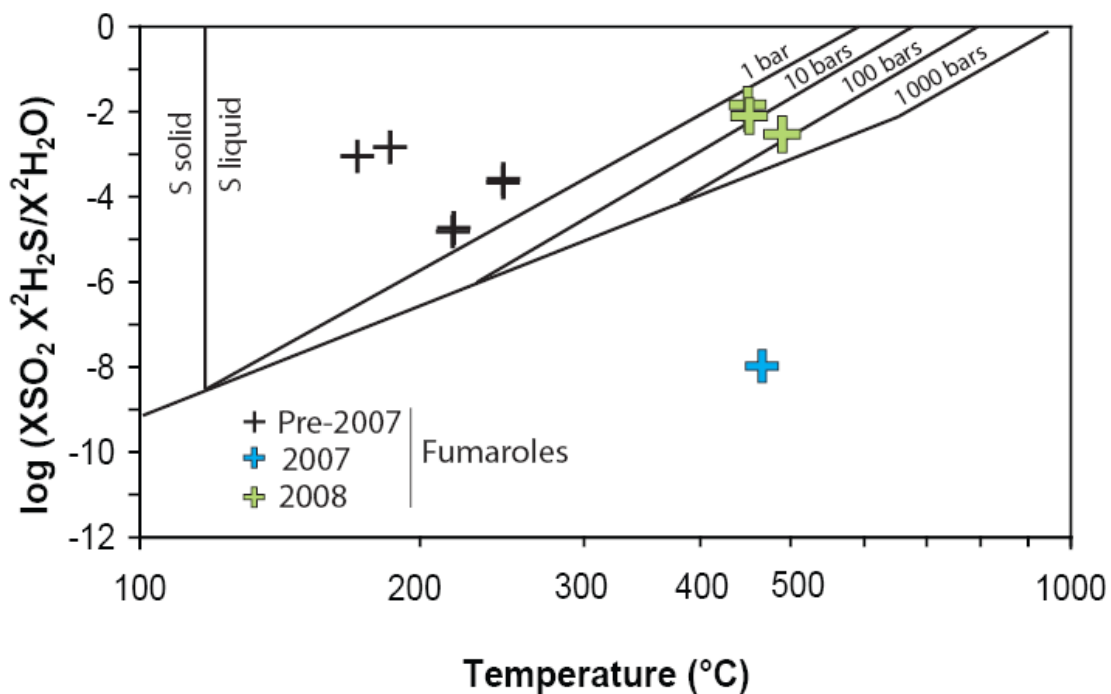


Figure 5-4 Saturation of Kawah Ijen fumarole gases with respect to native S. Phase relationships are from Giggenbach (1987). Pre-2007 samples taken at the exit of the pipes are clearly saturated in liquid S (Delmelle et al., 2000). The 2008 fumarole gas samples are also at or near saturation as they exit the dome, leading to S precipitation in the solid field as temperatures drop rapidly to ambient values. The 2007 fumarole samples are highly depleted in H₂S and SO₂ and only one sample has reliable H₂S, SO₂ and H₂O values as well as an accurately determined exit temperature. This sample plots in the S undersaturated field at its exit temperature, reflecting the high H₂O, low S_{total} content of the gas.

5.9 Tables

Table 5-1 MultiGAS plume measurements

Run #	Date	Location (dist. dome)	Atm. H ₂ O ^a	H ₂ O wt%	CO ₂ ppm	SO ₂ ^b ppm	H ₂ O/CO ₂	H ₂ O/SO ₂	CO ₂ /SO ₂	% dilution ^c
Hot fumarole 1	23/07/2008	Base of pipes (\leq 5 m)	6.7	7.6	938	19	81	4015	49	97
Hot fumarole 2	23/07/2008	Base of pipes (\leq 5 m)	6.7	9.9	9409	> 100	10	-	-	61
Hot fumarole 3	23/07/2008	Base of pipes (\leq 5 m)	6.7	10.2	13799	> 100	7	-	-	46
Hot fumarole 4	23/07/2008	Base of pipes (\leq 5 m)	6.7	10.2	15830	> 100	6	-	-	39
Plume 124230	05/08/2008	Path to crater (50-100m)	5.1	5.2	550	90	94	574	6	98
Plume 1312	05/08/2008	Path to crater (< 50m)	5.4	4.8	659	83	73	577	8	97
Fumarole	05/08/2008	Base of pipes (\leq 5 m)	6.1	8.5	2679	> 100	32	-	-	89
Fumarole 1	05/08/2008	Base of pipes (\leq 5 m)	6.1	-	1730	54	-	-	32	-
Fumarole 2	05/08/2008	Base of pipes (\leq 5 m)	6.1	-	1524	50	-	-	31	-
Dome 1	19/07/2009	Base of pipes (\leq 5 m)	6.6	7.6	1907	210	40	364	9	92
Dome 2	19/07/2009	Base of pipes (\leq 5 m)	6.6	7.4	1538	58	48	1272	26	93
Dome 3	19/07/2009	Base of pipes (\leq 5 m)	6.6	6.7	1470	97	46	694	15	93
Dome 4	19/07/2009	Base of pipes (\leq 5 m)	6.6	6.6	2281	152	29	434	15	87
Dome 5	19/07/2009	Base of pipes (\leq 5 m)	6.6	6.7	1858	141	36	476	13	90
Dome 2-1	28/07/2009	Base of pipes (\leq 5 m)	3.4	7.5	10764	281	7	268	38	44
Dome 2-2	28/07/2009	Base of pipes (\leq 5 m)	3.4	7.0	5883	343	12	205	17	68
Dome 2-3	28/07/2009	Base of pipes (\leq 5 m)	3.4	6.3	2974	250	21	252	12	83
Dome 1	29/07/2009	Base of pipes (\leq 5 m)	3.4	9.5	20019	262	5	363	76	21
Dome 2	29/07/2009	Base of pipes (\leq 5 m)	3.4	7.4	5377	142	14	520	38	72

^a Atmospheric H₂O contents (wt%) were determined prior to each run in clear atmosphere. H₂O contents in the atmosphere and plume are calculated from the relative humidity, temperature and ambient pressure.

^b SO₂ contents were determined using a Interscan Corp. electrochemical cell in 2008, with a saturation limit of 100 ppm. In 2009, an Alphasense Ltd. electrochemical cell was added with a saturation limit of 500 ppm.

^c % dilution was calculated for each run using the average background atmospheric H₂O and CO₂ contents measured for that run. Atmospheric CO₂ levels varied between 350-450 ppm.

Table 5-2 Flyspec SO₂ flux measurements

# of good traverses ^a	Date	Location	Av. wind speed m s ⁻¹	st. dev.	Av. SO ₂ flux ^b t d ⁻¹	st. dev.	Av. SO ₂ flux ^b kg s ⁻¹	st. dev.
4	8/21/2006	SE crater rim	6.1	-	41	6	0.5	0.1
6	8/23/2006	SE crater rim	3.9	-	28	8	0.3	0.1
5	7/11/2007	SE crater rim	3.9	1.0	25	10	0.3	0.1
7	7/12/2007	SE crater rim	3.7	1.0	28	7	0.3	0.1
4	7/27/2007	SE crater rim	2.7	0.5	43	11	0.5	0.1
3	7/22/2008	SE crater rim	1.4	0.3	17	8	0.2	0.1
1	7/24/2008	SE crater rim	3.5	-	26	-	0.3	-
7	7/28/2008	SE crater rim	3.8	0.6	24	8	0.3	0.1
5	7/21/2009	SE crater rim	2.7	0.6	14	5	0.2	0.1
2	8/9/2010	SE crater rim	4.5	0.5	32	5	0.4	0.1
Average (St.Dev)					28 (9)	8	0.3 (0.1)	0.1

^a Traverses are considered "good" when the scan shows no detector saturation, plume stalling overhead or lack of resolvable plume puffs.

^b SO₂ flux values were calculated using the average wind speed and separating out individual puffs of plume from the total traverse scan. The flux reported is the average of the various traverses.

Table 5-3 Partial fumarole compositions (wt%)^a

Sample	Date	Temp. (°C)	H ₂ O	CO ₂	SO ₂	H ₂ S
401	2007	>452	99	0.4	0.12	0.00
404	2007	>370	98	1.1	0.31	0.02
412	2007	371	96	2.2	0.95	0.00
423	2007	461	98	1.2	0.26	0.02
424	2007	461	97	1.7	0.57	0.00
3	2008	489	76	18.4	2.55	2.57
10	2008	450	70	21.2	3.57	4.48
14	2008	450	73	20.7	2.42	3.80

^a Complete fumarole gas compositions can be obtained from Chapter 4.

5.10 References

- Aiuppa, A., Inguaggiato, S., McGonigle, A. J. S., O'Dwyer, M., Oppenheimer, C., Padgett, M. J., Rouwet, D., and Valenza, M., 2005a, H₂S fluxes from Mt. Etna, Stromboli, and Vulcano (Italy) and implications for the sulfur budget at volcanoes: *Geochimica et Cosmochimica Acta*, v. 69, p. 1861-1871.
- Aiuppa, A., Federico, C., Giudice, G., and Gurrieri, S., 2005b, Chemical mapping of a fumarolic field: la Fossa crater, Vulcano Island (Aeolian Islands, Italy): *Geophysical Research Letters*, v. 32, p. L13309.
- Allen, A. G., Oppenheimer, C., Ferm, M., Baxter, P. J., Horrocks, L. A., Galle, B., McGonigle, A. J. S., and Duffell, H. J., 2002, Primary sulfate aerosol and associated emissions from Masaya Volcano, Nicaragua: *Journal of Geophysical Research*, v. 107, p. 4682.
- Bruno, N., Caltabiano, T., and Romano, R., 1999, SO₂ emissions at Mt. Etna with particular reference to the period 1993–1995: *Bulletin of Volcanology*, v. 60, p. 405-411.
- Caltabiano, T., Romano, R., and Budetta, G., 1994, SO₂ flux measurements at Mount Etna (Sicily): *Journal of Geophysical Research*, v. 99, p. 12809.
- Delmelle, P., Bernard, A., Kusakabe, M., Fischer, T. P., and Takano, B., 2000, Geochemistry of the magmatic-hydrothermal system of Kawah Ijen volcano, East Java, Indonesia: *Journal of Volcanology and Geothermal Research*, v. 97, p. 31-53.
- Fischer, T. P., Arehart, G. B., Sturchio, N. C., and Williams, S. N., 1996, The relationship between fumarole gas composition and eruptive activity at Galeras Volcano, Colombia: *Geology*, v. 24, p. 531-534.
- Gerlach, T. M., 2004, Volcanic sources of tropospheric ozone-depleting trace gases: *Geochemistry, Geophysics, Geosystems*, v. 5, p. Q09007.
- Giggenbach, W. F., 1987, Redox processes governing the chemistry of fumarolic gas discharges from White Island, New Zealand: *Applied Geochemistry*, v. 2, p. 143-161.
- Giggenbach, W. F., 1975, A simple method for the collection and analysis of volcanic gas samples: *Bulletin of Volcanology*, v. 39, p. 132-145.
- Giggenbach, W. F., Goguel, R. L., 1989, Collection and analysis of geothermal and volcanic water and gas discharges: Chemical Division of Department of Scientific and Industrial Research, Petone, New Zealand Report CD, v. 2401, p. 81.

- Goff, F., Janik, C. J., Delgado, H., Werner, C., Counce, D., Stimac, J. A., Siebe, C., Love, S. P., Williams, S. N., and Fischer, T., 1998, Geochemical surveillance of magmatic volatiles at Popocatepetl volcano, Mexico: *Bulletin of the Geological Society of America*, v. 110, p. 695-710.
- Hamilton, W. 1979. Tectonics of the Indonesian region. USGS Prof. Paper 1078 345.
- Horton, K. A., Williams-Jones, G., Garbeil, H., Elias, T., Sutton, A. J., Mougini-Mark, P., Porter, J. N., and Clegg, S., 2006, Real-time measurement of volcanic SO₂ emissions: validation of a new UV correlation spectrometer (FLYSPEC): *Bulletin of Volcanology*, v. 68, p. 323-327.
- Kazahaya, K., Shinohara, H., and Saito, G., 2002, Degassing process of Satsuma-Iwojima volcano, Japan: Supply of volatile components from a deep magma chamber: *Earth Planets and Space*, v. 54, p. 327-336.
- Kazahaya, K., Shinohara, H., and Saito, G., 1994, Excessive degassing of Izu-Oshima volcano: magma convection in a conduit: *Bulletin of Volcanology*, v. 56, p. 207-216.
- Martin, R. S., Mather, T. A., and Pyle, D. M., 2006, High-temperature mixtures of magmatic and atmospheric gases: *Geochemistry Geophysics Geosystems*, v. 7, p. Q04006.
- Martin, R. S., Roberts, T. J., Mather, T. A., and Pyle, D. M., 2009, The implications of H₂S and H₂ kinetic stability in high-T mixtures of magmatic and atmospheric gases for the production of oxidized trace species (eg, BrO and NO_x): *Chemical Geology*, v. 263, p. 143-150.
- Mather, T. A., McCabe, J. R., Rai, V. K., Thiemens, M. H., and Pyle, D. M., 2006, Oxygen and sulfur isotopic composition of volcanic sulfate aerosol at the point of emission: *Journal of Geophysical Research*, v. 111, p. D18205.
- Mauri, G., 2009, Multi-scale analysis of multiparameter geophysical and geochemical data from active volcanic systems. Ph. D. Thesis, Simon Fraser University, Burnaby, Canada, 436 pp.
- Oppenheimer, C., Francis, P., and Stix, J., 1998, Depletion rates of sulfur dioxide in tropospheric volcanic plumes: *Geophysical Research Letters*, v. 25, p. 2671-2674.
- Porter, J. N., Horton, K. A., Mougini-Mark, P. J., Lienert, B., Sharma, S. K., Lau, E., Sutton, A. J., Elias, T., and Oppenheimer, C., 2002, Sun photometer and lidar measurements of the plume from the Hawaii Kilauea Volcano Pu'u O'o vent: Aerosol flux and SO₂ lifetime: *Geophysical Research Letters*, v. 29, p. 1783.

- Roberge, J., Delgado-Granados, H., and Wallace, P. J., 2009, Mafic magma recharge supplies high CO₂ and SO₂ gas fluxes from Popocatepetl volcano, Mexico: *Geology*, v. 37, p. 107.
- Shinohara, H., 2005, A new technique to estimate volcanic gas composition: plume measurements with a portable multi-sensor system: *Journal of Volcanology and Geothermal Research*, v. 143, p. 319-333.
- Smithsonian Institute, 2002, *Ijen. Bulletin of the Global Volcanism Network* 27 (08).
- Smithsonian Institute, 2007, *Ijen. Bulletin of the Global Volcanism Network* 32 (02-09).
- Smithsonian Institute, 2009, *Ijen. Bulletin of the Global Volcanism Network* 34 (02).
- Stevenson, D. S., Blake, S., 1998, Modeling the dynamics and thermodynamics of volcanic degassing: *Bulletin of Volcanology*, v. 60, p. 307-317.
- Stix, J., 2007, Stability and instability of quiescently active volcanoes: The case of Masaya, Nicaragua: *Geology*, v. 35, p. 535-538.
- Symonds, R. B., Reed, M. H., 1993, Calculation of multicomponent chemical equilibria in gas-solid-liquid systems: Calculation methods, thermochemical data, and applications to studies of high-temperature volcanic gases with examples from Mt. St. Helens: *American Journal of Science*, v. 293, p. 758-864.
- Syracuse, E. M., Abers, G. A., 2006, Global compilation of variations in slab depth beneath arc volcanoes and implications: *Geochemistry, Geophysics, Geosystems*, v. 7, p. Q05017.
- van Hinsberg, V. 2001, Water-rock interaction and element fluxes in the Kawah Ijen Hyperacidic Crater Lake and the Banyu Pait river, east Java, Indonesia. M. Sc. Thesis, University of Utrecht, Netherlands, 299 pp.
- van Hinsberg, V., Berlo, K., van Bergen, M., Williams-Jones, A. E., 2010a, Extreme alteration by hyperacidic brines at Kawah Ijen volcano, East Java, Indonesia: I. Textural and mineralogical imprint: *Journal of Volcanology and Geothermal Research*, v. 198, p. 253-263.
- van Hinsberg, V., Berlo, K., Sumarti, S., van Bergen, M., and Williams-Jones, A. E., 2010b, Extreme alteration by hyperacidic brines at Kawah Ijen volcano, East Java, Indonesia: II. Metasomatic imprint and element fluxes: *Journal of Volcanology and Geothermal Research*, v. 196, p. 169-184.
- Witter, J. B., Kress, V. C., Delmelle, P., and Stix, J., 2004, Volatile degassing, petrology, and magma dynamics of the Villarrica Lava Lake, Southern Chile: *Journal of Volcanology and Geothermal Research*, v. 134, p. 303-337.

6: CONCLUSIONS

6.1 Volatile Transfer During Slab Subduction

Melt inclusion volatile and trace element ratios from mafic arc magmas in Indonesia (Kawah Ijen and Galunggung volcanoes) are compared to ratios in other mafic arc magmas from Mexico, Central America and Kamchatka. These volatile and trace elements are incompatible during the evolution of primary mantle melts to form the basalts and basaltic andesites erupted in arcs. As such, the use of incompatible element ratios allows for the comparison between magmas of variable source characteristics and degrees of differentiation. In order to constrain the nature of the subduction-derived enrichment at each arc volcano, these element ratios are compared to modeled mantle melt compositions after the addition of fluids/melts derived from the subducted slab. These fluids/melts are modeled as: 1) sediment-derived melts which can mobilize the moderately fluid-mobile elements such as La and Th, and which contain high concentrations of Ba and Pb, 2) H₂O-rich fluids derived from the dehydration of the altered oceanic crust (AOC), which are enriched in the most fluid-mobile elements, particularly Sr, and 3) H₂O-rich fluids, similar to those from the AOC, derived from the dehydration of the serpentinized oceanic lithosphere. These melts and fluids are modeled using published reservoir compositions (oceanic sediment, AOC and serpentinized mantle) and experimentally-derived solid-fluid and solid-melt partition coefficients at the pressures, temperatures and compositions of interest.

Positive correlations between slab surface temperature (H_2O/Ce), Cl and Sr are observed. Coupled with the high Sr/Ba ratio of most arc magmas, this suggests that most of the H_2O and Cl content of arc front magmas originates from the dehydration of the AOC. The involvement of H_2O and Cl derived from sediment melt is secondary to the AOC in most arc front magmas, although sediment melt does contribute to Ba, Pb, and LREE contents. The serpentinized mantle is likely to be an important source of H_2O -rich fluids only in arc segments with hot slab geotherms and steep slab dips such as Nicaragua, Central America. These results agree with thermo-mechanical models of fluid release in subduction zones and reinforce the role of melt inclusion studies as a complementary method of estimating the nature and amount of fluid release beneath arc volcanoes.

The source of sulphur and fluorine in arc magmas is not as easily discerned although a moderate correlation between Sr and S contents suggests that either some S is supplied by the dehydrating AOC, or S can be efficiently scavenged from the overlying meta-sediment layer by fluids rising up from the AOC. Highly variable S and F contents in subducted sediment (e.g., Wei et al., 2005; Alt et al., 1989), complex and poorly understood solubility mechanisms for S and F, respectively, and the lack of experimental studies on the mobility of S and F in subducted materials make it difficult to evaluate the source of these volatiles. More F analyses in melt inclusions from arc magmas and better constraints on S and F in slab and mantle components will improve our understanding of S and F recycling in subduction zones.

The different behaviours of H₂O, Cl, S and F in these arc magmas suggests that there is a preferred coupling of H₂O and Cl during slab dehydration/melting at sub-arc front depths, whereas S and F are partially to completely decoupled, respectively. As a result, enrichment of certain arc magmas in S or F is not primarily a function of fluid addition from the slab but is more likely to reflect anomalously S- or F-rich sediment sources or the involvement of metasomatized mantle. Kawah Ijen magmas are highly enriched in F compared to other arc magmas and have S and H₂O contents at the upper end of the range of magmas sampled. This mantle-derived enrichment is reflected in the composition of the volcanic gases emitted at Kawah Ijen (S-rich) and the nature of the mineral assemblage present in the magmas (F-rich apatite). Compared to Galunggung volcano, located above a different segment of the subducting Indian ocean plate, Kawah Ijen displays a higher degree of enrichment in volatile (H₂O, Cl, S) and fluid-mobile elements (Sr), reflecting higher AOC-derived fluid fluxes (4-5 wt% compared to ~ 1 wt% for Galunggung). The elevated H₂O and Sr contents of the Kawah Ijen magmas are comparable to some of the wettest volcanic front magmas worldwide (e.g., Mexico, Central America), which would suggest that the eastern Java arc may be one of the wettest cold slab subduction zones in the world.

6.2 Volatile Transfer During Magma Ascent Through the Crust and Degassing

The partitioning of the volatile elements between the melt and fluid phase upon ascent, degassing and crystallization of a magma is explored at both Sierra

Negra and Kawah Ijen. Contrasting tectonic settings impart different primary volatile ratios to the magmas. At Sierra Negra volcano, relatively dry mantle melts contain undegassed H₂O/CO₂ ratios that likely approach unity whereas at Kawah Ijen, fluid addition from the subducting slab imparts a higher H₂O/CO₂ ratio (up to 40) to the primary melts. In both systems, due to the relatively low solubility of CO₂ in calc-alkaline and alkaline basalts, fluid saturation occurs at depths of > 15 km and > 30 km at Kawah Ijen and Sierra Negra, respectively. The major difference between the two systems is that elevated H₂O contents at Kawah Ijen, which will result in H₂O-saturation of the magma at high pressures (\geq 200 MPa, corresponding to mid-upper crustal depths: \geq 7 km), whereas low H₂O contents at Sierra Negra (\leq 1 wt%) result in H₂O undersaturated conditions upon ascent of the magma until very shallow levels (< 1 km).

The suppression of H₂O degassing until very shallow levels and the overall lower fluid content of the hot-spot magmas facilitates their ascent through the crust and their emplacement into shallow sills/chambers without generating significant overpressures. Combined with elevated heat flow in hot-spot areas, which allows for more efficient accommodation of space in the crust, the conditions are favourable for the emplacement of large volumes of magma at shallow levels. At Sierra Negra, emplacement of originally deep-seated magma into shallow levels will lead to the exsolution and accumulation of large volumes of CO₂-rich gas at the top of the magma chamber creating a foam-like layer. Not modeled but also likely to contribute, is the effect of prolonged storage, cooling and crystallization of this magma during repose periods, eventually leading to

H₂O-saturation of the magma and exsolution of an additional H₂O-rich vapour. Modeling of the microgravity and elevation data in the years preceding the 2005 eruption of Sierra Negra suggests that this foam-like layer of highly vesicular magma was able to expand in response to elastic deformation of the magma chamber roof until overpressures exceeded the elastic strength of the surrounding rocks and a highly explosive initial eruptive phase began. The eruption lasted for 8 days and erupted aphyric basaltic lavas and tephra, representing the evacuation of 0.15 km³ of magma and a minimum of 0.07 km³ of gas from the uppermost level of the chamber. Witness accounts of the eruption do not report any visible change in the flux of gas emitted from the fumaroles prior to or during the 2005 eruption. This suggests that the hydrothermal system in the SE corner of the caldera is not directly connected to the active magma plumbing system.

At Kawah Ijen, melt inclusion H₂O and CO₂ contents record the ascent, degassing and crystallization of the basaltic magma from > 15 km depth to the surface. H₂O-saturation would normally be attained at mid-upper crustal levels (\geq 7 km depth), however, CO₂-rich vapour fluxing of the magma (system open to mass flux into the magma) causes the melt to lose H₂O and gain CO₂ (driving it away from H₂O-saturation) in an attempt to equilibrate with the vapour phase. This results in melt inclusions with highly variable H₂O/CO₂ ratios, most of them recorded at crystallization pressures of 200 MPa (~7 km depth). Vapour-fluxing of a magmatic system to the degree recorded at Kawah Ijen requires open system degassing conditions. The persistent flux of gas being emitted from the surface of

the volcano and through the crater lake attests to the open system nature of degassing at Kawah Ijen. No magmatic eruption has been recorded at Ijen for over 100 years yet degassing of the volcano has been persistent throughout this time. Such large volumes of degassed magma (up to 2.9 kg s^{-1}), unaccompanied by eruption, require a magmatic plumbing system which is highly permeable, open to the flux of both melt and gas from depths of at least 15 km. This contrasts greatly with Sierra Negra, where negligible permeability (but significant elastic accommodation) of the shallow crust during repose periods allows for significant gas and overpressures to develop, leading to periodic eruptions of gas-rich magma (~ every 10-30 years on average in the last 200 years). At Kawah Ijen, explosive magmatic eruptions will only occur if the permeability of the plumbing system is reduced enough to prevent the escape of magmatic vapours to the crater lake and the atmosphere, as well as drain back of degassed magma to deeper levels, or if magma intrusion rates increase significantly. This has not occurred for over 100 years and given the potential for highly explosive eruptions at Kawah Ijen, continued monitoring of the activity is imperative.

The volatile elements S, Cl and F play a minor role in the degassing budget of these two volcanoes due to substantially lower concentrations in the magmas. However, the exsolution of these volatile species from the melt upon ascent, degassing and evolution of magma has important consequences for both the composition of the gas phase at the surface and any hydrothermal fluids at depth. The relative concentration of these minor species as measured in the

surface gases can be used to track shallow magmatic processes and S is especially important because its flux at the surface can be measured, allowing estimates of the total volatile flux to be made if combined with gas phase volatile element ratios such as $\text{H}_2\text{O}/\text{SO}_2$ and CO_2/SO_2 . Obtaining these volatile ratios in the gas phase is not a trivial matter. Direct sampling of the gases emitted at the surface is only possible at some volcanoes and under certain levels of volcanic activity. Even then, there are issues which may lead to underestimates of the total volatile flux (see below). Another approach, used in this study, is to combine the melt inclusion data with theoretically- and experimentally-based models of degassing (vapour-melt partitioning of volatiles), which can allow for the magmatic gas phase to be estimated for different system conditions (e.g., style of degassing, depth of degassing, magma composition).

At Kawah Ijen, magmatic fluid compositions are modeled for various initial and final melt compositions and $\text{H}_2\text{O}-\text{CO}_2$ fluids fluxing the system using mass balance equations. Model outputs are partition coefficients for S and Cl between the melt and vapour phase at various pressures and for various melt compositions. The model that generates the highest $D^{\text{vap-melt}}$ values for S and Cl and the most realistic magmatic fluid composition is a basaltic magma evolving to a dacitic/rhyolitic magma with the system being fluxed with a fluid of composition $X_{\text{H}_2\text{O}} = 0.9$ originating (at least in part) from deeper mafic magma. Comparison of this model fluid with measured fumarole gas compositions suggests that the surface vapours are relatively enriched in S compared to the model fluid. Additionally, acid sulphate-chloride waters at Kawah Ijen are relatively depleted

in S and enriched in Cl and F compared to the model fluid composition. This suggests that upon ascent and cooling of the magmatic fluid, unmixing into a S-rich vapour and Cl- and F-rich acidic liquid occurs. Further cooling of the liquid phase and mixing with air-saturated groundwater and diffuse magmatic gases leads to the formation of highly acidic sulphate-chloride waters. The degassing flux recorded at the surface of the dome (25 tonnes day⁻¹ of SO₂) suggests rapid fluid rise rates within the shallow plumbing system beneath the dome, limiting cooling and interaction with groundwater. As a result, the elevated S contents of the magmatic fluid are mostly conserved until they are degassed at the surface (and through the crater lake bottom).

The combination of initially elevated magmatic S contents (> 2000 ppm), highly efficient exsolution of S during the evolution of basaltic to dacitic/rhyolitic magma and the limited scrubbing of fluid phase S by the hydrothermal system beneath the dome contribute to making Kawah Ijen one of the most productive active volcanic sulphur mines in the world.

6.3 Volatile Ratios in Volcanic Plumes and Effects of Cooling and Mixing with Air

The integration of various geochemical tools to sample and measure volcanic gases (direct fumarole “Giggenbach” sampling, plume MultiGAS sampling and FLYSPEC SO₂ flux determinations) allows for a more complete understanding of volcanic degassing at the surface and interactions with the atmosphere. Through this approach, this study reveals the potential for large underestimates in total SO₂ flux emitted from open-vent degassing arc volcanoes

when S deposition and near-vent oxidation of S species are important factors. High total S concentrations in the fumarole gases at Kawah Ijen lead to high temperature precipitation of native S in the plume, which may enhance heterogeneous oxidation of SO₂ and H₂S by atmosphere. This loss of SO₂ in the near-vent area results in disproportionately high H₂O/SO₂ and CO₂/SO₂ ratios measured in the plume. This can have important consequences for our understanding of the degassing process at depth. Furthermore, compared to other open vent arc volcanoes, Kawah Ijen ranks as a small edifice yet a very important S emitter not previously recognized due to significant S deposition and degassing through its crater lake.

Evidence for either near-vent, high temperature conversion of S species to aerosol compounds or high temperature S deposition at volcanoes needs to be taken into account. These processes can lead to very large underestimates of total gas and unerupted magma fluxes, which has important implications for modeling of magmatic plumbing systems such as convective overturn of degassed magma and storage / accommodation of unerupted magma in the mid- to upper-crust.

6.4 Concluding Remarks

The comparison of Sierra Negra and Kawah Ijen volcanoes reveals that differences in style of volcanic activity are primarily a function of magmatic plumbing system as opposed to differences in initial volatile content. In both cases, permeability of the crust and degassing style has exerted a dominant control over the style of activity. Eruptions at Sierra Negra, as well as at other

large basaltic volcanoes, are not necessarily associated with magma recharge into shallow reservoirs but can be caused by subtle changes in the pressure regime of a magma chamber, a process which is closely associated with degassing and crustal structure. Large explosive eruptions at Kawah Ijen are impeded by the open system (permeable) flow of magma and gas through the plumbing system. These results encourage more research into the link between degassing and crustal structure.

Possible factors leading to a change in the permeability of a magmatic system might include hydrothermal fluid interactions, emphasizing the need to devote more attention to the study of hydrothermal – magmatic gas interactions. Hydrothermal systems, when present, also play an important role in controlling/buffering the composition of the gases measured at the surface. This implies that measured gas compositions, routinely used as a monitoring tool, need to be carefully analysed for the influence of the hydrothermal system. The comparison of theoretically modeled gas compositions with actual measured compositions at open vent volcanoes is an effective approach to this problem. With continued study at a variety of volcanoes worldwide, we may find that hydrothermal systems are nearly ubiquitous, with very few volcanoes emitting gases that remain unaffected on-route to the surface. If surface gas compositions are to be effectively used as a monitoring tool for volcanic activity, these hydrothermal effects need to be better quantified.

APPENDICES

Appendix A

Table 6-1 Major and volatile element concentrations in basaltic glasses and melt inclusions from Sierra Negra^a

host/glass (wt%)	SNg1 glass	SNg2 glass	SN1 cpx	SN2 plag	SN3 plag	SN4 plag	SN4_2 plag
SiO ₂	47.5 ± 0.2	48.6 ± 0.2	45.9 ± 0.2	46.6 ± 0.3	48.0 ± 0.1	48.0 ± 0.1	48.0 ± 0.3
TiO ₂	3.19 ± 0.25	3.10 ± 0.31	2.39 ± 0.09	2.58 ± 0.16	3.21 ± 0.04	2.50 ± 0.11	2.38 ± 0.07
Al ₂ O ₃	13.2 ± 0.1	13.4 ± 0.0	17.6 ± 0.0	13.1 ± 0.1	12.9 ± 0.0	12.9 ± 0.0	12.9 ± 0.1
FeO _{total}	13.2 ± 0.1	12.5 ± 0.1	12.6 ± 0.2	12.3 ± 0.1	12.5 ± 0.1	11.7 ± 0.1	11.8 ± 0.1
MnO	0.23 ± 0.00	0.21 ± 0.01	0.19 ± 0.01	0.21 ± 0.01	0.22 ± 0.02	0.19 ± 0.02	0.19 ± 0.03
MgO	5.2 ± 0.1	5.6 ± 0.0	5.7 ± 0.2	6.9 ± 0.0	6.6 ± 0.1	7.2 ± 0.1	7.3 ± 0.2
CaO	9.5 ± 0.3	10.0 ± 0.1	8.8 ± 0.5	9.4 ± 0.2	9.9 ± 0.3	10.7 ± 0.2	10.6 ± 0.2
Na ₂ O	3.31 ± 0.25	2.99 ± 0.09	3.40 ± 0.14	4.74 ± 0.11	3.13 ± 0.11	2.92 ± 0.14	2.79 ± 0.21
K ₂ O	0.62 ± 0.06	0.54 ± 0.02	0.52 ± 0.04	0.53 ± 0.02	0.58 ± 0.08	0.42 ± 0.03	0.43 ± 0.02
P ₂ O ₅	0.41 ± 0.13	0.27 ± 0.15	0.27 ± 0.09	0.23 ± 0.15	0.31 ± 0.13	0.21 ± 0.14	0.22 ± 0.11
S	0.123 ± 0.012	0.153 ± 0.017	0.104 ± 0.030	0.161 ± 0.009	0.129 ± 0.019	0.118 ± 0.028	0.139 ± 0.007
Cl	0.058 ± 0.009	0.032 ± 0.007	0.020 ± 0.004	0.046 ± 0.003	0.024 ± 0.005	0.013 ± 0.010	0.022 ± 0.006
H ₂ O	1.03 ± 0.07	- ± -	0.90 ± 0.03	0.29 ± 0.06	0.97 ± 0.01	0.84 ± 0.00	0.80 ± 0.00
CO ₂ (ppm)	b.d.l. ± -	- ± -	375 ± 29	244 ± 4	269 ± 2	836 ± 3	850 ± 12

^a Major element and S, Cl analyses were conducted at the University of Oregon using a Cameca SX-100. Analytical conditions were as follows: 15 kV current, 10 nA beam intensity and a beam size of 5 µm. H₂O and CO₂ contents were determined at the University of Oregon using an FTIR. Total H₂O contents were determined from the 3550 cm⁻¹ peak only using an average glass density of 2.8 g ml⁻¹ and an absorption coefficient of 63. Absorption coefficient used for CO₂ was 370. See Appendix B for additional details of the methodology.

Appendix B

Sample preparation

The scoria deposits from tephra layers TO and OT are well sorted and overall clast size grades from ash to lapilli (Fig. 6-1). Texturally, the tephra consists of dense to moderately vesicular clasts, which are generally subrounded to angular. The tephra contains abundant, loose crystals of olivine up to 2 mm in length (Fig. 6-1), along with trace amounts of plagioclase (≤ 0.5 mm in length) both as loose crystals and within the scoria clasts. Rare clinopyroxene is also present. Olivine crystals are fragmented with numerous healed fractures and planes of secondary inclusions¹. The olivine lack any mineral inclusions (e.g., spinel) but contain abundant glassy primary melt inclusions suitable for analysis. Some opaque (devitrified) and partly crystallized melt inclusions¹ are also present (not analysed) and generally associated with cracks running through the olivine. Most of the glassy melt inclusions contain a small shrinkage bubble formed upon cooling and contraction of the melt (Fig. 6-1). A few melt inclusions contain larger (≥ 20 vol%) vapour bubbles (not analysed), suggesting that the magma was vapour saturated during melt inclusion entrapment. These two-phase inclusions are best described as “mixed” inclusions (Lowenstern, 1995). Details of the morphologies, dimensions and

¹ Secondary inclusions are defined as occurring along a healed fracture plane once the crystal has stopped growing from a silicate melt (Roedder, 1984; Lowenstern, 1995). They may consist of fluid, melt, or a mixture of two or more phases. These were too small to characterize. Primary inclusions are defined as occurring during crystal growth (Lowenstern, 1995) and generally occur in “random” distribution within a crystal (Roedder, 1984).

other characteristics of the melt inclusions analysed in this study are given in Figure 6-1 and Table 6-2.

Olivine crystals were hand-picked from tephra samples (~ 250 crystals) and viewed under the microscope in immersion oil with an index of refraction of 1.675 in order to select melt inclusions for analysis. Crystals with suitable melt inclusions (< 10% of olivine crystals observed) were ground and polished into wafers with the melt inclusion doubly intersected. Final wafer thickness varied from 15 to 90 μm .

Infrared spectroscopy

Transmission spectra were collected in the range 650 to 6000 cm^{-1} , and for most melt inclusions, absorbance at $\sim 3550 \text{ cm}^{-1}$, corresponding to the fundamental O-H stretching vibration, was used to obtain total water content. For inclusions which saturated at the 3550 cm^{-1} band, the combination of the molecular H_2O and hydroxyl (OH-T; T=Si, Al, etc. ;) stretching and bending modes at $\sim 5200 \text{ cm}^{-1}$ and $\sim 4500 \text{ cm}^{-1}$ respectively, was used. Absorbance peak heights were measured after fitting a straight line background for the 3500 cm^{-1} peak and a curved background for the 4500 and 5200 cm^{-1} peaks. The curved background in the region of $3700\text{-}6000 \text{ cm}^{-1}$ is a result of a broad peak centered around $5500\text{-}5700 \text{ cm}^{-1}$ corresponding to crystal-field transitions of Fe^{2+} , as well as influence from a small water-related band at $\sim 4000 \text{ cm}^{-1}$ (Stolper, 1982). To fit this curved background, two Gaussian curves, one centered around 5600 cm^{-1} and the other around 4000 cm^{-1} , were fit following the method of Ohlhorst et al. (2001).

Dissolved carbonate (CO_3^{2-}) was measured from the absorbance value of the bands at 1430 and 1515 cm^{-1} , which correspond to antisymmetric stretching of distorted carbonate groups (Dixon et al., 1995). Due to the complex shape of the background in the region of the carbonate doublet, it is necessary to subtract a carbonate-free reference spectrum to obtain a flat background. A peak-fitting program that fits the sample spectrum with a straight line, a devolatilized spectrum, a pure 1630 cm^{-1} band for molecular H_2O , and a pure carbonate doublet was used (unpublished program by S. Newman).

Absorbances were converted to concentrations using the Beer-Lambert law. Glass densities were calculated at room temperature using the method described by Luhr (2001) and range from 2.60 to 2.75 g ml^{-1} . For the $\sim 3550 \text{ cm}^{-1}$ band, an absorption coefficient (ϵ) value of 63 $\text{L mol}^{-1} \text{ cm}^{-1}$ (standard for basalts) was used (Dixon et al., 1995). Absorption coefficients for the 4500 and 5200 cm^{-1} peaks are from Yamashita et al. (1997) for a high-Al basalt similar in composition to the Ijen basalts. Total H_2O values obtained from the 3550 cm^{-1} band and the 4500 and 5200 cm^{-1} bands are within 0.4 wt% of each other on average. Absorption coefficients for the carbonate doublet were calculated for each melt inclusion using the equation of Dixon & Pan (1995) and the uncorrected melt inclusion Na and Ca molar concentrations. Values range from 331 to 383 $\text{L mol}^{-1} \text{ cm}^{-1}$.

The thickness of each inclusion was obtained via two methods. The first was to collect a reflectance spectrum of the olivine crystal next to the inclusion and following the method described by Nichols & Wysoczanski (2007), convert

the spacing of the interference fringes to wafer thickness. The refractive index of each crystal was obtained from the composition (forsterite content) of the olivine.

The second method involved mounting the edge of the crystal on the tip of a needle using crystal bond. The crystal was then immersed into a glass holder filled with refractive index oil ($n = 1.67$). The wafer could then be rotated so that its width was perpendicular to the field of view of the microscope. Using the calibrated microscope ocular, the thickness of the inclusion was measured with an average accuracy of $\pm 5 \mu\text{m}$. The two techniques agree within 30 % of each other on average. We found a much lower standard deviation using the reflectance method (multiple olivine reflectance spectrum collected around the melt inclusion) and used those preferred measurements when possible.

Electron microprobe

Olivine major element composition was analysed using a focused beam, 15 kV and a 30 nA current. On-peak counting times were ≥ 60 s for all elements analysed. Beam conditions for melt inclusion major element and volatile (S, Cl, F) analysis were: 15 kV, 10 nA current for all elements except for Ti, P, S, Cl and F, for which a 50 nA current and a 10 μm diameter beam were used. On-peak counting times for the melt inclusions were as follows: 60 s for Fe; 40 s for Na, K and Al; 30 s for Si and Mg; 20 s for Ti, Ca, P, S, Cl and F. Sulphur peak position was set to a wavenumber corresponding to 2/3 of the wavelength distance between pyrite and anhydrite based on detailed determination of the S peak position of the glasses (see below). The glass standards BIR-16 and NBS K-412

were run as unknown samples, and analysed versus published compositions (Appendix B Table 6-2).

S K α peak positions were determined by performing detailed wavescans on all five spectrometers with a beam voltage of 15 kV, current of 50 nA and a 5 μ m beam diameter. Anhydrite, pyrite and pyrrhotite standards were analysed at the beginning and end of each melt inclusion wavescan. The standard wavescans were performed by counting 10 s per step for 100 steps, each step representing a shift of 5 wavenumbers. The melt inclusions were analysed for 60 s per step for 100 steps. The beam was moved 1 μ m every minute to minimize the effects of auto-oxidation or reduction (Rowe et al., 2007; Jugo et al., 2007). A Gaussian curve was fitted to each spectra to obtain the peak position.

References

- Dixon, J.E., Pan, V., 1995. Determination of the molar absorptivity of dissolved carbonate in basaltic glass. *Am. Mineral.* 80 (11-12), 1339-1342.
- Dixon, J.E., Stolper, E.M., Holloway, J.R., 1995. An experimental study of water and carbon dioxide solubilities in mid-ocean ridge basaltic liquids. Part I: Calibration and solubility models. *J. Petrol.* 36 (6), 1607-1631.
- Jugo, P. J., Wilke, M., Susini, J., 2007. Disequilibrium experiments and micro-XANES analysis: Novel tools to unravel the speciation of sulfur in silicate melts. *Eos Trans. AGU* 88 (52) Fall Meet. Suppl. Abstract V22B-04.
- Luhr, J.F. 2001. Glass inclusions and melt volatile contents at Parícutin Volcano, Mexico. *Contrib. Mineral. Petrol.* 142 (3), 261-283.
- Lowenstern, J.B., 1995. Applications of silicate melt inclusions to the study of magmatic volatiles. In: J.F.H. Thompson (ed). *Magmas, Fluids and Ore Deposits*. Mineralogical Association of Canada Short Course 23, 71-99.
- Nichols, A.R.L., Wysoczanski, R.J., 2007. Using micro-FTIR spectroscopy to measure volatile contents in small and unexposed inclusions hosted in olivine crystals. *Chem. Geol.* 242 (3), 371-384.

- Ohlhorst, S., Behrens, H., Holtz, F., 2001. Compositional dependence of molar absorptivities of near-infrared OH-and H₂O bands in rhyolitic to basaltic glasses. *Chem. Geol.* 174 (1-3), 5-20.
- Roedder, E., 1984. *Fluid inclusions: Reviews in Mineralogy* vol. 12, Mineral Society of America.
- Rowe, M.C., Kent, A.J.R., Nielsen, R.L., 2007. Determination of sulfur speciation and oxidation state of olivine hosted melt inclusions. *Chem. Geol.* 236 (3-4), 303-322.
- Stolper, E. 1982. Water in silicate glasses: An infrared spectroscopic study. *Contrib. Mineral. Petrol.* 81 (1), 1-17.
- Yamashita, S., Kitamura, T., Kusakabe, M., 1997. Infrared spectroscopy of hydrous glasses of arc magma compositions. *Geochem. J.* 31 (3), 169–174.

Table 6-2 Analyzed olivine-hosted melt inclusion compositions from Kawah Ijen (uncorrected for post-entrapment modification)

	OT-1-1	1 σ	OT-1-2	1 σ	OT-1-3	1 σ	OT-1-4	1 σ	OT-1-6	1 σ	OT-1-8	1 σ
(wt.%)												
SiO ₂	46.5	\pm 0.26	44.9	\pm 0.17	45.1	\pm 0.12	45.6	\pm 0.09	45.6	\pm 0.23	46.1	\pm 0.06
TiO ₂	1.34	\pm 0.00	0.75	\pm 0.01	1.09	\pm 0.03	1.09	\pm 0.03	1.00	\pm 0.03	0.97	\pm 0.03
Al ₂ O ₃	18.0	\pm 0.04	18.8	\pm 0.19	17.5	\pm 0.84	19.1	\pm 0.47	18.1	\pm 0.48	18.1	\pm 0.18
FeO ^T	9.3	\pm 0.16	10.0	\pm 0.04	9.8	\pm 0.24	9.4	\pm 0.13	10.1	\pm 0.06	10.0	\pm 0.09
MnO	0.18	\pm 0.01	0.20	\pm 0.00	0.18	\pm 0.00	0.17	\pm 0.01	0.15	\pm 0.02	0.18	\pm 0.01
MgO	4.8	\pm 0.07	5.9	\pm 0.11	5.2	\pm 0.02	4.2	\pm 0.04	5.8	\pm 0.05	6.3	\pm 0.05
CaO	10.6	\pm 0.06	10.4	\pm 0.08	11.0	\pm 0.15	11.4	\pm 0.03	10.7	\pm 0.01	10.4	\pm 0.03
Na ₂ O	2.00	\pm 0.07	1.83	\pm 0.01	1.82	\pm 0.32	1.96	\pm 0.22	2.52	\pm 0.04	2.64	\pm 0.08
K ₂ O	0.63	\pm 0.00	0.49	\pm 0.00	0.62	\pm 0.01	0.65	\pm 0.00	0.60	\pm 0.02	0.58	\pm 0.00
P ₂ O ₅	0.45	\pm 0.04	0.35	\pm 0.04	0.32	\pm 0.04	0.35	\pm 0.01	0.32	\pm 0.01	0.30	\pm 0.00
S	0.187	\pm 0.04	0.111	\pm 0.02	0.204	\pm 0.05	0.211	\pm 0.04	0.190	\pm 0.03	0.159	\pm 0.00
Cl	0.082	\pm 0.00	0.069	\pm 0.00	0.094	\pm 0.01	0.103	\pm 0.01	0.088	\pm 0.02	0.087	\pm 0.00
F	0.080	\pm 0.00	0.125	\pm 0.01	0.101	\pm 0.00	0.109	\pm 0.02	0.102	\pm 0.01	0.146	\pm 0.01
H ₂ O	3.62	\pm 0.07	5.09	\pm 0.02	4.12	\pm 0.00	6.26	\pm 0.06	3.94	\pm 0.02	3.56	\pm 0.00
CO ₂	0.113	\pm 0.004	0.029	\pm 0.003	0.100	\pm 0.006	0.123	\pm 0.017	0.133	\pm 0.033	0.135	\pm 0.004

(wt.%)	TO-I	1 σ	TO-VIII	1 σ	TO-IX	1 σ	TO-XI	1 σ	TO-XIV	1 σ	TO-XV	1 σ
SiO ₂	45.8	± 0.07	45.5	± 0.43	48.5	± 0.33	45.5	± 0.11	45.4	± 0.05	46.7	± 0.32
TiO ₂	1.07	± 0.02	1.03	± 0.04	1.27	± 0.01	1.05	± 0.04	1.07	± 0.01	1.01	± 0.01
Al ₂ O ₃	18.5	± 1.06	18.4	± 0.54	17.0	± 0.24	17.7	± 0.75	18.1	± 0.40	19.4	± 0.16
FeO ^T	10.0	± 0.19	10.0	± 0.06	11.1	± 0.33	10.0	± 0.11	10.2	± 0.27	9.4	± 0.07
MnO	0.17	± 0.00	0.18	± 0.00	0.21	± 0.01	0.16	± 0.00	0.17	± 0.01	0.17	± 0.01
MgO	5.2	± 0.24	5.8	± 0.06	4.1	± 0.07	5.2	± 0.23	5.2	± 0.20	4.6	± 0.16
CaO	10.6	± 0.04	10.7	± 0.01	10.3	± 0.08	10.4	± 0.17	10.5	± 0.09	10.7	± 0.01
Na ₂ O	1.95	± 0.27	2.08	± 0.13	3.10	± 0.25	1.66	± 0.40	1.63	± 0.36	1.48	± 0.04
K ₂ O	0.65	± 0.01	0.63	± 0.00	0.93	± 0.01	0.62	± 0.01	0.61	± 0.01	0.73	± 0.03
P ₂ O ₅	0.33	± 0.02	0.34	± 0.02	0.37	± 0.05	0.33	± 0.04	0.31	± 0.03	0.27	± 0.00
S	0.222	± 0.05	0.198	± 0.04	0.147	± 0.02	0.221	± 0.05	0.216	± 0.04	0.202	± 0.00
Cl	0.097	± 0.02	0.091	± 0.02	0.104	± 0.01	0.101	± 0.01	0.095	± 0.01	0.104	± 0.00
F	0.132	± 0.02	0.100	± 0.01	0.120	± 0.01	0.117	± 0.02	0.113	± 0.01	0.085	± 0.02
H ₂ O	4.24	± 0.06	5.29	± 0.02	1.65	± 0.02	6.45	± 0.36	7.25	± 1.06	4.59	± 0.05
CO ₂	0.101	± 0.005	0.070	± 0.007	0.044	± 0.004	0.131	± 0.004	0.169	± 0.010	0.089	± 0.000

	TO-XVI	1 σ	TO-XVII	1 σ	TO-XVIII	1 σ	TO-XIX	1 σ	TO-XX	1 σ	TO-XXII	1 σ
(wt.%)												
SiO ₂	44.6	\pm 0.32	45.7	\pm 0.14	47.3	\pm 0.06	45.3	\pm 0.11	44.9	\pm 0.04	44.5	\pm 0.23
TiO ₂	1.00	\pm 0.04	1.01	\pm 0.01	1.25	\pm 0.05	1.06	\pm 0.02	1.02	\pm 0.07	1.03	\pm 0.00
Al ₂ O ₃	18.3	\pm 0.00	19.4	\pm 0.07	19.5	\pm 0.07	19.2	\pm 0.21	18.8	\pm 0.01	19.3	\pm 0.18
FeO ^T	10.1	\pm 0.42	9.5	\pm 0.39	8.6	\pm 0.07	9.9	\pm 0.24	9.6	\pm 0.13	10.2	\pm 0.06
MnO	0.19	\pm 0.00	0.17	\pm 0.01	0.15	\pm 0.02	0.18	\pm 0.00	0.17	\pm 0.00	0.17	\pm 0.01
MgO	6.6	\pm 0.02	4.8	\pm 0.19	3.7	\pm 0.03	5.5	\pm 0.03	6.6	\pm 0.06	5.4	\pm 0.15
CaO	10.7	\pm 0.00	10.8	\pm 0.03	12.2	\pm 1.24	10.7	\pm 0.01	10.5	\pm 0.05	11.2	\pm 1.16
Na ₂ O	1.69	\pm 0.04	1.50	\pm 0.17	3.61	\pm 0.01	1.64	\pm 0.06	1.60	\pm 0.07	1.77	\pm 0.66
K ₂ O	0.56	\pm 0.03	0.66	\pm 0.01	0.83	\pm 0.00	0.62	\pm 0.01	0.56	\pm 0.01	0.57	\pm 0.00
P ₂ O ₅	0.24	\pm 0.01	0.28	\pm 0.00	0.34	\pm 0.00	0.26	\pm 0.00	0.26	\pm 0.00	0.26	\pm 0.00
S	0.200	\pm 0.00	0.205	\pm 0.00	0.212	\pm 0.00	0.215	\pm 0.00	0.205	\pm 0.00	0.218	\pm 0.01
Cl	0.099	\pm 0.00	0.106	\pm 0.01	0.129	\pm 0.00	0.107	\pm 0.00	0.100	\pm 0.00	0.103	\pm 0.00
F	0.100	\pm 0.01	0.101	\pm 0.03	0.129	\pm 0.04	0.146	\pm 0.03	0.151	\pm 0.01	0.140	\pm 0.03
H ₂ O	4.62	\pm 0.03	3.92	\pm 0.00	0.23	\pm 0.00	4.04	\pm 0.00	4.91	\pm 0.02	3.55	\pm 0.11
CO ₂	0.074	\pm 0.001	0.133	\pm 0.003	0.038	\pm 0.016	0.089	\pm 0.002	0.131	\pm 0.006	0.102	\pm 0.003

	TO-XXIII	1 σ	TO-XXIV	1 σ	TO-XXV	1 σ	K-412	1 σ	<i>Pub.</i>	BIR-16	1 σ	<i>Pub.</i>
(wt.%)												
SiO ₂	45.6	± 0.15	43.7	± 0.78	45.7	± 0.19	45.4	± 0.29	45.4	47.3	± 0.38	47.3
TiO ₂	1.09	± 0.04	1.07	± 0.05	1.02	± 0.01	0.00	± 0.01	-	0.93	± 0.02	0.96
Al ₂ O ₃	18.6	± 0.00	19.6	± 0.48	19.0	± 0.02	9.4	± 0.09	9.3	15.7	± 0.20	15.4
FeO ^T	10.0	± 0.01	9.5	± 0.21	9.6	± 0.14	10.1	± 0.41	10.0	10.2	± 0.23	-
MnO	0.18	± 0.01	0.17	± 0.01	0.17	± 0.01	0.08	± 0.01	0.10	0.17	± 0.01	0.17
MgO	5.5	± 0.16	4.5	± 0.48	5.8	± 0.04	19.4	± 0.12	19.3	9.6	± 0.06	9.5
CaO	11.2	± 0.07	11.3	± 0.07	10.8	± 0.01	15.3	± 0.04	15.3	13.3	± 0.05	13.1
Na ₂ O	1.93	± 0.08	1.80	± 0.02	2.04	± 0.06	0.06	± 0.01	0.06	1.84	± 0.04	1.71
K ₂ O	0.58	± 0.02	0.59	± 0.02	0.58	± 0.01	0.00	± 0.01	-	0.02	± 0.01	0.04
P ₂ O ₅	0.27	± 0.00	0.27	± 0.00	0.26	± 0.01	0.13	± 0.06	-	0.11	± 0.05	-
S	0.214	± 0.00	0.209	± 0.01	0.204	± 0.00	0.001	± 0.00	-	0.001	± 0.00	-
Cl	0.107	± 0.00	0.138	± 0.03	0.101	± 0.00	0.001	± 0.00	-	0.001	± 0.00	-
F	0.162	± 0.01	0.154	± 0.00	0.133	± 0.03	0.007	± 0.01	-	0.007	± 0.03	-
H ₂ O	-	± -	3.95	± 0.03	3.44	± 0.04	-	± -	-	-	± -	-
CO ₂	-	± -	0.110	± 0.004	0.091	± 0.009	-	± -	-	-	± -	-

(ppm)	OT-1-1	OT-1-2	OT-1-3	OT-1-4	OT-1-6	OT-1-8	TO-I	TO-VIII	TO-IX .	TO-XI	TO-XIV	TO-XV	TO-XVI
Rb	9.24	7.60	10.48	12.42	9.98	8.05	11.42	12.08	18.61	9.71	10.17	12.66	8.60
Ba	214	146	215	209	198	200	192	216	281	195	192	209	172
Th	0.86	0.87	0.87	1.09	1.09	0.72	1.07	1.10	1.97	0.91	0.95	1.43	0.90
U	0.22	0.14	0.23	0.19	0.28	0.21	0.32	0.36	0.56	0.27	0.25	0.48	0.18
Nb	2.02	1.36	2.58	2.05	2.19	1.95	2.45	2.45	3.15	2.07	1.92	2.57	1.79
Ta	0.07	0.04	0.14	0.07	0.13	0.11	0.10	0.04	0.22	0.07	0.06	0.12	bdl
La	8.64	6.15	8.20	7.72	7.21	6.19	7.99	8.21	11.75	8.30	8.65	9.27	6.55
Pb	4.39	2.81	3.87	4.12	3.43	3.50	3.78	4.76	6.74	4.04	4.50	4.43	4.06
Ce	20.66	14.20	19.28	22.67	19.15	18.02	20.90	23.11	28.85	20.76	19.97	20.94	16.21
Sr	576	573	531	568	527	532	510	549	517	544	536	518	466
Pr	2.86	1.97	2.54	2.63	2.62	2.14	2.76	2.74	3.64	2.68	2.48	2.60	1.94
Nd	13.38	8.31	11.54	12.38	10.23	9.08	11.91	10.62	17.05	12.90	13.12	12.14	9.45
Zr	38	28	40	36	35	30	45	35	59	37	37	46	31
Hf	0.67	0.92	0.97	1.11	1.23	0.90	1.12	1.26	1.63	1.20	1.06	0.98	1.12
Sm	3.09	2.20	2.87	3.02	2.98	2.74	3.18	2.53	3.80	2.70	3.14	3.18	1.79
Eu	1.34	0.77	1.05	1.21	1.04	0.91	1.20	1.23	1.36	1.07	1.01	1.09	0.88
Gd	2.69	1.97	3.57	3.39	3.01	2.34	3.44	1.88	3.61	2.77	2.23	2.70	1.38
Ti	8574	4735	7185	6563	5972	6146	6135	6487	8041	6351	6619	6063	6016
Dy	2.95	1.87	2.62	2.71	2.75	2.34	3.12	2.42	3.56	2.96	2.92	2.38	2.22
Li	7.53	7.76	6.83	8.09	6.34	6.68	7.78	6.68	13.00	6.88	7.93	6.67	7.21
Y	15.05	11.39	15.08	13.26	14.01	12.59	17.48	12.34	18.25	13.49	14.72	15.16	13.29
Yb	1.02	1.17	1.48	1.23	1.36	1.32	1.69	1.62	2.53	1.47	1.08	1.45	1.32

	TO-XVII	TO-XVIII	1 σ	TO-XIX	TO-XX	TO-XXII	TO-XXIII	TO-XXIV	TO-XXV	BHVO-2G		<i>Pub.</i>		
(ppm)														
Rb	12.11	10.75	\pm 0.00	9.26	8.25	8.51	9.85	8.05	9.78	8.93	\pm 0.55	9.20	\pm 0.04	
Ba	192	203	\pm 3	176	171	161	185	169	171	124	\pm 1	131	\pm 2	
Th	1.28	1.07	\pm 0.33	1.06	0.99	1.05	0.89	0.76	0.92	1.22	\pm 0.04	1.22	\pm 0.05	
U	0.34	0.31	\pm 0.00	0.24	0.17	0.25	0.27	0.18	0.23	0.45	\pm 0.06	0.40	\pm 0.00	
Nb	2.25	2.01	\pm 0.11	1.85	1.66	1.73	1.91	1.77	1.73	15.84	\pm 0.32	18.30	\pm 0.80	
Ta	0.07	bdl	\pm -	0.09	bdl	0.08	0.13	0.07	bdl	0.97	\pm 0.01	1.15	\pm 0.10	
La	8.39	9.11	\pm 0.08	8.11	7.69	7.98	7.61	7.16	7.36	14.12	\pm 0.17	15.20	\pm 0.20	
Pb	4.02	4.25	\pm 0.29	3.56	3.51	3.56	4.20	4.42	3.84	1.78	\pm 0.38	1.70	\pm 0.20	
Ce	20.03	20.52	\pm 1.34	16.95	16.79	17.35	19.86	18.90	18.78	35.71	\pm 0.54	37.60	\pm 0.20	
Sr	522	591	\pm 15	503	488	487	510	503	488	375	\pm 5	396	\pm 1	
Pr	2.38	2.76	\pm 0.21	2.49	2.07	2.13	2.51	2.38	2.63	4.95	\pm 0.20	5.35	\pm 0.22	
Nd	12.09	14.11	\pm 1.37	10.07	11.73	11.13	12.15	11.17	8.57	24.11	\pm 0.64	24.50	\pm 0.20	
Zr	40	49	\pm 1	40	39	36	37	32	34	151	\pm 4	170	\pm 7	
Hf	1.02	1.22	\pm 0.28	1.04	1.08	1.21	0.97	1.09	0.99	3.65	\pm 0.20	4.32	\pm 0.18	
Sm	3.22	2.68	\pm 0.16	2.95	2.54	3.51	3.27	2.78	2.62	5.16	\pm 0.02	6.10	\pm 0.03	
Eu	0.93	1.29	\pm 0.38	0.96	1.03	0.95	1.20	0.92	1.06	1.85	\pm 0.13	2.07	\pm 0.01	
Gd	1.99	3.41	\pm 0.42	2.99	2.38	2.42	2.48	2.59	1.67	5.33	\pm 0.47	6.16	\pm 0.05	
Ti	6205	6688	\pm 197	6037	5959	5895	6226	6160	5964	15971	\pm 135	16300	\pm 900	
Dy	2.23	2.71	\pm 0.11	3.17	2.39	2.49	2.40	2.61	2.64	4.47	\pm 0.29	5.28	\pm 0.05	
Li	7.85	6.71	\pm 3.03	4.90	6.02	5.69	7.99	7.05	7.78	4.62	\pm 0.47	4.40	\pm 0.80	
Y	13.71	17.79	\pm 1.67	14.80	14.93	15.70	13.47	13.54	13.45	21.41	\pm 0.71	26.00	\pm 2.00	
Yb	1.49	2.03	\pm 0.48	1.24	1.34	1.36	1.11	1.34	1.41	1.63	\pm 0.22	2.01	\pm 0.02	

Table 6-3 Description of melt inclusions analysed from Kawah Ijen

Sample	Shape	Type	Texture	Crystals ^a	Length (µm)	Width (µm)	Thick. min. (µm) ^b	Error ^c	Thick. max. (µm) ^d
OT-1-1	Sphere	primary	glassy	none	94	92	90	0.7	92
OT-1-2	Negative	primary	glassy	opaque	135	115	30	5	115
OT-1-3	Ellipsoid - Negative	primary	glassy	opaque	125	85	39	9	85
OT-1-4	Ellipsoid - Negative	primary	glassy	opaque	135	123	30	5	123
OT-1-6	Sphere-Negative	primary	glassy	none	192	185	15	0.7	185
OT-1-8	Irregular	primary	glassy	opaque	230	230	40	0.7	230
TO-I	Sphere	primary	glassy	none	80	60	60	0.7	60
TO-VIII	Sphere	primary	glassy	none	100	90	40	28	90
TO-IX .	Irregular	embayment	glassy	none	-	-	80	28	-
TO-XI	Sphere	primary	glassy	daughter	125	110	65	5	110
TO-XIV	Ellipsoid	primary	glassy	none	160	100	77	2.8	100
TO-XV	Negative	primary	glassy	none	200	140	50	0.7	140
TO-XVI	Ellipsoid	primary	glassy	none	280	220	31	0.7	220
TO-XVII	Negative	primary	glassy	none	140	120	49	0.7	120
TO-XVIII	Ellipsoid - Negative	primary	glassy	none	110	90	46	1.4	90
TO-XIX	Ellipsoid - Negative	primary	glassy	none	120	100	58	0	100
TO-XX	Ellipsoid	primary	glassy	quench	200	160	44	0	160
TO-XXII	Ellipsoid	primary	glassy	none	130	90	36	0.7	90
TO-XXIII	Negative	primary	glassy	opaque	200	180	-	-	180
TO-XXIV	Negative	primary	glassy	opaque	140	90	40	0	90
TO-XXV	Ellipsoid	primary	glassy	daughter	105	70	42	0	70

^a Visible daughter or quench crystals

^b Thickness of inclusion ground down for FTIR. Thickness determined either via the olivine reflectance method and/or the optical needle technique.

^c Either the standard deviation between the needle and spectra techniques, between two repeat spectra or the standard error for the needle technique.

^d Thickness of inclusion assuming equal length b and c axes of ellipsoid/negative crystal shape.

Sample	Vapor bubble diam. (μm)	Vapor bubble max. (vol. %)	Vapor bubble min. (vol. %)	Comment
OT-1-1	32	0.8	0.5	
OT-1-2	58	2.6	1.4	small opaque in corner of melt inclusion
OT-1-3	29	0.5	0.3	
OT-1-4	30	0.3	0.2	faceted inclusion exterior/shell
OT-1-6	65	1.6	0.5	small crystals inside bubble wall
OT-1-8	58	0.8	0.2	very dark brown glass, nearly opaque to light in center
TO-I	20	0.3	0.3	
TO-VIII	30	0.9	0.4	2 phase vapor bubble (contains crystals)
TO-IX .	none	-	-	visibly connected to the surface
TO-XI	35	0.6	0.4	
TO-XIV	35	0.4	0.3	near cracks, tiny crystals on edge of shrinkage bubble
TO-XV	50	1.1	0.4	near cracks, inclusion is faceted (negative crystal shape)
TO-XVI	110	8.7	1.2	near cracks, tiny crystals on edge of shrinkage bubble
TO-XVII	35	0.7	0.3	
TO-XVIII	45	2.5	1.3	2 radiating cracks leading away, faceted exterior/shell
TO-XIX	40	1.1	0.7	near cracks
TO-XX	50	1.1	0.3	tiny quench crystals in corner of inclusion and bubble wall
TO-XXII	20	0.2	0.1	faceted inclusion exterior/shell
TO-XXIII	60		0.4	maybe a small clear crystal on edge of inclusion
TO-XXIV	30	0.7	0.3	
TO-XXV	25	0.6	0.4	small daughter crystals on edge of inclusion

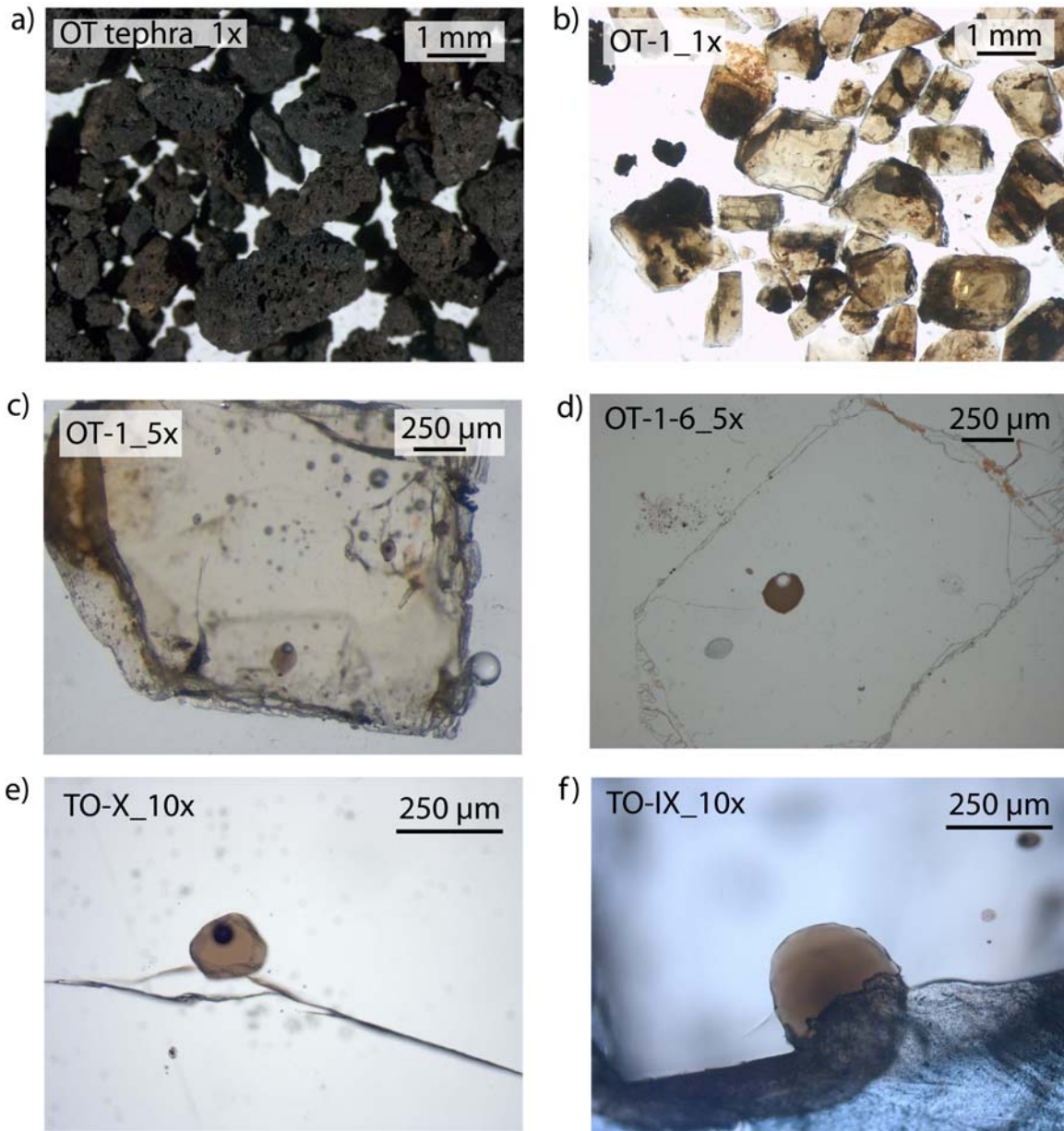


Figure 6-1 Microphotographs of a) tephra, b-c) olivine crystals and d-f) melt inclusions from sample layers OT and TO at Kawah Ijen. Crack running through melt inclusion in e) was produced during the grinding process to expose the melt inclusion. Melt inclusion f) is an embayed melt inclusion, connected to the surrounding groundmass.

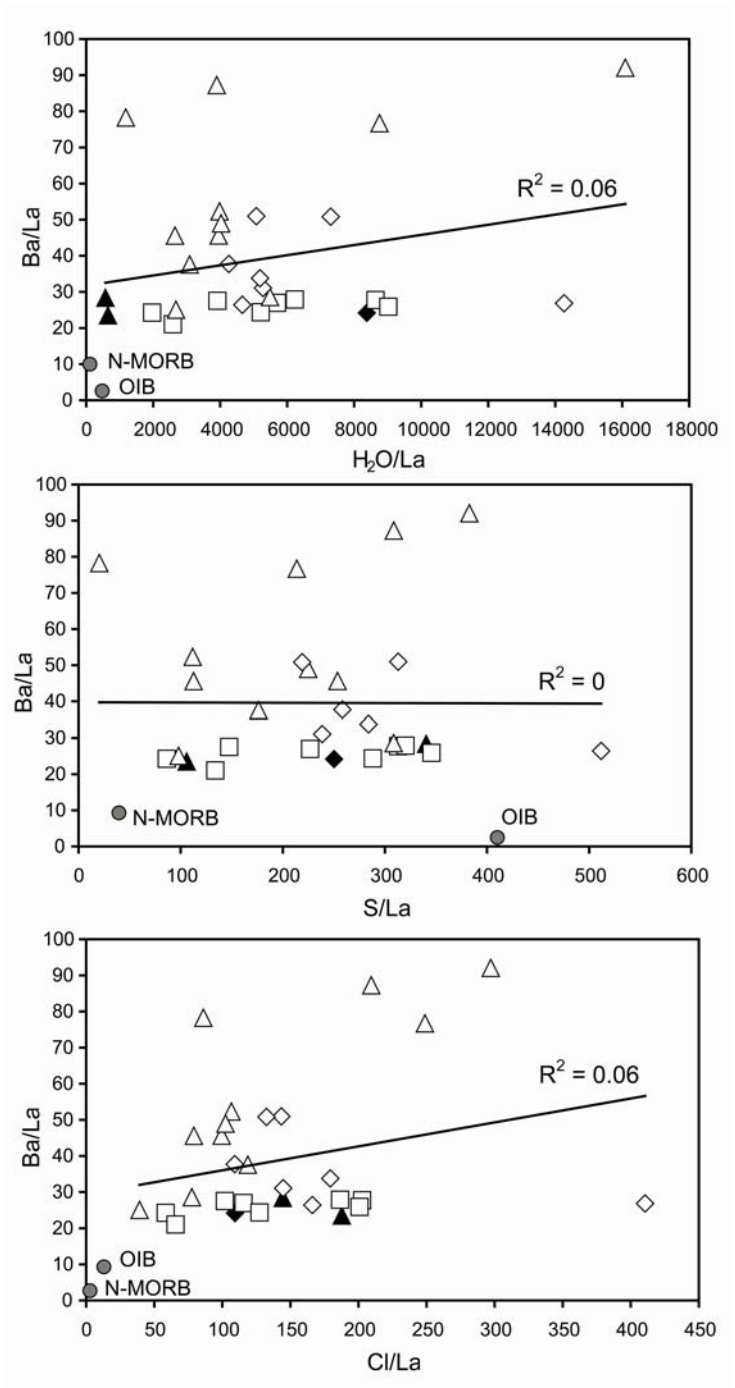


Figure 6-2 Ba contents versus volatile elements (both normalized to La). Data sources are the same as in Figure 3-9.

Appendix C

Modeling procedure for $D^{\text{vap-melt}}$ values

The following details of the degassing modeling are modified slightly from Johnson et al. (2010). The modeling procedure is described for S, Cl or F degassing although F was not modeled due to the presence of F-rich apatite in the Kawah Ijen magmas (Chapter 4).

The melt inclusion data is used to calculate apparent vapour-melt distribution coefficients during degassing according to both open- and closed-system degassing models, as described below. The approach is generally similar to that of Spilliaert et al. (2006). In all calculations, the bulk distribution coefficient, \bar{D}_i (where $i = \text{S, Cl or F}$) is defined as:

$$\bar{D}_i = \sum W_A D_i^A = W_{\text{xtl}} D_i^{\text{xtl-melt}} + W_{\text{vap}} D_i^{\text{vap-melt}} \quad (1)$$

where W_A is the weight fraction of phase A (where $A = \text{crystals or vapour}$) in the assemblage of crystals and vapour that form by crystallization and degassing, and $D_i^{\text{xtl-melt}}$ and $D_i^{\text{vap-melt}}$ are the distribution coefficients of element i in the crystals and vapour, respectively. We further assume that no S, Cl or F goes into any crystallizing phases, and therefore equation 1 simplifies to:

$$\bar{D}_i = W_{\text{vap}} D_i^{\text{vap-melt}} \quad (2)$$

Open-system degassing

We use the Rayleigh fractionation equation:

$$\frac{C_i^f}{C_i^i} = F^{(\bar{D}_i - 1)} \quad (3)$$

where C_i^i and C_i^f are the initial and final concentrations of element i ,

$$F = X_{melt} = 1 - X_{xtl} - X_{vap} = C_{K_2O}^i / C_{K_2O}^f \quad (4)$$

(X represents the mass fractions of crystals and vapour at the end of crystallization relative to an initial condition of 100% melt), and

$$W_{xtl} = \frac{X_{xtl}}{X_{xtl} + X_{vap}} \quad (5a)$$

$$W_{vap} = \frac{X_{vap}}{X_{xtl} + X_{vap}} \quad (5b)$$

Note that use of the Rayleigh fractionation equation requires the bulk distribution coefficient to be constant during the crystallization and vapour exsolution interval considered. According to equations 5a and 5b, this condition will be met if the relative proportions of vapour and crystals formed remain constant and the values of $D_i^{xtl-melt}$ and $D_i^{vap-melt}$ remain constant over a given interval of crystallization and vapour exsolution.

To calculate the mass fraction of crystallization that relates two melt inclusion compositions, we use a separate statement of the Rayleigh fractionation equation for K_2O and assume that K_2O is perfectly incompatible. This yields:

$$X_{xtl} = 1 - \frac{C_{K_2O}^i}{C_{K_2O}^f} - X_{vap} \quad (6)$$

where $C_{K_2O}^i$ and $C_{K_2O}^f$ are the initial and final concentrations of K_2O . To calculate X_{vap} , we assume, for simplicity, that only H_2O exsolution is important, i.e., that exsolution of S, Cl, F and CO_2 is small compared to the mass of H_2O that is exsolved, and thus may be ignored. As a starting point, we use:

$$\frac{C_{K_2O}^f}{C_{K_2O}^i} = \frac{C_{H_2O}^*}{C_{H_2O}^i} \quad (7)$$

where $C_{H_2O}^*$ is the final dissolved H₂O concentration that the melt would have after crystallization and in the absence of any H₂O exsolution. Therefore:

$$C_{H_2O}^f + \frac{X_{vap}}{X_{melt}} = C_{H_2O}^* \quad (8)$$

where $C_{H_2O}^f$ is the concentration of dissolved H₂O in the melt after degassing and crystallization (i.e. the H₂O content measured for each melt inclusion). This allows us to calculate X_{vapor} as:

$$X_{vapor} = X_{melt} \left[C_{H_2O}^i \left(\frac{C_{K_2O}^f}{C_{K_2O}^i} \right) - C_{H_2O}^f \right] \quad (9)$$

The combination of equation 4 and equation 3 can be used to solve for \bar{D}_i .

Equations 4, 6 and 9 can be combined to solve for X_{vapour} and X_{xtl} , allowing for the apparent distribution coefficients $D_S^{vap-melt}$ and $D_{Cl}^{vap-melt}$ for any melt inclusion to be calculated using the H₂O, S, Cl, F and K₂O contents of the least evolved and least degassed melt inclusion as the initial condition and the melt inclusion of interest as the final condition. We do this by using:

$$\bar{D}_i = 1 + \left[\frac{\log \left(\frac{C_i^f}{C_i^i} \right)}{\log F} \right] \quad (10)$$

together with equation 2. C_i^i is the initial dissolved concentration of either S, Cl or F, and C_i^f is the final dissolved concentration.

Closed-system degassing

For the closed-system degassing case (with no initial exsolved gas present) we assume a batch crystallization and degassing process described by:

$$\frac{C_i^f}{C_i^i} = \frac{1}{F + \bar{D}_i(1-F)} \quad (11)$$

where F and \bar{D}_i are defined as for the open-system case described above. We calculate X_{xtl} using K_2O in a separate statement of equation 11 and assuming K_2O is perfectly incompatible. This yields the same result as equation 6. Therefore equation 9 holds for the closed-system case as well.

As with the open-system case, we can then solve for the apparent distribution coefficients $D_S^{vap-melt}$ and $D_{Cl}^{vap-melt}$ for any melt inclusion using the H_2O , S, Cl, F and K_2O contents of the least evolved and least degassed melt inclusion as the initial condition and the melt inclusion of interest as the final condition. We do so by using a rearranged version of equation 11:

$$\bar{D}_i = \frac{\left(\frac{C_i^f}{C_i^i} - F \right)}{1-F} \quad (12)$$

from which we then calculate $D_S^{vap-melt}$, $D_{Cl}^{vap-melt}$ and $D_F^{vap-melt}$ using equation 2.

Closed-system degassing with initial exsolved gas present or open-system degassing with gas fluxing

In this case we assume an initial condition of melt plus some amount of exsolved H_2O-CO_2 vapour. The initial vapour is assumed to contain no S, Cl or F. This might be the case where magma and entrained vapour ascended rapidly

from great depth because at the higher pressure condition, the high solubilities and low vapour-melt partition coefficients of F, Cl and S (Scaillet and Pichavant, 2005; Alletti et al., 2009; Aiuppa et al., 2009) keep them dissolved in melt, with little partitioning into the vapour phase. The equations for this case can also be used to model the situation where magma residing in the crust is fluxed with vapour from higher pressure (so the vapour initially has no F, Cl or S) because the equations describe mass balance for a system that contains more gas than it can internally generate. In both of these physical scenarios, the effect of the initial exsolved vapour during subsequent cooling, crystallization and decompression is to draw more of the dissolved S, Cl and F out of the melt and into the vapour phase. The net result is that for a given initial and final dissolved S, Cl and F content, the presence of the initial gas results in lower apparent $D_S^{vap-melt}$, $D_{Cl}^{vap-melt}$ and $D_F^{vap-melt}$ values than in either the open-system or closed-system (no initial exsolved gas) cases because there is more gas into which S, Cl and F are partitioning.

For the initial condition (assuming no S, Cl or F in the initial exsolved vapour), the mass of S, Cl or F in the system is $X_i^i (1 - X_{vap}^i)$, where X_i^i is the initial weight fraction of S, Cl or F dissolved in the melt and X_{vap}^i is the weight fraction of initial exsolved vapour. For the final condition of the system, we define F as the weight fraction of melt, X_{xtl} as the weight fraction of crystals, and X_{vap} as the weight fraction of vapour. Therefore:

$$X_{vap} = X_{vap}^i + X_{vap\ new} \quad (13)$$

where $X_{vap\ new}$ is the newly exsolved vapour. By mass balance, the initial and final concentrations of dissolved S, Cl or F can be described by:

$$X_i^i (1 - \alpha_o) = X_i^f F + X_i^f D_i^{xtl-melt} + X_i^f X_{vap} D_i^{vap-melt} \quad (14)$$

Where α_0 is the same as X_{vap}^i and X_i^f is the final weight fraction of S, Cl or F dissolved in the melt. If we again assume that no S, Cl or F goes into any crystallizing phases ($D_i^{xtl-melt} = 0$), then this mass balance relationship can be simplified and rearranged to yield:

$$D_i^{vap-melt} = \frac{\left[\frac{X_i^i(1 - X_{vap}^i)}{X_i^f} \right] - F}{X_{vap}^i + X_{vap\ new}} \quad (15)$$

Note that the mass fraction of initial exsolved vapour (X_{vap}^i) must be independently specified. $X_{vap\ new}$ is calculated using equation 9, and F is calculated again using $F = 1 - X_{xtl} - X_{vap}$.

Sources of uncertainty

The results of the modeled $D^{vap-melt}$ values for the different degassing scenarios are generally within error of each other. This means that the standard deviation between model $D^{vap-melt}$ values is smaller than the uncertainty associated with each determination. The one exception is at very low X_{vap} and X_{xtl} conditions (i.e. high F values) when the model values for different degassing scenarios diverge significantly due to the form of equations 10 and 12.

The uncertainty associated with each model $D^{vap-melt}$ value is mainly a function of the uncertainty in the initial magma H_2O , K_2O , S, Cl and F contents. As discussed in Chapter 4, choosing the lowest K_2O and highest H_2O contents represented in the melt inclusion suite is the most logical choice, assuming the melt inclusions are related to each other via simple degassing and crystallization. In the case of Kawah Ijen there is evidence for CO_2 vapour fluxing (Fig. 4-6, Chapter 4). The model does not take into account this complication and relies on the following assumption: the variability in melt inclusion H_2O and K_2O content is inherited during crustal processes such as CO_2 fluxing (which produces the same effect on H_2O contents as H_2O -saturated degassing; see Chapter 4) and

crystallization, and are not inherent to system initially (i.e. the parental magma has a fixed starting H₂O and K₂O content). The maximum extent of X_{vap} overestimation for the most CO₂ rich melt inclusions is 0.04 (4 wt% vapour). However, changing the initial H₂O content to the low-H₂O, high-CO₂ composition (Fig. 4-6a, Chapter 4) results in unrealistically elevated $D^{vap-melt}$ values of > 10 for the CO₂-rich melt inclusions (see text for discussion of average $D^{vap-melt}$ values in basaltic arc magmas) and fails to explain the higher-H₂O melt inclusions. The maximum standard deviation on S analyses yields an uncertainty in $D_S^{vap-melt}$ values of 5. For Cl, the maximum uncertainty is 2.

References

- Aiuppa, A., Baker, D.R., Webster, J.D., 2009. Halogens in volcanic systems. *Chem. Geol.* 263 (1-4), 1-18.
- Alletti, M., Baker, D.R., Scaillet, B., Aiuppa, A., Moretti, R., Ottolini, L., 2009. Chlorine partitioning between a basaltic melt and H₂O-CO₂ fluids at Mount Etna. *Chem. Geol.* 263 (1-4), 37-50.
- Johnson, E. R., Wallace, P. J., Cashman, K. V., Granados, H. D., 2010. Degassing of volatiles (H₂O, CO₂, S, Cl) during ascent, crystallization, and eruption at mafic monogenetic volcanoes in central Mexico. *J. Volcanol. Geotherm. Res.* 197 (1-4), 225-238.
- Scaillet, B., Pichavant, M., 2005. A model of sulphur solubility for hydrous mafic melts: application to the determination of magmatic fluid compositions of Italian volcanoes. *Annal. Geophys.* 48 (4-5), 671-698.
- Spilliaert, N., Métrich, N., Allard, P., 2006. S-Cl-F degassing pattern of water-rich alkali basalt: modeling and relationship with eruption styles on Mount Etna volcano. *Earth Planet. Sci. Lett.* 248 (3-4), 772-786.

Table 6-4 Additional analysed olivine-hosted melt inclusion compositions from Kawah Ijen (uncorrected for post-entrapment modification)

	ijenbas9	ijenbas3	ijenbas11	ijenbas5	ijenbas12x	ijenbas12ya	ijenbas1	ijenbas8	ijenbas7
(wt%)									
SiO ₂	45.4	45.5	45.3	48.2	45.0	45.6	45.7	45.4	46.1
TiO ₂	1.02	1.02	0.97	1.21	1.00	0.92	1.04	1.08	0.99
Al ₂ O ₃	18.4	18.3	17.6	15.5	16.8	16.8	18.4	18.5	18.5
FeO ^T	9.8	10.1	10.0	11.1	10.3	10.4	9.4	10.3	9.1
MnO	0.19	0.19	0.16	0.15	0.18	0.24	0.16	0.16	0.17
MgO	5.6	5.7	5.7	6.1	6.4	6.6	5.4	5.5	5.2
CaO	10.9	10.9	11.1	9.2	10.1	10.0	10.4	11.0	11.2
Na ₂ O	2.59	2.45	2.57	3.00	2.33	2.31	2.64	2.43	2.59
K ₂ O	0.61	0.60	0.59	0.93	0.57	0.57	0.73	0.63	0.61
P ₂ O ₅	0.19	0.24	0.20	0.28	0.17	0.17	0.23	0.20	0.25
S	0.203	0.198	0.211	0.043	0.156	0.159	0.203	0.220	0.220
Cl	0.083	0.088	0.092	0.102	0.077	0.063	0.084	0.067	0.084
F	b.d.l.	b.d.l.	b.d.l.	b.d.l.	b.d.l.	b.d.l.	b.d.l.	0.056	0.050
H ₂ O	4.26	3.40	3.43	1.03	5.24	5.62	4.02	3.45	3.72
CO ₂ (ppm)	2184	3478	3509	19	151	189	1204	1552	1030
Host Fo	79.9	79.9	80.1	80.1	80.9	80.9	80.0	78.6	79.6

Appendix D

FLYSPEC scans were conducted on the SE rim of the Kawah Ijen crater which allowed for traverses to be made, on foot, through the plume as it passed overhead. Wind speeds could be quite variable from day to day and even within a sampling period. As a result, average wind speeds were obtained for every 15 minute traverse period. Dominant wind directions were relatively steady at 97-98° (+ 0.7°) during the acquisition of the scans, however the path of the plume did wander laterally (NE-SW) along the rim of the crater during traverses. As such, the plume was often encountered more than once during a traverse. This led to the “puffing” pattern of the concentration pathlength of SO₂ recorded during a single scan. Each “puff” corresponds to the intersection of the plume path with the FLYSPEC location on the rim. These “puffs” may represent partial plume sampling when the FLYSPEC crosses beneath the plume momentarily before the plume shifts away from the instrument (generally occurred at the edges of the traverse, which also correspond to the edges of the plume’s lateral wandering path). These “puffs” are labeled as “edge of plume” and are underestimates of the total flux of SO₂ in the plume (Fig. 6-3). Additionally, wandering of the plume through the central portion of the traverse leads to sampling of “puffs” without returning to background (zero) concentration pathlength values in between. This leads to “incomplete” plume sampling and underestimates the total SO₂ flux (Fig. 6-3). To best determine the flux of SO₂ from the dome at Kawah Ijen, individual “puffs” were identified, taking care to avoid “puffs” from the edges of the plume. It was harder to avoid “puffs” with incomplete profiles (non-zero background

values). As such, the total SO₂ flux values measured at Kawah Ijen are underestimated but this underestimate will be minimal compared to the standard deviation of the measurements made over a single day (Chapter 5).

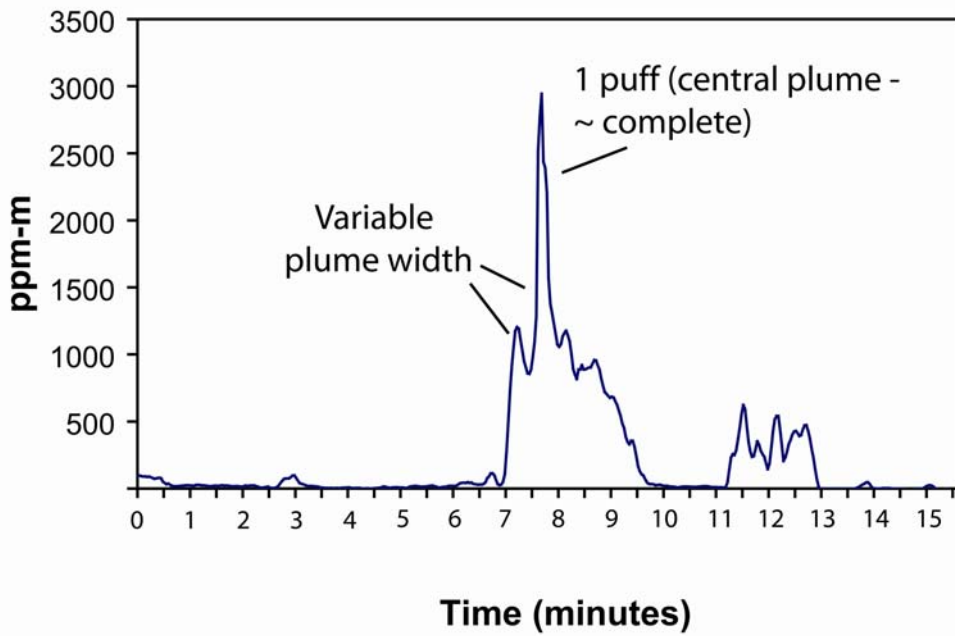
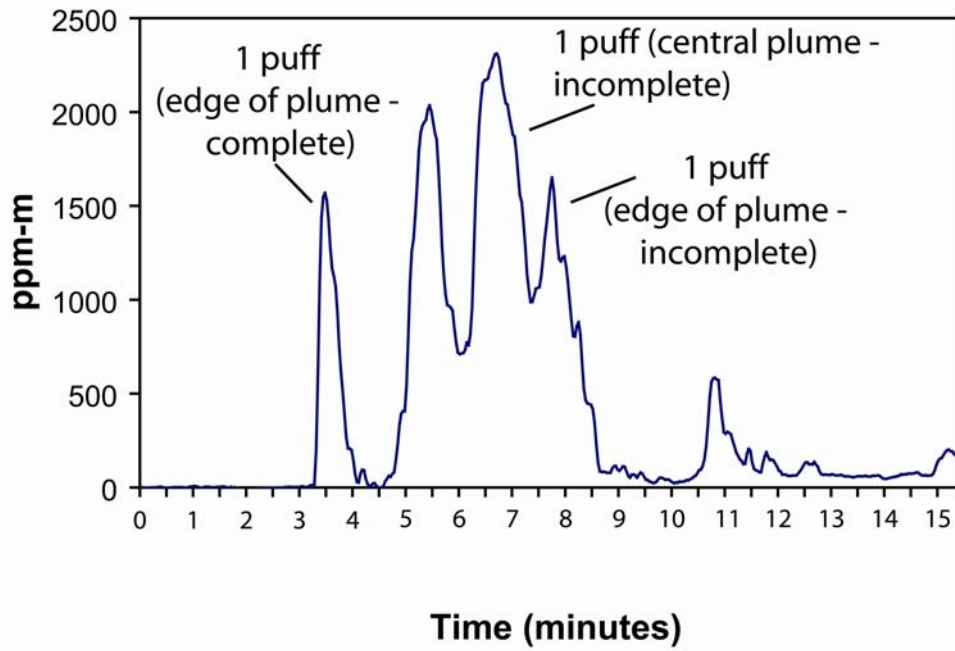


Figure 6-3 Concentration pathlength of SO₂ through the plume versus time (minutes) taken to traverse.